



U.S. Department
of Transportation
**Federal Railroad
Administration**

Novel Cryogen-free Actively Shielded Superconducting Magnets for Maglev Vehicles

National Maglev Initiative
Washington, D.C. 20590

DOT/FRA/NMI-92/07

June 1992
Final Report

This document is available to the
U.S. public through the National
Technical Information Service,
Springfield, Virginia 22161.

1. Report No. DOT/FRA/NMI-92/07		2. Government Accession No.		3. Recipient's Catalog No.	
4. Title and Subtitle Novel Cryogen-free actively shielded superconducting magnets for maglev vehicles				5. Report Date June 1992	
				6. Performing Organization Code	
				8. Performing Organization Report No.	
7. Author(s) M.E. Vermilyea				10. Work Unit No (TRIS)	
9. Performing Organization Name and Address General Electric CR&D P.O. Box 8 Schenectady, NY 12301				11. Contract or Grant No. DTR53-91-C-00079	
				13. Type of Report and Period Covered Final Report 8/91-6/92	
12. Sponsoring Agency Name and Address U.S. Department of Transportation, Federal Railroad Administration 400 Seventh Street, SW Room 8222, Washington, D.C. 20590				14. Sponsoring Agency Code RDV-7	
				15. Supplementary Notes COTR: Dr. A. Brecher U.S. Department of Transportation Volpe National Transportation Systems Center Kendall Square Cambridge, MA 02142	
16. Abstract <p>This report presents the results of a research effort into the design of a shielded superconducting magnet system for a maglev vehicle. The magnet design is based on a novel cryogen-free technology which allows operation without the use of any cryogenic fluids. This is accomplished by the use of a two-stage Gifford-McMahon (G-M) cryogenic refrigerator to provide cooling of the coil and a single cryostat thermal radiation shield by conduction. The design operating temperature of the magnet is 7.5 K, and that of the shield is 43 K. The magnet is wound with a tape form of niobium tin superconductor which allows operation at a module current density of 8100 A/cm² at a flux density of 3.4 T at the 7.5 K temperature with a margin of 4.5 K to critical temperature. The resulting magnet design is more reliable, rugged, and less expensive and heavy than a comparable pool cooled system, and is recommended for application to any maglev vehicles developed in the United States requiring superconducting magnets. Shielding of the passenger compartment of the vehicle from the DC magnetic field of the superconducting magnets is also investigated here for an assumed geometry. The geometry used is that of a sidewall, null-flux levitation and propulsion system, with the planes of the vehicle coils in a vertical orientation. Both active and passive shielding techniques are reviewed and applied to the assumed coil and vehicle geometry, with variations on the geometry considered to determine their effect on reducing the field in the passenger compartment. Options for reducing the field to certain levels are presented. The basic conclusion of the shielding study is that shielding using active coils is rather ineffective for the assumed geometry, and that the only realistic shielding methods are passive shielding (using iron in the vehicle structure) and shielding by distance (raising the vehicle farther above the magnets). The magnet design is coupled with a linear synchronous motor and null-flux sidewall levitation system to provide a workable maglev system design. Costs for several components of the design, including coils and cryostat, shielding, and power conditioning apparatus are estimated.</p>					
17. Key Words Superconducting magnet, maglev, shielding, cryogenics			18. Distribution Statement Document is available to the U.S. public through the National Technical Information Service, Springfield, VA 22161		
19. Security Classif. (of this report) UNCLASSIFIED		20. Security Classif. (of this page) UNCLASSIFIED		21. No. of Pages 221	22. Price

TABLE OF CONTENTS

ABSTRACT

SECTION 1: Introduction	1
1.1 Need for Superconducting Coils.....	2
1.2 Need for Refrigerated Magnet Technology	2
1.3 Need for Magnetic Shielding	4
1.4 Format and Content of this Report.....	5
1.5 Acknowledgements.....	8
SECTION 2: Superconducting Coil Design.....	9
2.1 Electromagnetic Design Including Winding Geometry.....	9
2.2 Support Structure Mechanical Analysis.....	15
2.2.1 Modeling	17
2.2.2 Results.....	18
2.2.3 Discussion of Results.....	23
Configuration 1.....	25
Configuration 2.....	25
2.2.4 Selection of Desired Configuration.....	28
2.2.5 Training of Superconducting Coil.....	30
2.3 Quench Analysis	31
SECTION 3: Levitation and Motor Coil Interactions.....	39
3.1 Linear Synchronous Motor Design.....	39
3.2 LSM Power Conditioning	45
3.2.1 Power Semiconductor Selection.....	45
3.2.2 Power Circuit Approach.....	46
3.2.3 Power Circuit Design	50
3.2.4 Power Conditioning Equipment.....	53
3.2.5 Summary.....	56
3.3 Null-flux Levitation/Guidance Coil Interaction.....	57
3.3.1 Null-flux Coil Electromagnetic Analysis	58
Magnetic Field Generated by superconducting Coils	59
Flux Linkage.....	64
Induced Current	64
EM Forces.....	65
3.3.2 Null-flux Coil Thermal Analysis	76

3.3.3	Skin Depth Effects in Null-flux Coil.....	77
3.3.4	Relative Vertical Locations of Null-flux, Armature and Superconducting Coils	78
3.3.5	Conclusions.....	79
3.4	AC Losses in Superconducting Coil	80
3.4.1	AC Fields Applied to the Superconductive Winding.....	81
3.4.2	Superconducting Winding AC Losses.....	87
	Superconductor hysteresis losses from transverse fields.....	87
	Stabilizer eddy current losses from transverse fields.....	88
	Superconductor hysteresis losses from longitudinal fields.....	91
	Stabilizer eddy-current losses from longitudinal fields.	91
	Total losses from combined longitudinal and transverse fields.....	92
	AC Field Shielding of Field Coil.....	97
	Other Operating Conditions: Low Speed, Thyristor Commutation Failure, Higher Motor Frequencies	99
SECTION 4:	Shielding	103
4.1	Active Shielding.....	103
4.1.1	Field Due to a Straight Current Filament	104
	Analysis Code	106
	Shielding Index.....	106
4.1.2	Passenger Compartment Fields with Various Arrangements of the Superconducting Coils.....	106
	Four coils per passenger compartment.....	107
	24 coils per passenger compartment	110
	24 coils per passenger compartment with reduced ampere-turns	115
	Symmetric vs. Antisymmetric Coil Arrangement.....	118
	Tilted Coils Configuration.....	118
4.1.3	Active Shielding Configurations.....	121
	Four-coil Configuration	121
	24 Coil Configuration.....	122
4.1.4	Conclusions.....	129
4.2	Passive Shielding	129
4.2.1	Stray Field Profile in the Absence of Shielding.....	129
4.2.2	Analysis Codes	130
	Two dimensional analysis.....	130
	Three dimensional analysis.....	130

Computer Hardware Used in Passive Shielding Analyses	131
4.2.3 Shielding Examples	131
Plate Shields on Train Car.....	135
Channel-Shaped Shields around Coils.....	140
Repositioning the Vehicle	146
4.3 Cost Estimate.....	150
SECTION 5: Cryostat Design.....	153
5.1 Structural Analysis.....	153
5.1.1 Design of Suspension Members.....	154
5.1.2 Analysis	156
5.1.3 Conclusions.....	161
5.2 Thermal Analysis Including Refrigeration	161
5.2.1 Thermal Radiation Shield.....	165
Radiation	165
Conduction.....	166
AC losses.....	168
5.2.2 Magnet Cold Mass	168
Radiation	168
Residual gas conduction.....	169
Conduction.....	169
AC losses.....	170
5.2.3 Relation to Cryocooler Performance	171
5.3 Cryostat and Magnet Cost Estimate.....	172
SECTION 6: Summary, Conclusions and Future Research recommendations	173
6.1 Summary of Research Performed Under this Contract.....	173
6.2 Conclusions of this Research Effort.....	174
Section 1: Superconducting magnet design	174
Section 2: Levitation and motor interactions	175
Section 3: Shielding.....	175
Section 4: Cryostat design.....	176
6.3 Recommendations for Further and Related Research.....	177
REFERENCES.....	179
APPENDIX A. Approximate Design Approach for a Superconducting Linear Synchronous Motor	181
A.1 Geometrical Assumptions	181
A.2 Basic Relations	182

A.3 Design Criterion	187
A.4 Examples	189
A.4.1 Large Magnets on Bogeys	189
A.4.2 Magnets Along the Vehicle with Increased Flux Density	190
A.4.3 Reduced Pole Pitch	190
A.5 Effects of Peaked Open Circuit Voltage	191
A.6 Conclusions	194
APPENDIX B. AC fields from a 3-phase linear winding	195
B.1 AC Fields from a 3-phase Linear Winding: Complex Exponential Formulation....	195
B.2 AC Fields from a 3-phase Linear Winding: Sine-Cosine Formulation.....	199
B.3 AC Field Spectrum.....	203
APPENDIX C. 3D EM Analysis Program H3D.....	204
APPENDIX D. Computer programs used in this study	209
APPENDIX E. Glossary	210
E.1 Nomenclature	210
E.2 Acronyms and Technical Terms	211

LIST OF FIGURES

Figure 1.1. Vehicle front view showing coordinate system.....	7
Figure 2.1.1. Critical surface for proposed niobium tin tape superconductor, showing SC coil load line.....	10
Figure 2.1.2. Racetrack coil geometry.....	11
Figure 2.1.3. Optimization parameter f vs. coil width w for 70 cm ² cross-section coil.....	14
Figure 2.2.1. End view of superconducting coil and support structure showing region analyzed for cooldown and excitation stresses.....	18
Figure 2.2.2. Support structure configurations analyzed.....	23
Figure 2.2.3. Displacement plot of the coil in the stand-alone configuration with cooldown and electromagnetic forces.	24
Figure 2.2.4. (a-d). Hoop (a), Axial (b), Radial (c) coil stresses and von Mises (d) aluminum stress under EM forces.	27
Figure 2.2.5. Engineering drawing of SC coil and preferred support structure.	29
Figure 2.3.1. Peak coil temperature vs. time during quench event.....	33
Figure 2.3.2. Temperature contours in z-r slice through hot spot at 8 seconds.....	34
Figure 2.3.3. Temperature contours in z-c slice through hot spot at 8 seconds.....	35
Figure 2.3.4. Coil thermal energy vs. time during quench event.....	36
Figure 2.3.5. Coil current vs. time during quench event.	37
Figure 2.3.6. Interlayer voltage in coil winding layers 1-2 vs. time during quench event.....	38
Figure 3.1.1. Schematic side view of guideway showing null-flux and armature coils with SC coils shown for scale.....	40
Figure 3.1.2. Schematic front view of guideway showing null-flux and armature coils with SC coil shown in actual position in cryostat.....	41
Figure 3.1.3. Side and front views of vehicle showing SC coils in bogey at end of vehicle....	44
Figure 3.2.1. Two transistor analogy of GTO.....	47
Figure 3.2.2. Block diagram of AC-DC-AC drive.	49
Figure 3.2.3. Alternating Resonant Commutated Pole (ARCP) phase leg.	49
Figure 3.2.4. Circuit diagram for AC-DC-AC, ARCP inverter, linear synchronous motor drive.	51
Figure 3.2.5. GTO/Diode/Resonant capacitor/Gate drive switch.....	54
Figure 3.2.6. AC-DC rectifier and GTO DC-AC inverter rated at 7000 hp (5.2 MW).....	55

Figure 3.3.1. The sidewall levitation system. A pair of superconducting coils passing a guideway composed of several null-flux coils, showing direction of motion of superconducting coils and one null-flux coil enlarged for detail.	58
Figure 3.3.2. Superconducting coils and single null-flux coil for analysis.....	59
Figure 3.3.3. A current loop showing geometry definitions.....	60
Figure 3.3.4. 3-D field profile of B_x from pair of SC coils of Figure 3.3.2 geometry.....	61
Figure 3.3.5. 3-D field profile of B_y from pair of SC coils of Figure 3.3.2 geometry.....	62
Figure 3.3.6. 3-D field profile of B_z from pair of SC coils of Figure 3.3.2 geometry.	63
Figure 3.3.7. Induced current in the null-flux coil for $v=140$ m/sec as a function of z , where $z=z_2$ as shown in Fig. 3.3.2.	66
Figure 3.3.8. Guidance force from a single null-flux coil interaction as a function of z for the geometry of Fig. 3.3.2.	66
Figure 3.3.9. Levitation force from a single null-flux coil interaction as a function of z for the geometry of Fig. 3.3.2.	67
Figure 3.3.10. Drag force from a single null-flux coil interaction as a function of z for the geometry of Fig. 3.3.2.	67
Figure 3.3.11. Forces over the length of a null-flux coil for a superimposed case where the ratio of the superconducting coil pair length to the null-flux coil length is 5.2.....	69
Figure 3.3.12. Levitation force vs. offset for superconducting coil pair at 140 m/s for Case 4 geometry.....	73
Figure 3.3.13. Levitation force vs. velocity for superconducting coil pair at a 10 cm offset for Case 4 geometry.....	73
Figure 3.3.14. Levitation force vs. velocity for superconducting coil pair at a 3 cm offset for Case 4 geometry.	74
Figure 3.3.15. Guidance force vs. velocity for superconducting coil pair at a 3 cm offset for Case 4 geometry.	75
Figure 3.3.16. Drag force vs. velocity for superconducting coil pair at a 3 cm offset for Case 4 geometry.....	75
Figure 3.3.17. Possible relative locations of null-flux, superconducting and armature coils.	79
Figure 3.4.1. B_x , B_y and B_z profiles vs z for 1 MA-t in motor coil, observation plane at $x=0.16$ m.	82
Figure 3.4.2. 120-degree motor current waveform.	83
Figure 3.4.3. Location of 14 sampling point around 1/4 racetrack.....	83
Figure 3.4.4. Unshielded B_x applied to field coil.	84
Figure 3.4.5. Unshielded B_l applied to field coil.....	85
Figure 3.4.6. Mutual flux (Wb) from 1 MA-t motor coil.....	86

Figure 3.4.7. Tape superconductor.	88
Figure 3.4.8. Magnetic Field Shielding by Conductive Slab.....	89
Figure 3.4.9. Transverse field screening in tape superconductor.....	90
Figure 3.4.10. Longitudinal field screening in tape superconductor.	91
Figure 3.4.11. Bx vs Bl loci around field coil.	93
Figure 3.4.12. Single unshielded field coil AC loss components from uniform applied Bx at 144 Hz.	95
Figure 3.4.13. Unshielded AC losses around field coil.	96
Figure 4.1.1. The formula (obtained by integrating the Biot-Savart (formula) for the magnetic field at the origin due to a straight filament carrying current I between r1 and r2.....	105
Figure 4.1.2. The 4-Coil Configuration.	108
Figure 4.1.3. Flux Patterns in a 4-Coil Configuration.....	109
Figure 4.1.4. Field Profile in the 4-Coil Configuration.. Stray Field Index vs Coil Separation for a 4-Coil Configuration.....	111
Figure 4.1.5. Stray Field Index vs Coil Separation for a 4-Coil Configuration.	112
Figure 4.1.6. The 24-Coil Configuration.....	113
Figure 4.1.7. Flux Patterns in a 24-Coil Configuration.	114
Figure 4.1.8. Stray Field Index vs Coil Separation for a 24-Coil Configuration.....	116
Figure 4.1.9. Stray Field Index vs Coil Separation for a 24-Coil Configuration (reduced current).	117
Figure 4.1.10. Coils located on either side of a compartment energized in the same sense to reduce the stray field in the compartment.	119
Figure 4.1.11. Stray Field Index vs Tilt Angle.	120
Figure 4.1.12. Shielding arrangement in which one row is added to the base 4-coil configuration.	123
Figure 4.1.13. Effect of Introducing One Intermediate Row of Shielding Coils.	124
Figure 4.1.14. Shielding arrangement in which one row is added to the base 24-coil configuration.....	125
Figure 4.1.15. Effect of Introducing One Intermediate Row of Shielding Coils.	126
Figure 4.1.16. Shielding arrangement in which two rows are added to the base 24-coil configuration.....	127
Figure 4.1.17. Effect of Introducing Two Intermediate Rows of Shielding Coils.	128
Figure 4.2.1. Train Car Without Shielding (cross-sectional view) Flux Density Iso-Contours in Gauss.	132
Figure 4.2.2. Train Car Without Shielding (side view) Flux Density Iso-Contours in Gauss..	133
Figure 4.2.3. 3-D Finite Element Model.....	134

Figure 4.2.4. Two Thin (1 cm.) Plates Flux Density Iso-Contours in Gauss.	136
Figure 4.2.5. Thick (7 cm.) Plate Flux Density Iso-Contours in Gauss.....	137
Figure 4.2.6. Thick (7 cm.) Plate With 1 Meter Extensions Flux Density Iso-Contours in Gauss.	138
Figure 4.2.7. Thick (7 cm.) Plate With 1 Meter Side Shield Flux Density Iso-Contours in Gauss.	139
Figure 4.2.8. 5 cm. Channel With 50 cm. Extensions Flux Density Iso-Contours in Gauss...	141
Figure 4.2.9. 7 cm. Channel With 50 cm. Extensions Flux Density Iso-Contours in Gauss...	142
Figure 4.2.10. 5 cm. Channel + 2 cm. Plate With 50 cm. Extensions Flux Density Iso-Contours in Gauss.	143
Figure 4.2.11. 5 cm. Channel + 2 cm. Plate With 50 cm. Extensions + Extra Corner Plate Flux Density Iso-Contours in Gauss.....	144
Figure 4.2.12. 5 cm. Channel + 2 cm. Plate With 50 cm. Extensions (Reduced Current 20%) Flux Density Iso-Contours in Gauss.....	145
Figure 4.2.13. Flux density variation with vertical distance from coil set.....	147
Figure 4.2.14. 2-D Model Without Shielding Flux Density Iso-Contours in Tesla.	148
Figure 4.2.15. 2-D Half Model. Channel + Plate With Extensions Flux Density Iso-Contours in Tesla.	149
Figure 4.2.16. 2-D Half Model. Side Shield 1.5 m High Flux Density Iso-Contours in Tesla.	151
Figure 4.2.17. 2-D Half Model. Side Shield 2.5 m High Flux Density Iso-Contours in Tesla.	152
Figure 5.1.1. 3-D Finite element model of magnet assembly.....	157
Figure 5.1.2. Displacement plot for case 2.....	157
Figure 5.1.3(a-d). Hoop (a), Axial (b), Radial (c) coil stresses and von Mises (d) aluminum stress under all forces.	160
Figure 5.2.1. Load map for 5 kW G-M cryocooler.....	164
Figure A.1. Typical flux density distribution, in the plane of the stator, from the SC magnet..	183
Figure A.2. Two winding concepts for the guideway.	186
Figure A.3. Comparison of power converter terminal voltages for various flux density distributions.....	192
Figure A.4. Effect of redistributing the SC coil current.....	193

LIST OF TABLES

Table 2.1.1. Superconducting coil operating parameters	15
Table 2.2.1. Mechanical properties of superconducting coil composite material	16
Table 2.2.2. Mechanical strength of superconducting coil composite material.....	16
Table 2.2.3. Mechanical Properties of aluminum 6061	17
Table 2.2.4. Strength of aluminum (6061-T6 plate, welded, heat treated to T6 and tested).....	17
Table 2.2.5. Stresses and displacements in the superconducting coil in a stand-alone configuration.....	19
Table 2.2.6a. Stresses in the coil and support structure in assembled configuration 1.	21
Table 2.2.6b. Stresses in the coil and support structure in assembled configuration 2.	22
Table 3.1.1. Design parameters and characteristics of six linear motor designs	43
Table 3.2.1. Alternate motor requirements	45
Table 3.2.2. Power conditioner designs.....	52
Table 3.2.3. Power conditioning costs.	56
Table 3.3.1. Cases chosen for superconducting - null-flux coil interaction study.....	70
Table 3.3.2. Levitation, guidance and drag forces for cases 1 through 10 and various null-flux coil itches	71
Table 3.4.1. AC losses for base case including cryostat shielding	97
Table 3.4.2. AC losses with copper cladding on cryostat.....	98
Table 3.4.3. AC losses at reduced speed	99
Table 3.4.4. AC losses for base cryostat design at 720 Hz	101
Table 3.4.5. AC losses with copper cladding at 720 Hz.....	101
Table 5.1.1. Dimensions and estimated properties of the suspension members	156
Table 5.1.2. Stresses in the coil and support structure for the complete assembly.....	158
Table 5.1.3. Stresses in the suspension members.....	159
Table 5.2.1. Heat inputs to the thermal shield along magnet mechanical supports	167
Table 5.2.2. Heat inputs to the thermal shield of the proposed magnet.....	168
Table 5.2.3. Heat inputs to the cold mass along magnet mechanical supports.....	169
Table 5.2.4. Heat inputs to the cold mass of the proposed magnet.....	171
Table 5.3.1. Magnet and cryostat costs.....	172

ABSTRACT

This report presents the results of a research effort into the design of a shielded superconducting magnet system for a maglev vehicle. The magnet design is based on a novel cryogen-free technology which allows operation without the use of any cryogenic fluids. This is accomplished by the use of a two-stage Gifford-McMahon (G-M) cryogenic refrigerator to provide cooling of the coil and a single cryostat thermal radiation shield by conduction. Because of the high heat removal capacity of the G-M unit, only a single thermal radiation shield is required, as compared to two for a typical helium pool cooled magnet. The design operating temperature of the magnet is 7.5 K, and that of the shield is 43 K. The magnet is wound with a tape form of niobium tin superconductor which allows operation at a module current density of 8100 A/cm² at a flux density of 3.4 T at the 7.5 K temperature with a margin of 4.5 K to critical temperature. This margin represents an adequate amount to handle expected thermal disturbances. The resulting magnet design is more reliable, rugged, and less expensive and heavy than a comparable pool cooled system, and is recommended for application to any maglev vehicles developed in the United States requiring superconducting magnets. Shielding of the passenger compartment of the vehicle from the DC magnetic field of the superconducting magnets is also investigated here for an assumed geometry. The geometry used is that of a sidewall, null-flux levitation and propulsion system, with the planes of the vehicle coils in a vertical orientation. Both active and passive shielding techniques are reviewed and applied to the assumed coil and vehicle geometry, with variations on the geometry considered to determine their effect on reducing the field in the passenger compartment. Options for reducing the field to certain levels are presented. The basic conclusion of the shielding study is that shielding using active coils is rather ineffective for the assumed geometry, and that the only realistic shielding methods are passive shielding (using iron in the vehicle structure) and shielding by distance (raising the vehicle farther above the magnets). The magnet design is coupled with a linear synchronous motor and null-flux sidewall levitation system to provide a workable maglev system design. All pertinent engineering calculations for the levitation, guidance, thrust, and drag forces are performed. A null-flux coil design is presented with a single turn and aluminum conductor. Several linear synchronous motor designs are considered, and a rationale for selection of the preferred design suggested. The power conditioning for the motor armature windings is also considered. Costs for several components of the design, including coils and cryostat, shielding, and power conditioning apparatus are estimated.

SECTION 1: INTRODUCTION

The United States is struggling to develop a new transportation strategy for future generations. Our present dependence on fossil fuels for our transportation needs, consumed in an inefficient manner by millions of individual cars, trucks and aircraft for transportation is widely decried as a problem which requires immediate attention at the highest levels. One method of improving the transportation system is with high-speed ground transportation (HSGT), which is understood to mean inter-city transport and which typically refers to steel-wheel-on-rail trains or maglev vehicles. While the latter alternative is in its infancy when compared to the former, it has attracted much positive attention in the news media and in the federal legislative and executive branches. The reasons for this interest include the unrealized potential and the still-present belief of the American populace in high technology as a solution to their problems. For these and other reasons, the implementation of maglev transportation systems in the United States is being considered by several states, local municipalities, and the Federal government.

An important step to understanding the issues involved in implementing such a transportation system is the determination of innovative technologies that could differentiate a United States-developed maglev system from those systems presently under development or already developed in Germany and Japan. Such a study has been undertaken by the Federal Railroad Administration, an arm of the United States DOT, in the form of its 1990 Broad Agency Announcement.

The technology investigated in this report has the potential to improve the reliability and to reduce the costs of maglev systems. The general theme is the application of conduction-cooled or refrigerated superconducting magnets to an electrodynamic suspension (EDS) maglev system, replacing conventional superconducting magnets that are cooled by using liquid helium. This technology has been proved in the laboratory and is in the process of being evaluated for application to GE's magnetic resonance imaging magnet manufacturing line. The present research indicates that such magnets are ideally suited for use in maglev systems; they represent major improvements in the size, cost, and reliability of the magnet system and could be readily designed for a candidate system approximating the latest version of the Japanese technology. A prototype design for this system is presented here.

Magnetic shielding is another important topic to be considered prior to implementation of a maglev system. While DC magnetic fields above certain levels have proved to have deleterious effects on certain inanimate objects, their effects on biological systems are poorly understood. The topic of magnetic shielding is presently a controversial one, but one that is likely to persist into the foreseeable future. Therefore, the present study also treats the issue of passenger compartment shielding from the high DC magnetic fields generated by the superconducting vehicle coils of an

EDS maglev system. Both active (using other electromagnets) and passive (using ferromagnetic material) shielding means are investigated. The results of these studies indicate that reduction of the field from the unshielded case by orders of magnitude, as would be required to meet a field specification of 10 gauss or below, comes at a high price in terms of vehicle weight or cost.

1.1 Need for Superconducting Coils

Electrodynamic suspension (EDS) maglev systems may well be the technology of choice for the United States because of their low magnetic drag, high efficiency, and their ability to operate with large levitation gaps resulting in high tolerance to guideway imperfections and obstructions. Such systems require superconducting magnets to provide the high magnetic fields which produce the large vehicle-guideway gaps. Of our foreign competition, the Japan Railways group has also opted for this technology and has developed several prototype vehicles using various configurations of superconducting magnets. They have proved that this technology is available and workable [1].

Of the technology areas which impact EDS maglev system design, superconductivity has perhaps seen the most advances since the mid-1970's, when early United States and international maglev studies and system developments were performed. The advent of MR imaging as a major medical diagnostic technology has led to the large-scale commercial manufacture of large superconducting magnets for the first time in history, resulting in considerable improvements over early laboratory-based systems in the reliability and manufacturability of both superconducting wires and superconducting magnets. Furthermore, the discovery of high-temperature ceramic superconductors and subsequent developments increasing their critical currents and manufacturability, bode well for a future in which the technology of superconductivity will become more widely applied.

1.2 Need for Refrigerated Magnet Technology

There exist several potential difficulties in implementation of an EDS maglev system using superconducting magnets. Despite the great strides made in improving the reliability and manufacturability of the magnets, they are still typically cooled by immersion in a pool of liquid helium. This pool is usually maintained at or above the required level in one of two ways.

The first is simply to refill it on a regular basis. Unfortunately, the refilling interval is inversely proportional to the volume of the reservoir, and directly proportional to the size of the heat-carrying mechanical supports required to position the magnet inside a thermally insulating vacuum envelope. A maglev vehicle has constraints on size and weight of its components inherent

in any transportation technology. Therefore the magnet, and hence the reservoir volume, should be minimal in size and weight. Furthermore, the magnet supports must bear all static and dynamic loads involved in supporting the vehicle and would contribute a significant heat load to the helium reservoir.

While the helium boiloff rate for a pool-cooled maglev vehicle magnet would depend on the specific design, the necessity of carrying the entire vehicle load coupled with cryostat size limitations could drive the interval between refills down significantly from the interval presently obtained. For example, a typical MRI magnet has a helium reservoir of about 1000 liters, and a boiloff rate of about 0.15 liters per hour, leading to a refill time of about nine months. The mass which the supports must carry in such a magnet is about 1000 kg. For comparison, a maglev vehicle might use four magnets for support of a total mass of 24000 kg, thus each set of magnet supports must carry about 6000 kg. Each magnet would be of a size comparable to, or larger than, an MRI magnet. Therefore, to maintain the nine-month refill interval with larger supports and possibly a larger cryostat, a helium reservoir volume of greater than 4000 liters would be required. In the event that economical considerations limit the size of the reservoir to less than 4000 liters, the refill time would be shorter than nine months. While the helium pool could be replenished at every terminal, in which case the refill interval could be much shorter, the time involved in liquid helium transfer and the expense of helium losses incurred in such a system could be prohibitive.

The second method of maintaining the reservoir level involves either recondensing or reliquefying the boiloff helium gas using a cryogenic refrigeration device called a recondenser or a liquefier. This is the approach used by the Japan Railways (JR) systems and is possibly the best of the two conventional approaches. Unfortunately, the reliability of helium liquefiers, even in a laboratory or hospital environment, is known to be poor. Typically, such machines require service at 1000-hour intervals or less. It is known that the JR systems have had some problems with their systems, although the exact data on their system reliability are not known to this author. Furthermore, the weight and size of these machines is considerable. A comparison to the two-stage cryorefrigerator, which this report investigates for cooling, will be made later.

Two other issues regarding the use of liquid helium are the large pressures that can be generated by a loss of superconductivity in the coils or a loss of vacuum insulation and resulting sudden increase in heat load to the helium pool and the fluid dynamic analysis required to ensure that the magnets will operate stably in a dynamic environment. In the event of vacuum loss or a quench, the high-pressure helium gas must be quickly vented, or an explosion of the vessel could occur. Modern dewars are designed with pressure relief devices which essentially eliminate the

chances of such a catastrophic event, but the issue of venting large volumes of boiloff vapor from the vehicle is a real one. The fluid dynamic issue also requires investigation; anecdotal information indicates that the Japanese design had some difficulties related to such effects.

Given these cost, safety, and reliability issues associated with the use of pool-cooled magnets, the method of cooling the vehicle superconducting magnets is an important area for technology development. In this study, we evaluate the applicability of a new magnet technology to maglev vehicle coils. We refer to this technology as "refrigerated magnet technology," by which we mean that the magnet structure is cooled by conduction to a closed cycle refrigerator rather than by immersion in a pool of cryogenic fluid. The advantages of such a technology are numerous. First, the large heat removal capability of the refrigerator at two stages – one operating at the coil temperature and the other at that of the thermal radiation shield – allows the design of a cryostat with a single thermal radiation shield, rather than the two required to limit the helium boiloff in a pool-cooled system to a reasonable level, allowing for reductions in the size, weight, and cost of the cryostat. The magnitudes of such reductions will, of course, depend on the specifics of the design. Second, the same increase in heat-removal capability allows the operation of the magnet with the current leads permanently connected. In a helium pool-cooled system, the amount of heat input, and consequent helium boiloff, from permanently connected leads is high because of the high thermal conductivity of these leads. Finally, the higher temperature coil operation results in more cryogenic stability because of the higher material heat capacity at these higher temperatures (heat capacity varies as the cube of temperature in this low-temperature range) – i.e., the coil can withstand a higher amount of frictional heating without transitioning to the normal state. The size, weight, cost, and reliability of the refrigerated magnet design are all improved over that of a conventional magnet. The sole potential difficulty in implementing this technology is the requirement that the superconducting material be able to operate at a temperature of 8 K or higher. This rules out the use of the most widely available and most ductile superconducting material, niobium titanium, and requires the use of a more brittle and less widely available intermetallic material such as niobium tin. While niobium tin superconductors actually predate niobium titanium in application, they remain more difficult to obtain and work with. However, proven niobium tin superconductors are available from several commercial vendors in several forms and can also be ordered to a design specification. Therefore, the difficulties of working with the material are far outweighed by the benefits of vastly improved magnet performance.

1.3 Need for Magnetic Shielding

Another potential passenger safety issue arises because of passenger and crew exposure to electromagnetic fields, both time varying (AC) and static (DC). There have been many studies on

the subject of environmental issues associated with DC and/or AC magnetic fields. For example, Blanchard [1989] explores the current state of knowledge on magnetic field effects upon animals (including man) and electronic devices and communication, citing more than fifty references. These studies have not resulted in the determination of any biological effects which would lead to the necessity of imposing limits on AC and DC fields. However, there are some firm limits on the DC field which certain devices should experience. Such devices include cardiac pacemakers and magnetic media in computer diskettes, and credit cards [Hayes 1987]. We wish to show how the configuration of maglev vehicle magnets might be driven by the requirement of reducing the stray DC field.

Developing a magnet design which provides the large DC magnetic field (0.5 tesla or greater) necessary for levitation and linear motor excitation while maintaining the static field in the passenger compartment at much lower levels (0.005 tesla or less) proves a significant design challenge, especially when weight, volume, and cost considerations are included. For vertical plane, null-flux geometry systems exhibiting a reasonably small vertical separation between the magnets and the passenger compartment, active shielding coils may well be required as part of the superconducting magnet package. In addition, passive shielding material in the form of iron or steel will probably be required. In the event that a system design with the vehicle located far above the coils is possible, designs employing only passive shielding may be realistic. Of course, the important criterion is the level to which the field must be reduced.

1.4 Format and Content of this Report

The work performed under this contract, while all pertaining to a single general topic, fell into several disparate technical areas. Therefore, the underlying assumptions for the different parts of the study differed slightly to ensure that the various analyses could be performed efficiently and, often, simultaneously. For instance, a canonical superconducting coil geometry was chosen to facilitate structural analysis of the cryostat and support structure, while the null-flux interactions generating levitation and guidance forces were analyzed for various superconducting coil geometries. The four technical sections of the report are presented separately, and the results of each should be interpreted as much as possible without considering the other sections. If a complete system design were required, these various analyses would have to be performed in concert, with any attendant optimizations receiving inputs from all pertinent analyses. An example of the complexity involved here is the combined motor and levitation/guidance analysis required. With the sidewall levitation system, the interaction between the armature windings for the motor and the null-flux coils cannot be ignored as has been done for simplicity in this study. Since the null-flux coils are mounted in the guideway in a position that yields a mutual inductance with the

armature windings of the motor, currents will be induced in them by the motor current. These currents have been ignored in the analysis presented in Section 3 of this report. The results and designs presented here are optimal to the extent that the analyses considered the many factors affecting optimality and should not be considered to be representative of a truly optimized system design. More factors influence the system design than were accounted for in these analyses, and the undertaking of a complete system optimization was far beyond the scope of this study.

The statement of work for this contract called for analysis of a superconducting coil design using refrigerated magnet technology for a maglev vehicle. The analysis included shielding of the passenger compartment, development of the coil and cryostat design, and a first order treatment of the motor and levitation coil interactions to ensure that the coil design presented was adequate for its purpose. Sections 2 through 5 of this report correspond to tasks 1 through 4 from the statement of work, respectively. Thus Section 2, coil design, represents work done to fulfill Task 4.1; Section 3, motor and levitation interactions, represents Task 4.2; Section 4, Shielding, represents Task 4.3; and Section 5, cryostat design, Task 4.4.

For each technical section, the analyses presented, and the conclusions drawn therefrom, were designed so that the insights gained would be applicable to the design of a complete system. Where simplifications were made to facilitate obtaining some useful results, the important simplifications are noted, and their probable effect discussed. If a complete system design were desired, these effects would all have to be accounted for, and the analysis tasks would become far more complex and interrelated. The SI system is used throughout the report.

Numerous computer programs were used throughout this work. Descriptions of the programs are to be found in the sections where their results are presented. In addition, Appendix D contains short descriptions of each program and analyses for which each was used.

Appendix E details nomenclature, acronyms, and technical terms which appear throughout this report.

Cost estimates have been provided for the superconducting coil, its cryostat, and its refrigeration system. These estimates can be considered to be reasonably accurate, based as they are on the principal author's familiarity with commercial manufacturing of superconducting coils. The passive shielding materials chosen are common grades of steel, and their costs are estimated on a per pound basis. The power conditioning apparatus costs were estimated using conservative "ballpark" figures provided by GE Drive Systems in Salem, VA. While many other systems were

analyzed as part of this study, estimating their costs with any degree of accuracy is beyond the capability of the principal author.

The use of the terms "field" and "flux density" should be noted at this point. The units of tesla and gauss measure magnetic flux density (B), not magnetic field (H) – which is measured in A/m or oersted. However, in air, the relationship between these two quantities is given by

$$B = \mu_0 H \tag{1.1}$$

where μ_0 is the permeability of free space. Since this linear relation exists between the two quantities, the term "field" is often used to refer to flux density, and is presented with units of gauss or tesla. We will use the terms interchangeably in this report, as was done in the introductory section discussing shielding, to avoid confusing readers who aren't aware of the above relationship.

The coordinate system used for almost all analyses is shown in Figure 1.1. The z-axis is out of the page in this figure.

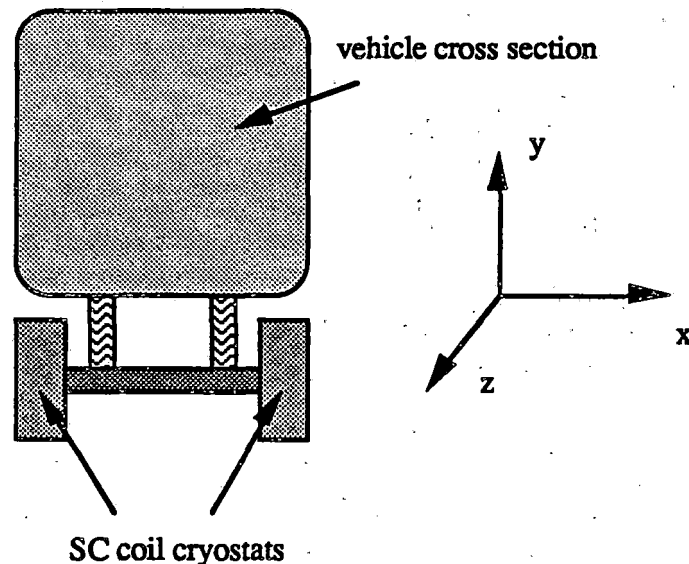


Figure 1.1. Vehicle front view showing coordinate system.

Coordinates x, y, and z refer to the transverse, vertical, and longitudinal directions of the vehicle, with the longitudinal direction being the same as the direction of motion. The origin of the coordinate system varied depending on the particular analysis in question. For example, the superconducting coil electromagnetic analysis had its origin at the center of mass of the

superconducting coil, while that used for shielding analyses had as its origin the center of mass of a bogey containing several coils. The superconducting coil structural analysis was performed with the x- and z-axes rotated about the y-axis because of the requirements of the particular finite-element analysis package used. For an analysis where the location of the origin is required for understanding, that location will be made clear.

1.5 Acknowledgements

The GE R&D Center is fortunate to have, situated at a single site, world-class researchers in many disciplines. The analytical efforts undertaken for this contract, which included motor and electrodynamic analysis as well as superconducting coil design, required significant input from no less than ten such individuals, who are named here. Dr. Mark Vermilyea was the project manager, and performed electromagnetic analysis of the superconducting coil, thermal analysis of the cryostat, and cost analyses of both. Dr. Lembit Salasoo analyzed the AC losses in the superconducting coil and cryostat components, and assisted in motor and levitation analyses. Dr. Costas Minas performed extensive structural analysis of the coil and cryostat. Dr. Kamal Kalafala led the effort in shielding studies, and performed the principal analysis of active shielding. Ms. Michele Ogle and Mr. Tom Sober performed active and passive shielding analyses. Dr. Jerry Kliman performed linear motor analysis and assisted in the specification of the power electronic system, as did Dr. Rik DeDoncker. Mr. Fred Turnbull performed the principal analysis of the power conditioning circuitry for the linear motor. Dr. Habib Massoudi performed the principal analysis of the interaction between the vehicle coils and the guideway null-flux coils which provides levitation forces. The authors would like to thank Mr. Al Cooper for his professional and capable assistance in preparing the engineering drawings included with this report, and Ms. Rosanne Raid for her patience and diligence in preparing and proofing.

SECTION 2: SUPERCONDUCTING COIL DESIGN

2.1 Electromagnetic Design Including Winding Geometry

The first issue to be addressed in any superconducting coil design deals with the peak field in the winding at design current and temperature. Since magnetic field (which may be used interchangeably with flux density in this context) is one of the three quantities along the axes of which the critical surface is defined for any material, its magnitude directly affects the operation of the coil. Specifically, as the field increases, the "operating margin" of the coil decreases. The operating margin is generally defined as the amount of localized energy deposition or temperature rise the coil can withstand without some portion of the superconductor transitioning to the normal state. When some of the coil transitions to the normal state and continues to increase in temperature, the resulting event is referred to as a quench. The critical surface, i.e., the surface defining the superconducting state for a given material, can be plotted on a simple two-axis plot of current (or current density) vs. field (or flux density) as a series of curves, each representing the intersection of the critical surface with a constant temperature plane at a particular temperature. Since the field is linearly related to the conductor current for systems without other field sources, a "load line" representing this linear relationship can be defined on the same plot. Figure 2.1.1 depicts a critical surface for our proposed tape superconductor along with the load line for our proposed coil geometry.

While the critical surface for a given material is plotted using current density, the more useful form for magnet design is plotted using current. The determination of current requires the specification of a geometry for the wire. For this study, we have chosen a superconducting "tape" made of niobium tin sandwiched between two copper sheets. Such materials have been developed in the past by several research organizations, primarily for research magnet applications. Other conductors would certainly be applicable to a maglev vehicle magnet, including multifilamentary and "jelly-roll" conductors made using the internal tin or bronze processes. In fact, such conductors are advantageous from a standpoint of reducing the AC losses that are created when the superconducting coil is placed in a time-varying magnetic field (to be discussed later in this report). However, the tape geometry conductor has the potential to be lower cost because of the simpler manufacturing technology required for its production. While the choice of superconductor is important for several reasons, for the purposes of the present study, the choice of tape is reasonable. If this study were to be extended to the prototype development stage, other conductor choices would certainly be considered.

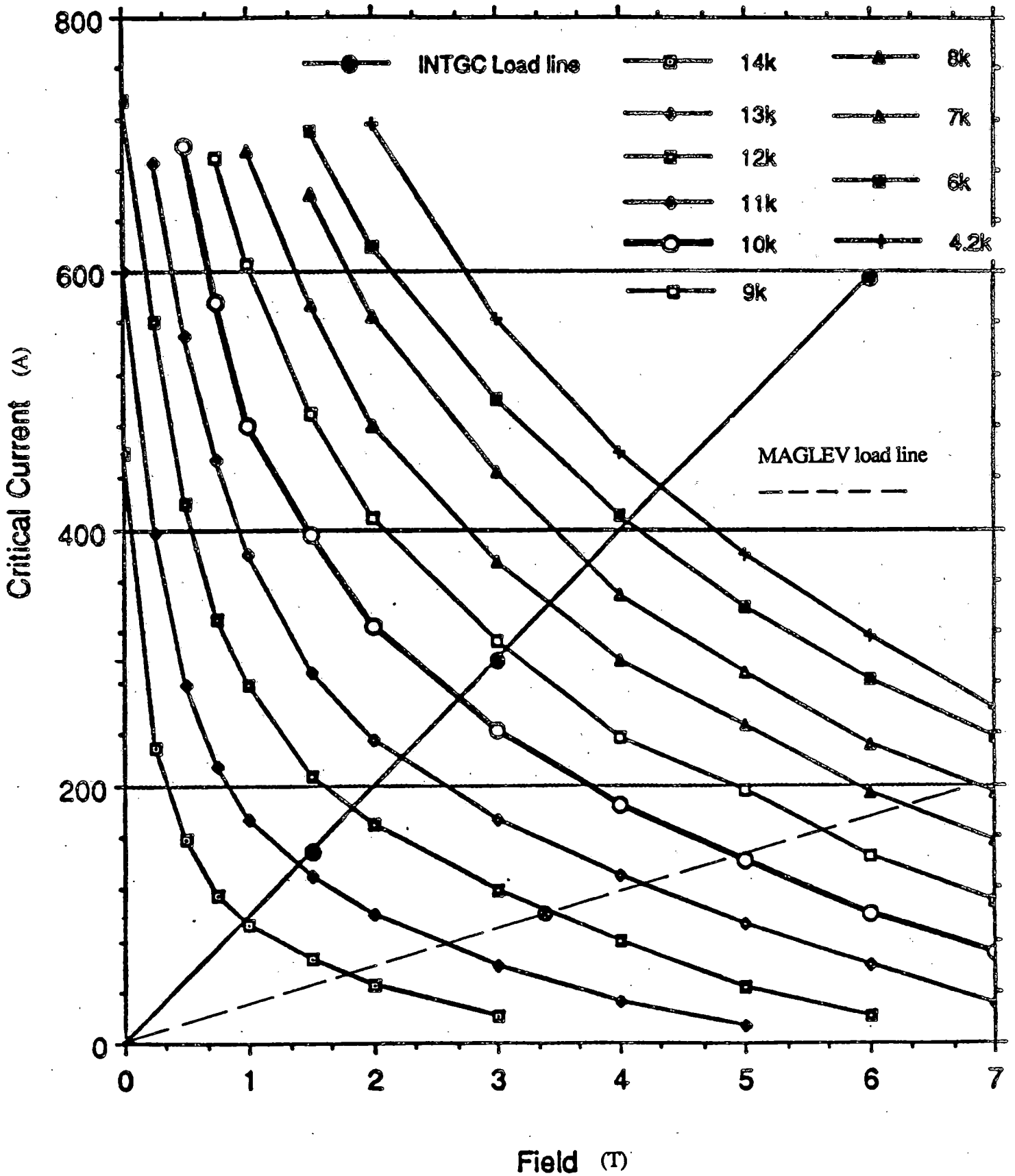


Figure 2.1.1. Critical surface for proposed niobium tin tape superconductor, showing SC coil load line.

The determination of the optimal coil geometry for a given application must take into account the desired operating characteristics of the coil. For the coil under consideration here, (its basic geometry is shown in Figure 2.1.2), its function would be to provide horizontal (x-directed) magnetic flux at the windings in the guideway. This flux, upon interaction with the null-flux coils and motor armature windings, must produce the desired levitation, guidance, and propulsion forces. For both of these purposes, higher flux levels are generally better. Therefore, our objective for the coil design was to provide the highest possible flux density at the guideway coils with the least possible superconductor. This objective function effectively allows us to determine the optimal aspect ratio of coil width, w , to radial build, b , for a given height, H and length, L .

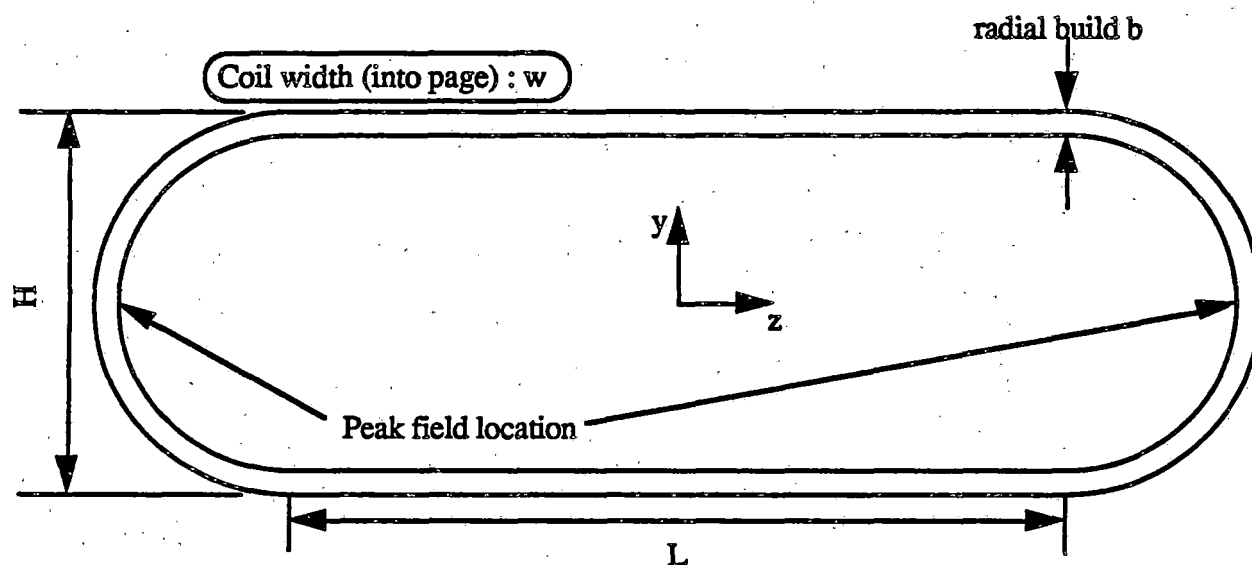


Figure 2.1.2. Racetrack coil geometry.

The determination of the optimal values of H and L for the superconducting coil requires a complete optimization of the motor and levitation systems. While the analyses performed for this study addressed most of the important aspects leading to such an optimization, a comprehensive analysis was beyond our scope here. Therefore, the values of H and L were chosen as 0.5 and 2.0 m, respectively. These values were not chosen arbitrarily, in fact they represent approximations to the recently redesigned coils for the newest Japan Railways design to be implemented in the Yamanashi test facility, which are also to be used together with null-flux windings and a linear synchronous motor.

With H and L specified, the coil volume is proportional to the product (w)(b). Therefore, a simple objective function to be used to maximize the useful transverse flux at the guideway windings for a given coil volume becomes

$$f = B_x(g,0,0)/wb \quad (2.1.1)$$

where g represents the x location of the guideway coil of interest, which may be either the null-flux winding or the armature winding depending on whether the levitation or motor operation is being treated. This function should be maximized by appropriate choice of w and b. An approach to the coil optimization can therefore be broken down into three steps:

- 1) Choose values of w and b, which determine the peak field B_{max} for a given current I and which define the load line for the coil;
- 2) Specify an operating temperature and temperature margin, which fixes the intersection of the load line with the critical surface;
- 3) Determine the peak field B_x at the design location of the guideway coils, and thus the optimization parameter f (using Eq. 2.1.1).

Additional information, which must be assumed or provided from other analyses, includes the required field at the guideway, B_x , and the transverse (x-direction) distance from the superconducting coil to the guideway, g. The required field cannot simply be scaled by increasing superconducting coil current because of limitations imposed by the current-carrying capability of the superconductor. For the refrigerated magnet technology considered here, the operating temperature of the magnet cold mass (which includes the coil and its support structure, as well as other systems such as the superconducting switch) is dictated by the refrigerator cold head temperature, which in turn depends on the heat loads imposed on the refrigerator. Therefore, the heat transfer to the cold mass from radiation and conduction determines the operating temperature for a given refrigerator. The coil operating temperature is somewhat higher because of the temperature difference across the thermal joints connecting the refrigerator to the coil. For the two-stage refrigerator type proposed here, the heat loads to both stages jointly determine the operating temperatures. A complete thermal analysis of the cryostat is given in Section 5 of this report, with a figure depicting the stage operating temperatures of a commercially available refrigerator as a function of their heat loads. The remainder of this discussion will be based partly on the conclusions of Section 5, in which the operating temperatures of the cryostat members are predicted - one of the areas mentioned in the introduction where the different sections of the analysis are intricately interwoven.

The coil operating temperature will therefore be taken to be 10 K. This conservatively chosen temperature is higher than that obtained from the analysis of Section 5, but additional margin is built into the proposed design to provide additional robustness of operation. This 10 K temperature can easily be reached with commercially available cryogenic refrigerators and with the heat loads to be expected for a maglev vehicle magnet. Using a temperature margin of 2 K, the choice of which is based on our experience in building and testing similar magnets, the next step in determining the coil operating point is to specify the current as that at which the load line intersects the 12 K contour of the critical surface in Figure 2.1.1. Using this critical surface and a nominal operating temperature of 10 K with a temperature margin to the critical surface of 2 K, steps 1 to 3 of the optimization process described above were taken for an assumed coil straight side length of 2.0 m, a coil overall height of 0.5 m, a flux density at the armature windings of 0.6 T, and a transverse gap from the superconducting coil to the armature winding of 0.15 m. The latter two values were obtained from initial motor analyses (presented in Section 3) and from an estimate of the clearance from the cryostat outer vessel to the guideway. The gap estimate was developed for a given cryostat and guideway design which we consider to be reasonable (see layout drawings included with this report). Using the chosen values of operating temperature and temperature margin, we use the 12 K critical current characteristic of the superconductor, which may be represented in terms of flux density as

$$I_c = 9 B^2 - 100 B + 338 \quad (2.1.2)$$

Determination of the coil cross section to be used requires some trial and error, but with the chosen flux density of 0.6 T at a distance of 15 cm from the superconducting coil center, a coil cross section of 70 cm² is required. The optimization parameter f is plotted in Figure 2.1.3 as a function of coil width for a coil cross section of 70 cm². As can be seen, the maximum value of the parameter is achieved at a width of about 5 cm, which implies a coil build of 14 cm. GE's experience in superconducting winding fabrication indicates that coils with large build:width ratios are more difficult to wind and support effectively. Since GE-CRD has never built a coil with such a large build:width ratio, the proposed design has a width of 7 cm, with a build of 10 cm, which we feel comfortable that we could wind and support. This choice represents a small reduction of less than 4% in flux density at the guideway for the given coil cross section, as seen by comparing the value of f for the chosen design of about 90 to that for the optimal design of about 93. While it is possible that a coil with an aspect ratio of almost 3:1 could be wound and supported, we feel that the small increase in flux density is not justified by the decreased mechanical integrity of the coil.

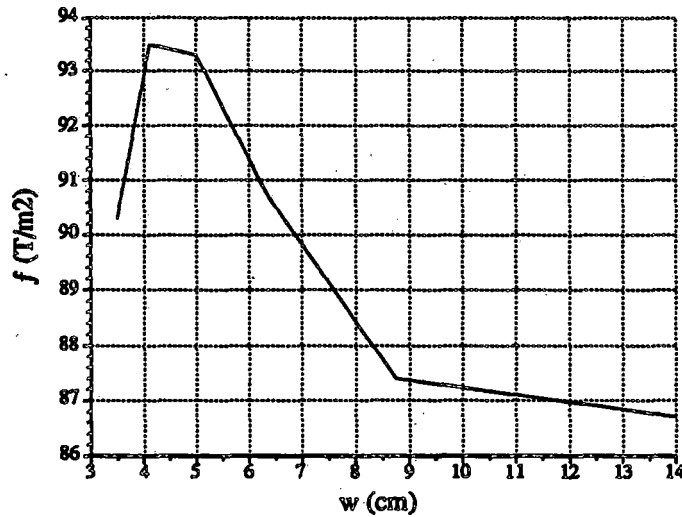


Figure 2.1.3. Optimization parameter f vs. coil width w for 70 cm^2 cross-section coil.

The load line for the optimized coil geometry is drawn on Figure 2.1.1. The tape superconductor corresponding to Figure 2.1.1 is a composite formed by soldering copper foil with a thickness of approximately $76 \mu\text{m}$ on either side of a niobium foil with a thickness of $25 \mu\text{m}$. The resulting sandwich is then annealed at high temperature to form an intermetallic compound which is predominantly niobium tin at the interlayer boundaries. This intermetallic compound is the superconductor, and the copper forms the stabilizer into which current can transition in the event of a quench. The coil's peak flux density, which is at the radially inner surface of the center of the end turns, as shown in Figure 2.1.2, is used to define the load line. The relation between this peak flux density and the coil current density is given by

$$B_{\max} = (2.19\text{e-}4) J \quad (2.1.3)$$

where B_{\max} is the peak flux density in T, and J is the coil current density in A/cm^2 . The coil current density can be related to the current in the tape superconductor using the as-wound cross section of the tape. This cross section, which is significantly larger than the tape itself because of insulation and impregnating epoxy, is about 0.038 by 0.33 cm , which leads to the relation

$$J = (79.4) I \quad (2.1.4)$$

where I is the current in A. Therefore, the peak coil flux density may be expressed in terms of the conductor current as

$$B_{\max} = (0.0174) I \quad (2.1.5)$$

This relation allows us to draw the load line in Figure 2.1.1. The current at which the load line intersects the 12 K contour is 102 A, and the corresponding peak flux density in the coil is 3.4 T. Table 2.1.1 summarizes the important operating parameters of the proposed coil.

Mechanical:

Conductor cross section (mm).....	3.0 wide by 0.28 thick
As-wound conductor dimensions, including insulation (mm).....	3.3 wide by 0.38 thick
Number of layers.....	263
Number of turns/layer.....	21.2
Superconductor length (m).....	29300
Superconductor weight (kg).....	170
Coil weight (including insulation and epoxy) (kg).....	192
Nominal safe operating temperature (K).....	10

Electrical:

Operating current (A).....	102
Total ampere-turns.....	568700
Current density (A/cm ²).....	8100
Peak flux density in coil (T).....	3.4
Flux density at midheight of armature winding (T).....	0.63

Table 2.1.1. Superconducting coil operating parameters

Several design parameters could be varied if other considerations warranted. Reducing the straight side length is beneficial from a coil mechanical support standpoint, as the straight sides experience Lorentz forces that tend to ovalize the racetrack and that are difficult to react. However, the mechanical support structure presented for this coil, described in the following subsection, is not unreasonable in terms of cost or weight, the two primary design criteria here. In the limit of a circular coil, the construction and support become far simpler. In fact, our linear motor analysis suggests that circular coils are attractive in reducing the pole pitch of the motor windings and consequently increase the motor efficiency (see results from Task 4.2 in Section 3). They have been proposed in other publications [Hayes 1987]. However, levitation force considerations tend to drive the straight side length higher, so circular coils are not necessarily the optimal design.

2.2 Support Structure Mechanical Analysis

The forces generated on the straight sides of a racetrack-shaped coil are large and lead to large stresses in the coil if the coil is unsupported. Therefore, a support structure that contains the coil

and limits these stresses and strains has been designed. We have developed several different designs of mechanical support systems. Using the ANSYS finite element stress analysis package and with inputs from a computer program called RACEFOR, which computes the forces within a racetrack coil resulting from its electrical excitation, we have analyzed the states of stress of the unsupported coil during both cooldown and excitation. The separate analysis of the cooldown forces is generally unnecessary for an unsupported coil, but such an analysis becomes important when the coil is mounted in a support structure because of the different thermal contraction coefficients typically exhibited by the support structure and the coil. After several iterations on the mechanical design of the support structure, a suitable geometry was found. Use of this geometry will limit the cooldown and excitation stresses to within acceptable limits for the support material as well as the coil composite. The acceptable limits for the coil composite were determined through extensive testing of actual composites at GE-CRD.

E_x	5.895	ν_{xy}	0.201	31.68
E_y	39.832	ν_{yz}	0.414	12.95
E_z	55.794	ν_{xz}	0.299	11.29
Shear Modulus in 10^9N/m^2				
Prediction		Using equation (3)		
G_{xy}	5.516		4.882	
G_{yz}	23.51		17.279	
G_{xz}	5.516		5.040	

Table 2.2.1. Mechanical properties of superconducting coil composite material

Strength in MN/m^2	Tension	Compression
S_x	7.980 (± 0.683)	
S_y		-101.2 (± 0.52)
S_z		-228.4 (± 25.11)
Shear Strength in MN/m^2		
S_{xy}	6.883 (± 1.317)	
S_{xz}	5.603 (± 2.255)	

Table 2.2.2. Mechanical strength of superconducting coil composite material

The ultimate tensile strength (UTS) of the anisotropic superconducting coil composite was experimentally measured at room temperature and the results are presented in Table 2.2.2. Some of the entries in the table have not been filled because of lack of data. The mechanical properties and the strength (UTS) of the aluminum are presented in Tables 2.2.3 and 2.2.4 [Battelle 1975].

Young's Modulus in 10^9N/m^2	Poisson's ratio	Thermal Expansion coefficient in $10^{-6}/\text{K}$
68.0	0.33	14.7

Table 2.2.3. Mechanical Properties of aluminum 6061

UYS @ 293 K in MN/m^2	@ 10K	UTS @ 293 K	@ 10K
248	309	299	452

Table 2.2.4. Strength of aluminum (6061-T6 plate, welded, heat treated to T6 and tested)

2.2.1 Modeling

An analysis was carried out on the racetrack coil in a stand-alone configuration and in an assembled configuration. The assembled magnet configuration presented in Figure 2.2.1, consists of the racetrack superconducting coil, an aluminum collar and an aluminum side plate. Only one eighth of the complete coil is necessary for modeling if one takes into consideration the symmetry of the coil about the three axes. The stress analysis was carried out in the ANSYS environment, using the linear static analysis option with 3D brick elements (STIF45) [ANSYS 1989]. The elements were defined with an appropriate node order such that the orthotropic material properties align with the model's radial, axial and hoop directions. As a result, the calculated stresses can be resolved in radial, axial and hoop directions. The finite element model of the assembly consisted of 4000 nodal points and 2401 3D elements. For example, the nodal distribution along the three coordinates of the superconducting coil were 10, 6 and 50 nodes in the radial, axial and hoop directions respectively, which caused an element distribution of 9, 5 and 49 elements in the radial, axial and hoop directions.

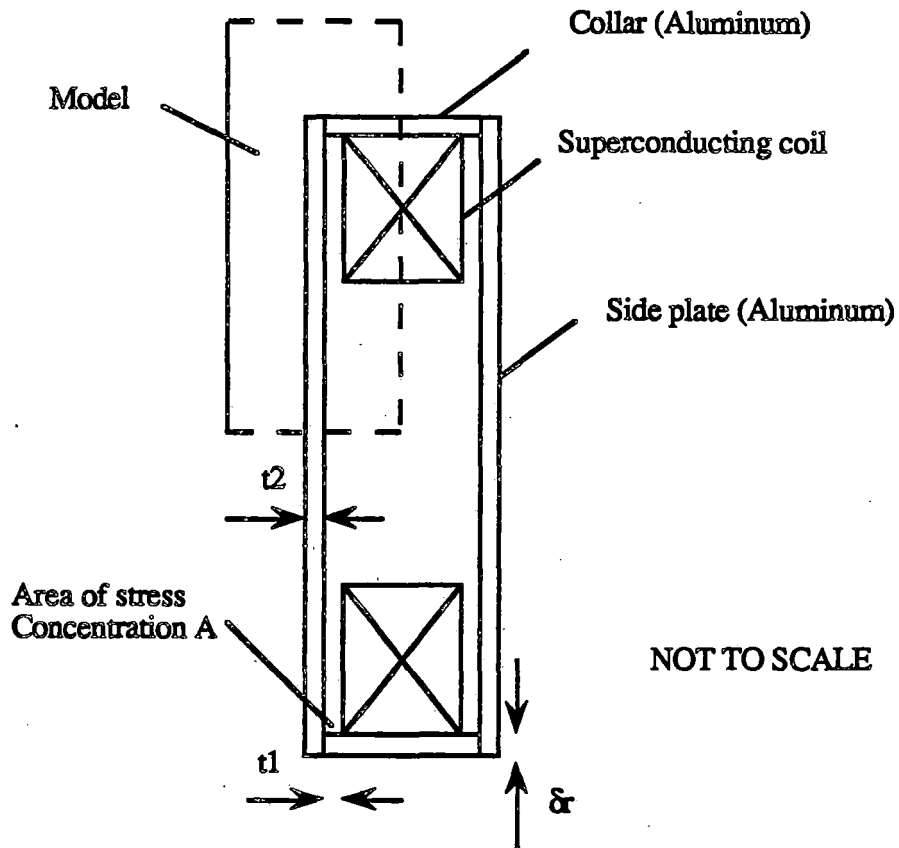


Figure 2.2.1. End view of superconducting coil and support structure showing region analyzed for cooldown and excitation stresses

The cooldown analysis was carried out in a linear fashion from 293 to 10 K. The electromagnetic forces were distributed on the nodes of the coil in the form of x, y, and z forces, where x, y, and z are the cartesian coordinate system shown in Figure 2.2.1. The net forces applied to the analyzed section of the coil were 34.72, 127.8 and 361.0 KN in the x, y, and z directions, respectively.

2.2.2 Results

Initially the analysis was carried out on the racetrack coil itself in a stand-alone configuration. The stress analysis results are presented in Table 2.2.5, in the form of maximum compressive (negative) and tensile (positive) stresses in the coil in the three directions, and maximum displacements in the cartesian coordinate system. The cooldown stresses are shown to be very low with negligible radial and axial stresses. On the contrary, under the electromagnetic load, the hoop stresses are shown to be very high at 854 MN/m^2 which will cause fracture of the superconducting coil composite. The radial tensile stress is at 82.6 MN/m^2 , which is over ten

times higher than the radial strength of the superconducting coil composite. The coil displacement presented in Figure 2.2.3 is shown to have a maximum value of 6.2 cm occurring at the middle of the coil because of excessive bending. Clearly, a support structure is required to react these high loads on the coil. This analysis was performed primarily to show the magnitude of the forces which the structure must withstand.

	Cooldown	Cooldown with EM forces
	Stress in MN/m ²	
Hoop	-1.19 to 1.44	-534.0 to 854.0
Axial	-0.002 to 0.006	0.330 to 5.39
Radial	-0.003 to 0.154	-5.84 to 82.6
	Maximum Displacement in mm	
ux	-3.92	-9.00
uy	-1.07	61.73
uz	-0.30	-0.44

Table 2.2.5. Stresses and displacements in the superconducting coil in a stand-alone configuration

The second analysis was carried out on the racetrack coil in an assembled configuration presented in Figure 2.2.1. A support structure was designed with the following requirements:

- (a) minimize the stresses in the coil composite
- (b) reduce the displacement of the coil
- (c) add minimum weight to the system
- (d) add minimum axial buildup to the system
- (e) provide means for the suspension of the system
- (f) good conductivity characteristics

The selected material for the support structure was aluminum alloy 6061-T6 which is light weight with good strength and conductivity characteristics. The idea was to enclose the coil inside the support structure such that it cannot bend outwards when the large electromagnetic forces are applied. The support structure presented in Figure 2.2.1, consists of an aluminum collar and an aluminum side plate. Under cooldown the aluminum collar shrinks on the coil causing a low compression interface. The side plate which can only support tension is under tension because it is

constrained from shrinking by the collar. When the coil is energized, the side plate reacts the vertical electromagnetic force which tends to spread the straight sides of the racetrack coil causing high stresses and excessive bending.

Two different configurations which were analyzed are presented in Figure 2.2.2. The first one consisted of a long collar that covered the coil in the straight section and extended to the end of the curved section of the coil. The main advantage of this boxed structure is the fact that it is simple to manufacture and assemble. The second configuration consisted of two collars, one over the straight section and one of the curved section of the coil, with the side plate extended only to a part of the straight section. The advantage of this configuration is the fact that it is lighter than the first one and does not have the area of stress concentration B, presented in Figure 2.2.2. In both configurations, there existed an area of stress concentration A, shown in Figure 2.2.1, where the side plate meets the collar. Several parameters such as the radial thickness of the collar (δr), the thickness of the side plate (t_2), and the clearance of the side plate (t_1) were determined such that the stresses in the coil and the aluminum were reduced. The results are presented in Tables 2.2.6a and 2.2.6b, for configurations 1 and 2, respectively, in the form of maximum compressive (negative) and tensile (positive) stresses in the coil in the three directions. The stresses in the aluminum support structure are presented in the form of minimum and maximum von Mises stress in the same Table. The maximum displacements of the structure are also presented in Tables 2.2.6a and 2.2.6b.

Case	δR	t_1	t_2	Coil Composite			Aluminum			ux	uy	uz
				Hoop Stress	Axial Stress	Radial Stress	Von Mises	Stress in MN/m ²				
		in mm										
1a ¹	25.4	3.175	3.175	-37.7 to 22.5	-4.98 to 25.3	-31.9 to 11.6	0.08 to 131.0	-4.72	-1.21	-0.43		
1b ²				-41.0 to 40.1	-4.57 to 25.3	-37.8 to 7.71	0.14 to 173.0	-4.69	-1.21	-0.30		
2a	19.05	3.175	3.175	-38.9 to 20.6	-4.66 to 24.1	-35.7 to 8.35	0.18 to 145.0	-4.69	-1.18	-0.49		
2b				-42.4 to 37.5	-4.15 to 23.8	-46.5 to 9.11	0.34 to 192.0	-4.65	-1.19	-0.30		
3a	25.4	1.588	3.175	-42.0 to 23.9	-4.93 to 25.3	-32.3 to 10.5	0.09 to 159.0	-4.71	-1.21	-0.41		
3b				-46.4 to 42.0	-4.50 to 25.3	-40.2 to 8.37	0.17 to 209.0	-4.68	-1.21	-0.30		
4a	25.4	3.175	1.588	-34.6 to 21.5	-5.17 to 25.7	-30.3 to 10.2	0.09 to 116.0	-4.67	-1.23	-0.50		
4b				-37.2 to 39.8	-4.84 to 26.1	-35.7 to 6.27	0.17 to 157.0	-4.67	-1.24	4.82		
5a ³	25.4	3.175	1.588	-35.0 to 21.7	-5.17 to 25.8	-30.4 to 10.3	0.09 to 117.0	-4.69	-1.22	-0.31		
5b				-37.7 to 39.9	-4.84 to 26.1	-35.7 to 6.31	0.19 to 159.0	-4.67	-1.24	-0.30		

Table 2.2.6a. Stresses in the coil and aluminum in the assembled configuration 1

1 : Cooldown Analysis from 293 to 10 K

2 : Cooldown Analysis and Electromagnetic forces distributed on the coil

3 : This configuration has axial connections passing through the coil

Case	δR_1 in mm	δR_2 in mm	L in m	Coil Composite				Aluminum			ux	uy in mm	uz	
				Hoop Stress	Axial Stress	Radial Stress	Von Mises	Stress in MN/m ²						
6a ¹	25.4	25.4	1.0	-31.4 to	-1.65	-2.98 to	22.0	-31.8 to	12.2	3.22 to	94.0	-4.41	-1.20	-0.52
6b ²				-27.6 to	2.89	-0.94 to	22.0	-35.7 to	4.71	2.61 to	131.0	-4.31	-1.12	-0.32
7a	25.4	25.4	0.75	-31.2 to	4.33	-2.95 to	22.0	-28.9 to	12.8	6.86 to	94.3	-4.41	-1.20	-0.49
7b				-27.3 to	24.4	-1.05 to	22.0	-36.4 to	6.77	11.7 to	157.0	-4.37	-1.12	-0.32
8a	12.7	25.4	1.0	-31.4 to	7.48	-3.48 to	22.0	-35.1 to	13.1	3.98 to	102.0	-4.34	-1.20	-0.53
8b				-27.5 to	13.9	-1.07 to	21.6	-41.5 to	4.95	2.97 to	140.0	-4.23	-1.12	-0.37
9a	12.7	12.7	1.0	-30.1 to	7.28	-3.49 to	20.8	-48.4 to	8.69	4.44 to	120.0	-4.27	-1.16	-0.76
9b				-27.4 to	10.0	-1.37 to	21.1	-62.1 to	5.38	2.57 to	168.0	-4.15	-1.08	-0.43
10a	12.7	12.7	20x0.05 ³	-26.1 to	5.45	-3.47 to	20.8	-34.1 to	8.44	0.36 to	91.7	-4.16	-1.11	-0.90
10b				-19.8 to	17.9	-0.89 to	21.4	-37.6 to	4.76	12.4 to	103.0	-4.03	-0.90	-2.14

Table 2.2.6b. Stresses in the coil and aluminum in the assembled configuration 2

- 1 : Cooldown Analysis from 293 to 10 K
- 2 : Cooldown Analysis and Electromagnetic forces distributed on the coil
- 3 : The side plate is replaced with Individual beams
- 4: $t_1 = 3.175$ mm and $t_2 = 3.175$ mm in all cases

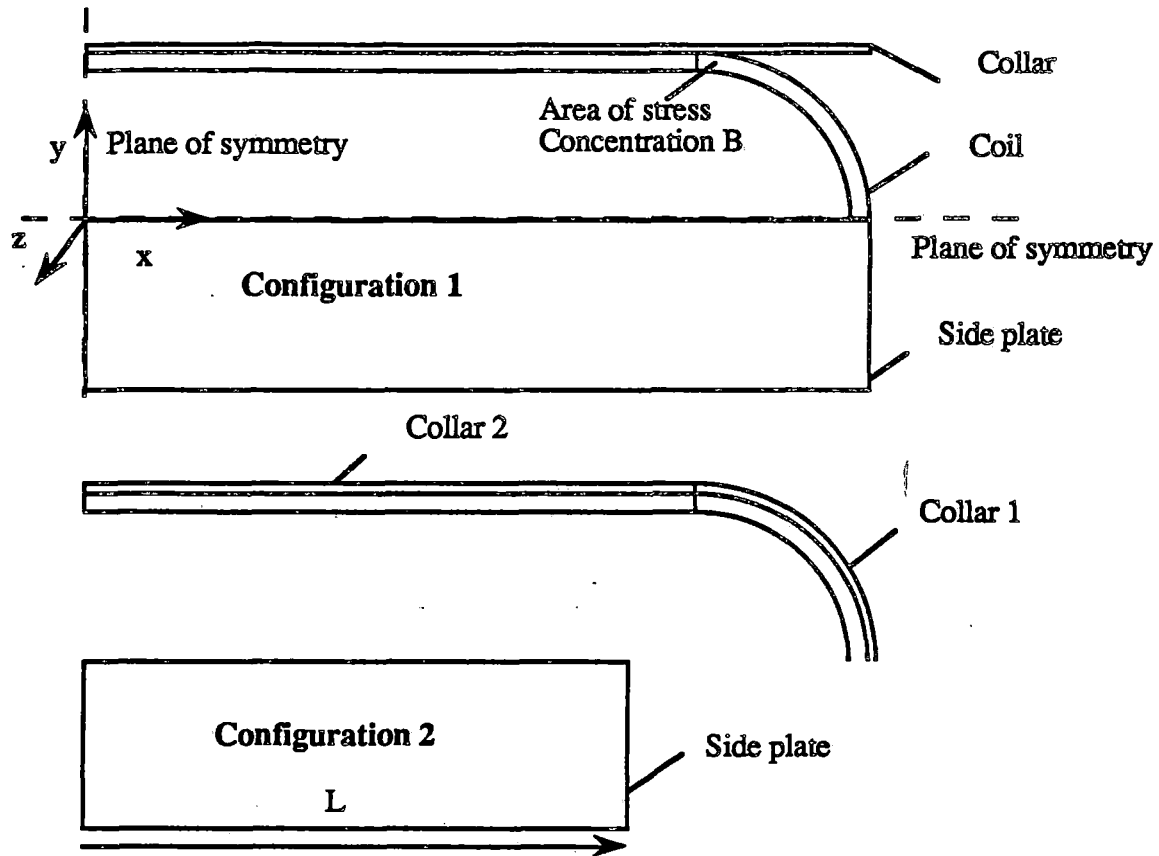


Figure 2.2.2. Support structure configurations analyzed.

2.2.3 Discussion of Results

The results in Tables 2.2.6a and 2.2.6b clearly indicate that the cooldown stresses in the coil in the assembled configurations are no longer negligible. This is caused by the fact that the aluminum collar shrinks on the coil creating a high compression interface. The axial stress shows a low value of -5.17 to 26.1 MN/m^2 and no significant variation throughout both tables. This is because of the fact that the axial forces are well distributed in the entire cross-section of the coil. The hoop stress in the coil composite is in the range of -46.4 to 39.9 MN/m^2 which is within the strength of the material. The radial tensile stress is shown to be higher than the radial tensile strength of the coil composite in several cases. The von Mises stress in the aluminum has values far below the yield strength of the material in all cases.

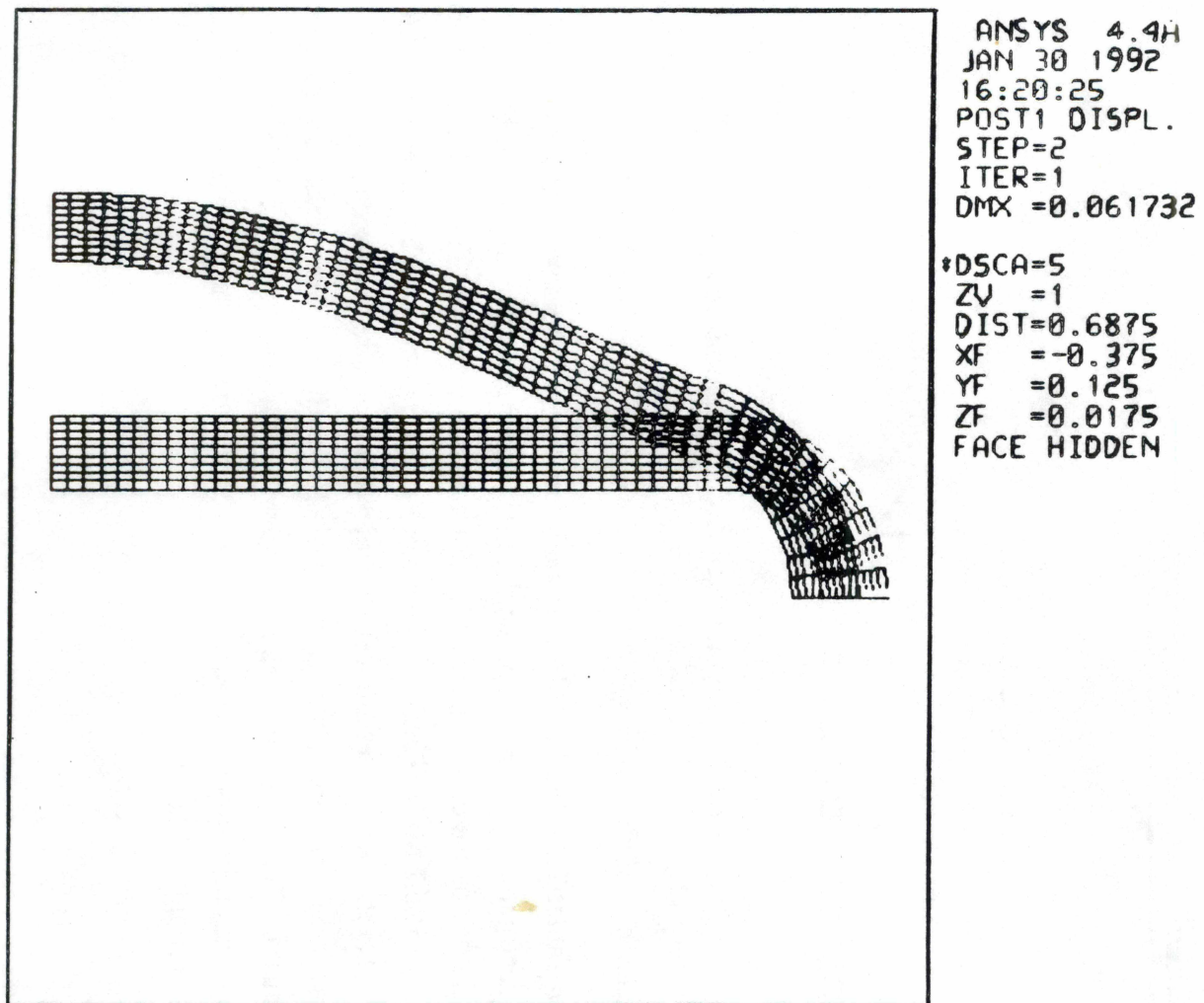


Figure 2.2.3. Displacement plot of the coil in the stand-alone configuration with cooldown and electromagnetic forces.

Configuration 1

Five cases are presented in Table 2.2.6a with different parameters. Each case consists of two sub-cases where, sub-case a represents the cooldown analysis from 293 K to 10 K, and sub-case b the cooldown with the electromagnetic forces analysis. Case 1 is considered to contain the parameters at their original state from which they are varied in the subsequent cases. The maximum stress in the aluminum structure is caused at the area of stress concentration A, where the aluminum collar tends to move outwards due to electromagnetic forces, but it is stopped by the side plate. In Case 2 the thickness of the collar δR is reduced by 25 %, while keeping the other parameters unchanged. This causes no significant changes in the stresses in the coil composite, but causes a higher von Mises stress in the aluminum which increases from 173 to 192 MN/m². In Case 3, the clearance of the side plate t_1 , is reduced by 50 %, which causes an increase of the von Mises stress in the aluminum structure by 20 % to 209 MN/m². A further decrease of t_1 , to a smaller value caused the von Mises stress in the aluminum structure, to rise even further to 313 MN/m² (case not tabulated).

In Case 4 the thickness of the side plate t_2 was reduced by 50%. The results showed a reduction in the von Mises stress of the aluminum, but a very high displacement in the z direction of 4.82 mm, which occurred at the middle of the coil. In Case 5, axial beams were added to the side plate, reducing the z displacement to -0.30 mm, and causing no significant change in the stresses.

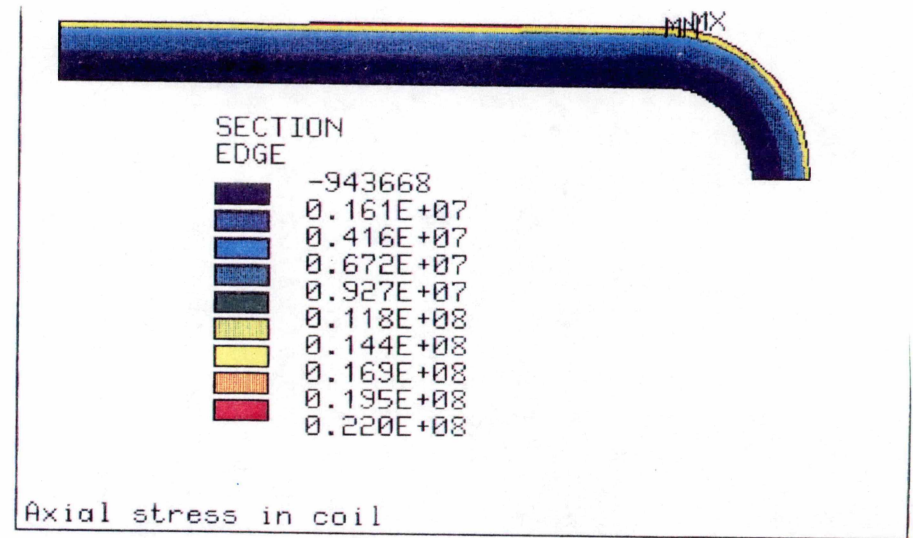
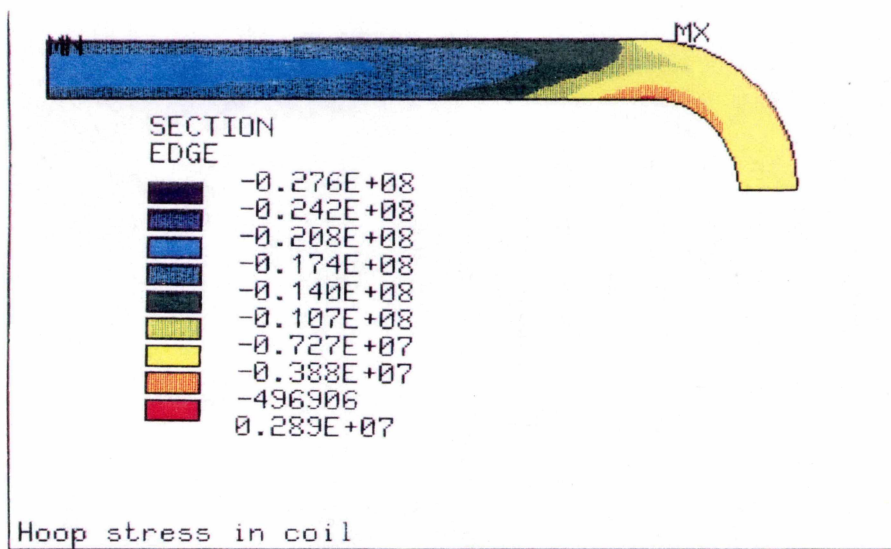
At the area of stress concentration B, the coil hoop and radial stresses change from maximum compression to maximum tension. This stress concentration is caused by the material interface discontinuity, where the straight section of the coil is enclosed in the boxed structure, while the curved section is free to contract under the thermal load and expand under the electromagnetic load. This stress concentration was less important in configuration 2, in which the curved collar compresses the curved section of the coil.

Configuration 2

Five cases are presented in Table 2.2.6b with different parameters. Here, Case 6 is considered to contain the parameters at their original state from which they are varied in the subsequent cases. The clearance of the side plate t_1 , and the thickness of the side plate t_2 , were kept constant throughout this analysis.

The average stress distribution of the cross-section for Case 6 is presented in Figure 2.2.4. The area of stress concentration A, is clearly shown in Figure 2.2.4d. The radial stress under cooldown is shown to be clearly compressive at the curved section of the coil, and very close to zero at the straight section. Under the electromagnetic load the radial stress is shown to be compressive throughout the entire coil. The hoop stress in both states is shown to be all compressive, caused by the shrinkage of the collar on the coil, and the reaction of the electromagnetic forces by the side plates. The axial stress shows no significant change in the two states, because of the uniform distribution of the axial electromagnetic load throughout the entire coil.

In Case 7 the length of the side plate was reduced by 25 %, causing the von Mises stress in the aluminum to increase by 20%, to 157 MN/m². The reduction of the radial thickness δR_1 of the curved collar by 50% in Case 8, showed insignificant change in the stresses. A reduction of the radial thickness of both the curved collar and the straight collar by 50% in Case 9, caused an increase of the tensile hoop stress in the coil composite from 39 (Case 6b) to 53.6 MN/m², and an increase of the von Mises stress in the aluminum by 28%, to 168 MN/m². In Case 10, the side plate was replaced by individual beams parallel to the y axis. This caused a reduction of the von Mises stress in the aluminum by 21%, to 103 MN/m², but a significant increase of the axial displacement to 21.4 mm.



27

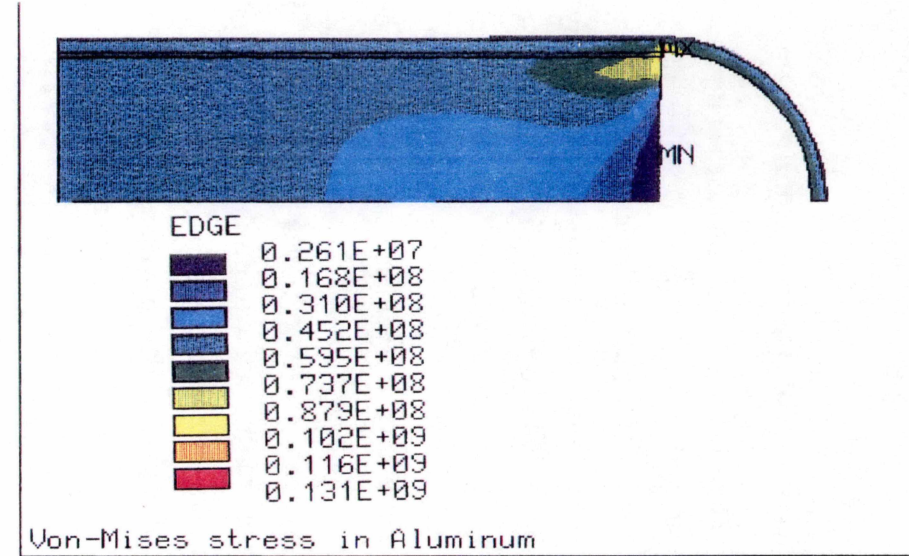
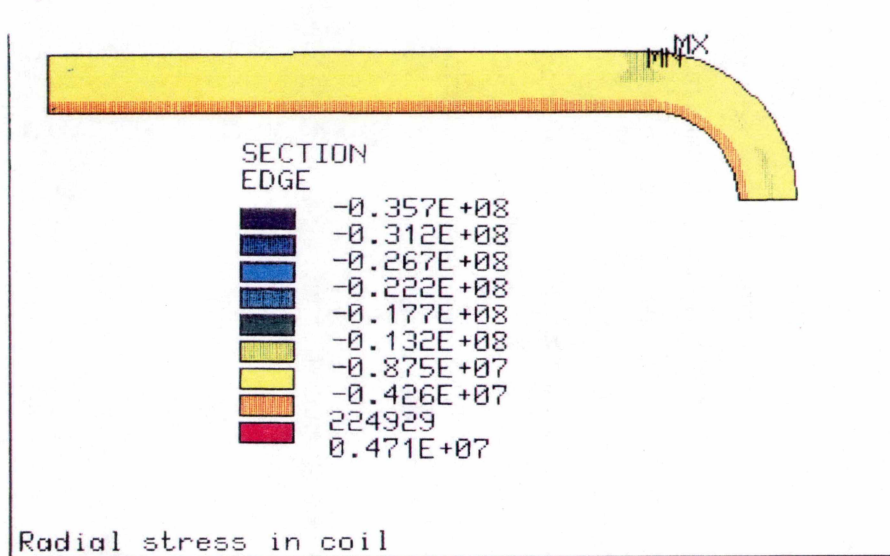


Figure 2.2.4(a-d). Hoop (a), Axial (b), Radial (c) coil stresses and von Mises (d) aluminum stress under EM forces.

2.2.4 Selection of Desired Configuration

The radial tensile stress in several cases of both configurations is shown to be higher than the radial tensile strength of the composite ($7.980 \pm 0.683 \text{ MN/m}^2$). The graphical representation of the radial stress in Figures 2.2.4c, indicates that the tensile radial stress is a point stress at a stress concentration area. Therefore, it would not present any real problem. The design presented in Case 4 must be excluded because of the large axial displacement of 7.95 mm at the middle of the side plate. The designs presented in Cases 3 and 4 showed a large von Mises stress of 192 and 209 MN/m^2 , respectively, which is 20-50% higher than the other designs. For configuration 1, the best design is shown to be either 1 or 5. Note that design 5 requires axial beams to limit the axial bending of the 50% thinner side plate. In configuration 2, the tensile hoop stresses in the coil are lower than in configuration 1, by at least a factor 2.0. The design shown in Case 10 must be excluded because of the high axial displacement. The other designs appear to be acceptable with tradeoff of higher von Mises stress for lower mass. The best design is presented in Case 9, where the thickness of the two collars is reduced by 50%. The results showed the lowest radial tensile stress with a value of 8.69 MN/m^2 and an acceptable von Mises stress of 168.0 MN/m^2 . The design presented in Case 9 is used in the magnet assembly stress analysis in a following chapter.

The three-dimensional (3D) stresses in a racetrack superconducting magnet assembly have been analyzed and evaluated in this subsection. The structural model of the assembly consisted of a racetrack superconducting coil, an aluminum collar and an aluminum side plate. The coil composite was modelled as an orthotropic material with three planes of elastic symmetry, with mechanical properties derived from experimental measurements at room temperature and liquid nitrogen temperature. The stresses in superconducting coil are calculated under cooldown and under normal operating conditions, with the system energized at the design current value. The results are compared to the strength of the anisotropic superconducting coil composite in all three directions. Several parameters such as the radial thickness of the collar, the thickness of the side plate, and the clearance of the side plate were determined such that the stresses in the coil and the aluminum support structure were reduced.

The preferred support structure, along with the superconducting coil, is shown in Figure 2.2.5.

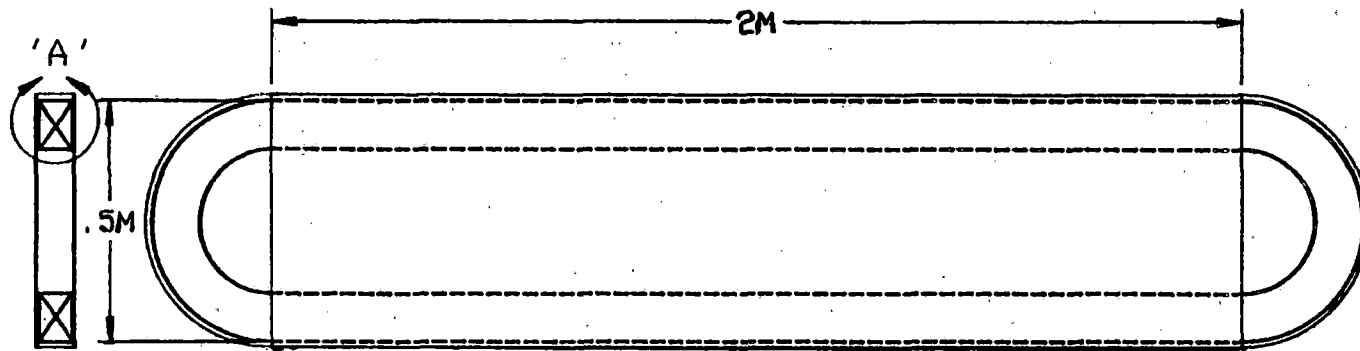
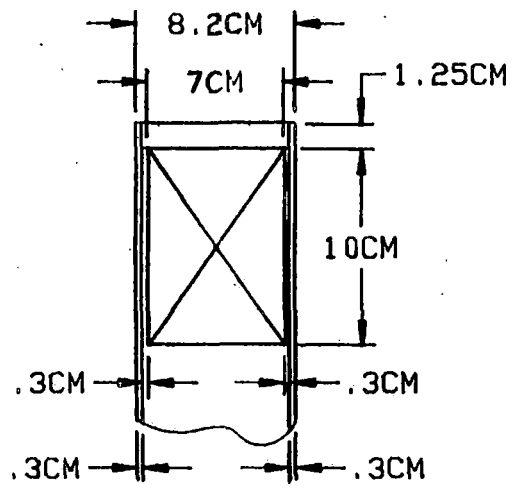


Figure 2.2.5. Engineering drawing of SC coil and preferred support structure.

2.2.5 Training of Superconducting Coil

Another important aspect of the coil design involving interaction between the coil and its support is that of training. In the context of superconducting coil operation, this term refers to the tendency of a coil to quench at a current significantly below its design current on its first excitation, but to achieve higher currents on each subsequent excitation until finally making a greater fraction of design current (sometimes 100%) than was initially achieved after several quenches. These training quenches are thermally induced and are not caused by exceeding the critical surface in current or field, and are known to be caused by motion of the conductors (in an unimpregnated coil) or the coil module (in an impregnated coil). The energy released by the frictional motion in the form of heat can raise the local temperature of the coil or conductor above the critical value and can quench the coil. The reason that the coil trains up to design current is that each motion of conductors or coil is not repeated on the following excitations, typically because the conductor or coil has jumped to a mechanically more stable position. While training is not a serious problem for a properly protected coil (that is, one that can survive a quench from any current without excessive local heating, thermal distortion, or current arcing), it does represent an additional cost of bringing the coil up to field, in terms of time and (for a pool-cooled system) helium consumption.

To avoid training in a coil, the design must either prevent any motion that could result in frictional heat, or ensure that the energy will be absorbed by members of the coil support structure or the helium pool before the temperature of the superconductor exceeds its critical value. One of the best ways to design for the latter in a pool-cooled system is to provide adequate thermal contact between the coil-support interface and the helium pool, and to count on the large heat capacity of liquid helium to absorb the energy. For our conduction-cooled design, this is not possible, and the preferred way to avoid training is to ensure that the coils will not move.

For our proposed coil design, the long aluminum support structure represents a potential source of coil training. When the assembly is cooled to the operating temperature of 10 K, the differential thermal contraction between the support structure and the coil induces thermal strains at the interface. When the coil is excited, the Lorentz forces can increase the total interface strain and can cause the coil to slip at the interface. Two methods exist to prevent training in this system. First, the coil can be bonded to the support with an epoxy adhesive that will withstand the thermal stress without cracking and will prevent motion. Second, the interface can be covered with an interface material that can withstand a large mechanical strain without slipping at either surface. Two such materials are known to exist – leather and polycarbonate insulation. Both have been tested for previous GE coil designs for their low-temperature stress-strain characteristics and have

been found to tolerate large shear deformations. Either of these two techniques are applicable to this design.

While training would not necessarily be considered to represent a serious drawback, the possibility also exists that the support structure could exhibit some motion relative to the coil which would be reversible. That is, the coil would quench at the same current, one below the design value, on consecutive ramps. Such coil operation would be considered a failure in most applications, where the design field is required and a reduced field would be of little or no value.

2.3 Quench Analysis

An analysis of the outcome of a quench of one of the racetrack coils has been performed to ensure that the coil design presented can survive such an event. This analysis requires the simultaneous solution of the coupled heat transfer and electrical circuit models with the critical surface of the superconductor taken into account. The basis of the solution is that a portion of the coil rises to a temperature above its critical value, and the superconductor in that region transitions to the normal state. The copper stabilizer, which is in intimate electrical and thermal contact with the superconductor, then begins to carry the current, with resultant resistive heating. This heating causes adjacent portions of the coil to transition to the normal state, while also introducing resistance into the electrical circuit which was lacking when the entire coil was superconducting. Eventually, the current in the coil will dissipate to zero with the energy represented by the original magnetic field raising the coil temperature. The magnitude and distribution of this temperature rise are of importance because the absolute temperature or thermal stresses may exceed the melting point of some component or the coil composite strength. In addition, the voltages generated during the quench event may exceed the interlayer or coil-coil dielectric capability of the insulation systems.

A quench analysis of the racetrack field coil configuration with 6.51 m mean circumference and 73.8 H inductance was carried out using the SUITE-Q quench analysis program suite developed at GE-CRD for use in evaluating our prototype coils. The analysis is somewhat conservative because it does not incorporate AC losses created by the rapid current change possible in a quench, which may aid quench propagation and thus lower the temperature peaks. Quench of a single field superconducting coil with no special quench protection features (such as interlayer copper foils to improve heat conduction, segmentation of the coil into several distinct electrical sections, etc.) gave acceptable results. The quench produces a maximum hotspot temperature of 206 K (Figure 2.3.1), within our design limits for the refrigerated magnet technology since the thermal strains developed with the temperature difference within the coil for such a hotspot are

known to be within the coil composite strength. The axial temperature differential is 70 K (Figures 2.3.2 and 2.3.3), the radial is 195 K (Figure 2.3.2), and the circumferential is 195 K (Figure 2.3.3). The quench propagates completely in the axial direction, but only propagates 60% of the radial build and 80% around the circumference. The quench event lasts approximately 10 seconds (Figures 2.3.1, 2.3.4 and 2.3.5), by which time the coil current is negligible. Peak layer-to-layer voltage is 38 V (Figure 2.3.6), well within the dielectric strength of our interlayer insulation system.

Properly designed coils will experience no physical degradation from the quench process, it is simply a thermal excursion in which the magnetic energy raises the coil temperature. Subsequent to the quench event, the coils must be re-cooled to their operating temperature and ramped back to their design current. This process would take several days using the cryocoolers, as they are not designed to remove heat at the high rates which would be required to cool a coil faster. Building a system of cryogenic piping into the coil support structure is recommended to accelerate the cooldown by introducing cryogenics (first liquid nitrogen, then liquid helium) into the pipe. GE has developed this technology and implemented it in its MR magnets with success, reducing cooldown times from room temperature to a more reasonable two to three days.

The issue of how to handle a quench during vehicle operation is primarily a safety and systems issue. For the purposes of this study, we have limited our treatment of the subject to determining that the coil can safely withstand a quench without its subsequent performance being degraded. In addition, the dynamic variation in levitation and propulsion forces from the loss of a magnet must be considered. Levitation should be maintained in the event of a single magnet quench, so for the bogey system, where four magnets contribute to the levitation of a single vehicle, the vehicle should remain levitated with only three magnets active.

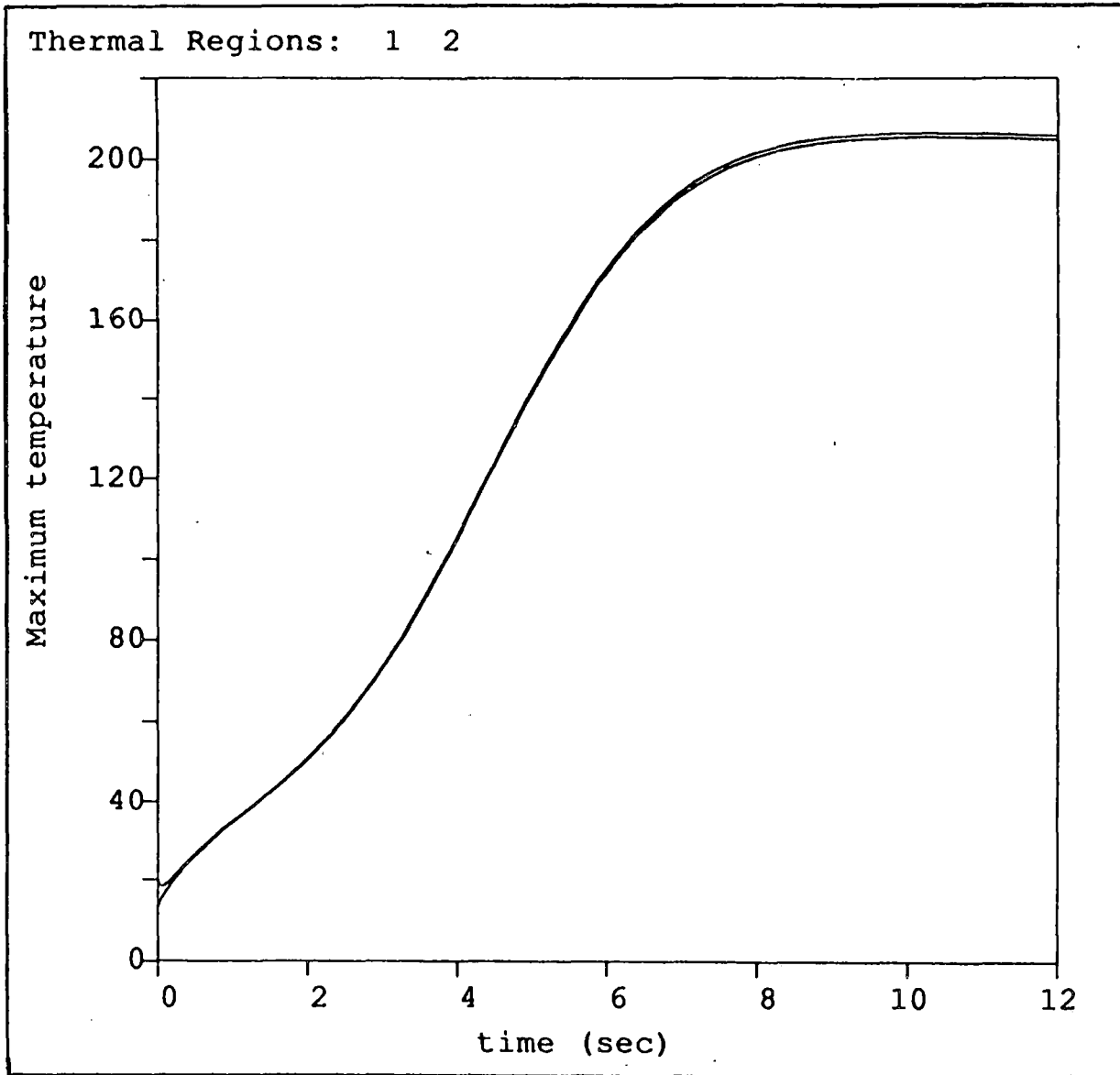


Figure 2.3.1. Peak coil temperature vs. time during quench event.

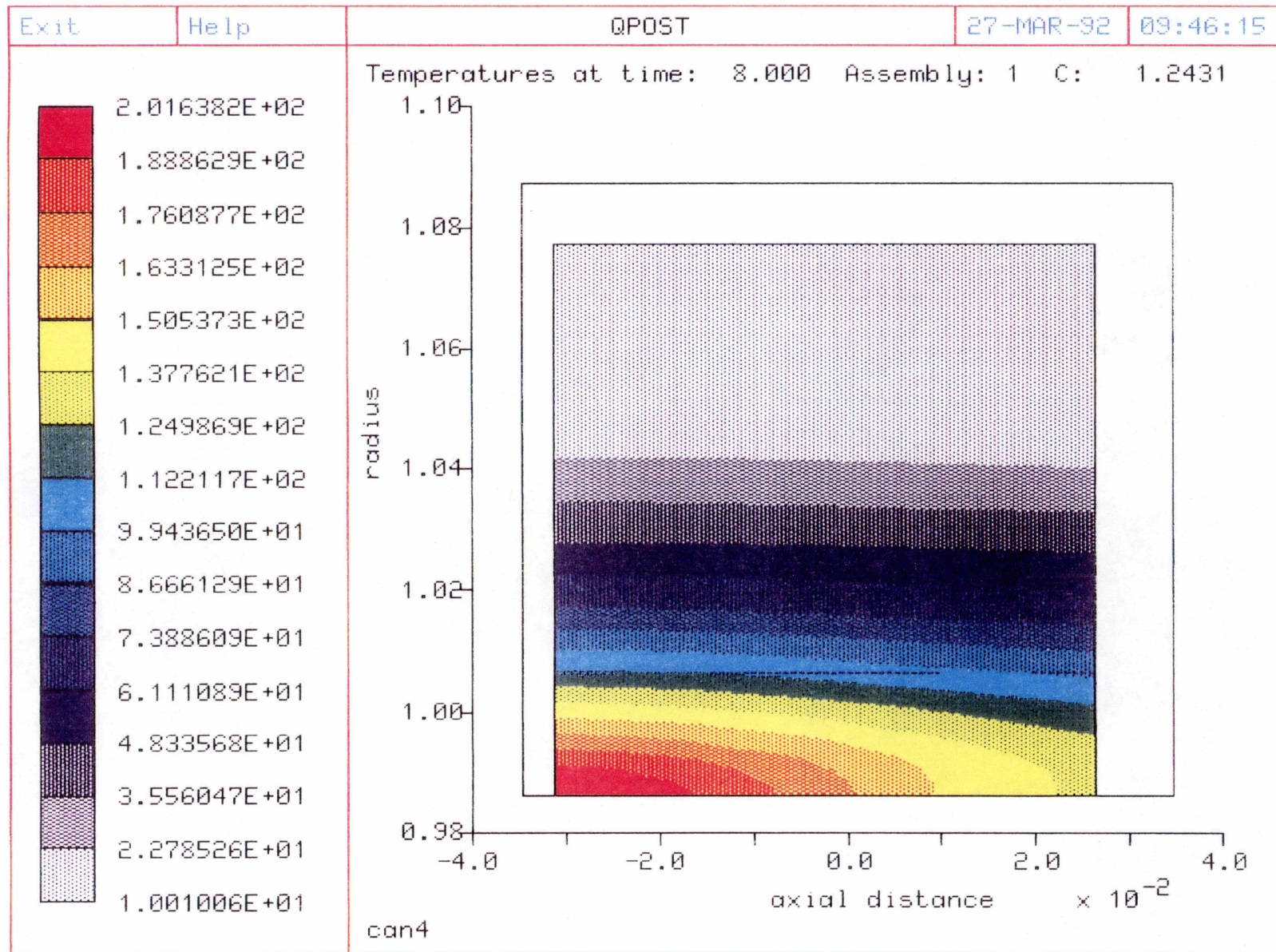


Figure 2.3.2. Temperature contours of z-r slice through hotspot, 8 sec.

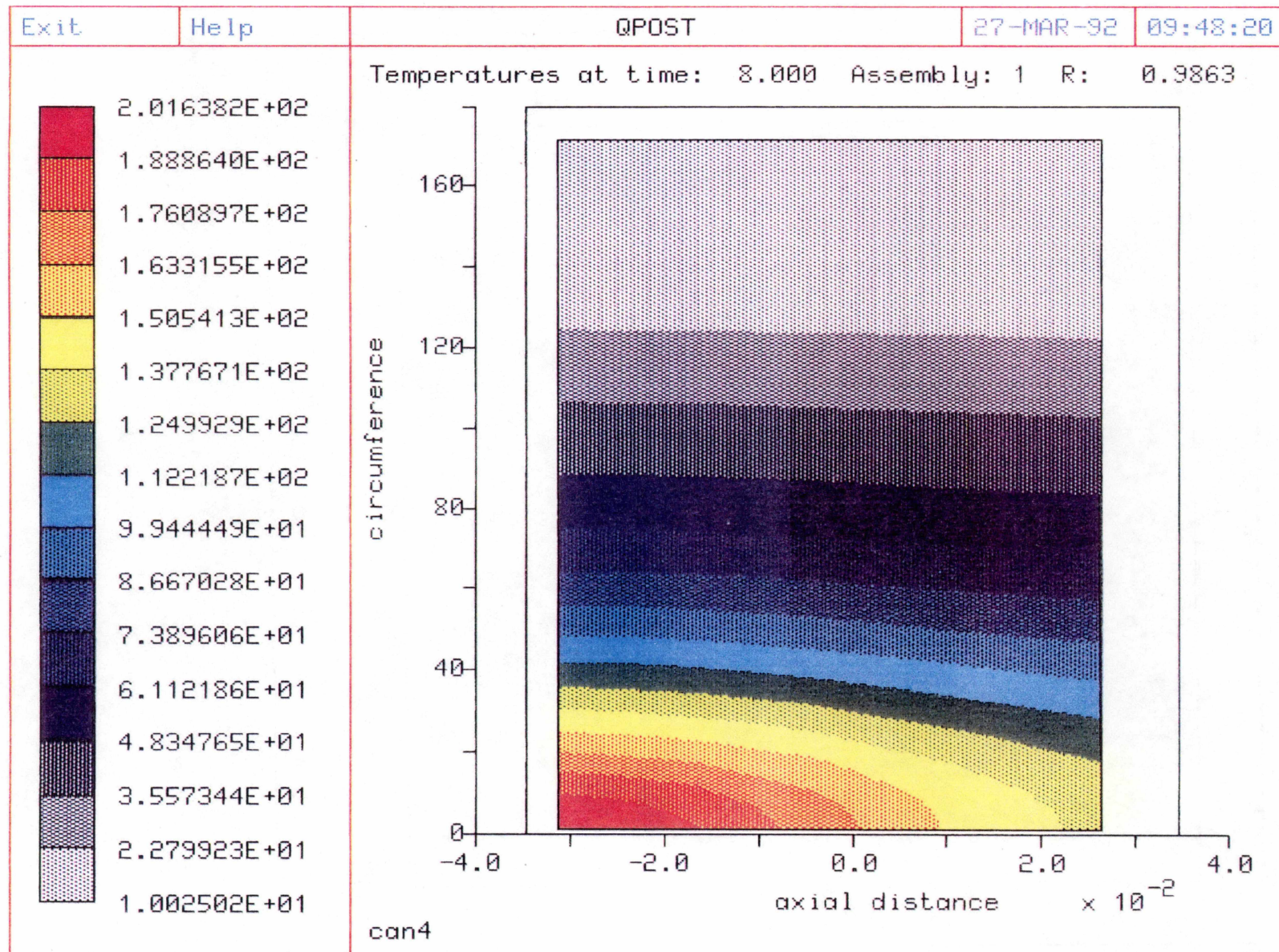


Figure 2.3.3. Temperature contours of z-c slice through hotspot, 8 sec.

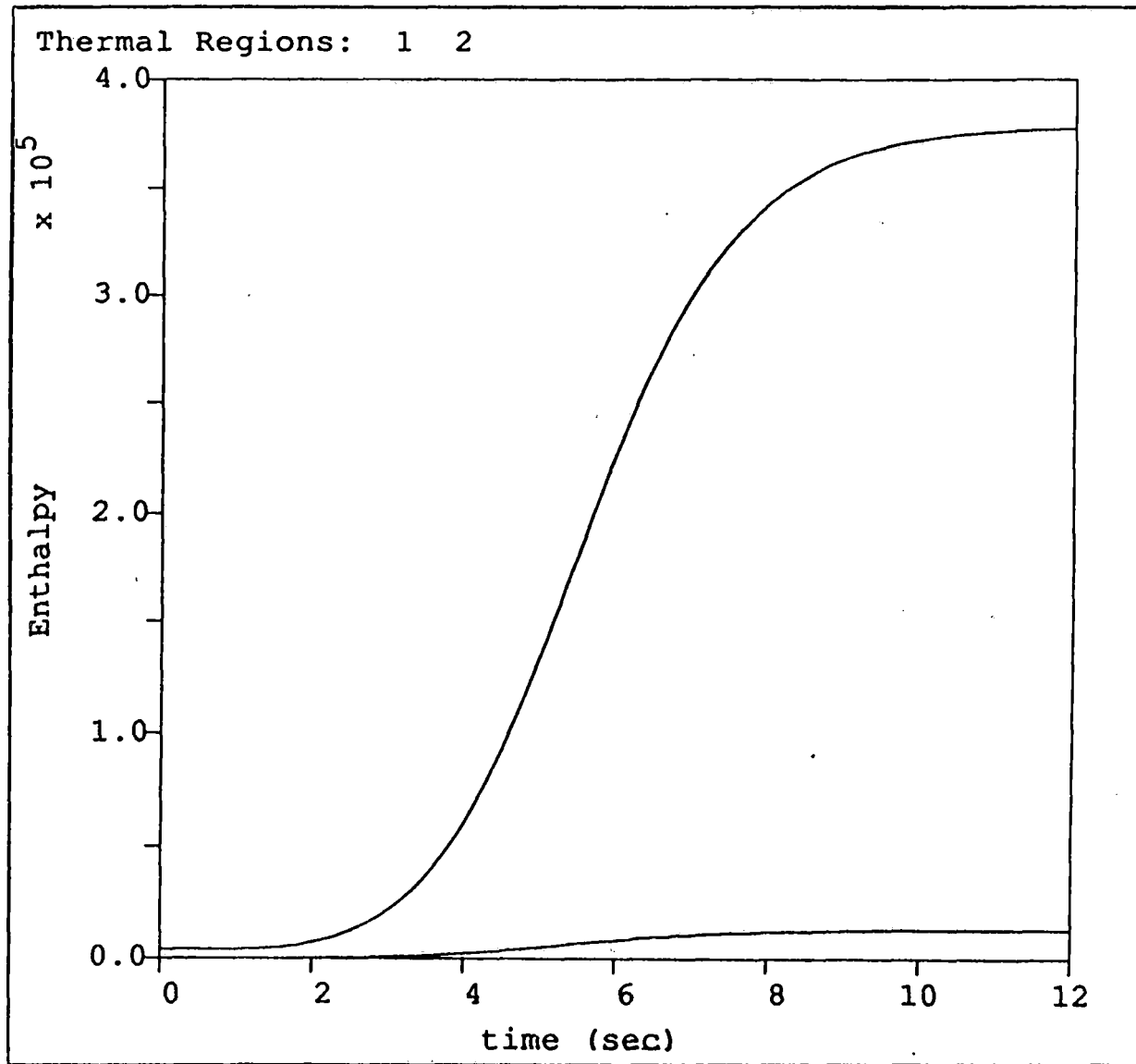


Figure 2.3.4. Coil thermal energy vs. time during quench event.

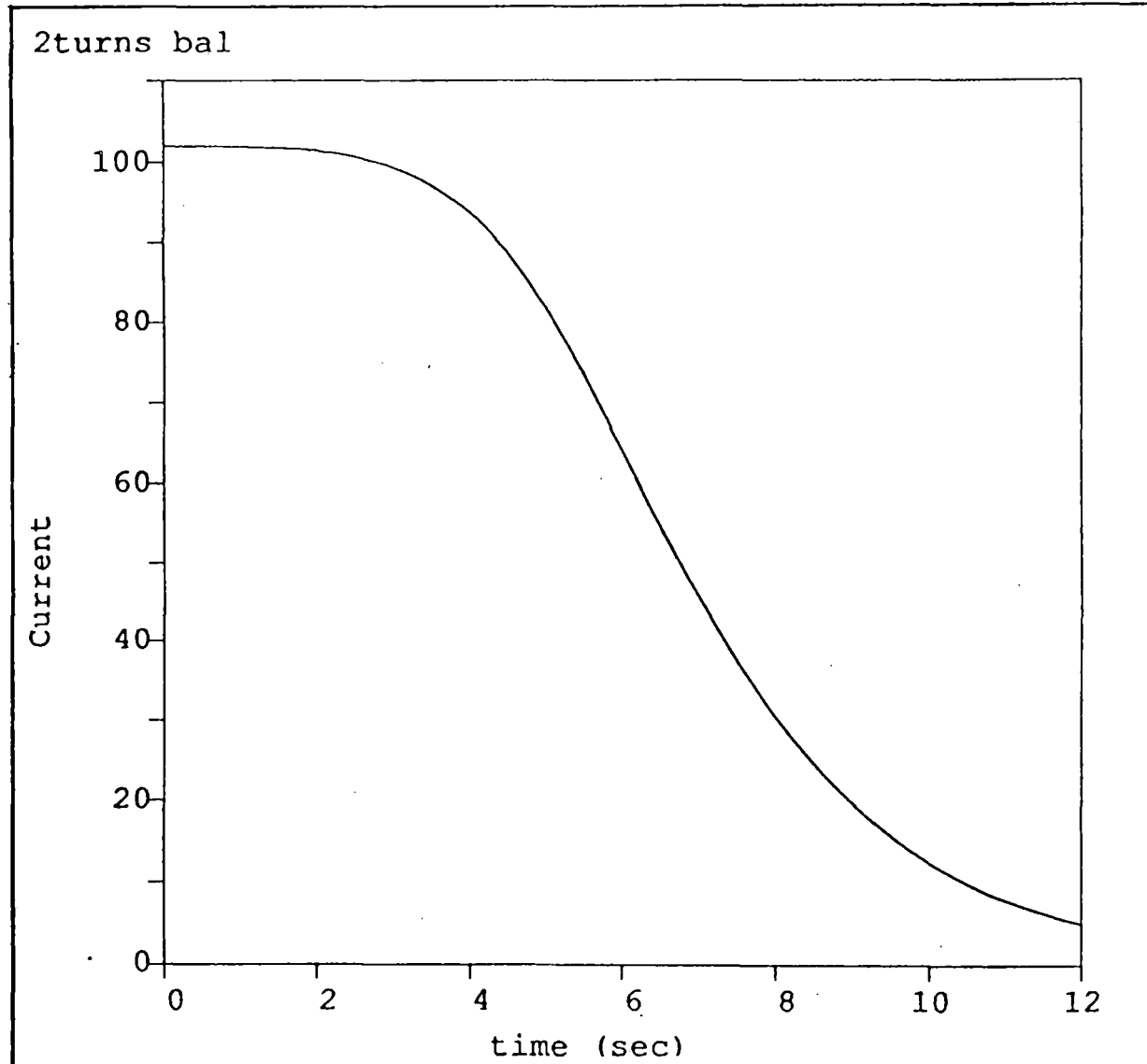


Figure 2.3.5. Coil current vs. time during quench event.

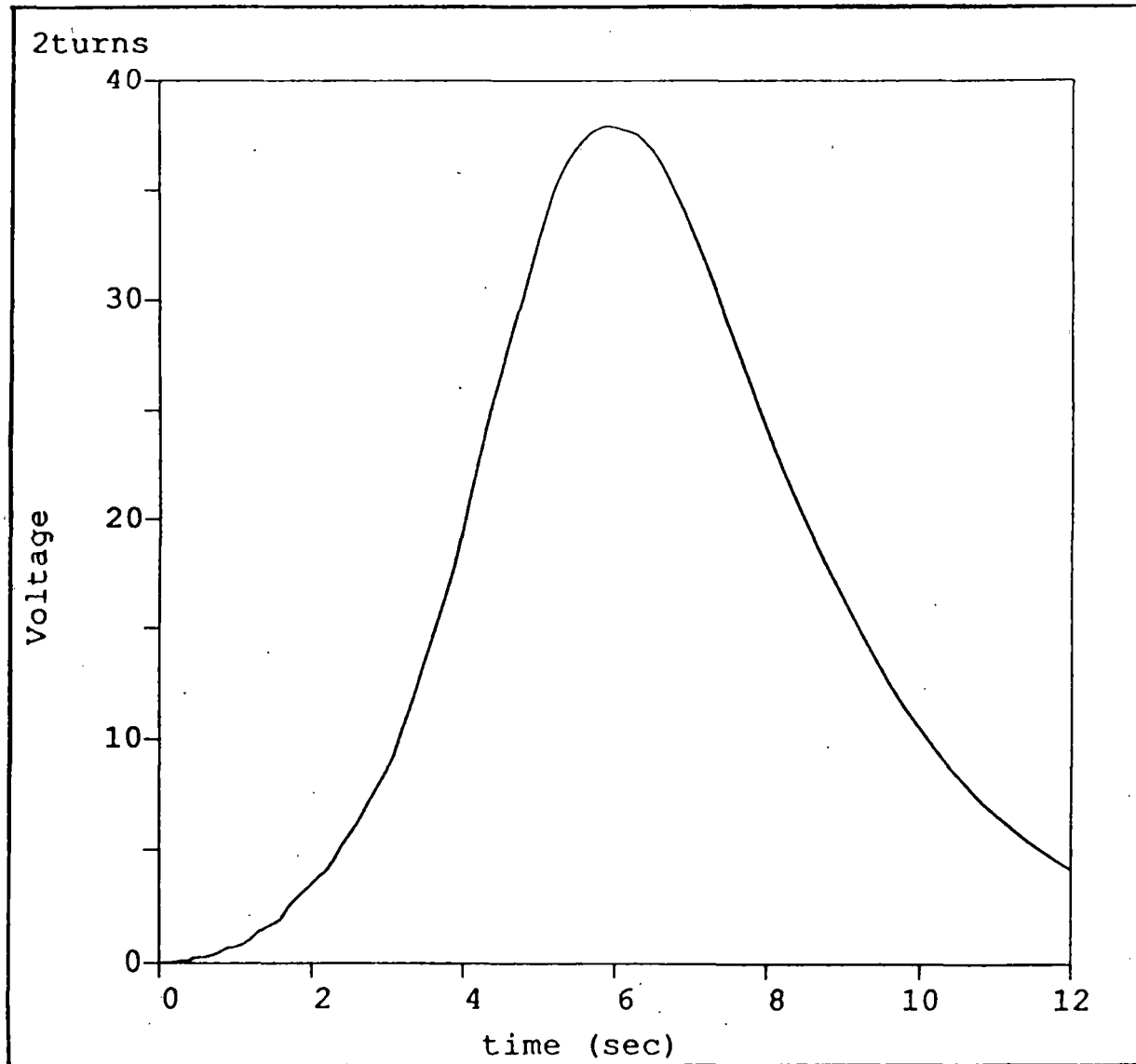


Figure 2.3.6. Interlayer voltage in coil winding layers 1-2 vs. time during quench event.

SECTION 3: LEVITATION AND MOTOR COIL INTERACTIONS

3.1 Linear Synchronous Motor Design

An analysis of the linear synchronous motor for the proposed geometry was performed to a first order level of detail. The results of this analysis are presented here.

The perpendicular flux density provided by the superconducting windings averaged within the plane of an armature coil was taken to be 0.6 T. This value may be slightly optimistic (actual values may be slightly lower), but it was considered reasonable for the present analysis. Since it is a simple multiplicative parameter in determining the outputs of the motor analysis, results can be easily obtained for other values of flux density using this analysis.

The armature coils are arranged in a double layer winding, with those in the rear layer (farther from the plane of the vehicle coils) overlapping those in the front layer by 1.0 m at each end, as shown in Figures 3.1.1 and 3.1.2. Such an arrangement makes sense from the standpoint of construction and is proposed by the Japanese for use at their Yamanashi test facility. The analysis leading to the estimation of thrust was based on the armature windings being powered with 120 degree square waves. Because of the large inductance of the motor windings, an actual motor would be powered with sinusoidal current. The thrust produced by the motor is given by

$$T = 16HIB \quad (3.1.1)$$

where H and I are the armature coil height and current and B is the flux density produced at the armature coil by the vehicle coils. The factor of 16 assumes that 4 vehicle magnets are acting, with each magnet including two rectangular coils. Such an arrangement would be provided by a single vehicle mounted on bogeys, with one bogey at each corner, and each bogey containing one two-coil magnet on each side of the vehicle. For the thrust of 50 kN required to propel a 9 m² vehicle with a drag coefficient of 0.3 at 500 km/hr, with the assumption of $B = 0.6$ T and $H = 0.5$ m, the armature coils require 10420 ampere-turns each. The number of turns in each coil represents a tradeoff between the required motor current and the reactive voltage, which is dictated largely by the coil inductance. Since there is 1 coil of each phase per 2τ of track length, and the inductance of the coil L_c , the total reactive voltage of a motor section of length L m is

$$V_{\text{reactive}} = 2p\nu IL_c L / 2\tau \quad (3.1.2)$$

where ν is the motor frequency and I the motor current.

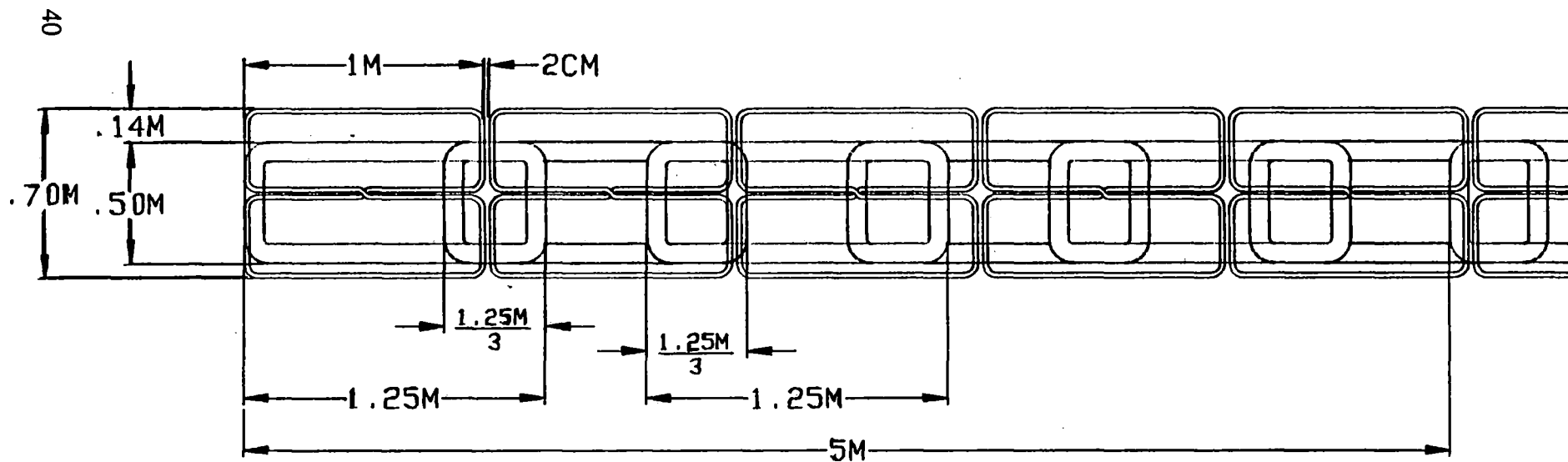
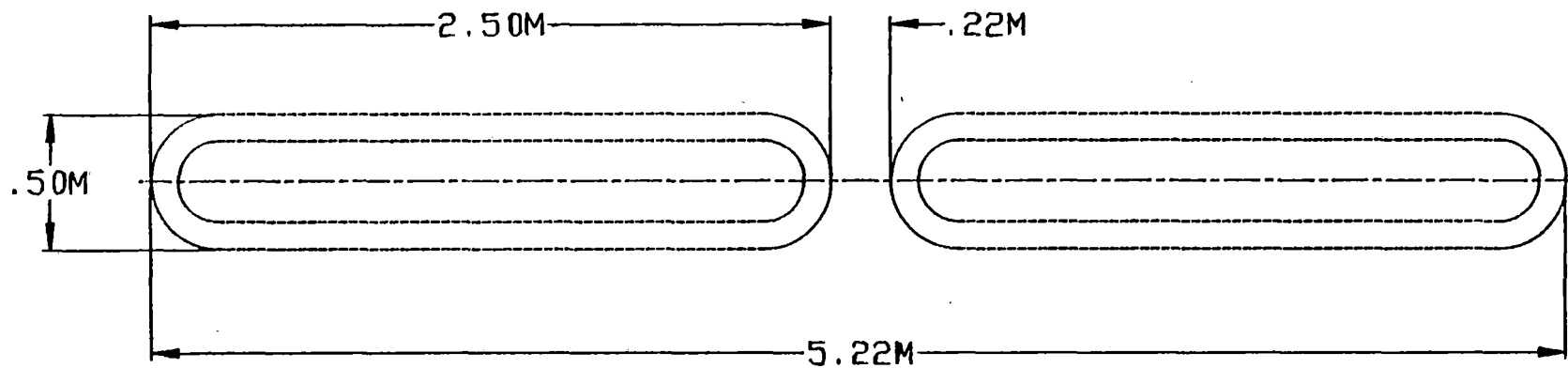


Figure 3.1.1. Schematic side view of guideway showing null-flux and armature coils with SC coils shown for scale.

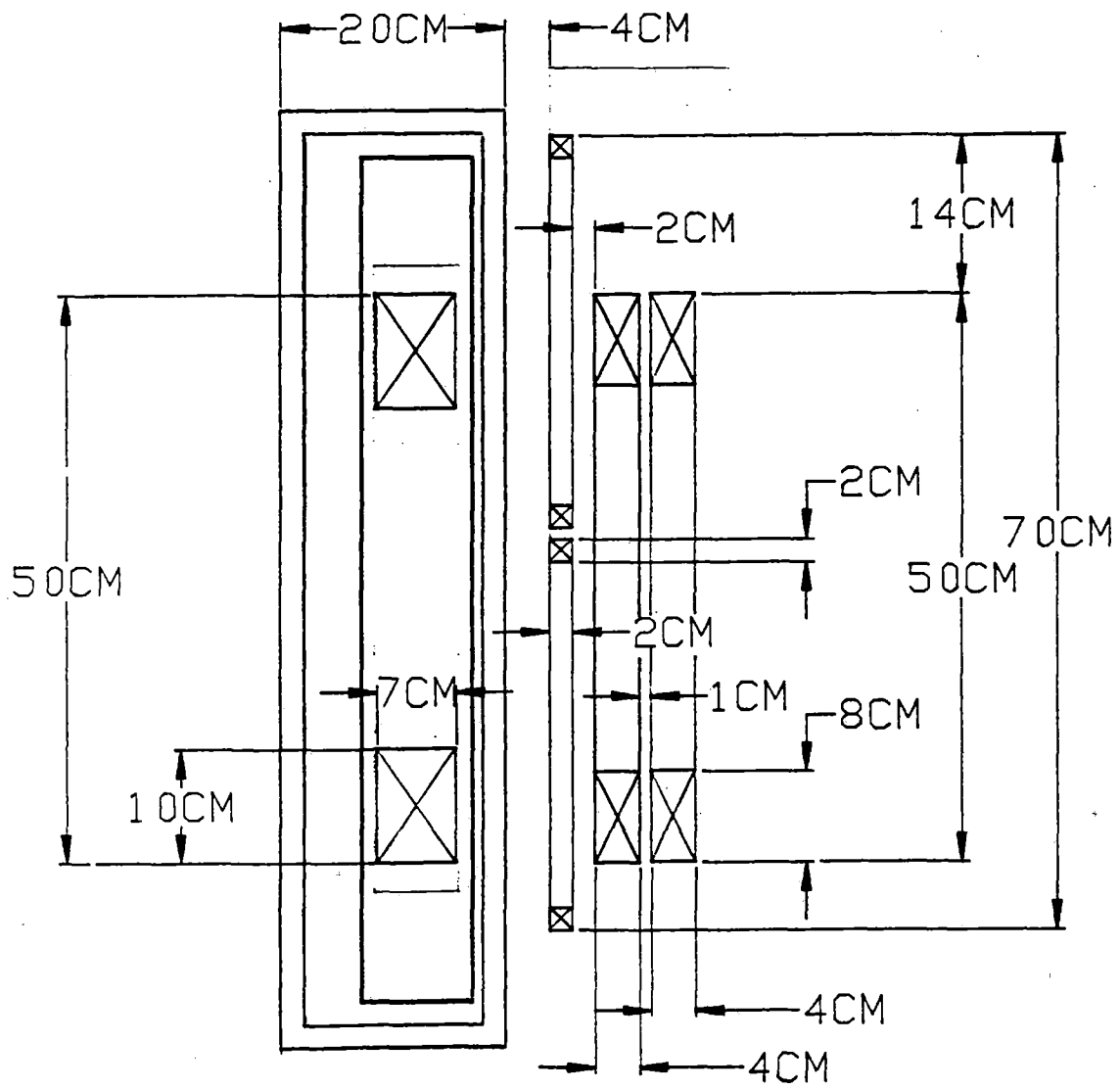


Figure 3.1.2. Schematic front view of guideway showing null-flux and armature coils with SC coil shown in actual position in cryostat.

The open-circuit voltage is given by the product of the field at an armature coil, the current in the coil, and the velocity of the coil relative to the field. For the configuration considered here, the equation for the open-circuit voltage is

$$V_{oc} = 4NBHv \quad (3.1.3)$$

where N is the number of turns per armature coil and v the vehicle velocity. The leading factor of 4 represents the two armature coil vertical bars that are acted on by one vehicle magnet and the two bogeys per vehicle in the direction of travel. For this derivation, the two sides of the motor are assumed to be powered in parallel, so that this voltage is developed across each half of the motor.

Using these equations and those presented in Appendix A, we have developed six possible motor designs and analyzed them to first order to compare and contrast them. The designs demonstrate the results of variations in three basic design parameters: the number of magnets along the vehicle length; the pole pitch of the windings; and the flux density at the armature windings provided by the vehicle coils. Results are summarized in Table 3.1.1. It must be emphasized that these results are based on fairly simple rules and assumptions and that the predictions of efficiency and power factor are useful for comparison purposes among this set of designs only. A "brushless DC" operation mode for the motor is assumed in these analyses. In this mode, the armature current of each phase is turned on and held constant for 120 electrical degrees, then turned off. This is to be contrasted with a sinusoidal current variation.

The values in Table 3.1.1 are: flux density at the mid-height of an armature winding provided by the vehicle coils (B); motor pole pitch, which equals vehicle coil spacing in the direction of travel (t); total length of coils on the vehicle (L_m); maximum allowable length of a block, or powered motor section (L_{bm}); assumed length of a block (L_b), motor efficiency (η); power factor (pf); motor current (I); number of turns in the armature coils (N_t); terminal voltage for the motor (V); and inverter rating (MVA).

Explanation of some of these values is provided here. Flux density B is an average value along the length of the winding. The maximum powered section length is chosen by arbitrarily setting the reactive and open circuit voltages equal, which maintains the power factor at a reasonable level. The motor efficiency is defined as the power provided to the vehicle (two-thirds of open circuit voltage times current for our brushless DC operation mode) divided by the real power (the sum of the vehicle and resistive power). The power factor is defined as the real power, multiplied by 4 to account for both sides of the vehicle (really two motors), the three phases, and

the 2/3 factor mentioned above, and divided by the inverter rating. This is a somewhat arbitrary definition of power factor, which has a maximum value of 0.67 because of the 2/3 factor in the numerator, but for our case with non-sinusoidal current, it is as valid as any other.

Design	B (T)	τ (m)	L_m (m)	L_{bm} (m)	L_b (m)	η	pf	I (A)	N_t	V (V)	MVA
1	0.6	2.5	10	110	110	.53	.59	1042	10	3079	19.3
2	0.6	0.5	10	338	338	.91	.49	1042	2	2146	13.4
3	0.6	0.5	30	3035	3035	.81	.51	694	1	3327	13.9
4	0.6	0.5	30	3035	2000	.90	.58	694	1	2790	11.6
5	0.8	0.5	30	5400	5400	.86	.51	520	1	4425	13.8
6	0.8	0.5	30	5400	2000	.94	.63	520	1	3242	10.1

Table 3.1.1. Design parameters and characteristics of six linear motor designs

An interesting note to observe here is that the latest Japanese design calls for concentrating the coils in bogies at the ends of the vehicles, which seems from this analysis to be relatively costly. One possible explanation of this apparently poor design choice is that they have not determined a reasonable method to limit the passenger compartment field to their desired value with coils distributed along the vehicle.

Table 3.1.1 shows that the motor pole pitch is seen to be an important parameter in determining the motor efficiency (note the low efficiency of design 1). However, it must be emphasized that this is a motor design process and that the levitation requirements of the system are not considered here. The designs with a single turn in the armature windings allow the use of a meander winding, which can reduce winding and installation costs. The best choice overall would be a design that allows a long block length to limit inverter costs which maintaining high efficiency and power factor.

Figure 3.1.3 shows side and front views of the proposed coils and vehicle on which our analyses were based. Appendix A of this report details the background analysis performed to allow these motor designs to be developed.

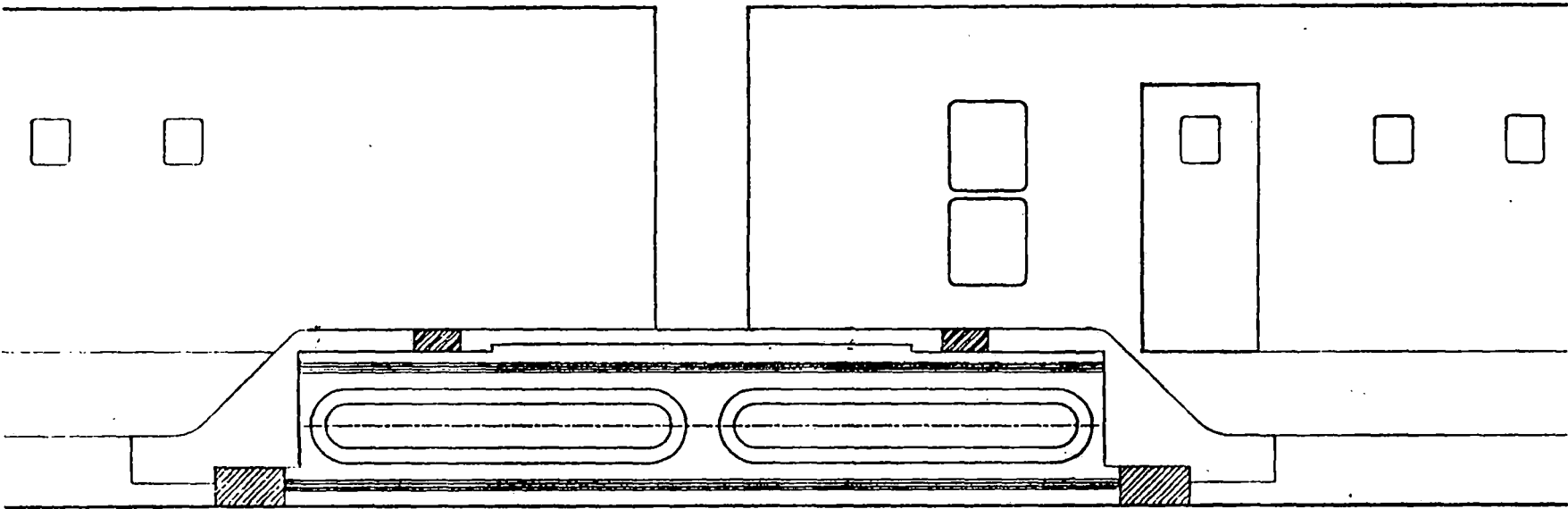
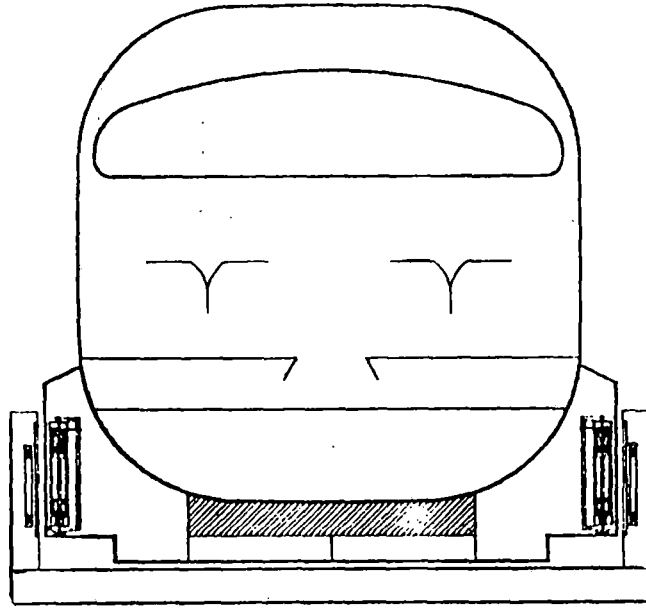


Figure 3.1.3. Side and front views of vehicle showing SC coils in bogie at end of vehicle.

3.2 LSM Power Conditioning

This section of the report uses the six motor voltages, currents, total volt-amps and frequencies given in Table 3.1.1 of this report as the basis for the conceptual design of a suitable power conditioner. Table 3.2.1 summarizes the input data pertinent to this analysis.

Design	Peak Voltage (V)	Peak Current (A)	Frequency (Hz)	Peak Volt-Amps (MVA)
1	3079	1042	24	19.3
2	2146	1042	120	13.4
3	3327	694	120	13.9
4	2790	694	120	11.6
5	4425	520	120	13.8
6	3242	520	120	10.1

Table 3.2.1. Alternate motor requirements.

The peak MVA rating was obtained by multiplying the peak current per phase times the peak voltage per phase times number of phases (3) times number of sides of the vehicle (2). The peak current is actually the peak value of the 120 degree block of current described in Appendix A as the "brushless DC" mode of operation. It is further assumed that the supply voltage (either AC or DC) is approximately 15% higher than the peak phase voltage in order to provide sufficient voltage for forcing the current into the phase winding and to account for the fundamental frequency voltage that is not available because of limitations in the pulse width modulation (PWM) duty cycle.

3.2.1 Power Semiconductor Selection

The maximum motor frequency of 120 Hz for designs 2 to 6 precludes the use of conventional reverse blocking thyristors (SCR) in naturally commutated AC-AC circuits. These circuits, called naturally commutated cycloconverters, are generally restricted to provide an output frequency that is less than the supply frequency, that is, 60 Hz. The SCR must be turned off by a reversal of the utility AC voltage waveform. Murphy et al [1988], Mohan et al [1989] and Gyugi and Pelly [1976] all describe naturally commutated cycloconverters. Since the output frequency is greater than the utility frequency, a semiconductor that has a self-turn off capability is required. The gate turn-off thyristor (GTO) is a silicon-based semiconductor that has voltage and current ratings that are commensurate with the 10 MVA ratings without having to place significant numbers of devices in series or parallel.

The gate turn-off thyristor (GTO) is a 3-junction PNP device where the PNP and NPN component transistors are connected in a regenerative feedback mode (see Figure 3.2.1). The GTO is triggered into condition with a current signal into the gate terminal, which starts the regenerative action and causes the device to latch on. In a GTO, a negative gate current can be extracted from the gate terminal and this breaks the regenerative cycle and the device turns off. The instantaneous current gain, that is, the ratio of controllable anode current to gate current is typically 3/1 to 5/1. Because of high switching loss during turn-off, GTOs are limited in conventional inverters to a switching frequency of less than 1 kHz. The GTO requires a large polarized turn-off snubber to limit the rate of rise of anode voltage during turn-off. GTOs are available from several manufacturers with maximum ratings to 4500 V and 3000 A. Lower current and voltage-rated GTOs are also available.

High-voltage and current-rated diodes are also available to operate in conjunction with the GTOs in DC applications. Both GTOs and diodes are available from multiple domestic and foreign sources.

3.2.2 Power Circuit Approach

Previous applications of power electronics to high power equipment have used naturally commutated cycloconverters [Murphy et al 1988, Mohan et al 1989 and Gyugi and Pelly 1976]. These circuits are characterized by a large number of power semiconductors connected in inverse parallel to provide bidirectional current control. Since it is a naturally commutated system, the input power factor is always lagging and is always less than the load power factor. In this application, the load power factor is low (0.49 to 0.63), and the input power factor would be further reduced (estimated to be in the range of 0.35 to 0.44). The input harmonic currents are composed of the sums and differences of multiples of the input and motor frequencies. The multiplying factor is dependent on the specific cycloconverter circuit. The problem is that these harmonic frequencies are functions of the motor frequency and can, at times, approach a very low frequency and are difficult to filter. The low power factor and the harmonic currents increase the size, weight, and cost of the utility step-down transformer. Power factor correction is provided with capacitors and series inductors to prevent resonances.

Modern power electronics systems employ power semiconductors with self-turn-off capability similar to the GTO described in the preceding section. These devices do not depend on the reversal of the utility voltage for commutation and as such the system power factor can approach 0.95. The harmonics on the utility are multiples of the utility frequency with the lowest one being eleven times the utility frequency or 660 Hz.

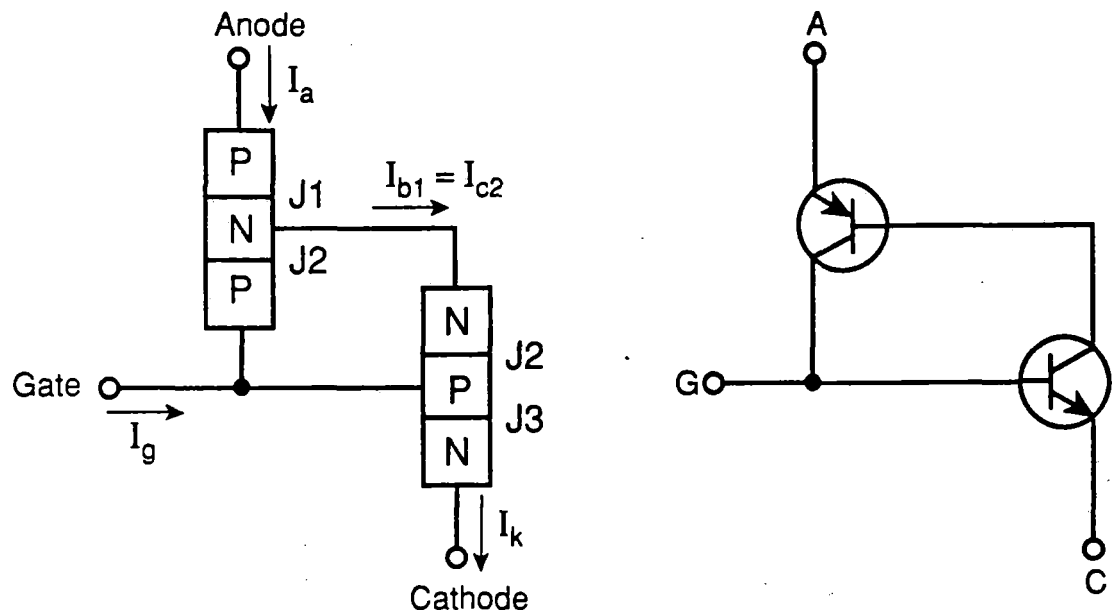


Figure 3.2.1. Two Transistor Analogy of GTO.

As mentioned in the previous section, the output frequency is higher than the utility frequency, which eliminates the use of direct ac-to-ac cycloconverters and requires the use of an AC-to-DC-to-AC rectifier and inverter. The double power conversion reduces the efficiency somewhat, but the efficiency of a diode rectifier can be in excess of 99% at these power levels. Figure 3.2.2 shows a block diagram of the selected approach. The two rectifier bridge circuits are fed from separate wye-delta windings on the utility step-down transformer. This provides a 12-pulse rectifier resulting in reduced harmonic currents in the utility and reduced levels of ripple voltage on the DC bus. The rectifier bridges are connected in series on the DC side. The DC output of the rectifier feeds a three-phase DC-to-AC inverter, which is directly connected to the linear synchronous motor.

Several techniques have been proposed and, in some cases, fabricated for high power (10 MVA) rated equipment. The technique proposed for this application has been categorized as a "soft-switched" resonant pole inverter. This approach allows the motor voltage to be controlled by the familiar technique of pulse width modulation (PWM) and the GTO switching on and off to be controlled by an auxiliary resonant circuit. This resonant action during the switching on and off of the GTOs results in reduced switching losses and a larger reverse biased safe operation area (RBSOA). These two advantages allow the switching frequency to be increased resulting in an improved waveform with lower harmonic currents. The enlarged RBSOA results in an increased turn-off capability of the individual GTO's.

The circuit chosen to provide the "soft-switching" has been designated the "auxiliary resonant commutated pole" (ARCP). A half-bridge of one inverter pole is shown in Figure 3.2.3. The two main GTO power semiconductor switches are shown as S1 and S2 together with their feedback diodes D1 and D2. The auxiliary circuit to provide the resonant action during switching is composed of auxiliary components A1, A2 and Lr, and both capacitors Cr/2. The sinusoidal resonant voltage transition of the load terminal is determined by the Lr-Cr resonant frequency. The theory of operation of this circuit for various levels of load current is shown by timing diagrams in DeDoncker et al [1990].

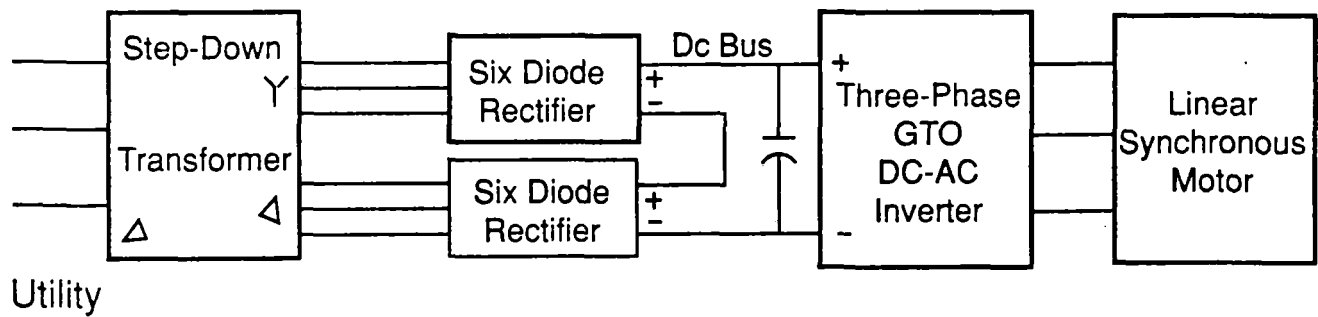


Figure 3.2.2. Block Diagram of AC-DC-AC Drive.

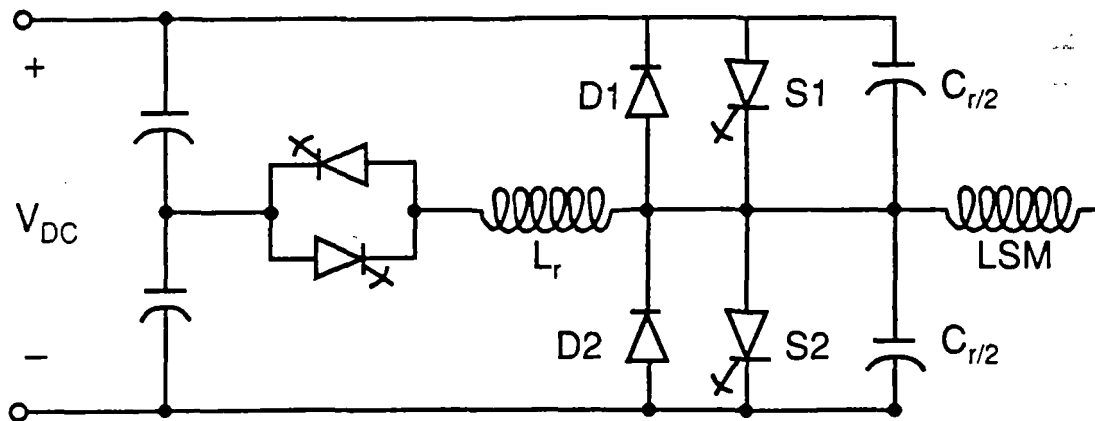


Figure 3.2.3. Alternating Resonant Commutated Pole (ARCP) Phase Leg.

Figure 3.2.4 shows a circuit diagram of the inverter system composed of three resonant pole phase legs. The magnitude of the supply voltage will, in some cases, require the use of series-connected GTOs. The magnitude of the motor current will, in some cases, require the use of a separate three-phase inverter, supplied from a common DC bus, for each side of the linear synchronous motor. Control circuits, not shown, control the load voltage magnitude by pulse width modulation of the main GTO devices. An inner current loop senses the motor current and controls it to be within an error band. This technique of only providing inverter switching when the load current is greater than or less than a prescribed deadband is called "bang-bang" control because it is event-driven rather than time-driven. Variations in the DC bus voltage caused by variations in the utility voltage are reduced because of the action of the outer voltage regulator loop. The motor frequency is determined by the need to accelerate or maintain the vehicle speed in the specific block of the right-of-way. It can be controlled from zero up to the value given in Table 3.2.1 for the six motor designs.

3.2.3 Power Circuit Design

Table 3.2.1 contains the motor requirements for the six motor designs. The method used for the calculation of the power circuit parameters is based on the closed form calculations as described in Ziogas et al [1985]. The point design is accomplished at the motor maximum power point since this is the worst case for power semiconductor dissipation and dynamic requirements. Based on this design procedure, with the given availability of GTO devices, some of the motor designs required series connected GTOs and other designs required that the GTO's operate in parallel.

The GTO used for this analysis was the Marconi DG 758AX rated at 4500 V peak and 2500 A peak controllable current. Marconi [1987] contains additional specifications for this device. It was selected for its high voltage and current capability and because turn-off and turn-on loss data was available. The feedback diode chosen for this conceptual design was the Toshiba 800GXHH21 rated at 4500 V and 800 A average. Toshiba [1991] contains additional information on this diode, which was selected for its voltage and current rating and specified reverse recovery time. DeDoncker et al [1991] describes the performance features of high-voltage GTOs in a "soft-switching" zero voltage power conditioner and provides switching loss data. Table 3.2.2 summarizes the full power point design for the six motors.

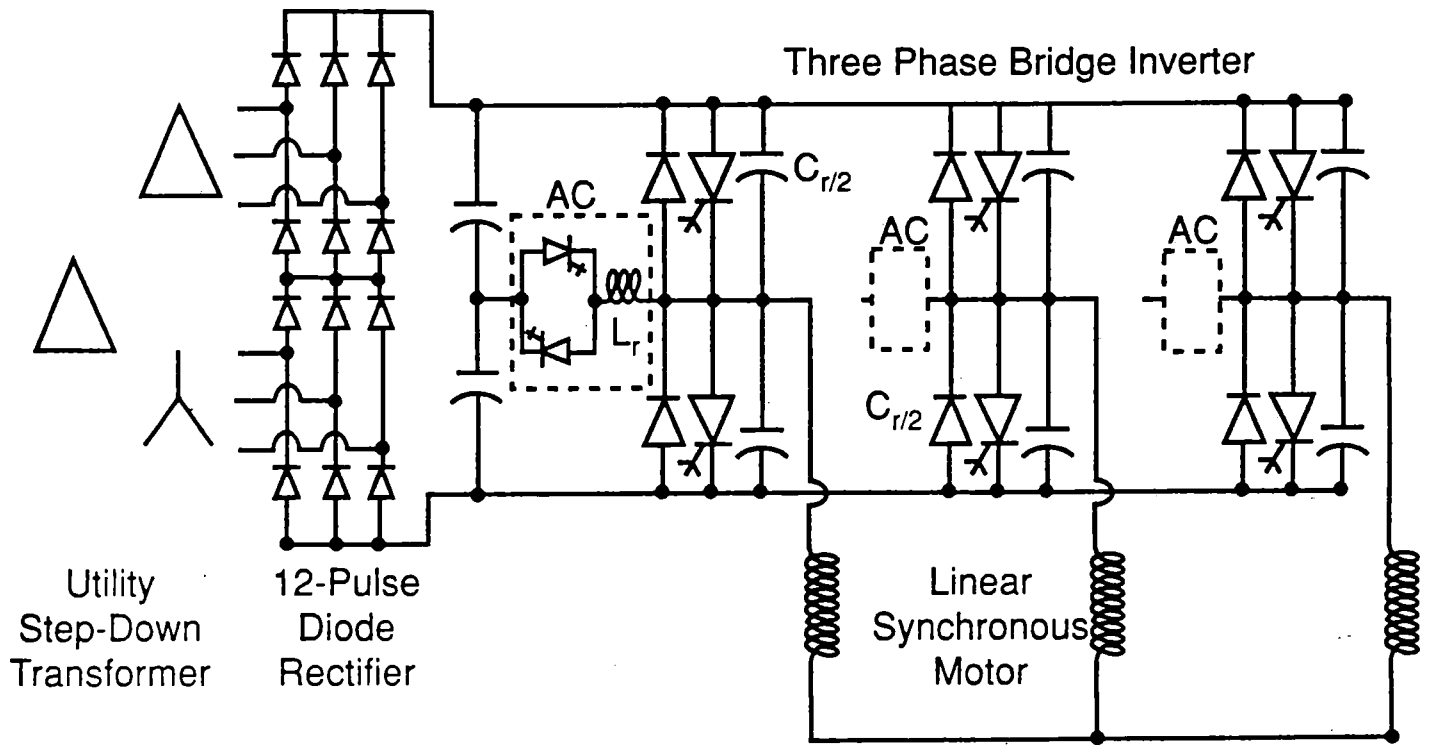


Figure 3.2.4. Circuit Diagram for AC-DC-AC, ARCP Inverter, Linear Synchronous Motor Drive.

Parameter	Motor Design					
	1	2	3	4	5	6
GTO average current (A)	280	265	179	185	268	286
GTO RMS current (A)	517	502	336	343	503	522
GTO peak current (A)	1276	1276	850	850	1274	1274
Diode average current (A)	103	118	77	70	115	97
Diode RMS current (A)	308	333	218	207	335	311
Diode peak current (A)	1276	1276	850	850	1274	1274
Number of series GTO's	2	1	2	2	3	2
Number of parallel GTO's	2	2	2	2	1	1
GTO and diode losses per device(W)	1765	1763	1049	1045	1379	1482
Resonant inductor (μ h)	6	6	6	6	6	6
Resonant capacitor (μ fd)	3	3	3	3	3	3
Total inverter circuit losses (kW)	236	155	164	141	163	119

Table 3.2.2. Power conditioner designs.

Where two parallel GTOs are indicated in Table 3.2.2, each GTO supplies the power to one side of the linear synchronous motor. The three-phase motor windings are isolated from each other. Motor designs 5 and 6 only require a single GTO, and the motor windings for each side are directly connected in parallel. Current sharing will be attained because the windings have the same impedance, and the motor loading is the same for each side.

The resonant components are relatively small since they operate only during the switching interval of the main GTOs. The peak current ratings of the inductors and auxiliary semiconductors are greater than the main GTOs, but their RMS ratings are reduced because of the low duty cycle. The DC voltage is of such a magnitude that series-connected DC capacitors are required. The establishment of a DC center-tap is achieved by providing an even number of series-connected capacitors on the DC bus.

The twelve-pulse diode rectifier can be accomplished with 12 diodes rated for the AC voltage and one-third of the DC current.

3.2.4 Power Conditioning Equipment

A General Electric operating department fabricates pulse width modulated inverters using gate turn-off thyristors for high horsepower induction motor drives. At 2300 V, the maximum motor rating is 2500 hp; at 4160 V, the maximum rated power is 7000 hp. This later rating is comparable to the power rating of the linear synchronous motors. The ARCP inverter with its "soft-switching" low loss characteristics is proposed for this application in order to allow a higher switching frequency to attain the desired 120 Hz output with relatively low harmonic distortion in the current waveform. The switching frequency chosen for this point design was 1000 Hz.

The utility step down transformer would be a standard three-phase three-winding rectifier transformer with an appropriate k-factor design to account for additional harmonic losses.

Figure 3.2.5 is a photograph of a water-cooled GTO/diode assembly with a representative resonant capacitor. The printed circuit in the foreground is the GTO turn-on and turn-off gate driver. This PC card supplies the gate current to turn the GTO on and the peak gate current to turn the GTO off.

The right-hand cabinet shown in Figure 3.2.6 is an assembly of four GTOs connected in series connected in a three-phase full-wave bridge inverter that feeds an AC motor. This is made up of 24 of the GTO/diode modules shown in Figure 3.2.5. The left-hand cabinet is the AC-to-DC portion of the circuit and is composed of 12 diodes connected in two three-phase bridges as shown in Figure 3.2.4. The estimated size of this equipment is 12 ft by 3 ft by 8 ft and weighs 7000 lb. This equipment is fabricated for industrial customers, and the actual size of outdoor rated equipment packaged for use along a railroad right-of-way may be different. GE [1991] contains additional information on this GTO-based AC drive system.

A General Electric operating department has fabricated a GTO-based power conditioner using a storage battery. The equipment includes a utility isolation transformer, multiple GTO-based inverter bridges, DC and AC filters and a unique four-quadrant controller. It is described in Walker [1991]. Bechtel [1988], which was prepared by the overall battery load leveling project manager, provides a cost estimate for the complete power conditioning subsystem (including the transformer) of \$60/kw based on a 100 quantity per year of a mature product.

Using the block lengths given in Table 3.1.1, this \$60/kw figure can be converted into M\$/km for the six designs. The results are tabulated in Table 3.2.3.

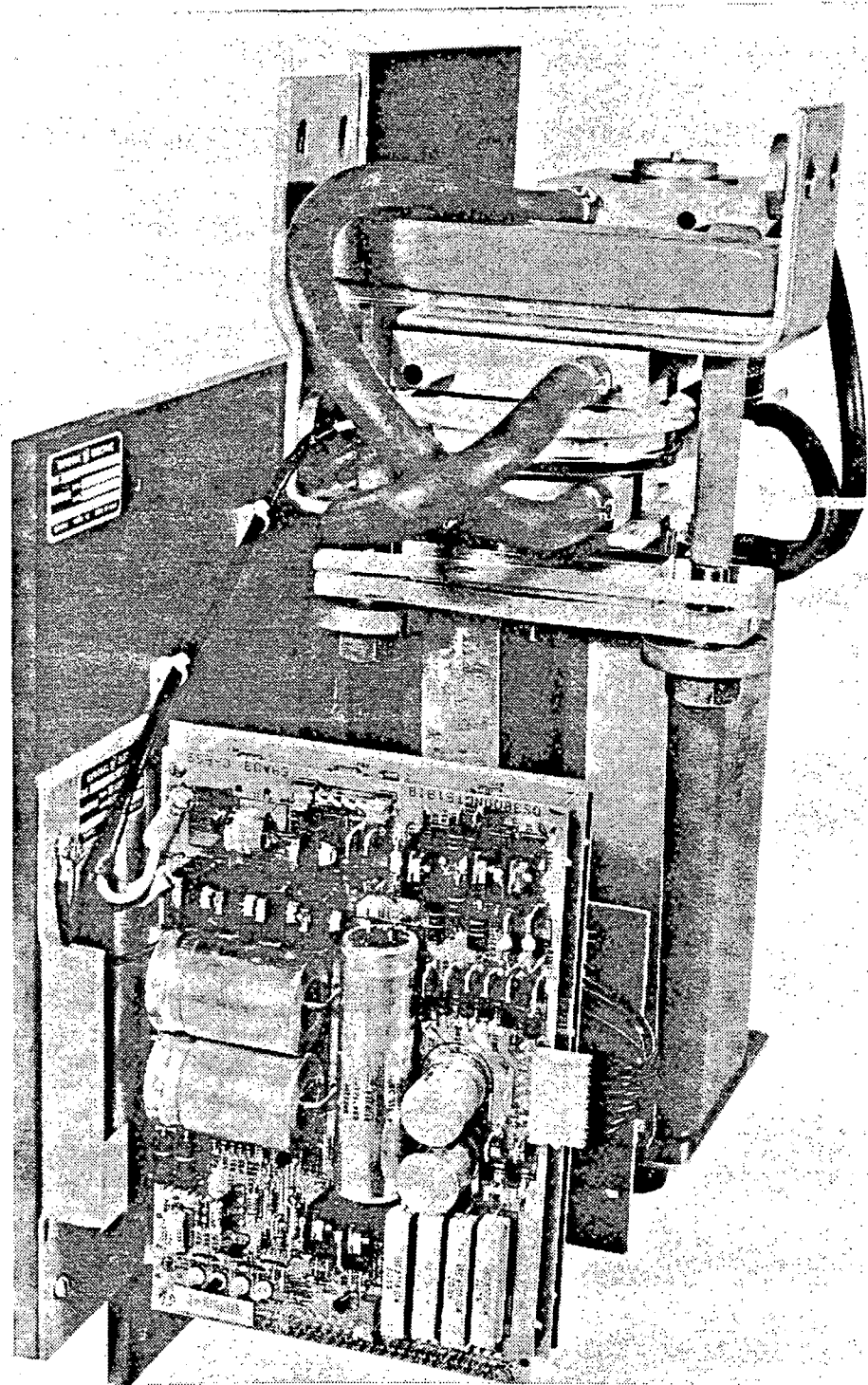


Figure 3.2.5. GTO/Diode/Resonant capacitor/Gate Drive switch.

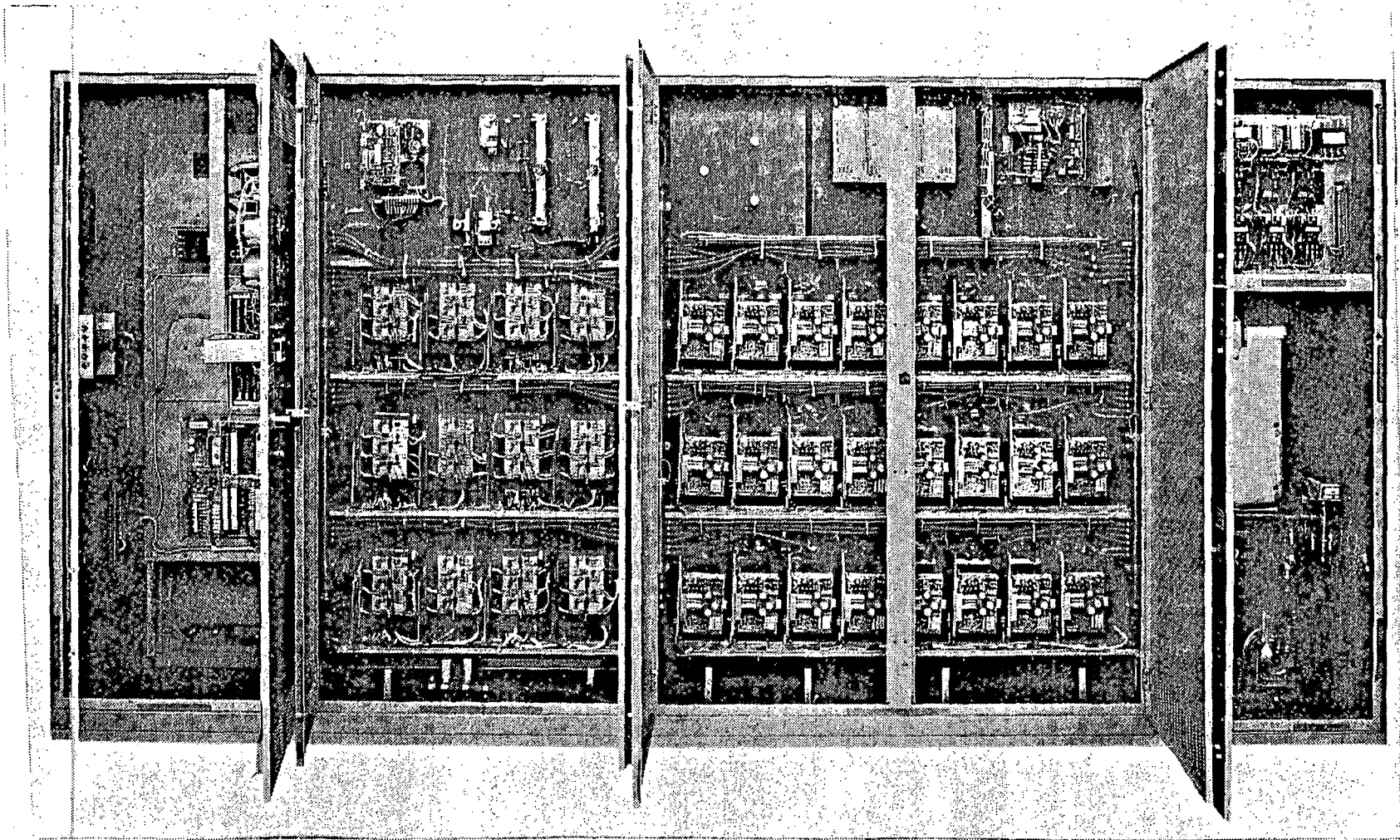


Figure 3.2.6. AC-DC Rectifier and GTO DC-AC Inverter Rated at 7000 hp (5.2 MW).

Motor design	Block length (km)	Price per km (M\$)
1	.110	10.53
2	.338	2.37
3	3.035	0.27
4	2.000	0.35
5	5.400	0.15
6	2.000	0.30

Table 3.2.3. Power conditioning costs.

This chart assumed that the price is \$60/kw and it is independent of the power rating. In actual fact, the cost per kilowatt of mature products decreases when the rating increases. This is described as the "economy of scale" and slopes of -15% have been reported in the literature, Key et al [1985]. This will have the effect of reducing the price per kilometer of motor design 1.

3.2.5 Summary

This section of the final report has selected a DC link power conditioning system to supply each of the six linear synchronous motor designs. The system consists of a three-winding utility step-down transformer and a 12-pulse diode rectifier feeding a GTO-based pulse width modulated inverter. Some of the motor designs required series connected GTO thyristors, others required two independent motor windings, one for each side of the vehicle. This system and power semiconductor were selected based on the motor frequency (120 Hz in 5 of the 6 motor designs), the peak MVA required (10.1 to 19.3), and the peak phase voltage (2146 to 4425 V). To obtain a low distortion waveform of motor current and to increase the inverter efficiency, a soft-switching resonant inverter was selected. The particular inverter is called an "alternating resonant commutated pole" (ARCP) and it uses auxiliary semiconductors and resonant circuit elements to reduce the peak power dissipation occurring in the GTO during both its turn-on and turn-off intervals. This reduction in switching loss increases the inverter efficiency.

System size, weight, and price estimates were developed from an existing GE product departments commercial motor drive and battery load-leveling facility of comparable rating as these linear synchronous motor drives. Although neither of these commercial applications use the ARCP approach, the existing data should be of sufficient accuracy for this conceptual design. Based on the block lengths, the price of the power conditioning subsystem (PCS) was calculated to be from 0.15 to 10.5 million dollars per kilometer.

3.3 Null-flux Levitation/Guidance Coil Interaction

The determination of the currents induced in the null-flux guideway coils, and the calculation of the resulting forces created by the interaction of the field created by these currents with the superconducting coils, is a significant analytical exercise. However, to ensure that the coil design presented here represents a workable one for a maglev vehicle, it was decided to undertake the solution of these equations for our proposed design. Once the analytical tools were developed for the basic geometry chosen, parametric studies were performed to determine the optimal null-flux coil geometry, suspension stiffnesses, and required vertical offset between the superconducting and null-flux coils to produce desired levitation and guidance forces.

We have undertaken a comprehensive study to analyze the interaction of electromagnetic (EM) forces between the superconducting vehicle coils and the null-flux guideway coils. A three-dimensional model, as shown in Figure 3.3.1 (see also Figure 3.1.1), is considered for the calculation of EM forces experienced by the system of coils, and the induced current on the null-flux coils. The model consist of a series of stationary normal-metal coils, placed on the $x = 0$ plane along the z -axis, and two superconducting coils energized with electric currents. The direction of the currents in the two superconducting coils are opposite to each other, which is required for them to behave as separate poles in the linear synchronous motor. A system could conceivably be configured with these coils operating with the same polarity, and the separate bogeys representing poles of the motor, but the resulting pole pitch would be so long as to create problems with the motor design (see Appendix A). The superconducting coils move, with a speed v , along the z -axis at a distance $x = g$ from the stationary null-flux coils. The magnetic field generated by the superconducting coils is constant in the moving coordinate system of the vehicle; to the stationary null-flux coils in the guideway, however, it appears time-varying. Therefore, a current is induced in the null-flux coils and the direction of this induced current is such that it creates a magnetic field of opposite polarity to that generated by the superconducting coils. The magnitude of this induced current depends on the electrical parameters (resistance and inductance) of the null-flux coils, shape and sizes of the coils, the distance between the coils, and finally the vehicle speed. Interaction of the induced current in null-flux coils with the current in the superconducting coils results in the attractive and repulsive EM forces that support the maglev system.

The forces required to levitate and guide the vehicle are based on its mass. With our assumed mass of 24000 kg and the equivalent of two magnets acting on each vehicle, the required forces per magnet can be obtained once the accelerations which the vehicle can undergo are selected. Using maglev design practices which have been presented in several seminars, we limit the desired

vertical, longitudinal and transverse accelerations to 1.0, 0.2 and 0.2 g, respectively. This allows the vehicle to be levitated and to make turns, starts and stops at the maximum accelerations which passenger comfort will allow. These g forces correspond to forces of 118, 24, and 24 kN, respectively, per magnet (coil pair). We will show that these forces are easily achievable with our canonical magnet design.

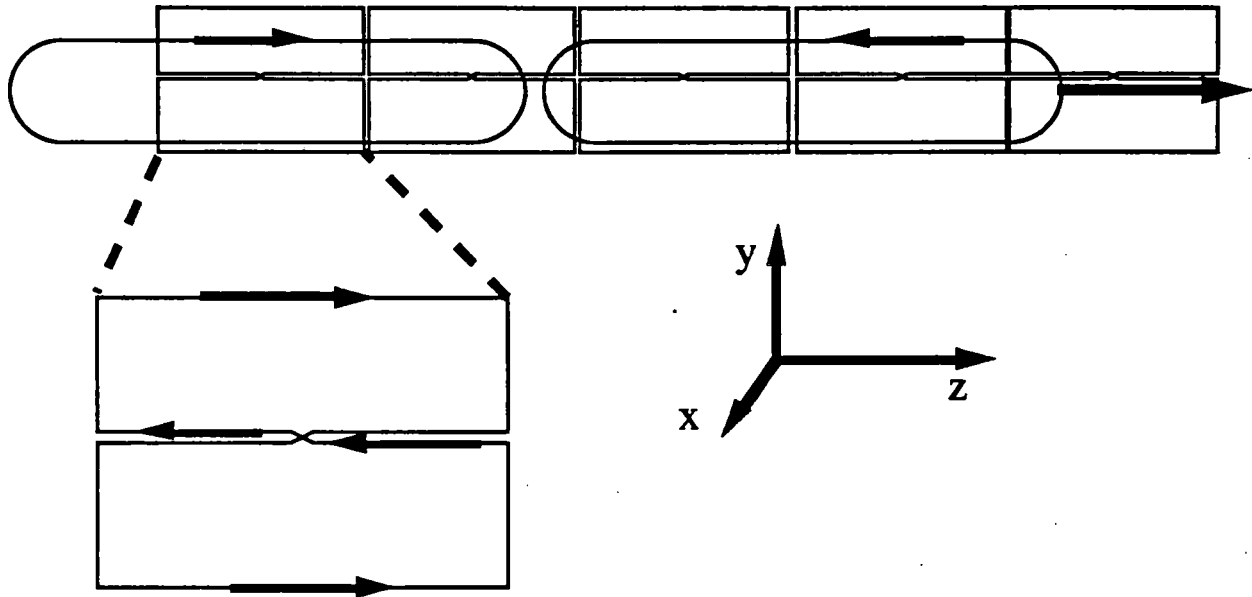


Figure 3.3.1. The sidewall levitation system. A pair of superconducting coils passing a guideway composed of several null-flux coils, showing direction of motion of superconducting coils and one null-flux coil enlarged for detail.

3.3.1 Null-flux Coil Electromagnetic Analysis

Interaction between a pair of superconducting coils and one of the null-flux coils is examined first and then through a superposition process the collective effect of the series of the null-flux coils is taken into account. We define a cartesian coordinate system, as our reference frame, located at the center of the null-flux coil as shown in Figure 3.3.2.

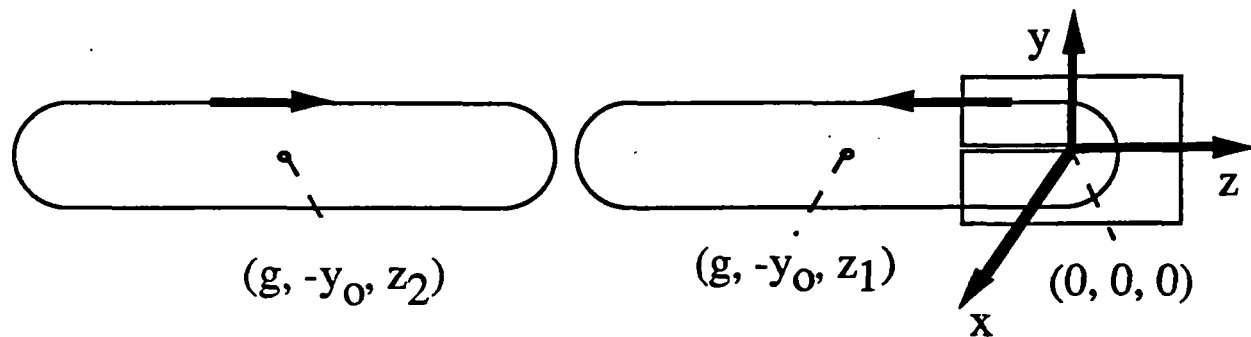


Figure 3.3.2. Superconducting coils and single null-flux coil for analysis.

The z-axis is in the direction of the vehicle motion, the y-axis is the vertical direction, and the x-axis is in the horizontal direction of the vehicle. The pair of current-carrying superconducting coils are located on the y-z plane with their centers initially at $(g, -d, z_1)$ and $(g, -d, z_2)$. The distance between the centroids of the two superconducting coils, $z_1 - z_2$, is assumed constant at all time as these pair of coils pass the stationary null-flux coil. This distance also represents the pole pitch of the motor, since each coil represents a motor pole. The steps toward calculating the induced current and the EM forces in the system are outlined here:

- i) Given the geometry of, and the current in the superconducting coils, the magnetic field generated by the pair of these coils on the surface of the null-flux coil is calculated.
- ii) Having the distribution of the magnetic induction vector at the surface of the null-flux coil, the magnetic flux linking the coil is evaluated.
- iii) Utilizing the induced electromotive forces obtained in step (ii), a lump circuit representation of the system is considered to calculate the induced current in the null-flux coil.
- iv) The currents in the superconducting and null-flux coils are fed into the Ampere's equation, and the EM interactive forces are calculated.

A brief discussion of each step is given in the subsections that follows.

Magnetic Field Generated by superconducting Coils

The value of the magnetic induction due to a current loop with current I , as shown in Figure 3.3.3, can be calculated from Ampere's law, which gives

$$B(\mathbf{r}) = \frac{\mu_0 I}{4\pi} \oint \frac{d\mathbf{l} \times (\mathbf{r} - \mathbf{r}')}{|\mathbf{r} - \mathbf{r}'|^3} \quad (3.3.1)$$

- where B = magnetic induction
 μ_0 = Free-space permeability
 I = electric current in the loop
 \mathbf{r} = $x\hat{x} + y\hat{y} + z\hat{z}$; position vector pointing to an observation point
 \mathbf{r}' = $x\hat{x} + y\hat{y} + z\hat{z}$; position vector pointing to a source point
 $d\mathbf{l}$ = a vector element on the loop in the direction of current flow and \hat{x} , \hat{y} , and \hat{z} are unit vectors in the cartesian system of coordinates.

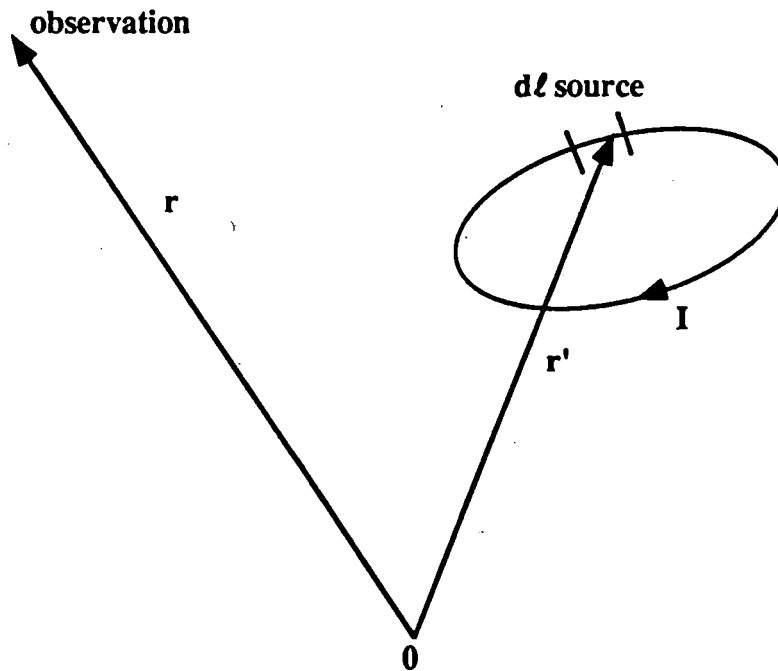


Figure 3.3.3. A current loop showing geometry definitions.

This equation is applied to the geometry of the superconducting coils, i.e., two racetrack coils carrying oppositely directed currents, to calculate the magnetic induction generated by these coils at any observation point in space. For two superconducting coils located in the $x = 0$ plane with their centers 2.6 meter apart from each other, Figures 3.3.4 through 3.3.6 show the three cartesian components of the induction vector, at $x = 0.1$ meter as a function of y and z . Note that the choice

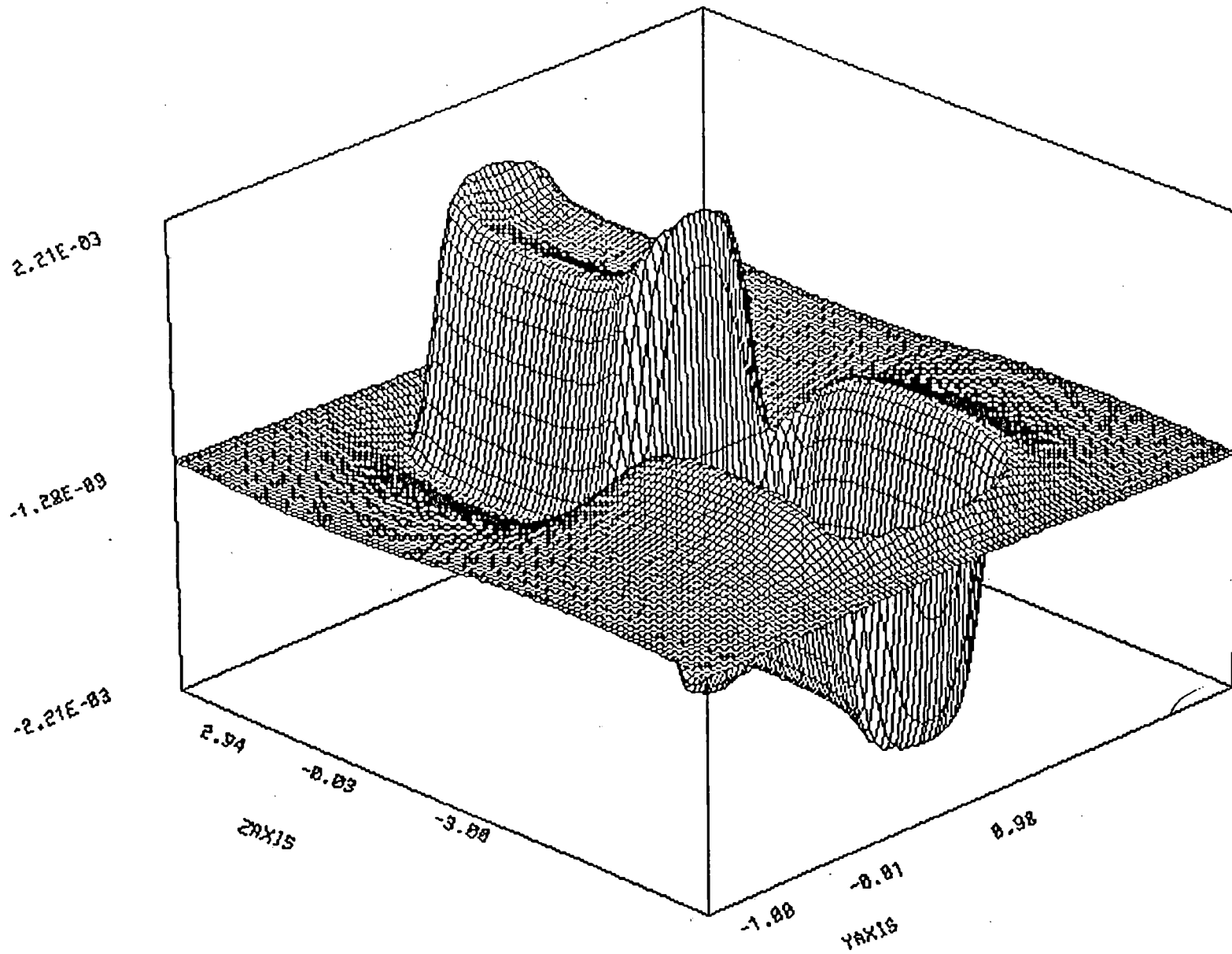


Figure 3.3.4. 3-D field profile of B_x from pair of SC coils of Figure 3.3.2 geometry.

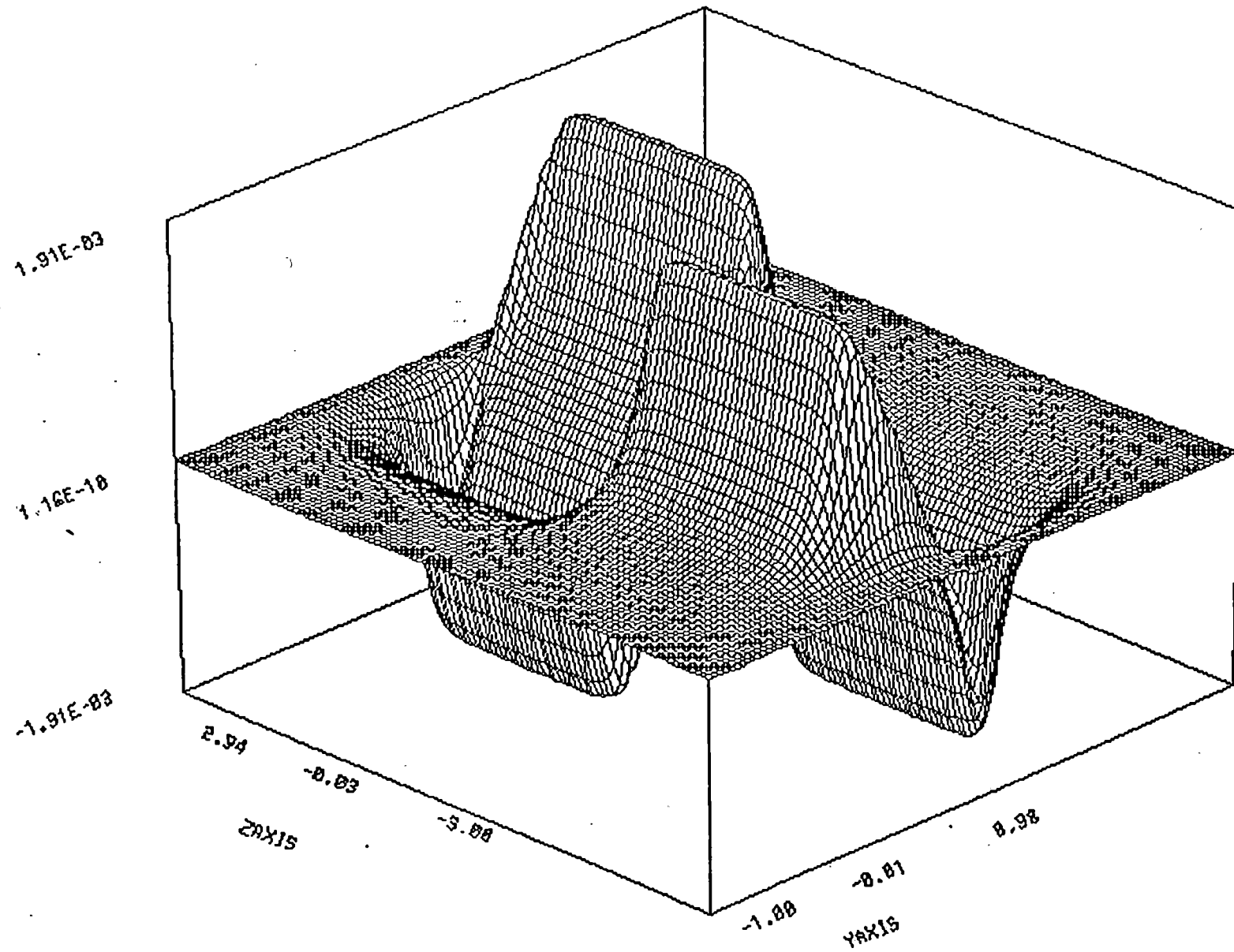


Figure 3.3.5. 3-D field profile of B_y from pair of SC coils of Figure 3.3.2 geometry.

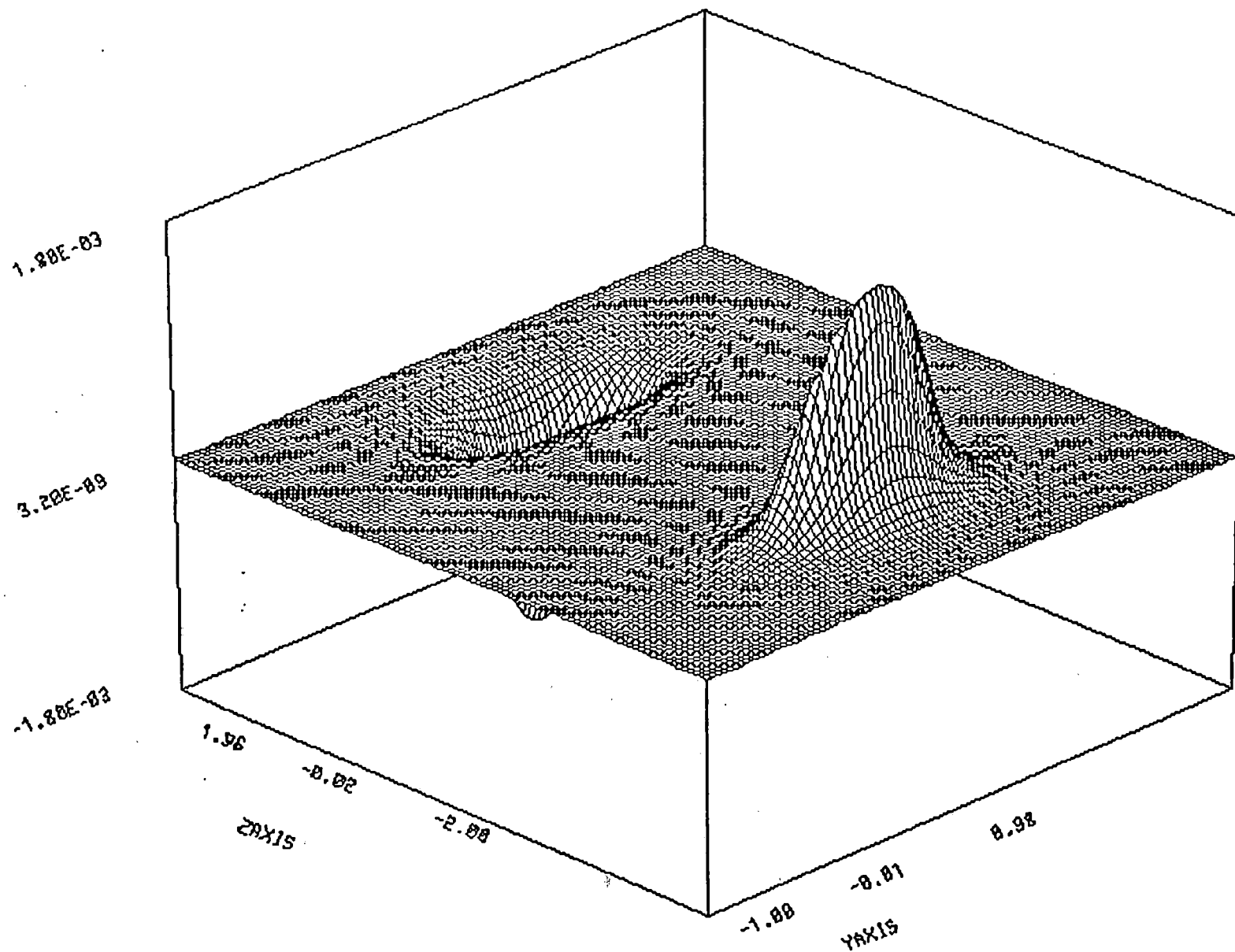


Figure 3.3.6. 3-D field profile of B_z from pair of SC coils of Figure 3.3.2 geometry.

of a 2.6 m spacing is for illustrative purposes only, and differs slightly from the 2.5 m spacing assumed for some of the analyses presented in this section.

Flux Linkage

The magnetic flux linking the null-flux coil is given by

$$\Phi = \iint B \cdot \hat{n} ds \quad (3.3.2)$$

where Φ = magnetic flux
 B = magnetic induction due to superconducting coil
 ds = null-flux coil area element
 \hat{n} = a unit vector perpendicular to the null-flux loop

The direction of \hat{n} depends on the direction of current in the loop. For a current loop located in counterclockwise.

Induced Current

From Kirchoff's Law, the equation governing the current induced in the null-flux coil is

$$IR_{nf} + L_{nf} \frac{dI}{dt} - \frac{d\Phi}{dt} = 0 \quad (3.3.3)$$

where I = induced current in the null-flux coil
 R_{nf} = null-flux coil resistance
 L_{nf} = null-flux coil self-inductance
 Φ = flux linkage

Transformation of this equation into the spatial domain using the chain rule, allows us to represent time derivatives as derivatives in the z -direction. In spatial domain the equation is

$$IR_{nf} + vL_{nf} \frac{dI}{dz} - v \frac{d\Phi}{dz} = 0 \quad (3.3.4)$$

where v is the speed of the superconducting coils (vehicle) along the z -axis. The induced current, given by this equation, is solved for using a finite difference scheme. As an example, Fig. 3.3.7 shows the induced current in the null-flux coil for the configuration of Fig. 3.3.2 with null-flux height of 0.5 m, length of 1.0 m, the vertical offset $y_o = 0.03$ m, and the transverse offset $g = 0.1$

m. as a function of z , where z represents the distance between the center of the null-flux coil and the center of the second superconducting coil.

EM Forces

According to Ampere's law of force between current loops, the EM forces between the superconducting and null-flux coils is given by

$$F_{12} = \frac{\mu_o}{4\pi} I_1 I_2 \oint \oint \frac{(d\ell_1 \cdot d\ell_2) R_{12}}{|R_{12}|^3} \quad (3.3.5)$$

- where I_1 = current in the null-flux coil
 I_2 = current in the superconducting coil
 μ_o = free-space permeability
 R_{12} = position vector pointing from a current element in null-flux coil to an observation point on superconducting coils.
 ℓ_1 = a vector in the direction of current element in null-flux coil
 ℓ_2 = a vector in the direction of current element in superconducting coils

Using this equation and with the aid of the previous equations, the three cartesian components of EM forces between the coils are calculated as a function of relative position of the coils with respect to each other, speed of the vehicle, and the electrical parameters of the null-flux coil. Figs. 3.3.8, 3.3.9, and 3.3.10 depict forces F_x (guidance), F_y (levitation), and F_z (drag) for the configuration of Fig. 3.3.2 with the same coil sizes are used for the current plot Figure 3.3.7.

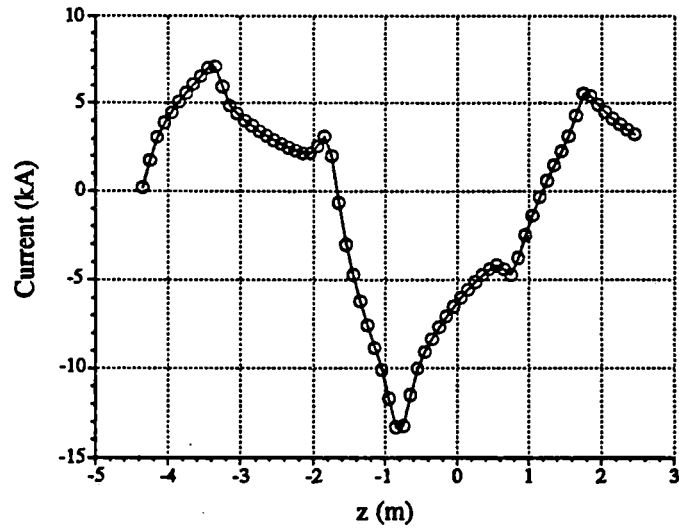


Figure 3.3.7. Induced current in the null-flux coil for $v=140$ m/sec as a function of z , where $z=z_2$ as shown in Fig. 3.3.2.

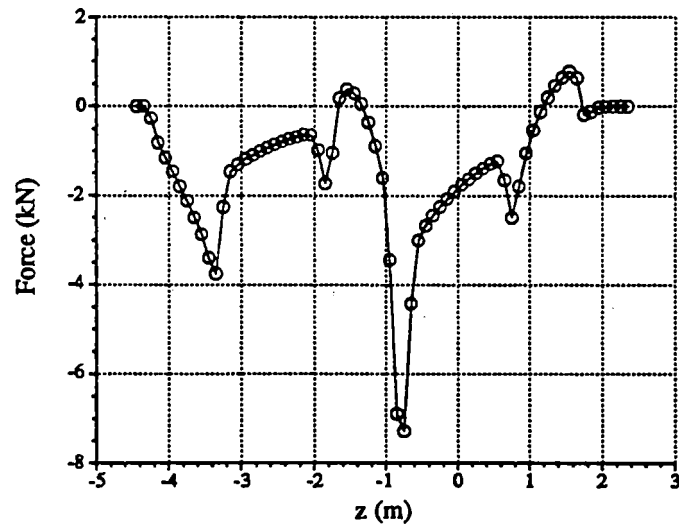


Figure 3.3.8. Guidance force from a single null-flux coil interaction as a function of z for the geometry of Fig. 3.3.2.

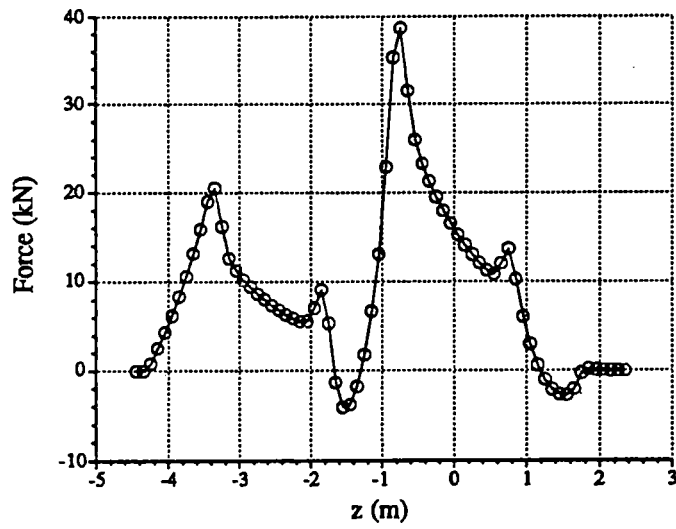


Figure 3.3.9. Levitation force from a single null-flux coil interaction as a function of z for the geometry of Fig. 3.3.2.

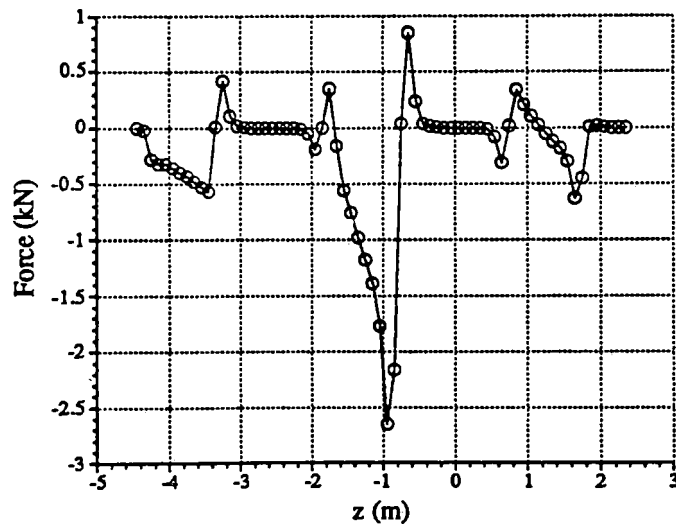


Figure 3.3.10. Drag force from a single null-flux coil interaction as a function of z for the geometry of Fig. 3.3.2.

Determination of the forces provided by the system in actual operation requires the superposition of the forces from the interaction of the superconducting magnet with a single null-flux coil to obtain the results for the system where the null-flux coils are placed all along the guideway. The results of this effort are presented here. In addition, the thermal analysis of the null-flux coil is presented here. A thermal analysis is required to evaluate whether the coil will overheat because of the high current which the resistive null-flux coil carries for the short time in which the vehicle passes it.

The required superposition of the forces can be made once the pitch P_{nf} of the null-flux coils is chosen. This null-flux coil pitch is to be distinguished from the pole pitch of the motor, which is defined by the longitudinal spacing of the superconducting coils. The pitch can be a parameter of the optimization of the null-flux coil design. For this study, several different null-flux coil geometries were analyzed so that we could recommend the geometry which, when used with our proposed superconducting vehicle coils, provided the largest desired levitation and guidance forces while maintaining the drag at a reasonable level. The force characteristic when a continuous guideway of null-flux coils is considered varies from that for a single null-flux coil (shown in Figures 3.3.8 - 3.3.10) in that the superposition leads to a different variation of force with z position of the superconducting coils. This "steady-state" behavior is realized when the superconducting coils have passed a number of null-flux coils equal to the total length of the two superconducting coils. To obtain the steady-state behavior, the number of null-flux coils which must be superimposed is equal to the z length over which the superconducting coils have an interaction with the null-flux coils divided by the pitch of the null-flux coils. The steady-state characteristic obtained by this superposition shows variation of the force over the length of the null-flux coil pitch, as do the forces in Figures 3.3.8 - 3.3.10, with the magnitude of this variation relative to the average force indicating the smoothness of the suspension and guidance. The force variation can be dramatically reduced relative to that observed for the single null-flux coil interaction, however, because of the simultaneous action of multiple null-flux coils. Clearly, an ideal system would have a perfectly smooth characteristic. An actual characteristic is shown in Figure 3.3.11. Note that while the forces still vary substantially over the repeated cycle, the variation is dramatically less than that seen in Figures 3.3.8 through 3.3.10 for a single null-flux coil interaction. The degree of smoothing depends on the length ratio of the superconducting coil pair to the null-flux coil, with larger ratios resulting in smoother rides.

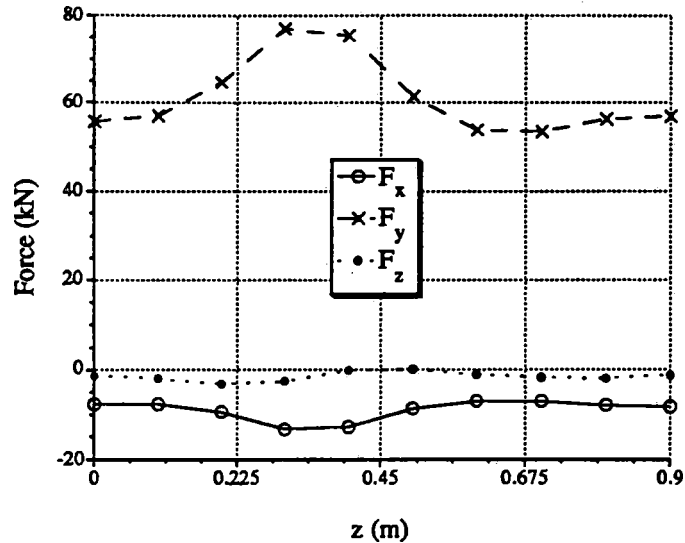


Figure 3.3.11. Forces over the length of a null-flux coil for a superimposed case where the ratio of the superconducting coil pair length to the null-flux coil length is 5.2:1 (Note: x, y, z represent guidance, levitation, drag).

The geometries studied are summarized in Table 3.3.1, where the physical dimensions are referred to Figure 3.3.2. In all cases, the superconducting coil current was fixed at 568700 Ampere-turns. The headings in Table 3.3.1 represent the overall length of the superconducting coil, L_{sc} , the length and height of the null-flux coil, L and H , its inductance and resistance in μH and $m\Omega$, L_{nf} and R_{nf} , the vertical offset of the superconducting coil mid-height from that of the null-flux coil, y_0 , and the transverse gap between the two coils' mid-planes, g . All dimensions are in meters.

Case	L_{sc}	L	H	L_{nf}	R_{nf}	y_0	g
1	2.5	1.0	0.4	3.28	0.39	0.03	0.1
2	2.5	1.0	0.5	3.65	0.41	0.03	0.1
3	2.5	1.0	0.6	3.94	0.43	0.03	0.1
4	2.5	1.0	0.7	4.22	0.44	0.03	0.1
5	2.5	1.0	0.8	4.49	0.46	0.03	0.1
6	1.5	1.0	0.5	3.65	0.41	0.03	0.1
7	2.5	1.5	0.5	5.31	0.58	0.03	0.1
8	2.5	2.0	0.5	6.98	0.75	0.03	0.1
9	2.5	1.0	0.6	3.94	0.43	0.06	0.1
10	2.5	1.0	0.6	3.94	0.43	0.03	0.12

Table 3.3.1. Cases chosen for superconducting - null-flux coil interaction study

The analyses were performed for all ten cases for a pitch equal to the length of the null-flux coils, and for several cases for pitches longer than the coils for comparison. The results of these analyses are presented in Table 3.3.2, where the variable pitch cases are identified by letter and the number corresponds to the case number. The average value of each of the three components of force, as well as the deviation about that average value over the length of the null-flux coil pitch, are presented for each case. The pitch was varied for cases 2 and 7 to allow comparison of the forces at identical pitches for different null-flux coil lengths. All forces in the Table are in units of kN, while the pitch is in meters.

Case	P_{nf}	\bar{F}_x	\bar{F}_y	\bar{F}_z	ΔF_x	ΔF_y	ΔF_z
1	1.0	3	7	-0.1	1	7	1.0
2A	1.0	-9	61	-1.5	6	24	3.2
2B	1.5	-6	41	-1.0	11	50	3.8
2C	2.0	-5	31	-0.7	6	23	3.3
3	1.0	-43	157	-3.8	11	37	5.0
4	1.0	-40	191	-4.3	10	38	5.0
5	1.0	-26	173	-3.7	7	33	4.1
6	1.0	-5	30	-0.6	4	16	2.0
7A	1.5	-5	38	-0.8	6	31	2.1
7B	2.0	-4	29	-0.6	3	20	1.8
8	2.0	-3	26	-0.6	4	23	1.8
9	1.0	-154	350	-17	37	70	20
10	1.0	-30	145	-3.3	7	27	3.5

Table 3.3.2. Levitation, guidance and drag forces for cases 1 through 10 and various null-flux coil pitches

Inspection of the results in Table 3.3.2 yields much important information that will lead to determination of the velocity of liftoff, the electromagnetic drag, and the suspension stiffnesses for the preferred system. From these studies, we concluded that the preferred design is Case 4. The levitation and guidance forces are highest for this case and decline as the null-flux coil height is increased from 0.7 m (see Case 5). Therefore, we evaluated the coil geometry of Case 4 for various vertical offset values, to determine (1) the velocity at which the vehicle will lift off wheels which are positioned so that the superconducting coils ride at a vertical offset of 10 cm from the null-flux coils; and (2) the vertical offset required to achieve levitation at a top speed of 140 m/s. Once these two values are known, the suspension system operation is bounded in terms of vertical offset vs. speed from initial levitation to top speed characteristics. While further investigations would be required to evaluate the force characteristics over the entire velocity spectrum, the depth to which this analysis has been carried to date is sufficient to demonstrate the viability of the proposed superconducting coil design for an operating maglev system, which was our original intent.

It should be noted that the choice of 10 cm for the offset at which wheels are used is arbitrary, and should be optimized further. For the null-flux coil levitation system, the stable levitation

regime only extends to a certain offset, beyond which the levitation force actually decreases with increasing offset. Since the minimum possible levitation speed is desirable, the wheel height should be set to provide the vertical offset which produces the peak force for a given velocity. Our initial analyses indicate that the 10 cm value is close to this peak for the geometry of choice.

Determination of the two values indicated above was made by analyzing (1) the levitation force vs. vertical offset at 140 m/s for offsets from 0.5 cm to 6 cm; and (2) the forces vs. velocity from 5 to 45 m/s for a vertical offset of 10 cm. Both analyses were performed using the coil geometry of Case 4: null-flux height of 0.7 m, null-flux length of 1 m, pitch of 1 m, and gap of 0.1 m. Results of the vertical offset study are shown in Figure 3.3.12, which presents the average component forces vs. offset at 140 m/s. As can be seen, the required levitation force of 118 kN per coil pair is achieved at an offset of 1.8 cm. Figure 3.3.13 depicts the levitation force vs. velocity at an offset of 10 cm. The levitation speed for this offset is about 42 m/s. While this value is somewhat higher than the 27 m/s at which the Japanese MLU002 vehicle levitates, the force generated by the null-flux system is known to be lower than that for the facing levitation system, so this result is expected. Operation with one superconducting magnet (coil pair) depowered would be possible. The required force per coil pair rises from 118 kN to 157 kN, and an increased gap at the remaining three coils of 2.5 cm would increase the levitation force to compensate for the depowered magnet. Vehicle dynamics at speed with one coil depowered are another matter, and would require a more complicated analysis beyond the scope of this study.

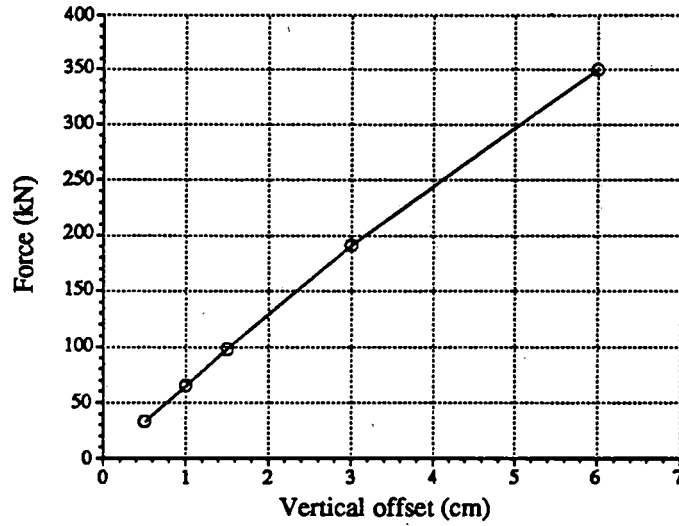


Figure 3.3.12. Levitation force vs. offset for superconducting coil pair at 140 m/s for Case 4 geometry.

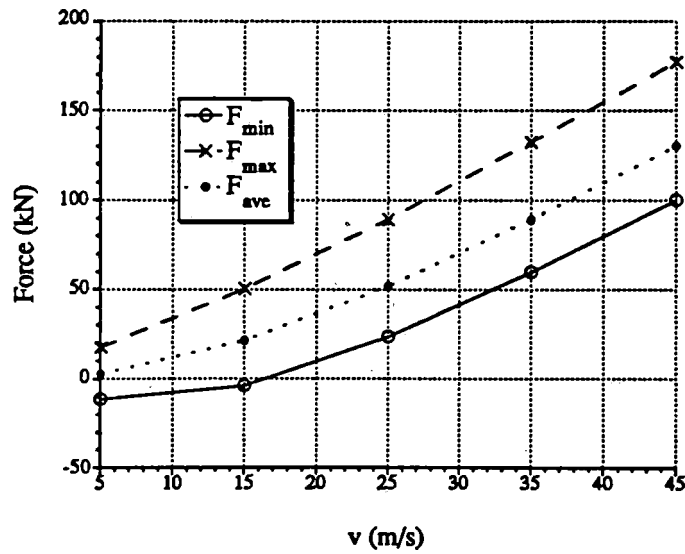


Figure 3.3.13. Levitation force vs. velocity for superconducting coil pair at a 10 cm offset for Case 4 geometry.

Graphs of the levitation, guidance and drag forces vs. velocity for the Case 4 geometry with a 3 cm offset are presented in Figures 3.3.14 through 3.3.16. Since the forces are approximately linear with offset in the range from 1.8 to 3 cm, scaled force values at operating conditions for the three force components are 118 kN (1.0 g) for levitation, -39 kN (0.2 g) for guidance, and -4.4 kN for drag. The guidance force turns out to be exactly the 0.2 g desired with the 1.0 g levitation force. The drag force represents a significant 9% of the 50 kN thrust provided by the linear motor.

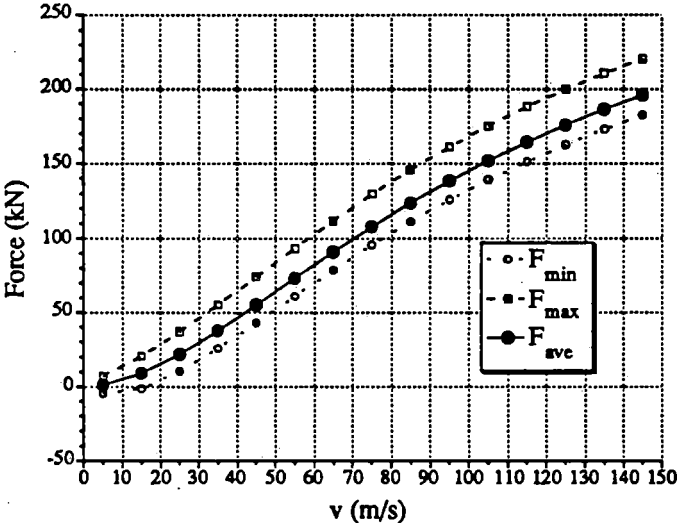


Figure 3.3.14. Levitation force vs. velocity for superconducting coil pair at a 3 cm offset for Case 4 geometry.

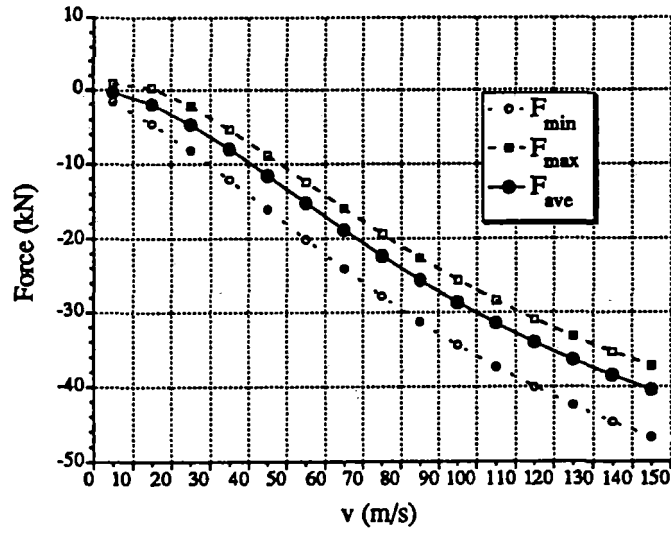


Figure 3.3.15. Guidance force vs. velocity for superconducting coil pair at a 3 cm offset for Case 4 geometry.

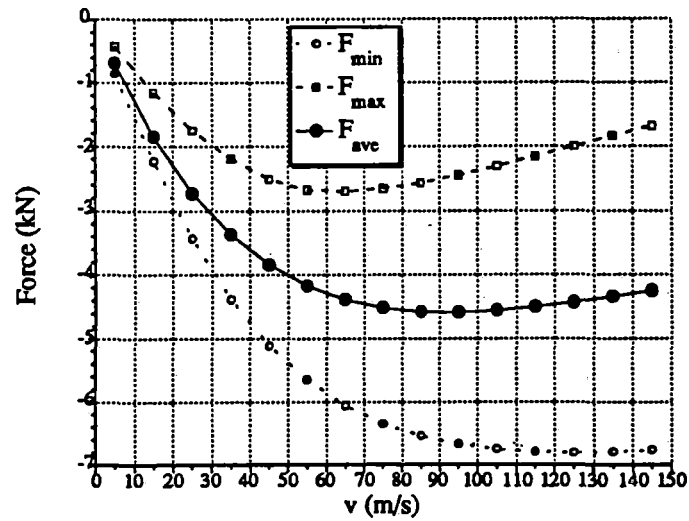


Figure 3.3.16. Drag force vs. velocity for superconducting coil pair at a 3 cm offset for Case 4 geometry

Additional information from Table 3.3.2 includes the suspension stiffness at a 3 cm vertical offset, obtained by comparing Cases 9 and 4 for the vertical suspension and Cases 10 and 4 for the transverse suspension. The former comparison leads to a stiffness of 53 kN/cm, or about 1 g/cm in terms of acceleration effects. The latter comparison yields a transverse suspension stiffness of 5 kN/cm, or 0.1 g/cm, in the gap range of interest. Comparing these stiffnesses to the suspension and guidance forces of 1 and 0.2 g, we see that the system should be very stable in both directions, although the evaluation of a secondary suspension is indicated.

3.3.2 Null-flux Coil Thermal Analysis

The null-flux coil design is shown in Figure 3.3.2. Its overall height is H , and its length L . We assume for this analysis that the coil has only one turn, since this allows the lowest cost coil fabrication. The coil resistance is given by

$$R_{nf} = \frac{\rho l}{A} \quad (3.3.6)$$

where ρ is the resistivity of the coil material, l the total length of conductor, and A the cross-sectional area of the conductor. We wish to determine the temperature rise of the coil when carrying its current I_{nf} for time Δt . The relation governing the adiabatic temperature rise (assuming no cooling of the coil) is

$$\Delta T = \frac{Q}{Mc_p} \quad (3.3.8)$$

where Q is the total energy deposited into the coil, M is the coil mass, and c_p its heat capacity at operating temperature. The energy deposition is given by the time integral

$$Q = \int I_{nf}^2 R_{nf} dt = \int I_{nf}^2 \frac{\rho l}{A} dt. \quad (3.3.9)$$

A simplified analysis can be performed by making the conservative assumption that the coil carry its peak current for the entire time interval, resulting in the relation

$$Q = I_{nf}^2 \frac{\rho l}{A} \Delta t \quad (3.3.10)$$

and the coil mass M by

$$M = \gamma V = \gamma l A \quad (3.3.11)$$

where V is the coil volume. Combining these equations, we arrive at an expression for the temperature rise over a time interval Δt of

$$\frac{\Delta T}{\Delta t} = \frac{I_{nf}^2 \rho}{\gamma A^2 c_p} \quad (3.3.12)$$

For 1100-00 aluminum at a temperature of 300 K, $\gamma = 2.8 \text{ g/cm}^3$, $\rho = 3.4 \text{ } \mu\Omega\text{-cm}$ and $c_p = 0.9 \text{ J/g-K}$. Substitution of these physical parameters yields

$$\frac{\Delta T}{\Delta t} = (1.35 \times 10^{-6}) \frac{I_{nf}^2}{A^2} . \quad (3.3.13)$$

Substituting current in A and area in cm^2 will result in temperature rise in degrees K/s. The time interval of interest is that which it takes a magnet, or a consist of vehicles, to pass the null-flux coil – which is the time interval during which the null-flux coil will carry current. A conservative analysis will assume that the time interval is the vehicle transit time, although with the coils concentrated in bogeys, the null-flux coil only carries current for part of this time. For a vehicle consisting of N cars, each of length L_c and traveling at velocity v, the transit time is

$$\Delta t = \frac{NL_c}{v} \quad (3.3.14)$$

so the null-flux coil temperature rise is

$$\Delta T = (1.35 \times 10^{-6}) \frac{I_{nf}^2}{A^2} \frac{NL_c}{v} . \quad (3.3.15)$$

We will assume a consist of 4 cars, which would carry at least 250 passengers, and a car length of 24 m. The cross-sectional area of the null-flux winding we propose is 4 cm^2 . Substitution of these values yields

$$\Delta T = (8.0 \times 10^{-6}) \frac{I_{nf}^2}{v} . \quad (3.3.16)$$

To estimate the temperature rise which will actually be experienced, we must match the levitation force provided to the vehicle mass. The analyses run for this study yielded null-flux coil currents of 38400 A at liftoff speed of 42 m/s with an offset of 10 cm and 17000 A at cruising speed of 140 m/s with an offset of 1.8 cm. The temperature rises for these two cases are 280 and 16.5 K, respectively. The temperature rise at cruise is clearly within acceptable limits, but that at low speeds is appreciable. For an actual system, it may be necessary to design a system with a multiple-turn null-flux coil to handle the low speed operation.

3.3.3 Skin Depth Effects in Null-flux Coil

One further note on the null-flux coil current is in order. Since the current rises and falls in a short amount of time, the skin effects can become important as in any conductor carrying an AC current. Since the current rise and fall in the null-flux coil is approximately sinusoidal, an estimate of the equivalent frequency represented by the current is given by the vehicle velocity divided by the length of the sinusoidal pattern in Figure 3.3.7. The distance between zero crossings for the

average current characteristic in the figure is about 5.5 m, so the equivalent frequency is about 25 Hz. The skin depth of a 25 Hz current in 1100-00 aluminum is given by

$$\delta = \sqrt{\frac{2\rho}{2\pi\mu_0\nu}} \quad (3.3.17)$$

where μ_0 is the free-space permeability of $4\pi \times 10^{-7} \Omega\text{-s/m}$, and ν the frequency of 25 Hz, and ρ the aluminum resistivity of $3.4 \times 10^{-6} \Omega\text{-cm}$. The skin depth obtained for the null-flux coil carrying this current is therefore 1.9 cm. At this depth, the current falls to 37% of its value at the surface. Since our proposed null-flux coil has a square cross section of 2 cm x 2 cm, its equivalent radius is 1.1 cm, which is only 0.6 skin depths – over which the current will fall to 55% of its surface value. Therefore, the surface current density will be somewhat higher than the average which the preceding thermal analysis assumes, but not enough to change the basic conclusions.

3.3.4 Relative Vertical Locations of Null-flux, Armature and Superconducting Coils

This issue was raised early in our analyses and bears mentioning, albeit peripherally. A further design decision that would have to be made in an actual system is the choice of the relative vertical positions of all coils in the motor and levitation systems. Since the horizontal centerline of the vehicle coils must ride below that of the null-flux coils to produce levitation force, the actual system design cannot have the null-flux and vehicle coils on the same horizontal centerline. Therefore, an actual system would have either the null-flux windings or the vehicle coils, but not both, vertically offset with respect to the armature coils. If the vehicle coils are offset, the motor thrust is reduced because of the reduced flux from the vehicle coils at the armature windings. If the null-flux windings are offset, the interaction between them and the armature coils must be taken into account in the motor design. Figure 3.3.17 shows the possible relative positions.

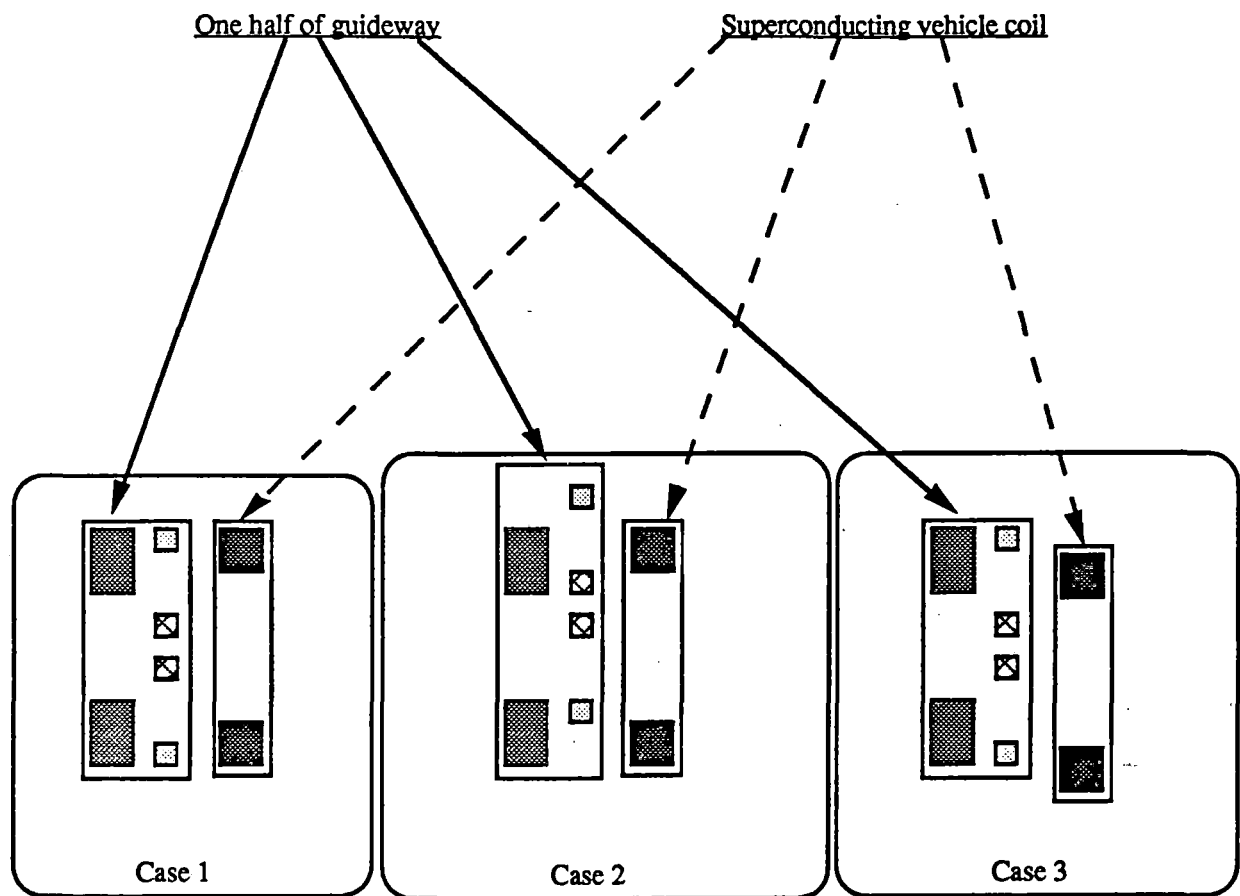


Figure 3.3.17. Possible relative locations of null-flux, superconducting and armature coils.

3.3.5 Conclusions

The analysis of the null-flux coil interactions was carried further than originally intended, but the results obtained are important and strengthen the conclusions which can be drawn here. The levitation of a vehicle in an electrodynamic system depends on many systems working properly, and the design of these systems is interrelated. The superconducting and null-flux windings both fall into this category. Thermal and skin depth calculations must be made for proper null-flux coil design, and the tradeoff between heating of the null-flux coils and the number of turns in the coils may necessitate the economically unattractive choice of a multiple-turn null-flux coil. In addition, the relative positions of the null-flux, armature and superconducting vehicle coils is an important design decision with implications for the operation of the motor and levitation sub-systems. Finally, the levitation force obtained by a single superconducting coil must be set to the value required in the worst-case scenario, which involves system level choices of operation with one or more superconducting coils depowered.

3.4 AC Losses in Superconducting Coil

It is well known among superconducting magnet designers that the issue of AC losses in the cryostat and the superconducting coils must be addressed to ensure a viable design. The term "losses" refers here to the generation of heat within any conductor, including the superconducting winding, because of its exposure to time-varying magnetic fields. These losses are typically created by two mechanisms: induction of eddy currents into the cryostat members and the resistive stabilizer of the superconducting composite; and hysteresis behavior in the superconductor caused by the motion of flux within it. The magnitudes of such losses must be included in estimates of heat loads to the cryogenic refrigeration system to ensure that the operating temperatures will fall within the desired range and that the possibility of the localized nature of the losses leading to local hot spots within the cryostat components or superconducting winding will be investigated.

The superconducting maglev excitation winding will experience heating from applied AC magnetic fields. Such AC field components will arise from the harmonic content of the motor current and the space harmonic structure of the field generated by the motor winding interacting with the traveling excitation winding. Field coil current fluctuations induced by AC components in the mutual flux will also produce losses. The losses experienced by a superconducting winding in an applied AC magnetic field are classified into hysteresis loss, eddy current loss, and penetration loss, all of which depend on the applied field frequency and excursion, and the superconductor-stabilizer composite wire characteristics.

To compute the AC losses in the superconducting maglev excitation winding, we first compute the AC magnetic field at the winding, then obtain the resultant local heating losses and finally integrate over the whole excitation winding. Excessive heating can then be reduced by encasing the superconducting excitation coil in a conductive shield, which will carry induced eddy currents that modify the AC fields.

It will be seen that the screening by the thermal shield is an important factor for the AC losses, and acceptable levels are easily achievable at cruising speed. The field coil winding losses are dominated by the stabilizer eddy-current losses, with superconductor hysteresis being a minor contributor. Operation with a failed thyristor will overcome the steady-state refrigeration capacity, but the motor block length and cold mass heat capacities will permit the vehicle to ride through defectively energized blocks without quench. Low velocity operation will also increase AC loss heating and further AC field shielding is required.

3.4.1 AC Fields Applied to the Superconductive Winding

The field at a stationary observation point may be obtained by convolving the stator current with the magnetic field (per Ampere) shape produced by the stator winding; the field at a moving observation point is then obtained by factoring in the moving point velocity. Frequency-domain analysis shows that a three-phase stator winding and a three-phase current, each with only odd harmonics, interact to produce fields at the synchronously moving field coil with frequencies $6n\omega$, where n is an integer and ω is the motor current fundamental frequency. The convolution can be carried out in either the time or frequency domains. Such a time-domain procedure was applied to single stator coil field profiles and a 120-degree switched current waveform applied to the three-phase stator winding. In the superconductor winding AC loss discussion below it is shown that the main loss-causing field components are B_x and B_l (longitudinal to superconductor). Figure 3.4.1 shows B_x , B_y and B_z profiles computed by GE_MAGLEV at a plane of constant $x = 0.16$ m away from a rectangular 2.5 by 0.5 m coil carrying 1 MA, while Figure 3.4.2 shows the three phase currents of an ideal 120-degree switched current wave.

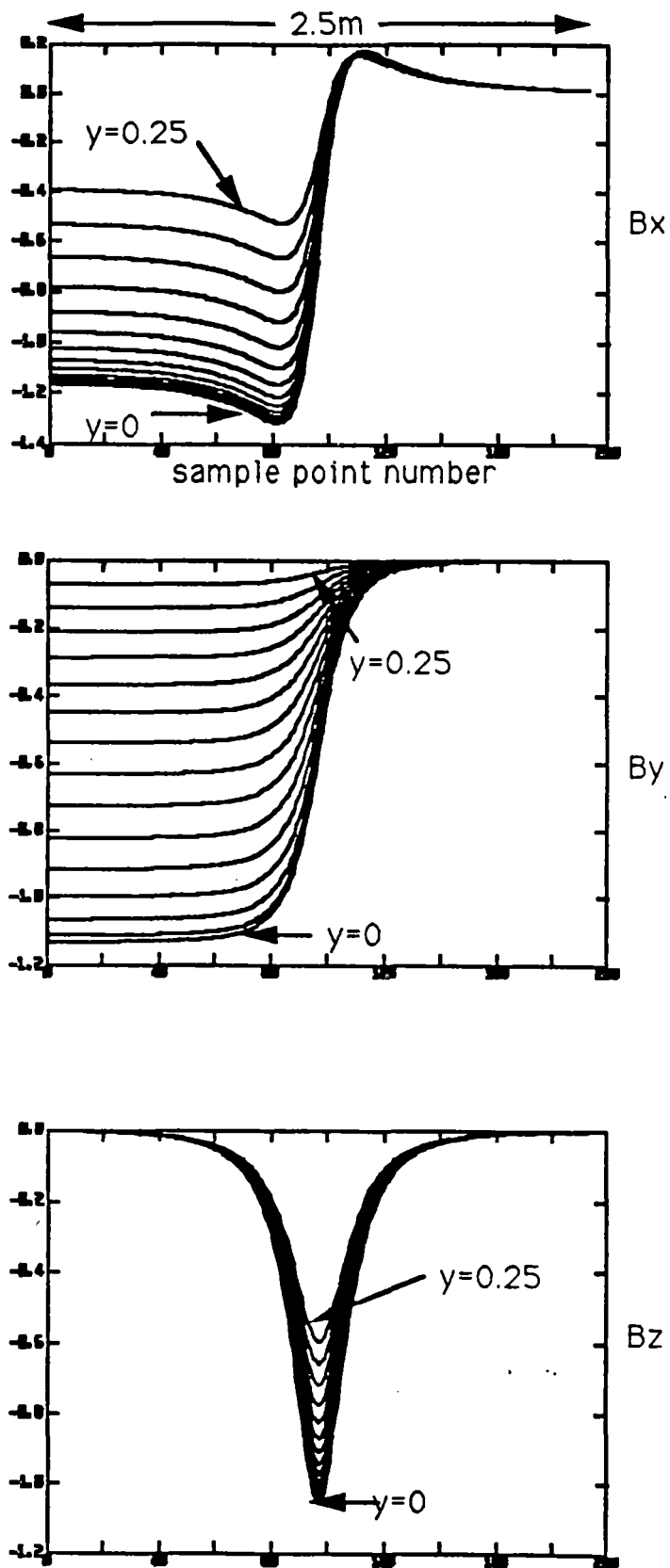


Figure 3.4.1. B_x , B_y and B_z profiles vs z for 1MA-t in motor coil, observation plane at $x=0.16\text{m}$.

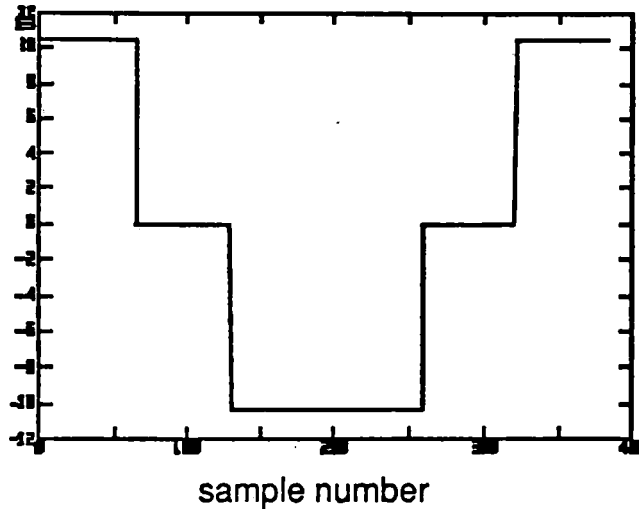


Figure 3.4.2. 120-degree motor current waveform.

In the brushless DC operating mode, the stator current will be controlled to give an effective machine angle of 90 degrees: that is, the centroid of the moving excitation racetrack coil will lag behind the fundamental-frequency moving stator field centroid by 90 degree, so that the leading edge of the racetrack coincides with the stator field centroid. The B_x and B_y results computed at 14 positions around 1/4 of the racetrack circumference as shown in Figure 3.4.3 are given in Figures 3.4.4 and 3.4.5. Since all waveforms have a period 1/6 of the fundamental stator period, only one cycle is shown. It can be seen that the AC field excursion ranges from 0.6-1.0 mT p-p at the end-turns to 7 mT p-p over much of the straight sides. Discontinuities seen in the waveforms due to the sharp current switching increase from none at all at the tip of the end-turn, to about a 5 mT jump experienced by much of the straight sides. Fourier decomposition of the waveforms shows that the fundamental harmonic dominates the total AC field energy, although other harmonics can provide a significant contribution.

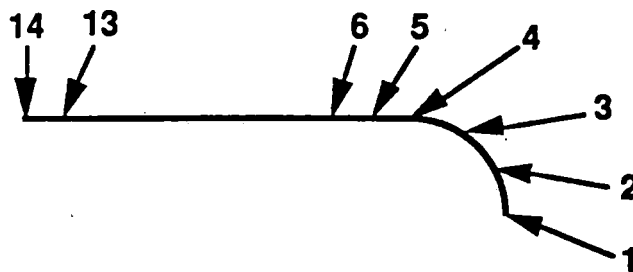


Figure 3.4.3. Location of 14 sampling point around 1/4 racetrack.

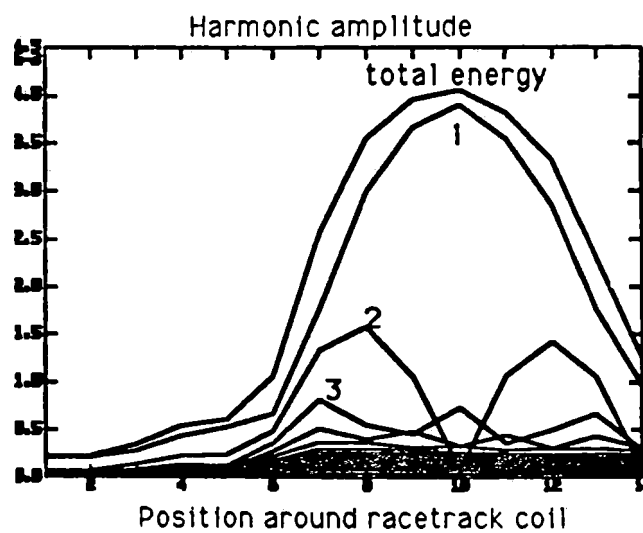
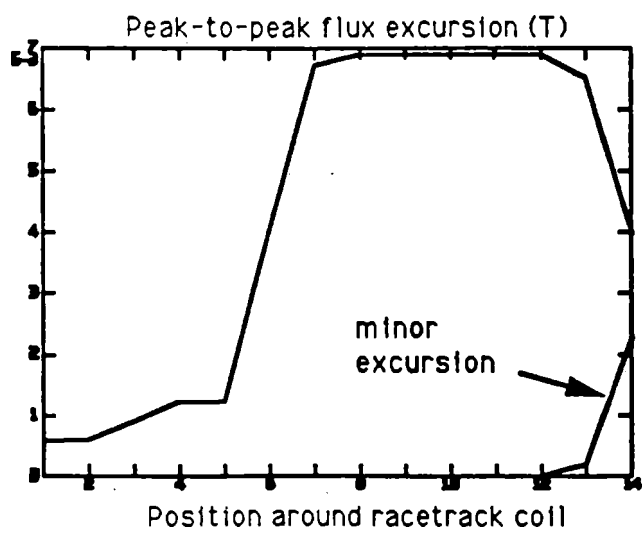
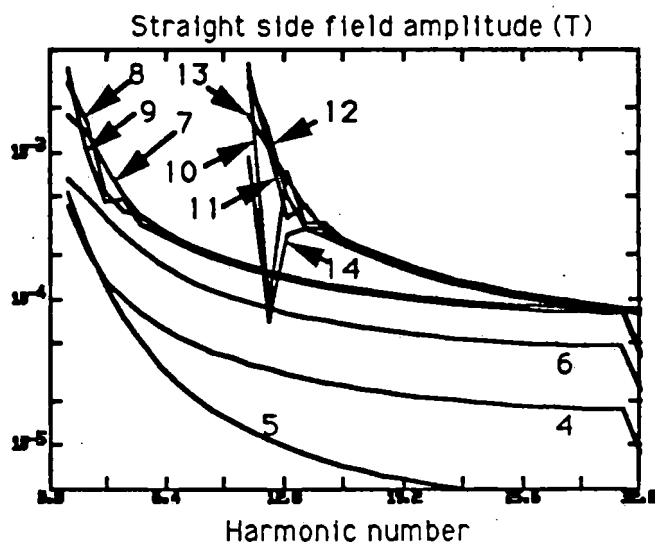
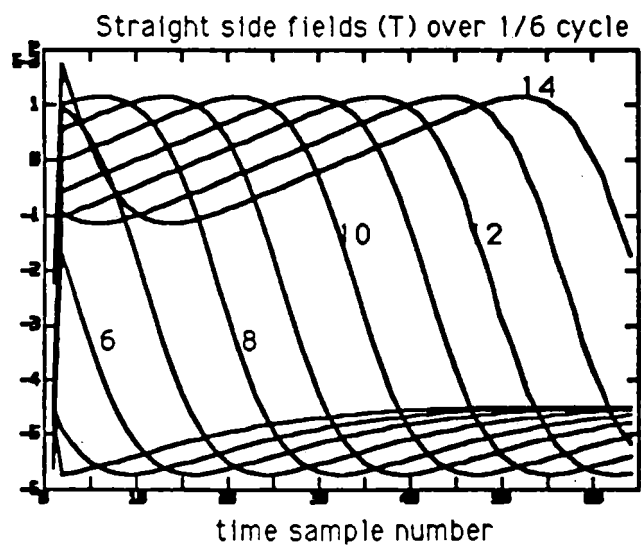
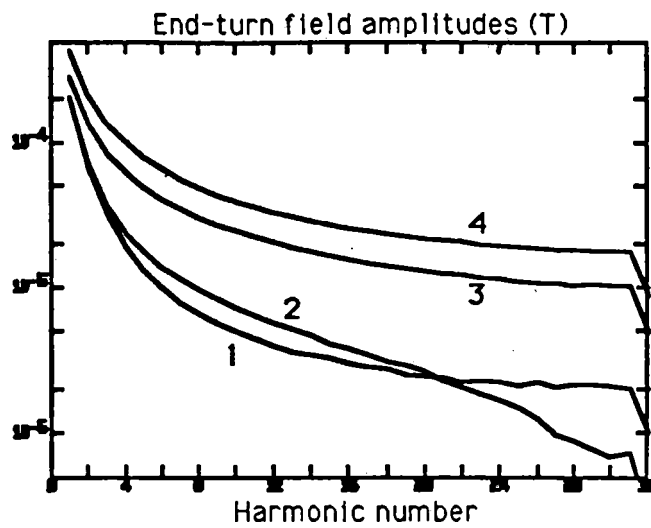
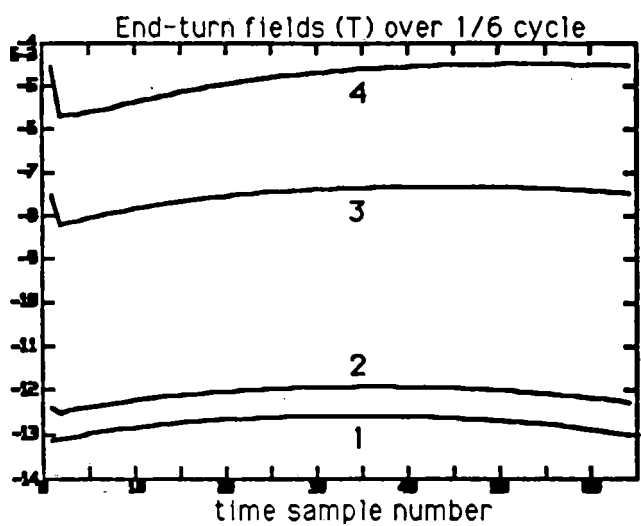


Figure 3.4.4. Unshielded Bx applied to field coil.

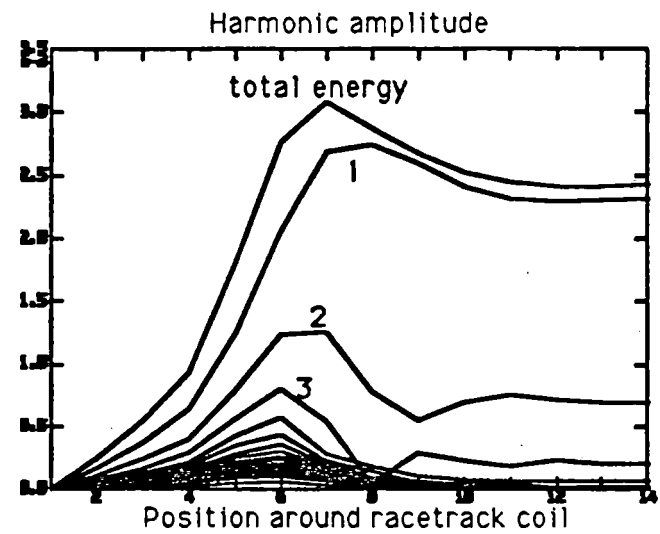
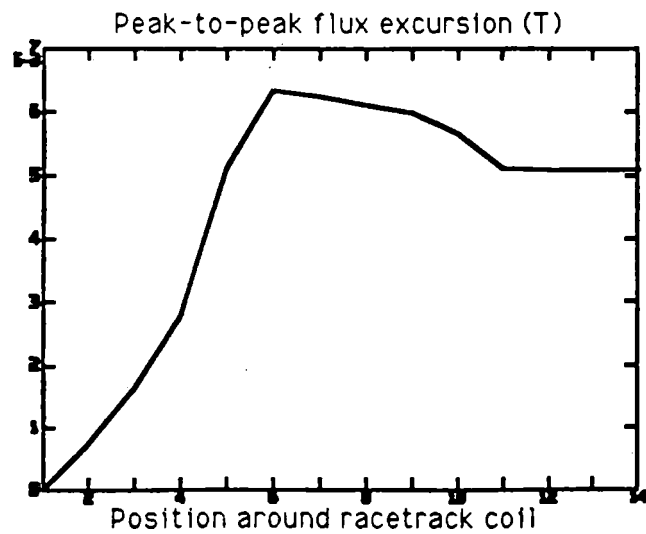
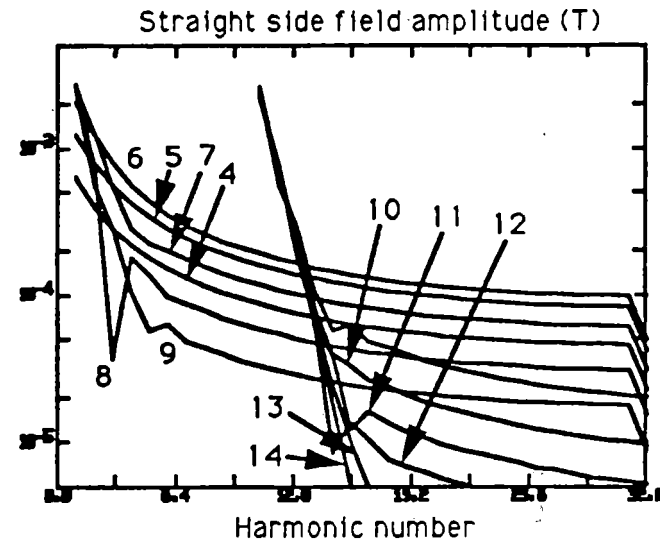
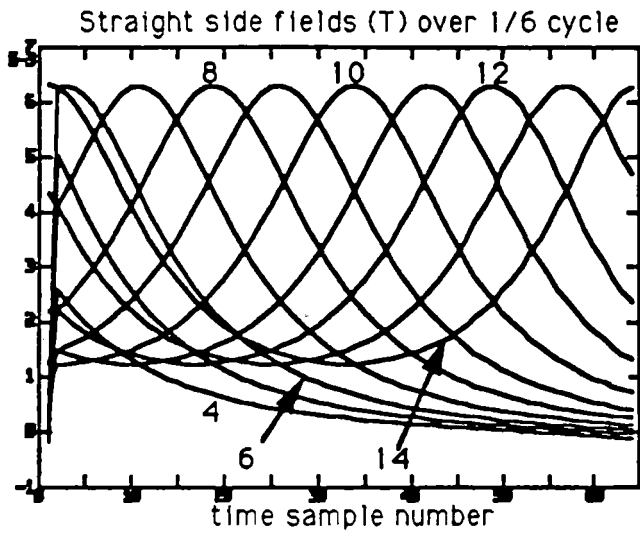
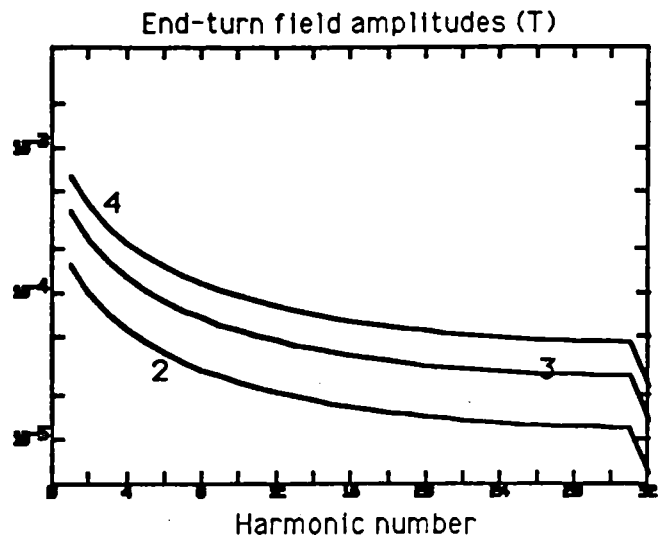
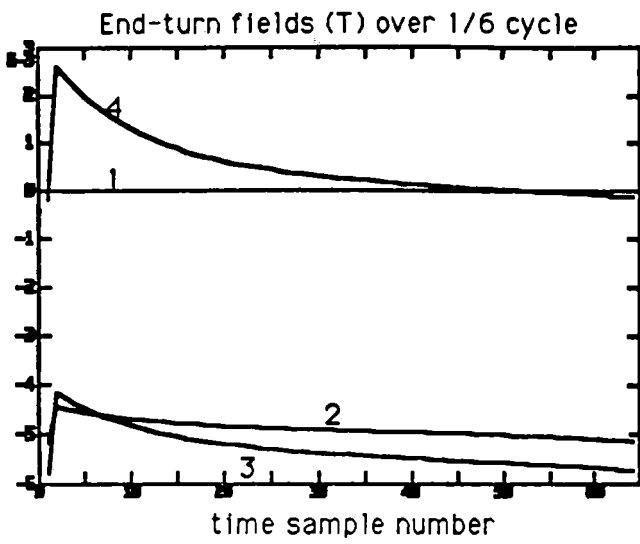


Figure 3.4.5. Unshielded BI applied to field coil.

As the field coil moves along the track, its mutual flux linkage from the three-phase motor winding is changing, resulting in a net induced field coil voltage which drives field coil current fluctuations to oppose the imposed flux changes. The field current fluctuations produce additional field fluctuations throughout the superconducting winding which may interfere constructively or destructively with the previously described AC fields. The B_x profiles such as in Figure 3.4.1 can be integrated over a range of field coil positions to give a mutual inductance vs. position characteristic (Figure 3.4.6).

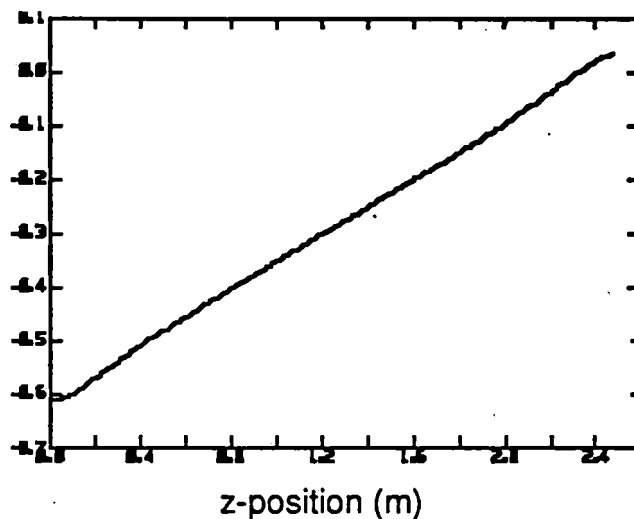


Figure 3.4.6. Mutual flux (Wb) from 1 MA_t motor coil

This is then combined with the 3-phase currents and winding displacement to give the time-varying mutual flux imposed on the field coil. From the field coil circuit equation the field current obeys the following relation:

$$L_f \frac{dI_f}{dt} = - N_f \frac{d\Phi_m}{dt} \quad (3.4.1)$$

where I_f , L_f and N_f are field coil current, inductance and number of turns respectively, and Φ_m is the mutual flux linking the field and motor coils.

In the present study, the field current fluctuations are a near-perfect sawtooth at 144 Hz, 0.340 A_{p-p}. The resultant coil self-field fluctuations are then computed for the coil winding. For a quick order-of-magnitude estimate, consider that the peak winding self-field from the 102 A DC current is 3.4 T, so the 0.340 A_{p-p} variation will produce a maximum 0.0113 T_{p-p} variation, comparable to the previous amplitudes.

In the following sections, the effects of these AC magnetic field excursions on the superconductor coil are examined. While these results have been obtained using time-domain methods, insight into the causes of the harmonic amplitudes can be obtained from a frequency-domain analysis of the production of the traveling magnetic field. Such analysis, analogous to rotating machine air-gap harmonic analysis, will be carried out in a subsequent section.

3.4.2 Superconducting Winding AC Losses.

As already stated, the losses experienced by a superconducting winding in an applied AC magnetic field are classified into hysteresis loss, eddy current loss, and penetration loss. Hysteresis losses arise from changing superconductor current distributions as the supercurrent adjusts itself to exclude applied magnetic field changes from the interior of the superconductor. In a tape superconductor, eddy-current losses due to current crossing the stabilizer between coupled superconductor filaments (the mode of loss usually considered as "eddy-current loss" in the superconductivity community) is not a major factor due to the structure of the composite conductor tape, but the following analysis shows that the stabilizer loss due to induced screening currents flowing in the stabilizer is an important (in fact dominant) contributor to AC loss. Penetration loss is unimportant for tape superconductor geometries.

Superconductor hysteresis losses from transverse fields.

Wilson [1983] derives the following expression for the volumetric energy loss Q per cycle of applied superconductor transverse field with peak-to-peak excursion B_m :

$$Q = \frac{B_m^2}{2\mu_0} \Gamma(\beta) \quad (3.4.2)$$

where β is the field penetration ratio

$$\beta = \frac{B_m}{B_p} = \frac{B_m}{2\mu_0 J_c t} \quad (3.4.3)$$

and $\Gamma(\beta)$ is an alternating magnetic field energy coupling factor which for a planar superconductor geometry is

$$\Gamma(\beta) = \begin{cases} \beta/3, & \beta < 1 \\ \frac{1}{\beta} - \frac{2}{3\beta^2}, & \beta > 1 \end{cases} \quad (3.4.4)$$

Here B_p is the full penetration field, J_c the superconductor critical current density and the superconductor layer thickness is $2t$.

Q rises as B_m^3 for small β (when the AC field does not fully penetrate into the superconductor) and B_m for large β (full field penetration). In a tape superconductor with width $2a$ and superconductor thickness $2b$ and $a \gg b$, the penetration field B_p is always much larger for fields parallel to the short side than for fields parallel to the long side, so that losses for the latter case (B_x in this study) dominate when the magnitudes of the two transverse field components are comparable.

Stabilizer eddy current losses from transverse fields.

The skin depth for copper stabilizer with 10 K resistivity $0.26 \text{ n}\Omega\text{-m}$ at 144 Hz is 0.676 mm, about 9 times the thickness of the stabilizer layer on each side of the superconductor (Figure 3.4.7). Therefore the attenuation of the applied AC field at the superconductor surface due to the stabilizer eddy currents is negligible, but the heating from the stabilizer eddy currents must be evaluated. For higher harmonic components in the applied AC field, the stabilizer skin depth is less, giving higher losses and more attenuation of the superconductor surface field. For the frequencies and conductor dimensions in this study, the field screening by the stabilizer is small.

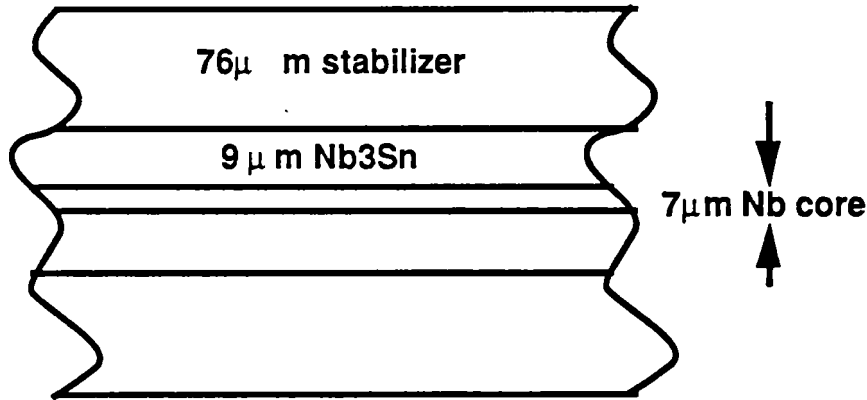


Figure 3.4.7. Tape superconductor.

The diffusion of a parallel magnetic field $B_0 \cos \omega t$ into a conductive slab of thickness $2b$ (Figure 3.4.8) is given by

$$B_x(y,t) = \frac{B_0}{\sinh^2 \frac{b}{\delta} + \cos^2 \frac{b}{\delta}} \left\{ \left(\cos \frac{b}{\delta} \cosh \frac{b}{\delta} \cos \frac{y}{\delta} \cosh \frac{y}{\delta} + \sin \frac{b}{\delta} \sinh \frac{b}{\delta} \sin \frac{y}{\delta} \sinh \frac{y}{\delta} \right) \cos \omega t + \left(\sin \frac{b}{\delta} \sinh \frac{b}{\delta} \cos \frac{y}{\delta} \cosh \frac{y}{\delta} - \cos \frac{b}{\delta} \cosh \frac{b}{\delta} \sin \frac{y}{\delta} \sinh \frac{y}{\delta} \right) \sin \omega t \right\}$$

(3.4.5)

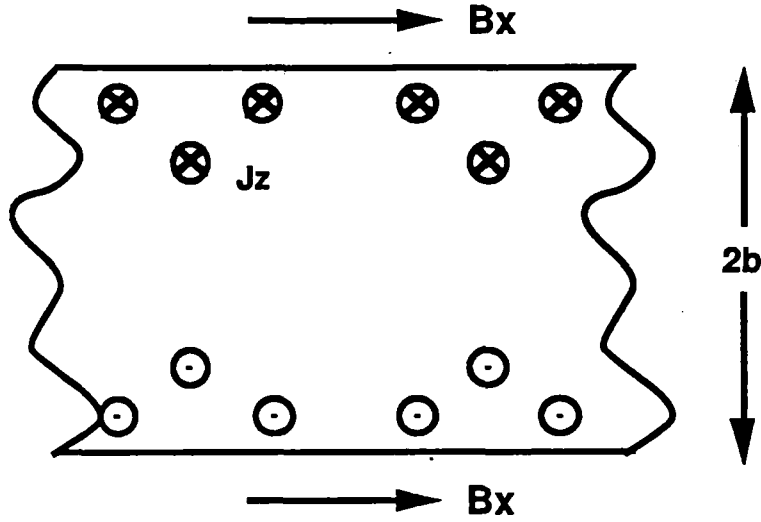


Figure 3.4.8. Magnetic Field Shielding by Conductive Slab.

with the eddy current density

$$\begin{aligned}
 J_z(y,t) = \frac{B_0}{\mu_0 \delta \left(\cos^2 \frac{b}{\delta} + \sinh^2 \frac{b}{\delta} \right)} & \left\{ \left[\left(\cos \frac{b}{\delta} \cosh \frac{b}{\delta} + \sin \frac{b}{\delta} \sinh \frac{b}{\delta} \right) \cos \frac{y}{\delta} \sinh \frac{y}{\delta} + \right. \right. \\
 & \left. \left(\sin \frac{b}{\delta} \sinh \frac{b}{\delta} - \cos \frac{b}{\delta} \cosh \frac{b}{\delta} \right) \sin \frac{y}{\delta} \cosh \frac{y}{\delta} \right] \cdot \cos \omega t \\
 & - \left[\left(\sin \frac{b}{\delta} \sinh \frac{b}{\delta} - \cos \frac{b}{\delta} \cosh \frac{b}{\delta} \right) \cos \frac{y}{\delta} \sinh \frac{y}{\delta} - \right. \\
 & \left. \left. \left(\cos \frac{b}{\delta} \cosh \frac{b}{\delta} + \sin \frac{b}{\delta} \sinh \frac{b}{\delta} \right) \sin \frac{y}{\delta} \cosh \frac{y}{\delta} \right] \cdot \sin \omega t \right\}
 \end{aligned}
 \tag{3.4.6}$$

The volumetric power dissipation density, $J \cdot J\rho$, averages over time and the $2b$ slab thickness to

$$Q = \frac{\rho B_0^2 \left(\sinh \frac{2b}{\delta} - \sin \frac{2b}{\delta} \right)}{\mu_0^2 4b \delta \left(\sinh^2 \frac{b}{\delta} + \cos^2 \frac{b}{\delta} \right)}
 \tag{3.4.7}$$

which simplifies for $b \ll \delta$ to

$$Q \approx \frac{(B_0 b \omega)^2}{6\rho} \quad (3.4.8)$$

There are some important differences in frequency dependence between superconductor hysteresis losses and stabilizer eddy-current losses. The superconductor hysteresis losses have a constant value per cycle (independent of field fluctuation frequency) and depend on the peak-to-peak monotonic AC field excursion. Therefore hysteresis losses increase linearly with frequency and minor harmonic content has no effect, as long as the applied field waveform maintains the same excursion and develops no new local extrema. In contrast, the stabilizer losses rise with the square of the frequency, and the harmonics of the applied field are decoupled so that each harmonic contributes independently to the total loss.

In the tape superconductor composite, the Figure 3.4.8 geometry is modified by interposing the superconductor layers (total thickness $25 \mu\text{m}$) in the middle of the stabilizer slab as in Figure 3.4.9, with the stabilizer loss equations applying unchanged, while the superconductor hysteresis is based on the attenuated field fluctuation at the superconductor surface.

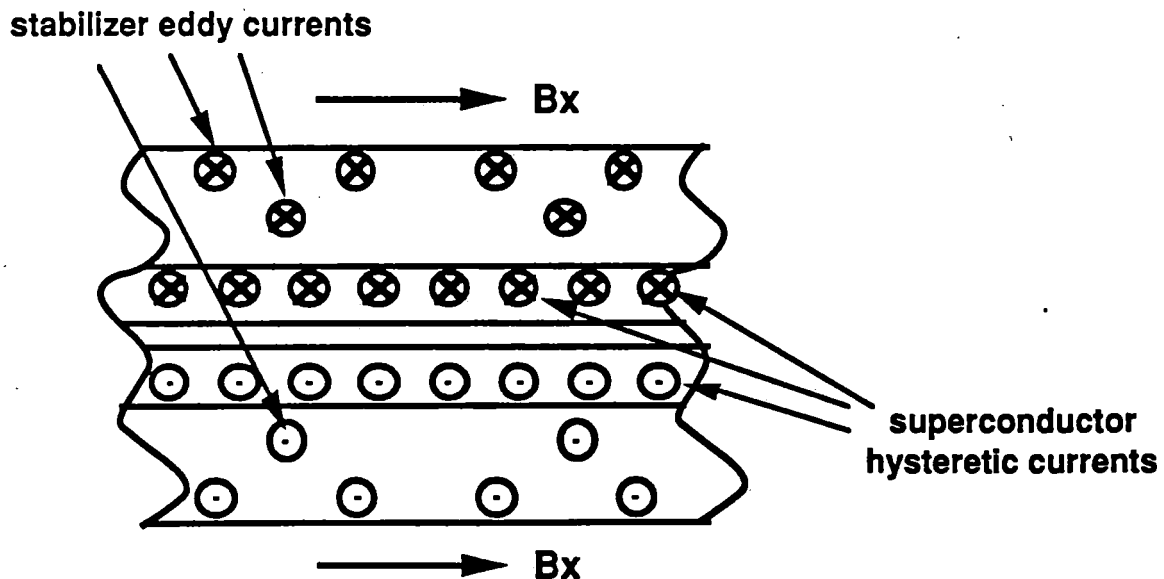


Figure 3.4.9. Transverse field screening in tape superconductor.

Superconductor hysteresis losses from longitudinal fields.

For the tape conductor composite, longitudinal applied AC fields induce the circulation of transverse screening currents in both the stabilizer and superconductor (Figure 3.4.9) which are dominated by the effects of the broad face. Therefore, the same equations can be applied for both stabilizer and superconductor losses as above. A complicating factor arises from the fine structure of the tape superconductor, where the 25 μm thick center is subdivided into a sandwich of 3 regions: 9 μm thick niobium tin superconductor layers on the surfaces and a 7 μm thick residual non-superconducting Nb core layer. The hysteretic currents in the two superconducting regions will couple if the coupling length in the hysteretic current direction is greater than

$$l_c = 4\sqrt{b_{sc}\rho J_c/2\frac{\partial B}{\partial t}} \quad (3.4.9)$$

For Nb resistivity $6 \times 10^{-7} \Omega\text{m}$ and dB/dt corresponding to 2 mT amplitude at 144 Hz, the critical coupling length is about 0.3-0.7 m, so clearly over the 3 mm tape width, the transverse hysteretic currents in the two superconductive strands are decoupled (Figure 3.4.10).

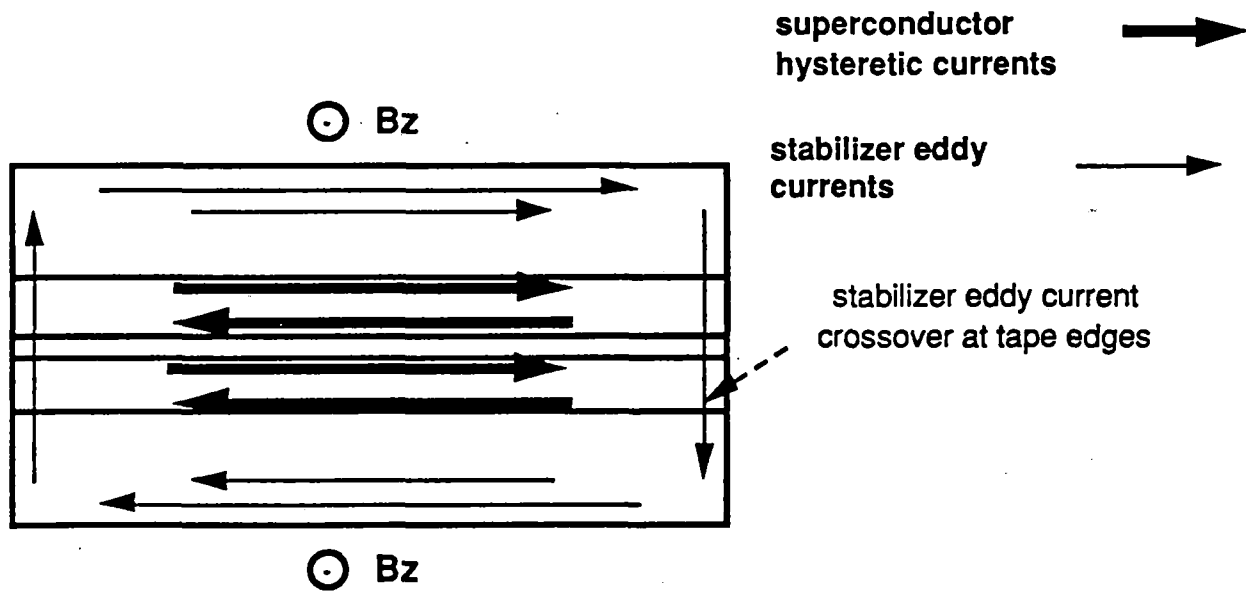


Figure 3.4.10. Longitudinal field screening in tape superconductor.

Stabilizer eddy-current losses from longitudinal fields.

Comparison of the copper resistance with the niobium resistance in the coupled eddy-current path (Figure 3.4.10) indicates that the copper resistance dominates by 3 orders of magnitude, so that the circulating eddy currents will be coupled between the two stabilizer layers.

Total losses from combined longitudinal and transverse fields.

When we examine the loci of B_x and B_l at several points around the racetrack (Figure 3.4.11), it is seen that the tape conductor is exposed to rotating AC fields. In this figure, the four loops shown correspond to calculations of the field in time at four distinct locations in the coil. As time elapses, a loop is traced for each location. At locations 2, 3, and 4, it is seen that the net effect is to produce a rotating field. An effort is made here to estimate the effect of such fields on the losses.

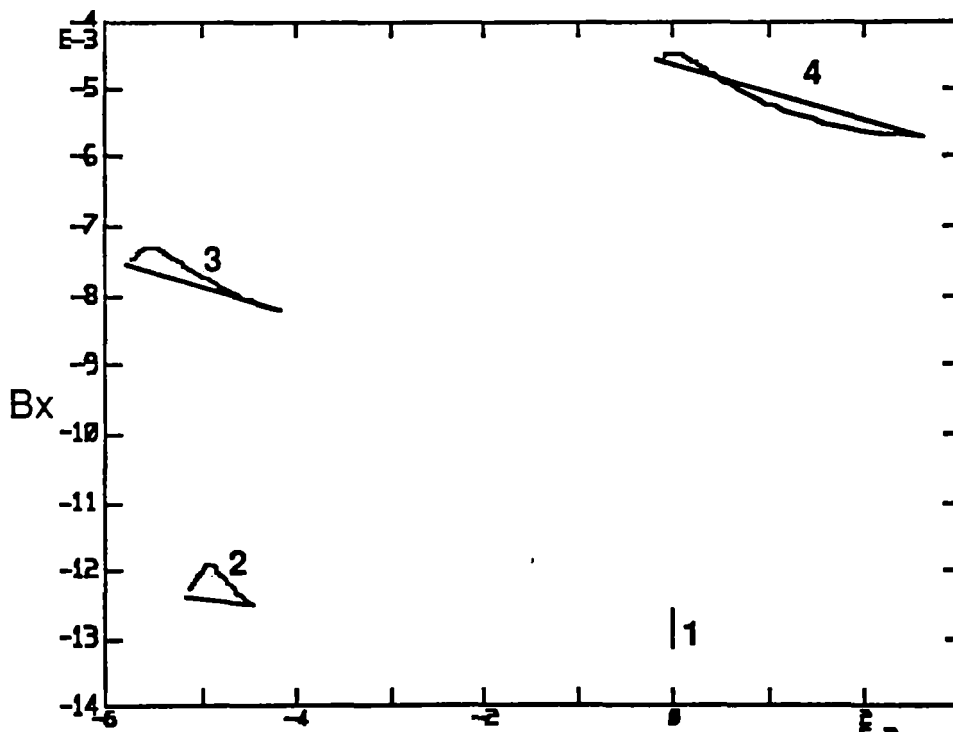
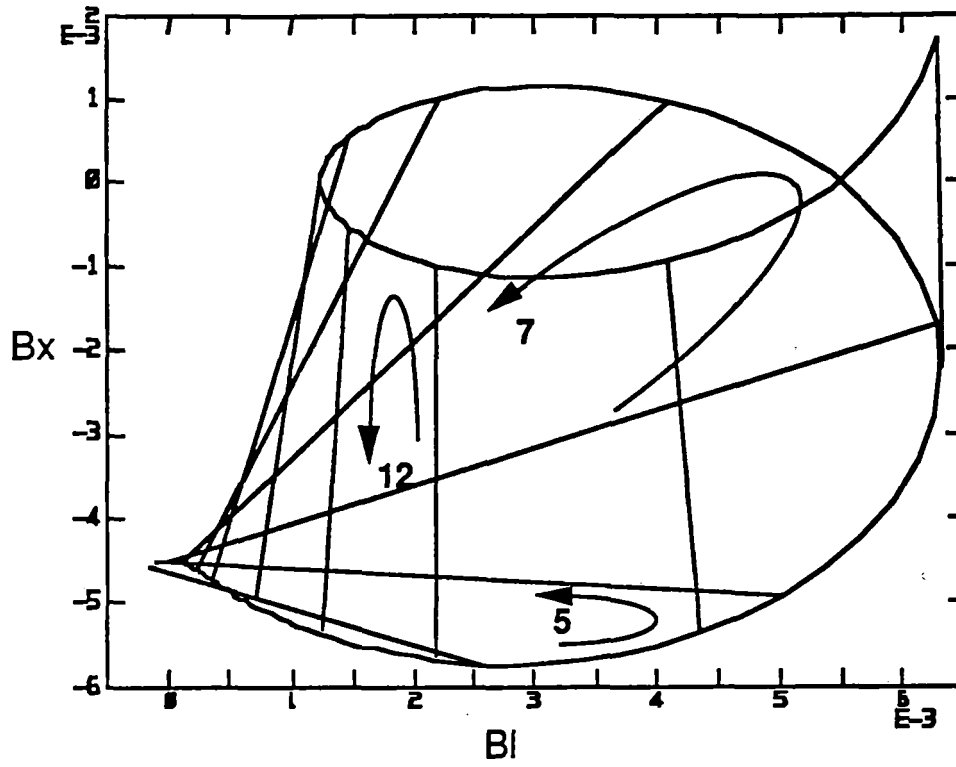


Figure 3.4.11. B_x vs B_l loci around field coil.

Since the stabilizer behavior is based on linear constitutive equations, its losses can be summed separate harmonic by separate harmonic and over both x- and l-directions. The superconductor hysteretic currents will be different on the exterior and interior faces of the twin niobium tin layers due to the absence of coupling for transverse hysteresis currents (leading these to flow over both interior and exterior faces) and the presence of coupling for the longitudinal hysteresis currents, which will flow only over the exterior faces. Therefore the internal face losses are purely due to longitudinal AC fields and can be evaluated from the above equations. However, the external face hysteretic currents will change direction over the $(144 \text{ Hz})^{-1}$ period, producing a more complicated current penetration pattern into the external superconductor faces. No general solutions of hysteresis loss for general multi-component applied fields are available, but Bean's 1970 solution for a circularly polarized applied field enables a bound to be inferred. The rotating applied field penetrates $\sqrt{3}$ deeper than a unidirectional field of the same amplitude, producing $\pi \cdot \sqrt{1.5}$ (approx 3.84) times the losses. On the other hand, if the two components of the applied field were in phase, the solution would be $2 \cdot \sqrt{2}$ (approx 2.83) higher than the unidirectional field result: that is, the rotational case produces 36% more loss than the in-phase situation. Therefore in the absence of the general result, the following conservative procedure will be applied: on the external superconductor faces, a 1.36 multiplier will be applied to hysteresis losses computed from an effective AC field excursion

$$\Delta B_{\text{eff}} = \sqrt{\Delta B_x^2 + \Delta B_l^2} \quad (3.4.10)$$

It is instructive to compute the losses for a representative situation, of our racetrack superconductor coil with $a=1.5 \text{ mm}$, $b_{\text{st}}=76 \text{ }\mu\text{m}$ and $b_{\text{sc}}=9 \text{ }\mu\text{m}$, in DC self-fields of 0 and 3 T (spanning the design values), at 10 K with stabilizer resistivity as above and 144 Hz applied transverse AC field. Figure 3.4.12 shows that the stabilizer eddy-current losses dominate for AC field amplitudes below 16 mT for 3 T DC field or 50 mT for a null DC field. As previous computations yield lower AC fields with no shielding, the stabilizer AC losses dominate. The effects of the DC field level on superconductor loss are seen to be moderate, with higher DC fields leading to higher losses (due to increased field penetration). To limit the coil losses to below 1 W, the applied 144 Hz AC field amplitude must be limited to 5 mT.

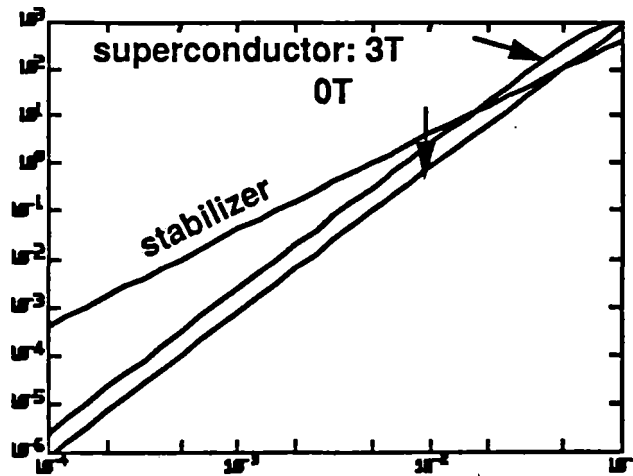
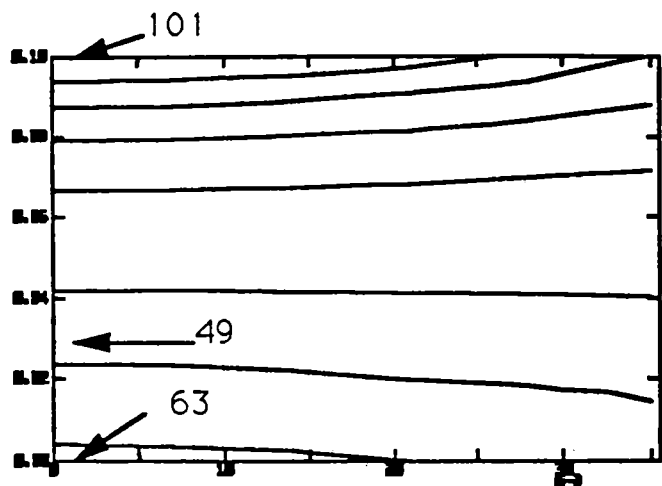


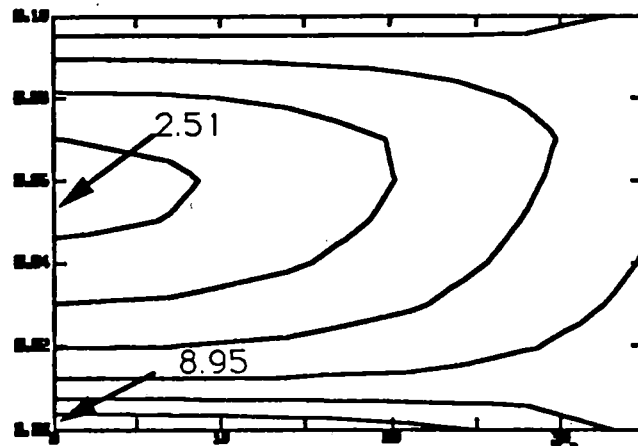
Figure 3.4.12. Single unshielded field coil AC loss components from uniform applied B_x at 144 Hz.

The previously computed AC field excursions together with Figure 3.4.12 suggest that the unshielded AC field will produce 2-10 W heating in the field coil winding pair, which would exceed the cryocooler capacity. However it will be seen that reduction in the AC field is quite feasible.

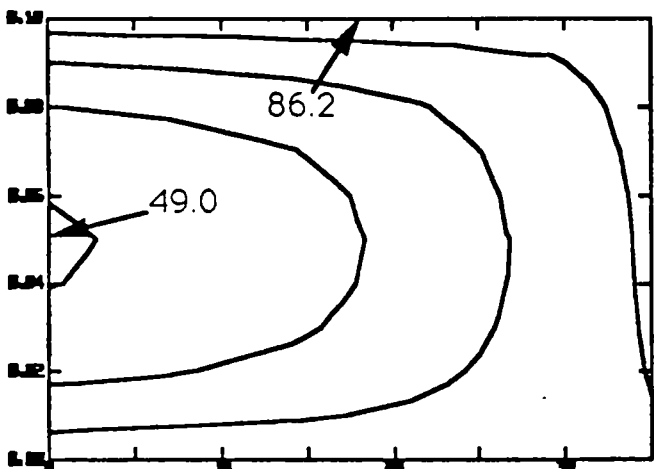
An accurate evaluation of the field coil AC loss heating was carried out by integrating over the superconducting coil pair volume the local AC losses computed from the AC field excursion distributions and critical current characteristics (developed from the DC field distributions caused by the field coil current), which yielded a total 4.79 W, with 0.39 W generated from superconductor hysteresis losses and the 4.40 W balance from stabilizer eddy-current losses. From the data plotted in Figure 3.4.12, these values correspond to a equivalent uniform 7.37 mT peak 144 Hz field for stabilizer losses and a 4.92 mT peak 144 Hz field for superconductor losses. Figure 3.4.13 shows typical power density profiles over a particular field winding cross-section, together with the distribution of loss density around the field winding circumference. It can be seen that the stabilizer losses are roughly 11 times the superconductor losses, and there is only a minor spread of power densities between different circumferential positions. This level of heat deposition in the field coil winding is too close to the full refrigeration capacity, so the following section considers reduction of these losses by conductive shielding.



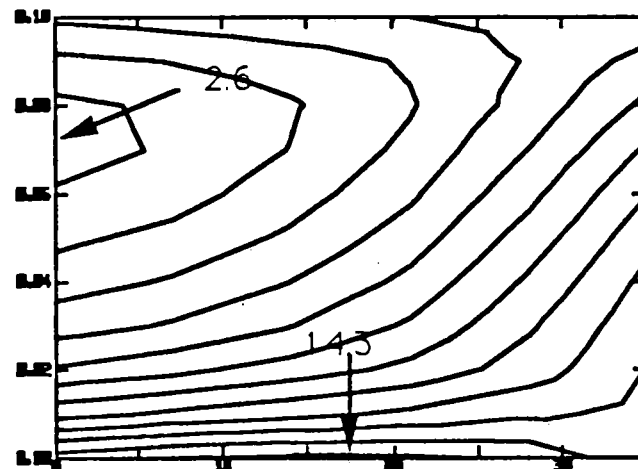
Slice 9 stabilizer loss (W/m^3)



Slice 9 hysteresis loss (W/m^3)



Slice 1 stabilizer loss (W/m^3)



Slice 1 hysteresis loss (W/m^3)

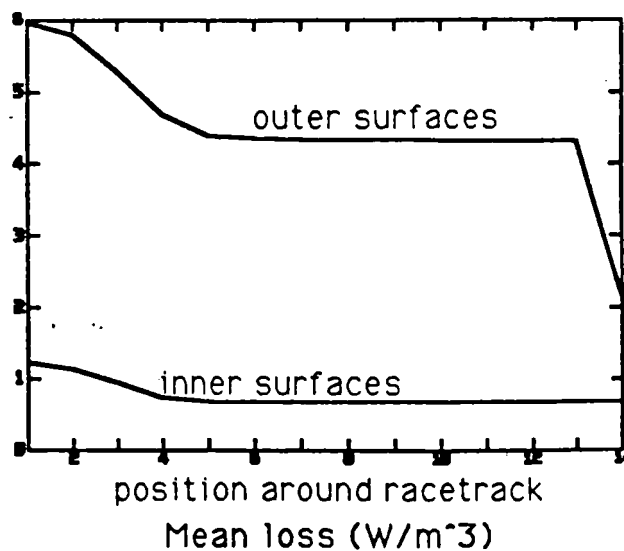
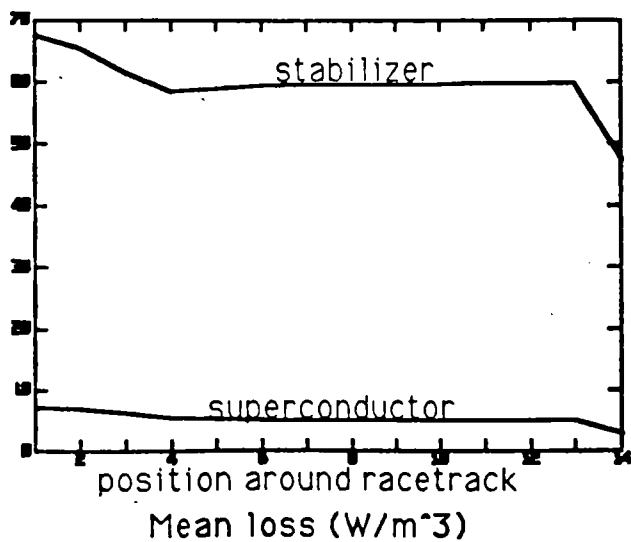


Figure 3.4.13. Unshielded AC losses around field coil.

AC Field Shielding of Field Coil

Eddy currents in the thermal shield, an essential thermal design component of the superconducting magnet cryostat which completely encloses the magnet winding, will attenuate the AC fields imposed on the superconducting coil. The thermal shield will be essentially a highly conductive box encasing a field coil pair, operating at a temperature around 40 K (depending on the heat deposited in the shield by conduction and radiation from higher temperature regions, and any eddy-current heating in the shield). In addition, the 2 cm-thick 304-stainless steel cryostat itself will provide some shielding. The dimensions of the thermal shield (probably 0.15x0.6x5.3 m, 3 mm-thick 1100 aluminum alloy) and cryostat (similar proportions, encasing the thermal shield) are such that no really valid simplifying assumptions can be made to reduce the 3-D eddy current problem in the shield to the 1-D problem treated in the stabilizer eddy-current loss results above, and a full 3-D eddy-current model should be applied in designing the conductive shielding.

However, an estimate can be made based on the stabilizer analysis, which would guide further analysis in any subsequent study. An attenuation factor and volumetric power density can be obtained from the stabilizer eddy-current loss equations applied to the cryostat and thermal shield with b set to the corresponding 2 cm and 3 mm thicknesses. The cryostat 304-stainless steel has a $700 \text{ n}\Omega\text{-m}$ resistivity at 300 K while the thermal shield aluminum alloy has a resistivity of $2.5 \text{ n}\Omega\text{-m}$ at 40 K, producing 144 Hz skin depths of 35.1 mm and 2.10 mm respectively. For this estimate, assume the applied AC field is all at 144 Hz (a conservative estimate for attenuation, since higher harmonics will be attenuated more). The 7.37 mT average applied field amplitude estimated above is applied to the exterior of the cryostat. The AC fields do not penetrate the superconductor fully, so that the hysteresis losses scale with the cube of the applied field, while the stabilizer losses scale with the square. The results are presented in Table 3.4.1.

	304-SS cryostat	1100-Al shield	stabilizer	superconductor
temperature	300 K	40 K		
resistivity	$700 \text{ n}\Omega\text{-m}$	$2.5 \text{ n}\Omega\text{-m}$		
thickness	20 mm	3 mm		
skin depth	35.1 mm	2.10 mm		
field attenuation factor	0.9666	0.5061		
resultant shielded field	7.12 mT	3.61 mT		
power loss	735 W	192 W	1.05 W	45.6 mW

Table 3.4.1. AC losses for base case including cryostat shielding

While no great accuracy is claimed for these shielded loss values, these results suggest that the AC losses in the thermal shield need to be reduced, while the magnet winding losses could be acceptable. It is desirable to reduce the thermal shield losses by a factor of 10 while not increasing the magnet winding losses. Substitution of a more conductive thermal shield material could be considered, but the losses scale as $\sqrt{\sigma}$ (see Eq. 3.4.7); the best engineering material would be high conductivity (electrolytic tough pitch) copper, which at 40 K has 0.4 nΩ–m, which reduces the 40 K loss to 71 W and improves field attenuation by a factor of nine for the same thickness. The 71 W figure is still too high for single cryocooler capacity. Therefore shielding at temperatures above 40 K is required and for illustration we select 12 mm of copper at 50 C operating temperature ($\rho=20.0$ nΩ–m) on the outside of the stainless steel cryostat, with the thermal shield material reverting to the aluminum. The losses for this case are presented in Table 3.4.2.

	Cu shield	304-SS cryostat	1100 Al shield	stabilizer	SC
temperature	323 K	300 K	40 K		
resistivity	2.00 nΩ–m	700 nΩ–m	2.5 nΩ–m		
thickness	12 mm	20 mm	3 mm		
skin depth	5.93 mm	15.7 mm	0.938 mm		
field attenuation factor	0.267	0.597	0.0815		
resultant shielded field	1.97 mT	1.90 mT	964 μT		
power loss	247.4 W	23.03 W	6.012 W	75.39 mW	872 μW

Table 3.4.2. AC losses with copper cladding on cryostat

The resultant AC loss heat loads are excellent: 6.01 W at 40 K and 76.3 mW at 10 K.

Another possible shielding material is ceramic superconductor operating at 40 K, which could be applied as a thin layer on the exterior surface of the aluminum thermal shield. Hysteretic currents in the superconductor layer would fully shield the interior providing the superconductor thickness exceeds the AC field amplitude penetration depth. The hysteresis loss equations presented above would apply equally well to the HTS shield layer. We wish to shield an 0.010 T AC amplitude (to give adequate capability for high-amplitude fields from abnormal operation

conditions such as presented in the following section) using for example BSSCO with a J_c of 500 MA/m² at 0.6 T, 40 K. The penetration depth is given by

$$p = \frac{2B_0}{\mu_0 J_c} \quad (3.4.11)$$

which here is 31.8 μm . Therefore consider a 40 μm -thick BSSCO layer with an applied 4.92 mT peak equivalent 144 Hz AC field (the value inferred above from the loss computations). The penetration parameter $\beta = 0.3915$, which coupled with the HTS volume and 144 Hz operating frequency gives a total hysteresis loss of 118 mW. This shield would fully eliminate AC losses in the aluminum thermal shield and the field coil composite.

Other Operating Conditions: Low Speed, Thyristor Commutation Failure, Higher Motor Frequencies

The applied field excursions at lower speeds depend on the motor current control algorithm, which is outside the scope of this study. If the switching rate corresponding to the cruising speed 120 degree waveform is maintained, better approximations to sinusoidal currents can be developed at lower vehicle speeds, with harmonic energy shifted to higher harmonic numbers. A worse case will result if the 120 degree switching waveform is maintained at lower frequencies, so that the current will have the same amplitude and harmonic spectrum as at full speed, but the harmonics will be scaled to lower frequencies. The skin depth will increase, reducing the field attenuation by the thermal shield. The frequency dependence of eddy-current losses (frequency squared) and hysteresis losses (frequency cubed) will factor in to reduce losses. As an example, the loss behavior at 10 % full speed corresponding to 2.4 Hz motor energization is presented in Table 3.4.3.

	Cu shield	304-SS cryostat	1100-Al shield	stabilizer	SC
skin depth	5.93 mm	15.7 mm	0.938 mm		
field attenuation factor	0.9484	0.9997	0.9863		
resultant shielded field	6.99 mT	6.99 mT	6.89 mT		
power loss	23.48 W	3.095 W	2.847 W	19.27 mW	15.94 mW

Table 3.4.3. AC losses at reduced speed

The shielding effectiveness practically disappears, but the 40 K heat load falls 53 % to 33.7 W, while the 10 K losses falls 54 % to 35.2 mW. The loss of shielding (7-fold AC field increase) is ameliorated by the lower frequency, reducing normal state conductor losses, but increasing superconductor hysteresis losses by a factor of 18. This case suggests that lower speed vehicle operation can be sustained.

A thyristor failure will lead to the elimination of one half of one phase's 120 degree current waveform. By superposition, the field coil will see a 120 degree blip of full-amplitude flux (0.010 T) at the fundamental, 24 Hz frequency, equivalent in energy to a 8.2 mT amplitude sinusoid. The 24 Hz field attenuation factor for the above cryostat, copper and aluminum shields is only 0.8403, raising the stabilizer loss to 200 mW and the superconductor loss to 47.2 mW. The aluminum shield will dissipate an extra 7.92 W, and the cryostat and copper shield an extra 9.01 W and 68.8 W respectively. The 10 K and 40 K heat generation will exceed the refrigeration capacity somewhat. These increased losses at the 10 K and 40 K stations are still well within the cryocooler capacity, so that the thyristor loss will not overheat the cryostat. This has important implications for the motor controls, which will not have any extra in thyristor failure detection speed requirements on account of the superconducting field coils.

With shorter motor winding pitch and wavelength, the AC fields imposed on the field coils will be at higher frequencies, increasing the shielding effectiveness of the cryostat, thermal shield and any resistive eddy-current shields due to reduced skin depths. However, the tolerable levels of AC fields will fall with the square of the frequency because stabilizer losses dominate and the thermal shield losses will also increase. The following case had no shielding (neither the stainless steel cryostat nor the aluminum thermal shield) operating at 5 times higher frequency of 120 Hz fundamental with the lowest AC field at 720 Hz. To produce the same thrust and levitation, an equivalent of 10 short coils was considered, to yield a total 206.6 W, with 2.26 W generated from superconductor hysteresis losses and the 204.4 W balance from stabilizer eddy-current losses, equivalent to 10.05 mT peak at 720 Hz applied to the stabilizer and 5.17 mT to the superconductor, from data analogous to Figure 3.4.12. The results with shielding by the cryostat and thermal shield are presented in Table 3.4.4.

	304-SS cryostat	1100-Al shield	stabilizer	superconductor
720 Hz skin depth	15.7 mm	0.938 mm		
field attenuation factor	0.5973	0.08148		
resultant shielded field	6.00 mT	489 μ T		
power loss	13676 W	280.9 W	2.66 W	3.36 mW

Table 3.4.4. AC losses for base cryostat design at 720 Hz

In comparison with the 24 Hz operating frequency case, the cryostat begins to have significant shielding effect as well as a high power loss. The thermal shield and stabilizer losses need to be reduced by shielding, which could be either resistive at ambient temperature or superconductive at 40 K. An HTS superconductive shield would be 40 % thinner than the 24 Hz operating frequency design above (24 μ m) due to the enhanced cryostat shielding, and dissipate a higher 590 mW due to the increased frequency. However, the 14 kW cryostat loss would stand, and this loss would total up to 55 kW for the 4 bogies, representing 0.8 % of the total 7 MW motor rating. To reduce the cryostat losses, an ambient temperature copper shield such as used previously should be placed on the exterior of the cryostat. The 720 Hz skin depth is 2.65 mm and a 5 mm thickness is selected; results are shown in Table 3.4.5.

	Cu shield	304-SS cryostat	1100-Al shield	stabilizer	SC
thickness	5 mm	20 mm	3 mm		
720 Hz skin depth	2.65 mm	15.7 mm	0.938 mm		
field attenuation factor	0.3094	0.9997	0.9863		
resultant shielded field	3.11 mT	1.86 mT	151 μ T		
power loss	1045 W	1309 W	26.90 W	254.3 mW	1.038 mW

Table 3.4.5. AC losses with copper cladding at 720 Hz

The ambient temperature losses have been reduced to 17 % (2.35 kW), while the 40 K and 10 K losses are comfortable values of 26.9 W and 255 mW respectively.

Appendix B presents the mathematical formulations which provide the basis for these time and space harmonic analyses.

SECTION 4: SHIELDING

Development of methods for reducing the DC magnetic field in the passenger compartment was one of the primary activities to be pursued in this effort. Both active and passive shielding systems were evaluated for the maglev vehicle, and many coil and iron configurations evaluated for each. The difficulty of active shielding in the chosen field coil configuration became evident early in our studies, and the only really effective method of reducing the field in the passenger compartment to levels below 20 gauss is to move the vehicle further above the coils, as will become evident.

One of the major design decisions to be made is the deployment of the vehicle coils. The two basic configurations which were investigated here are the coils in bogeys and the coils distributed along the length of the vehicle. The latter design is preferred from a standpoint of motor efficiency and guideway mechanical loading, since the reactive voltage of the motor section is lower and vehicle forces are distributed over a larger area leading to lower guideway stresses. The former design, of course, leads to a larger fraction of the passenger compartment in which the field falls below a given level. This tradeoff must be made at a system level, and the information presented here can provide useful insight to a system designer.

4.1 Active Shielding

Magnetic levitation is possible through the interaction of two magnetic fields; the traveling wave created by the linear motor and the on-board static field created by the superconducting magnets. The electromagnetic forces will be some function of the product of these two fields. Since the linear motor is a resistive circuit, one strong design driver will be to minimize the current in the linear motor to minimize ohmic heating losses. Since superconducting magnets produce no ohmic heating in DC operation, it follows that designers of these latter systems will be driven to provide the highest central field possible consistent with conductor characteristics. Passengers traveling on a magnetically levitated train will be subjected to the stray field from the superconducting magnets. Several studies have appeared over the years addressing design aspects of shielded trains, [Iwasa 1973; Okuma et al, 1980; Hayes 1987]. The studies use similar approaches, consisting of active and/or passive shielding arrangements. The exact solutions, however, are very dependent on the particular geometries being investigated.

The addition of extra coils, creating actively shielded configurations, and iron structures, creating passively shielded configurations, have traditionally been the means by which stray field levels are reduced. The choice of a shielding method is often made based on the results of tradeoff

analyses which take into consideration, for example, the linear response of an actively shielded system, together with its added complexity and cost. These factors should be weighed against the nonlinear response, yet simpler designs, of systems containing iron. Some design solutions encompass the two approaches, where one method might be adopted for a global reduction of the stray field to a certain level, and the other method taking over on a local scale to further reduce the stray field to a predetermined level.

The following sections present an investigation of the shielding requirements for the particular design adopted by GE CRD. The investigation is carried out by modeling the current carrying elements of the system as sequences of straight filaments and calculating the resultant magnetic fields. In the presence of non linear materials, such as iron, both 2-dimensional and 3-dimensional finite-element methods are employed. The inaccuracy involved in modeling the coils as filaments is small when fields far from the coils are desired.

4.1.1 Field Due to a Straight Current Filament

The expression for the magnetic flux density B generated by a current I flowing between two points r_1 and r_2 in a straight filament of length L is obtained by integrating the Biot-Savart formula (see Figure 4.1.1). This expression was used as the basis for calculating the field in space from the vehicle superconducting coils and any shielding coils which were used. In addition, it provided input to the nonlinear analysis packages used to analyze systems in which iron was included as a shielding device.

Figure 4.1.1. The formula (obtained by integrating the Biot-Savart (formula) for the magnetic field at the origin due to a straight filament carrying current I between r_1 and r_2 is:

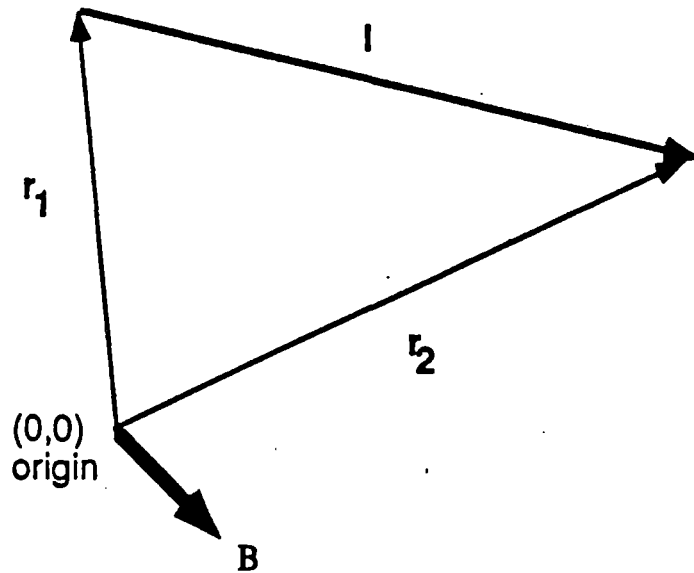
$$\mathbf{B} = \frac{\mu_0 I (r_1 + r_2) (\mathbf{r}_1 \times \mathbf{r}_2)}{4\pi (r_1 r_2) (r_1 r_2 + \mathbf{r}_1 \cdot \mathbf{r}_2)}$$

$$B_x = (y_1 z_2 - y_2 z_1) d$$

$$B_y = (z_1 x_2 - z_2 x_1) d$$

$$B_z = (x_1 y_2 - x_2 y_1) d$$

$$d = \frac{\mu_0 I (r_1 + r_2)}{4\pi r_1 r_2 (r_1 r_2 + \mathbf{r}_1 \cdot \mathbf{r}_2)}$$



Analysis Code

GE_MAGLEV is an in-house magnetic field analysis code which was written specifically with the maglev design features in mind. Liberal use was made of a library of graphic user interfaces (GUI) developed and maintained at CRD over recent years. The code allows the user to check the proposed model for proper representation of coils. Coils are represented by a series of straight line segments which are connected end-to-end. Quite complex coil configurations can be easily modeled and checked, including the racetrack geometries which are proposed here. The magnetic field is calculated over a user-defined region of interest (line, area, or volume). Results are presented graphically in the form of spatial vectors; values of the magnetic field level are written to files and saved. Typical examples of the GUI output, which the user sees at the terminal while running the program, are to be found throughout this section on shielding. This program gave us a powerful tool for rapid analysis of various active shielding configurations.

Shielding Index

In order to differentiate between various shielding schemes, it was necessary to develop a metric that would indicate the shielding effectiveness of a particular configuration and that could be used for the purpose of comparison between different shielding schemes. An obvious choice for such a parameter is the percent of the volume of interest throughout which the stray field is below a particular level. It was well recognized that such a parameter, though adequate for the present study, would need to be modified for any further detailed study since it does not convey any information on the distribution of the "field-free" region in the passenger compartment. Therefore, two shielding configurations may yield the same index, yet could differ drastically in the usefulness of the shielded region. Nevertheless, the parameter can be used to observe and guide the evolution of a particular configuration, since a design objective would be to maximize the volume of the "field-free" region. Unless otherwise stated, the stray field limit used in the calculation of our so-called "Stray Field Index" in the following analyses is 0.0010 tesla.

4.1.2 Passenger Compartment Fields with Various Arrangements of the Superconducting Coils

Several configurations have been analyzed for the levitation/propulsion coils; these configurations differed in their grouping scheme and amount of current (actually total ampere-turns). In one configuration, the coils are grouped at either end of the passenger compartment, as in the latest Japanese configuration; while in another, the coils are distributed along either side of the passenger compartment. This second grouping was further divided according to the amount of current per coil. The different level of coil current stems from the particular design driver in each

case: higher efficiency in the linear motor at the expense of increased stray field in the vehicle; or decreased stray field level in the vehicle at the expense of increased losses in the resistive linear motor. All configurations provide the same thrust to the levitated vehicle. In all of the following configurations, the coil dimensions have remained the same. The computer-generated schematic figures, accompanying the text, will show rectangular filament models representing racetrack coils that are 2.5 m long and 0.5 m high. Coils on either side of the passenger compartment are separated by 3 m (the width of the compartment) and are energized in such a sense as to aid the flux in each coil. In the following analysis reference is made to "return flux," which refers to the group of flux lines completing their magnetic circuits by linking two laterally opposite coils.

Two passenger compartments are modeled which differ only in their height above the coils; the dimensions of each compartment are 30 m x 3 m x 3 m. The first compartment is designated PASCAR1 and rides 0.5 m above the superconducting coils' mid-plane. The second compartment is designated PASCAR2 and rides higher at 0.75 m above the coils' mid-plane. The possibility of the vehicle riding even higher was not investigated in this study, because it was felt that the increased vehicle frontal area would represent an unacceptable penalty on the motor thrust. Our final results indicate that it may be necessary to have such an increased spacing to reduce the field below possible target levels. A novel approach to addressing the stray field problem, and one that has not been considered in the technical literature, is to adjust the lateral spacing between the levitation/propulsion coils. Analysis will show that the bulk of the stray field in the passenger compartments is due to "bulges" in the flux lines between two opposite coils and that the fraction of the volume, where the field exceeds a user-defined limit, will vary according to the coil separation.

The analyses performed for active shielding began with the base cases involving coils in bogeys (4 per vehicle) and distributed along the vehicle (24 per vehicle assumed). Other analyses were then performed using a third row of shielding coils along the vehicle centerline, as well as altering the positioning of the main coils in several ways.

Four coils per passenger compartment

For this base case, there are four coils per passenger compartment, each coil energized to 586.7 kA-turns. The coils are located at each compartment corner thus moving as far away as possible from the passenger seats (see Figure 4.1.2). The flux lines link coils on opposite sides of the passenger compartment (see Figure 4.1.3). In the absence of intermediate current regions, the flux lines are forced to expand outwards by the action of the magnetic pressure. Adjacent coils are also linked because of the alternating current flow in each.

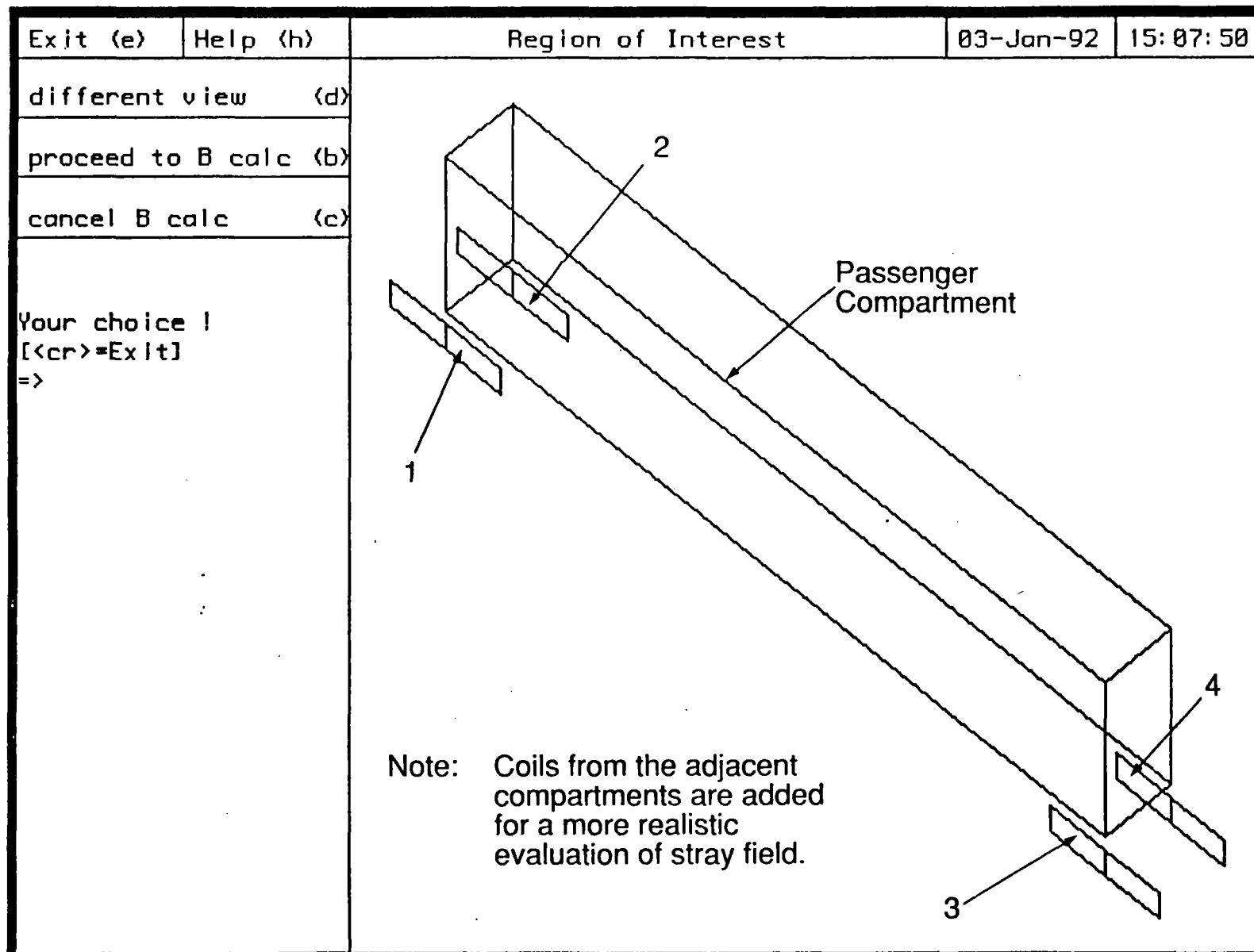


Figure 4.1.2. The 4-Coil Configuration.

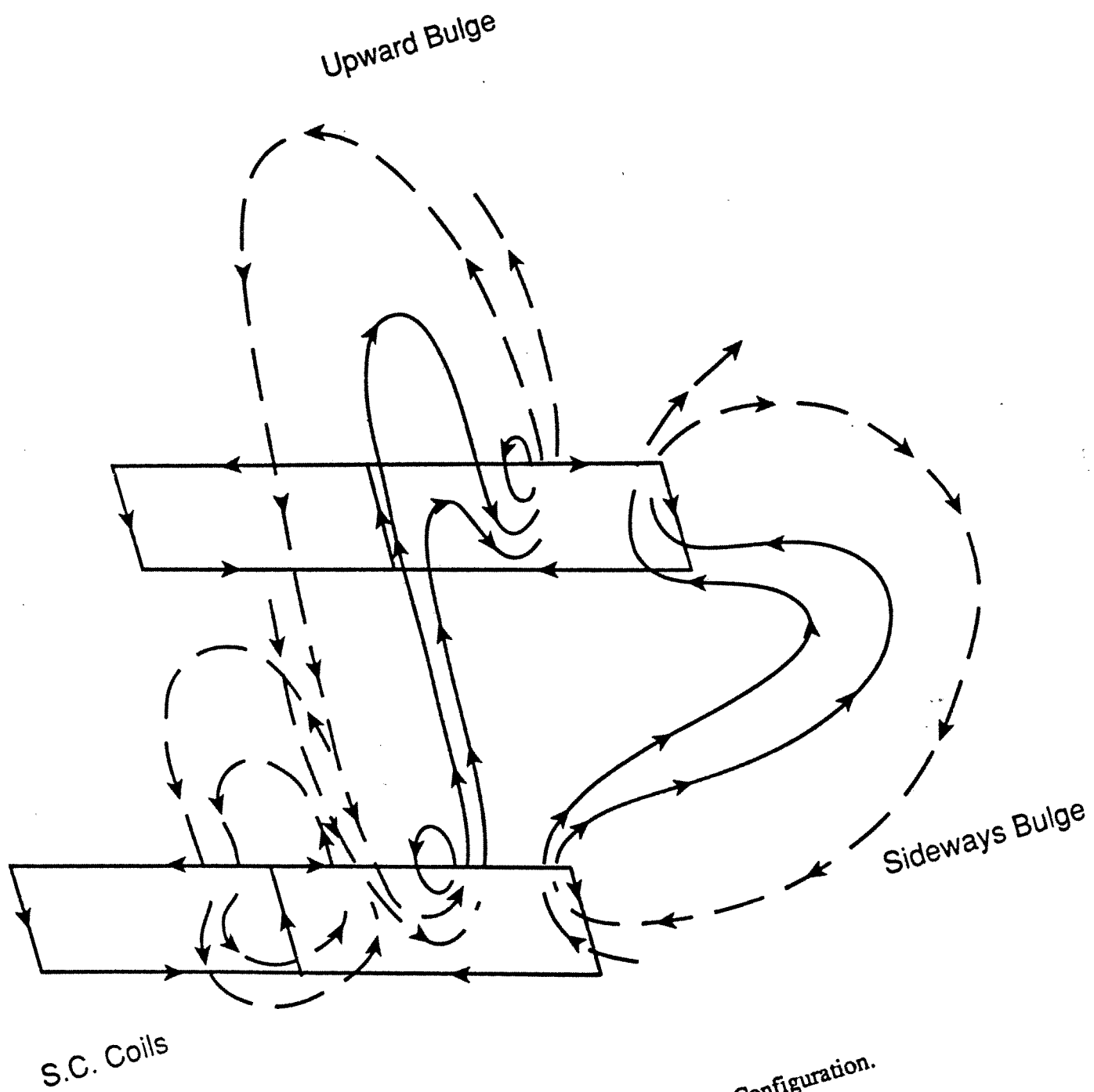


Figure 4.1.3. Flux Patterns in a 4-Coil Configuration.

The stray field index for this configuration is 81.8 for PASCAR1 and increases to 84.2 for PASCAR2. The stray field in the passenger compartment results from "bulges" in the flux lines between coils on either side of the compartment. Analysis indicates that only a small fraction of the volume is affected by the return flux (see Figure 4.1.4).

One possible design approach for reducing the stray field is to vary the spacing between coils located on either side of the passenger compartment. Results of a parametric analysis indicate that for the single-filament model, the spacing should be increased from 3.0 to about 3.6 (see Figure 4.1.5). The resulting improvement in the stray field index is only a few percent (from 81.8 to 83.0). However, it should be noted that a 7 point drop occurs (from a maximum of 83 to about 76) in the index as a result of reducing the lateral separation to 2.6 m. It is recognized here that these results are only applicable to the single filament model; a multi-filamentary model would need to be analyzed in a detailed design phase. Nevertheless, the results of such a parametric analysis do indicate that the stray field should be limited initially by making use of any adjustments to the existing coils prior to searching for shielding answers using active and/or passive shields.

24 coils per passenger compartment

With the coils distributed along the vehicle, there are 24 coils per passenger compartment, with each coil energized to 586.7 kA-turns. The coils are arranged along each side of the passenger compartment thereby allowing for a reduction in the linear-motor current (for the same amount of thrust) (see Figure 4.1.6). Lower current values in the armature windings of the motor lead to lower losses, increased energy-conversion efficiency, and, ultimately, lower subsystem costs (see Appendix A).

The flux pattern is similar to that for the four-coil configuration (see Figure 4.1.7). However, sideways (lateral) bulges are confined to the last coil pair on either end of the passenger compartment.

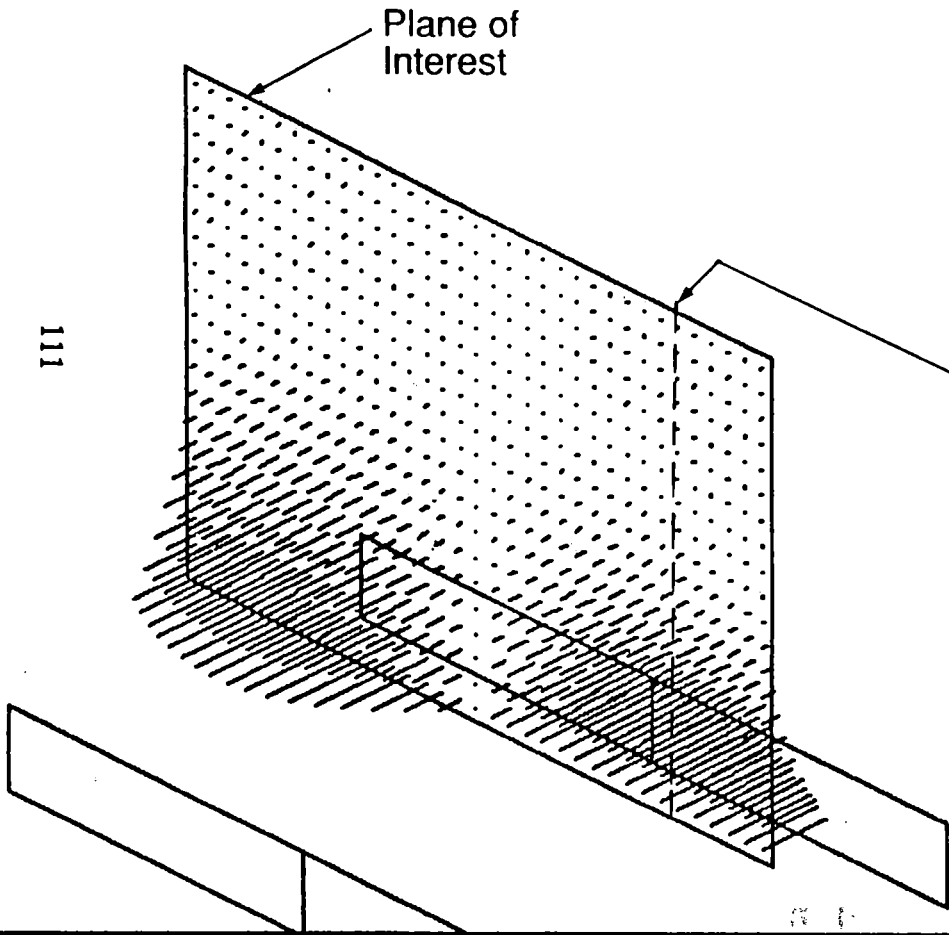
Field In Region of Interest

18-Mar-92

10:59:03

Plane of Interest

III



Field Profile in a Vertical Mid-plane

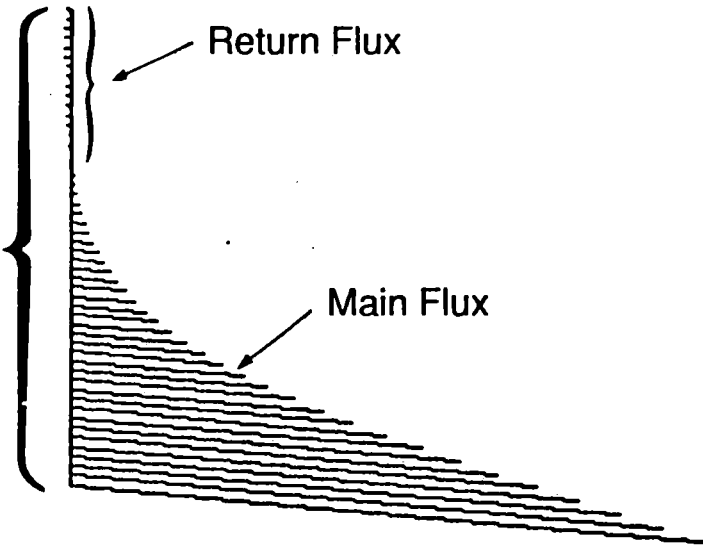
Field In Region of Interest

18-Mar-92

11:06:35

Return Flux

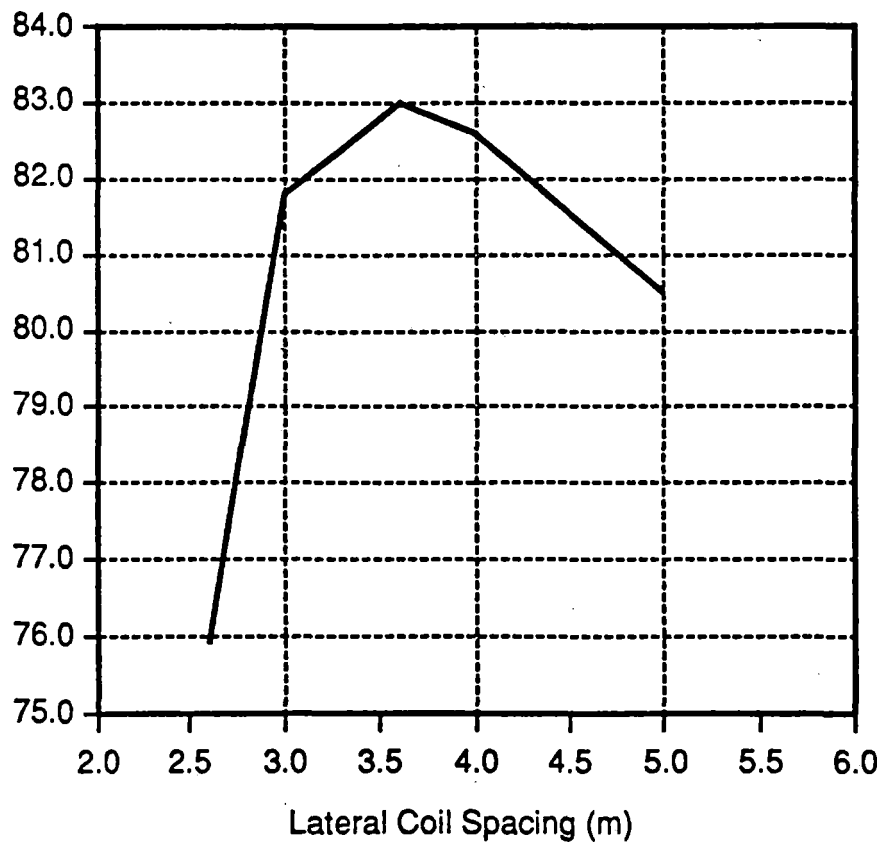
Main Flux



Field Profile Along a Vertical Line in the Mid-plane

Figure 4.1.4. Field Profile in the 4-Coil Configuration.

Figure 4.1.5. Stray Field Index vs Coil Separation for a 4-Coil Configuration.



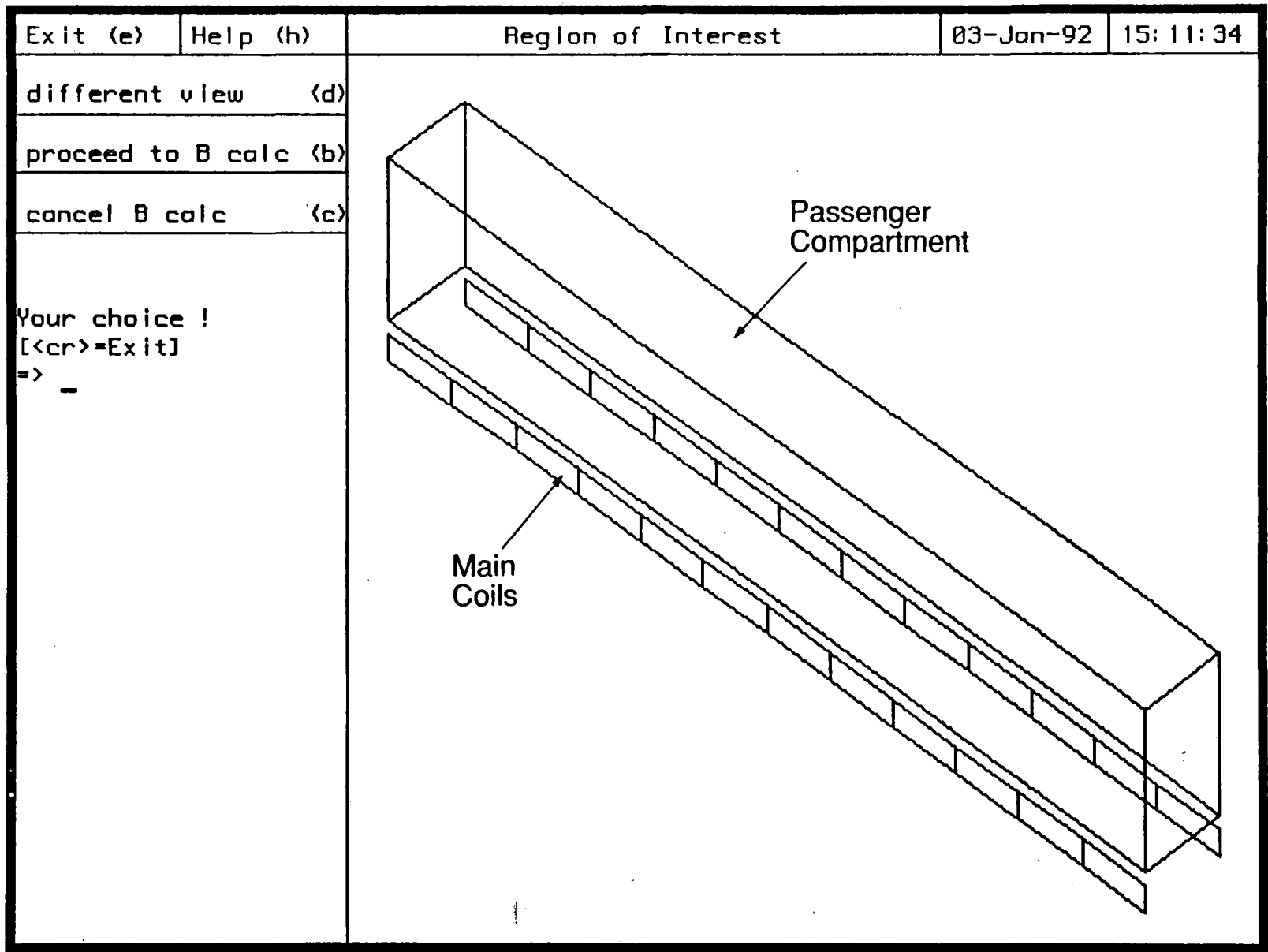


Figure 4.1.6. The 24-Coil Configuration.

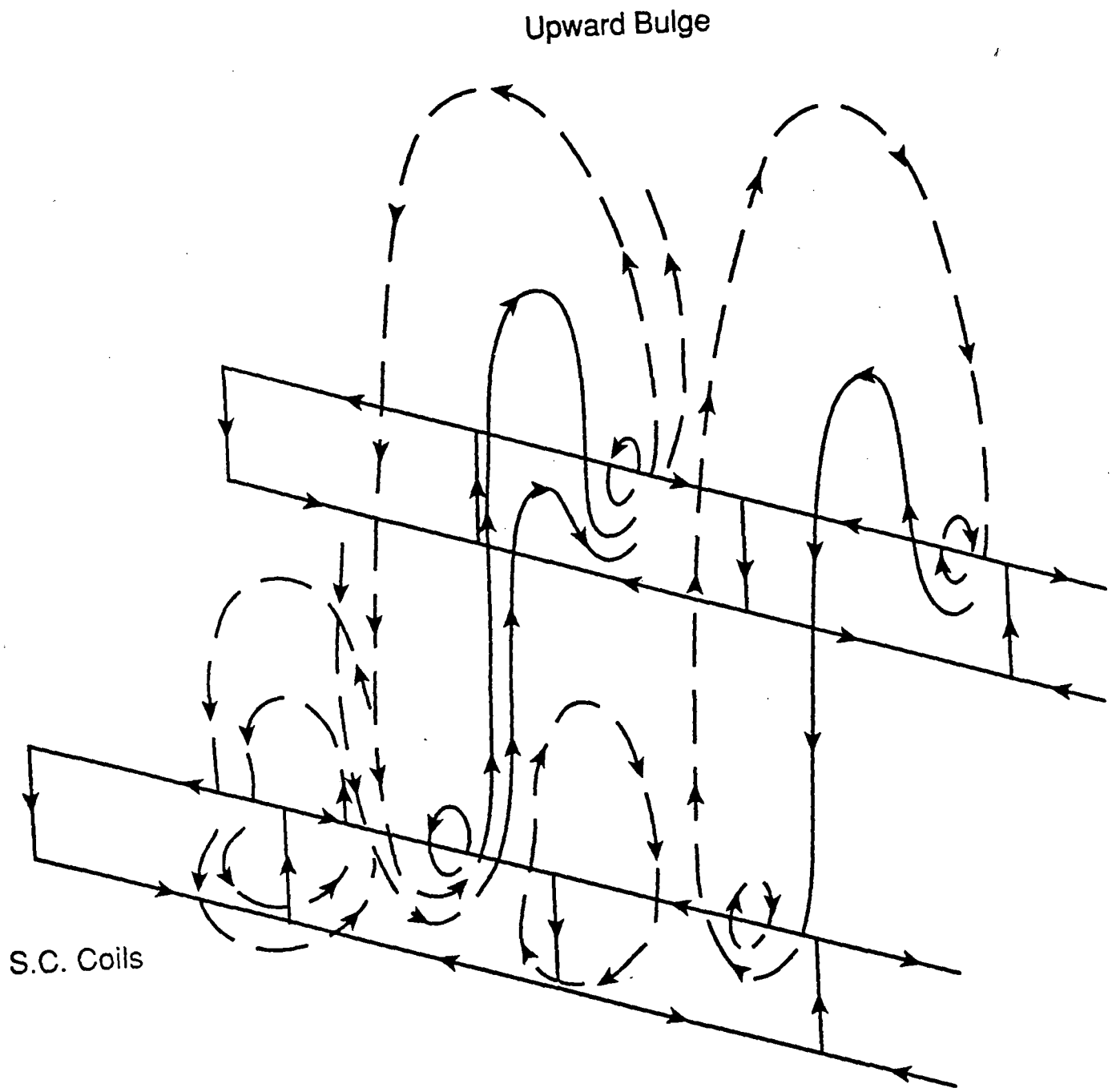


Figure 4.1.7. Flux Patterns in a 24-Coil Configuration .

The stray field index is 43.5 for PASCAR1 and 52.1 for PASCAR2. The noticeable reduction in the index relative to the four-coil configuration serves to highlight the fact that the stray field level increases in the passenger compartment as a result of attempting to reduce cost of the linear motor components in this fashion. The effect is quite dramatic, as evidenced by the magnitude of the decrease in the index.

The effect of varying the lateral coil spacing was also investigated for this configuration (see Figure 4.1.8). In this case the stray field index exhibits a maximum at the design spacing of 3.0 m, and falls off gradually on either side of this maximum. Therefore, the 3 m spacing is optimal.

24 coils per passenger compartment with reduced ampere-turns

A study was also made of the effect of maintaining the distributed 24 coils per passenger compartment, but with each coil energized to 94.8 (568.7/6) kA-turns. This value maintains the same number of ampere-turns per vehicle exhibited by the four-coil system (see Figure 4.1.6). The effect of the increased number of coils in this case is to allow for a reduced level of magnetomotive force developed by each coil. The linear motor armature current therefore must remain at the level required for the four-coil configuration.

The stray field index for this case is 68.6 for PASCAR1 and 76.9 for PASCAR2. There is still a noticeable reduction in the index from that for the four-coil configuration, caused by the even distribution of the coils along the vehicle. The effect of varying the lateral coil spacing for this configuration was also investigated. The stray field index increases from 68.6 to 69.9 as the lateral spacing between coils is reduced from 3.0 m to 2.0 m. Again, the improvement is small, and it could be argued, as in the four-coil configuration, that the present spacing is near optimum.

Figure 4.1.8. Stray Field Index vs Coil Separation for a 24-Coil Configuration.

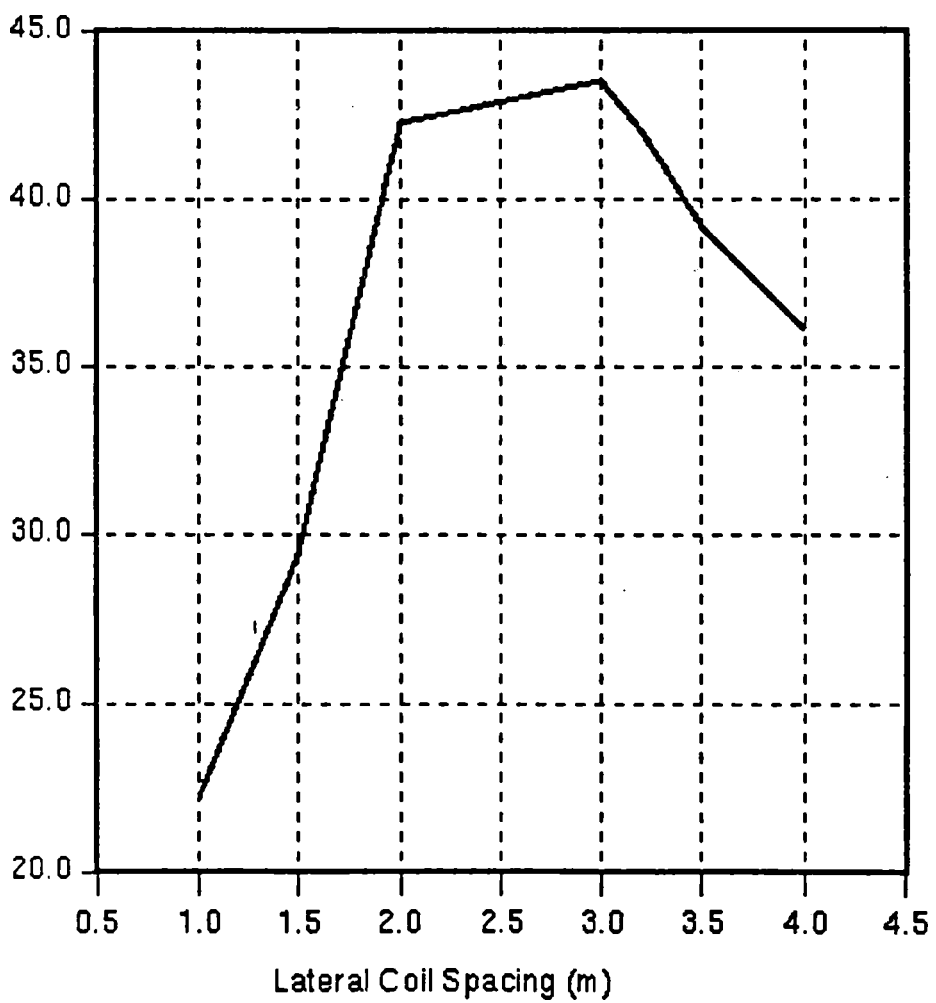
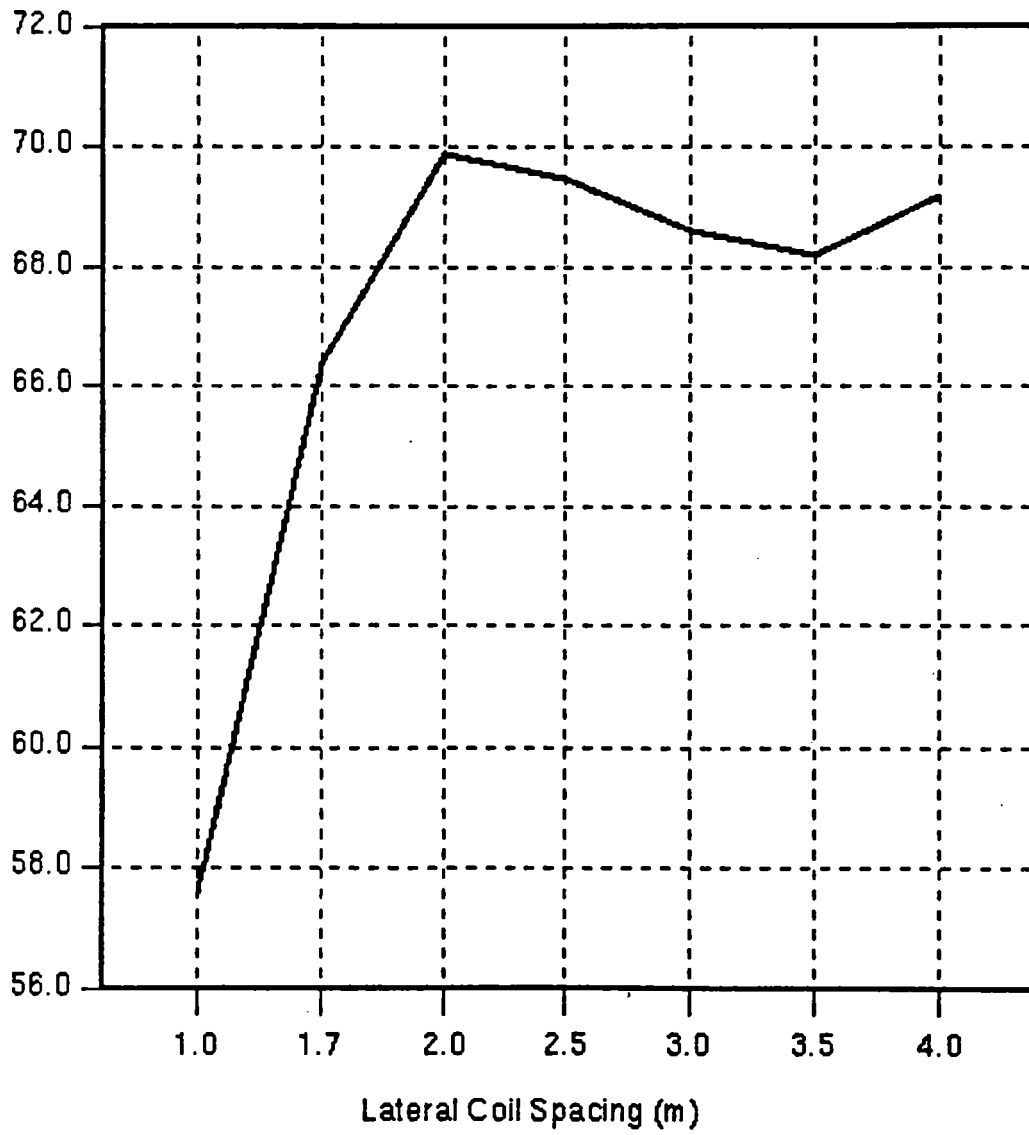


Figure 4.1.9. Stray Field Index vs Coil Separation for a 24-Coil Configuration (reduced current).



Symmetric vs. Antisymmetric Coil Arrangement

Since there is no requirement that the coils on either side of the passenger compartment be energized in the same sense (i.e. with their fields pointing in the same transverse direction), an analysis was undertaken to determine the effect of different energization schemes on the stray field index. The two possible schemes are $+/+$ in which opposite coils are energized in the same sense and $+/-$ in which opposite coils are energized in the opposite sense. It is expected, from analysis of simpler 2-coil systems, that the $+/-$ configuration would be less desirable since the opposite currents force flux lines into the passenger compartment along the mid-plane (see Figure 4.1.10). The results of this study show a reduction of the stray field index from 82 to 66 for the four-coil configuration and from 44 to 20 for the 24 coil configuration. Clearly, the configuration with the coils aiding in flux ($+/+$) is much more desirable for either concentrated or distributed coils. Therefore, unless otherwise stated, all analysis reported here is conducted on configurations where coils on opposite sides of the passenger compartment are energized in the same sense ($+/+$).

Tilted Coils Configuration

Small variations in angular orientation of the superconducting coils were investigated, and found to have a discernible effect on the stray field index (see Figure 4.1.11). It is interesting to note that the peak index occurs at -10 (degree) for the 4-coil configuration, and at $+10$ (degree) for the 24-coil configuration. If the linear motor windings were tilted at the same angle, there should be no effect on the thrust. However, the levitation force exerted by the null-flux coils would be reduced by a factor equal to the cosine of the tilt angle, and other geometrical considerations might make this configuration unattractive.

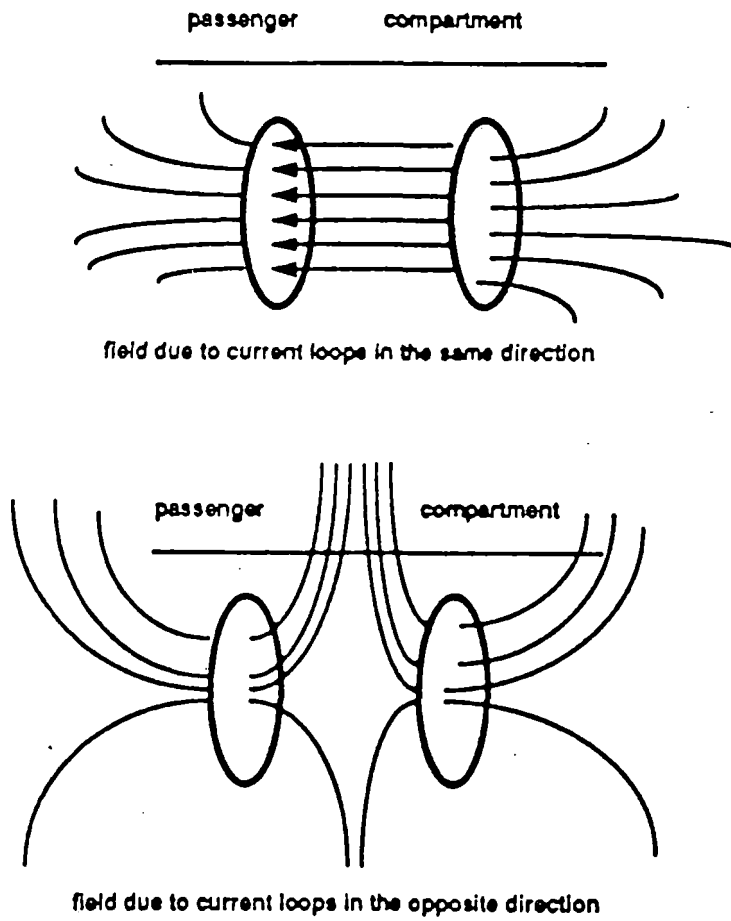
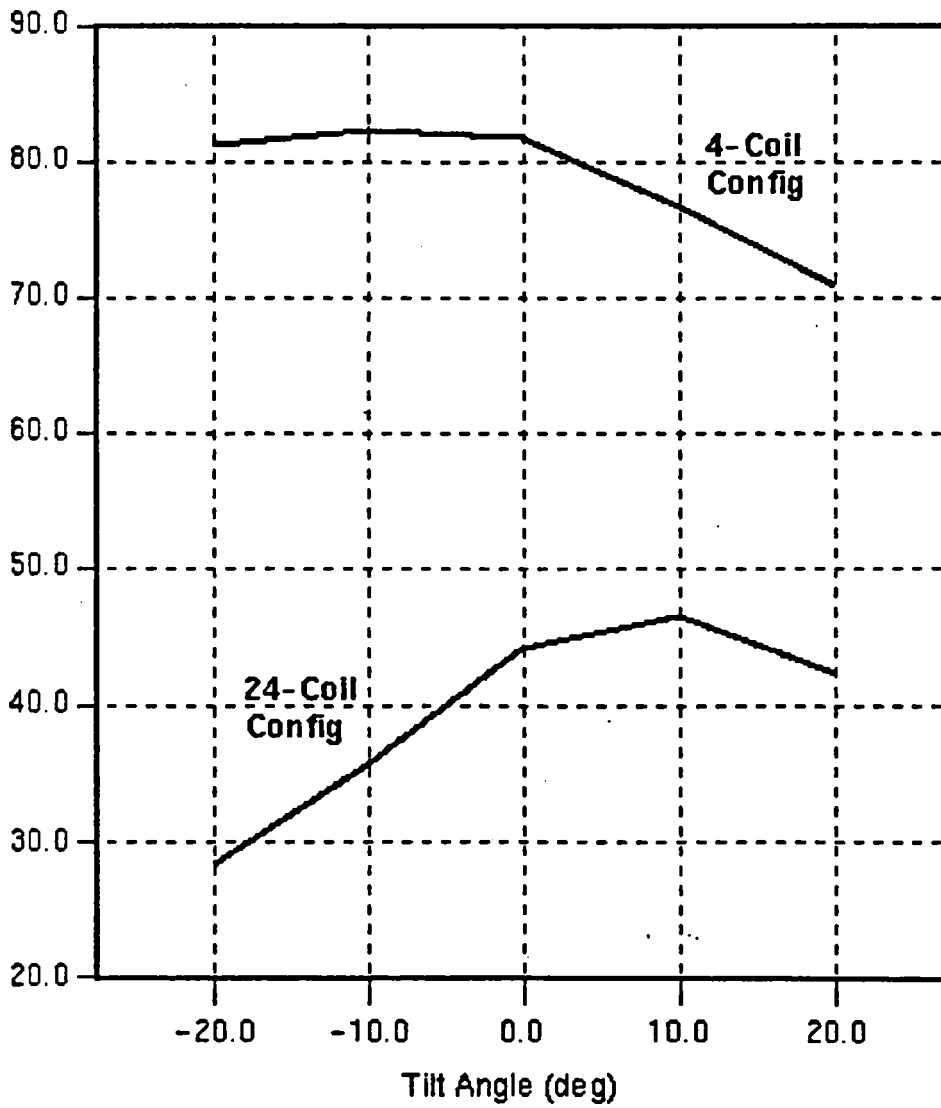


Figure 4.1.10. Coils located on either side of a compartment energized in the same sense to reduce the stray field in the compartment.

Figure 4.1.11. Stray Field Index vs Tilt Angle.



4.1.3 Active Shielding Configurations

Traditionally, active shield coils have been used to exclude flux from a volume in space where the background field can be characterized by a single direction and value. The active shield coils are then designed to deliver a field of equal magnitude but opposite in direction over the specified volume. The design becomes more complicated for the general case where the stray field is neither unidirectional nor single-valued. In the case of magnetic resonance imaging magnets, which typically generate a central field of 1.5 T, active shielding has been successfully adopted by surrounding the source with coils carrying currents in the opposite sense. Design optimization methods needed to be developed to arrive at configurations which successfully redirect the flux and limit its spatial extent. In the case of magnetically levitated trains, reduction of the stray field in the passenger compartment requires a redirection of the flux lines away from the compartment. However, because the on-board source coils provide lift, thrust, and side-ways stability, it is not expected that surrounding them with active shielding coils is a feasible design approach.

One possible method is based on a qualitative analysis of the flux patterns in each configuration. As stated previously, the stray field results mainly from the bulges in the flux lines; therefore, one approach would be to add coils in such a way as to reduce the bulges. In fact, this approach, when carried out to its limit, can be thought of as providing magnetic "tubes" which both surround and guide the flux lines around the space occupied by passengers. The application of this technique to our maglev vehicle configuration calls for shielding coils carrying currents in the same sense as the main coils, and added in the available space under the passenger compartment. The coils are added in one or more rows in an orientation paralleling the main coils, as will become clear from the following figures. Several configurations of these types were studied as the best possible way to reduce the passenger compartment field by active shielding alone.

Four-coil Configuration

One additional intermediate row was added that was made up of two coils per passenger compartment as shown in Figure 4.1.12. The current was varied in these added coils in an attempt to increase the computed value of the stray field index. Results are shown in Figure 4.1.13, where it is apparent that the introduction of the shielding coils actually increased the level of stray field in the compartment, and that the current should be introduced in the opposite sense before a very small improvement in the index is observed. Analysis of the field in the space above the main coils shows that the addition of the shielding coils, carrying current in the same sense as in the main coils, does actually reduce the field in that location. This result seems at odds with the observed

overall increase in the stray field level when the whole volume is considered. The explanation is most likely to be that end effects dominate this configuration. As the number of coils increases so does their contribution to the stray field in the compartment, through the sideways bulges which were previously shown in Figure 4.1.3.

24 Coil Configuration

One additional row was added initially to test if the stray field index responded favorably to the additional coils (see Figure 4.1.14). The results, shown in Figure 4.1.15, confirm that the stray field is reduced in the passenger compartment as a result of additional coils. Furthermore it is possible to optimize the value of the current in these additional coils to obtain the best shielding possible. The results indicate that a current equal to 50% of the main coil current is the optimum value. The different response to the addition of coils between this 24-coil configuration and the previous example of the 4-coil configuration has to be attributed to the differences in the flux patterns of the main coils. Several intermediate rows were then added sequentially as part of a parametric analysis. Each additional row was made up of twelve coils per passenger compartment; an example of two additional rows is shown in Figure 4.1.16. The results, shown in Figure 4.1.17, indicate a higher degree of shielding in response to the addition of a second row of shielding coils.

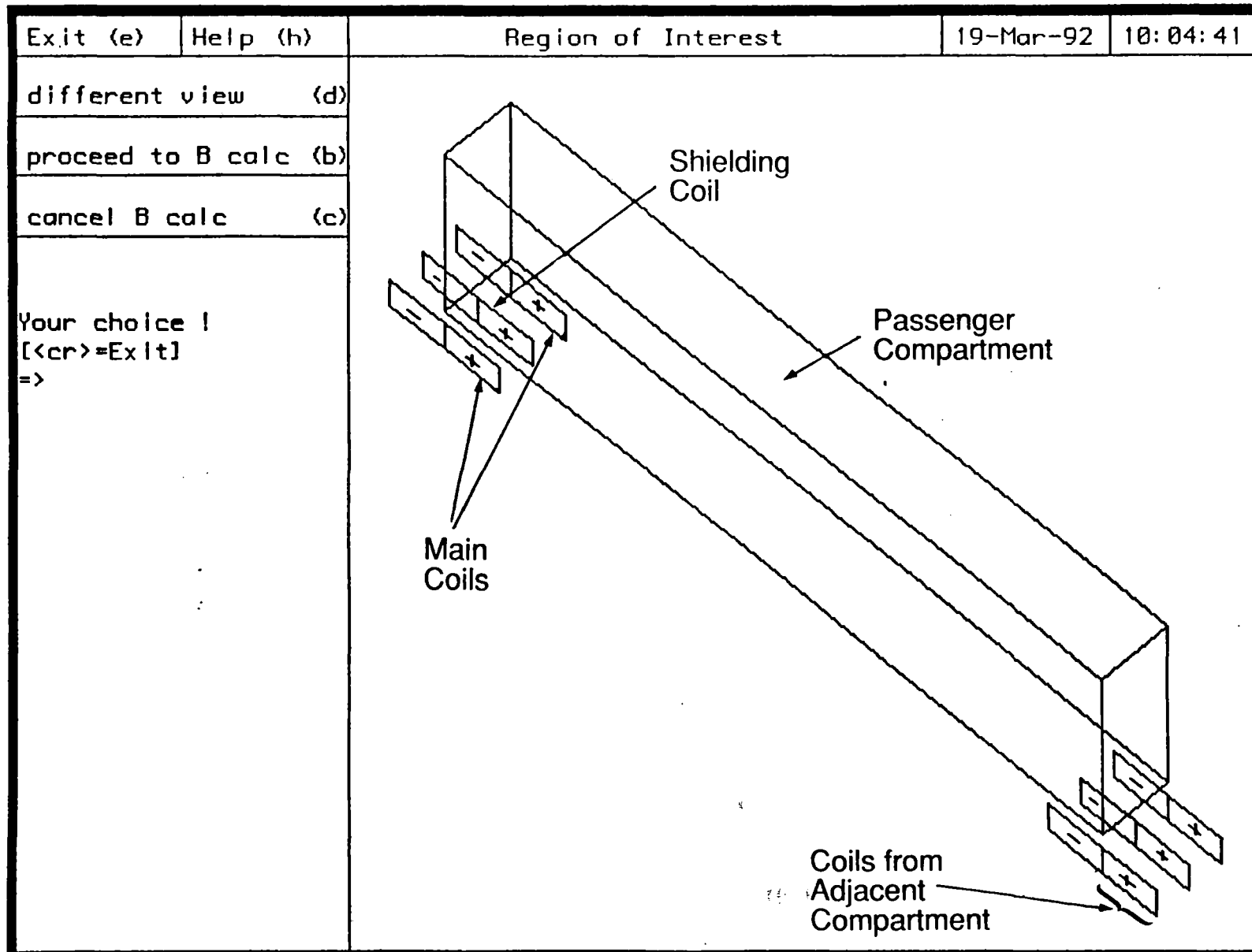
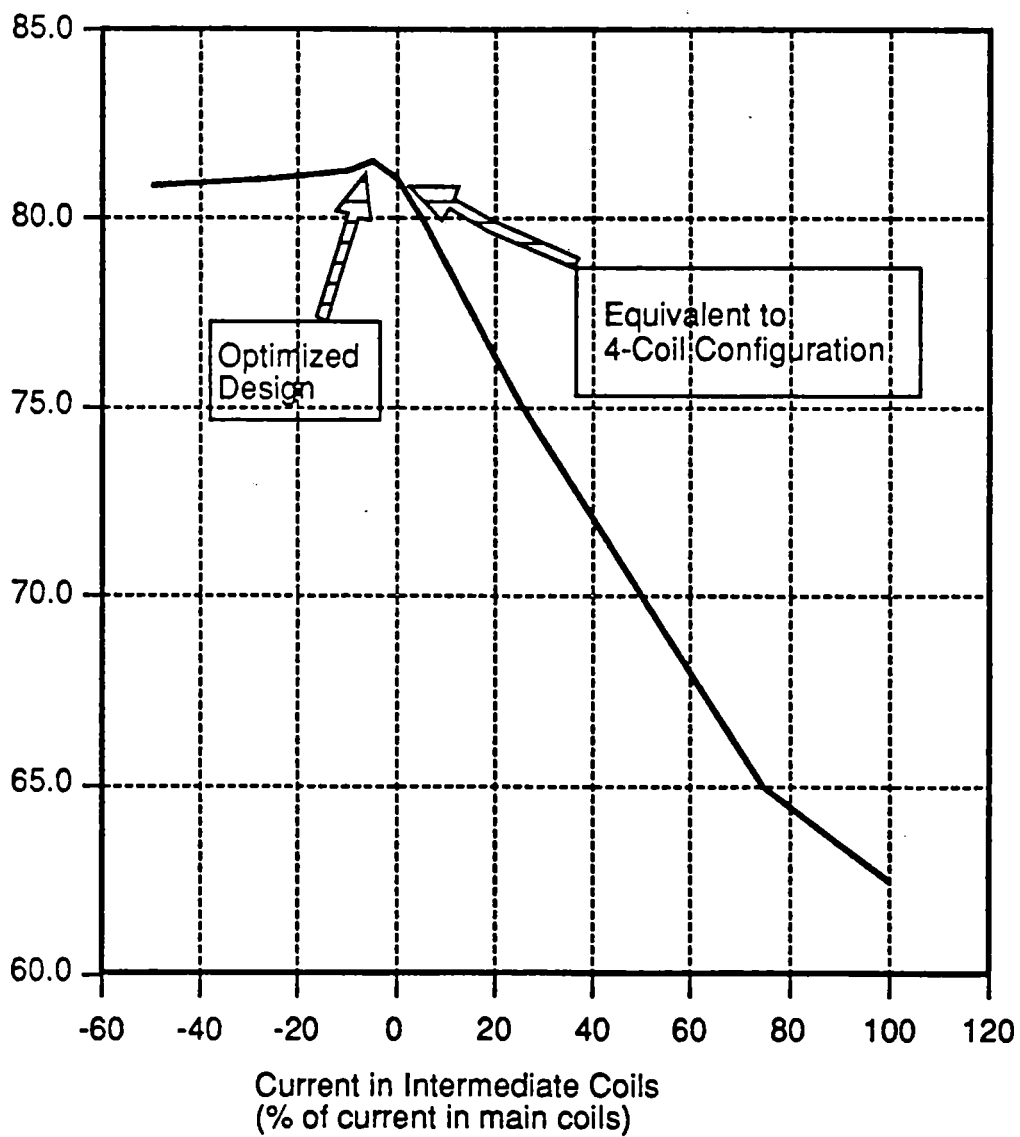


Figure 4.1.12. Shielding arrangement in which one row is added to the base 4-coil configuration .

Figure 4.1.13. Effect of Introducing One Intermediate Row of Shielding Coils.



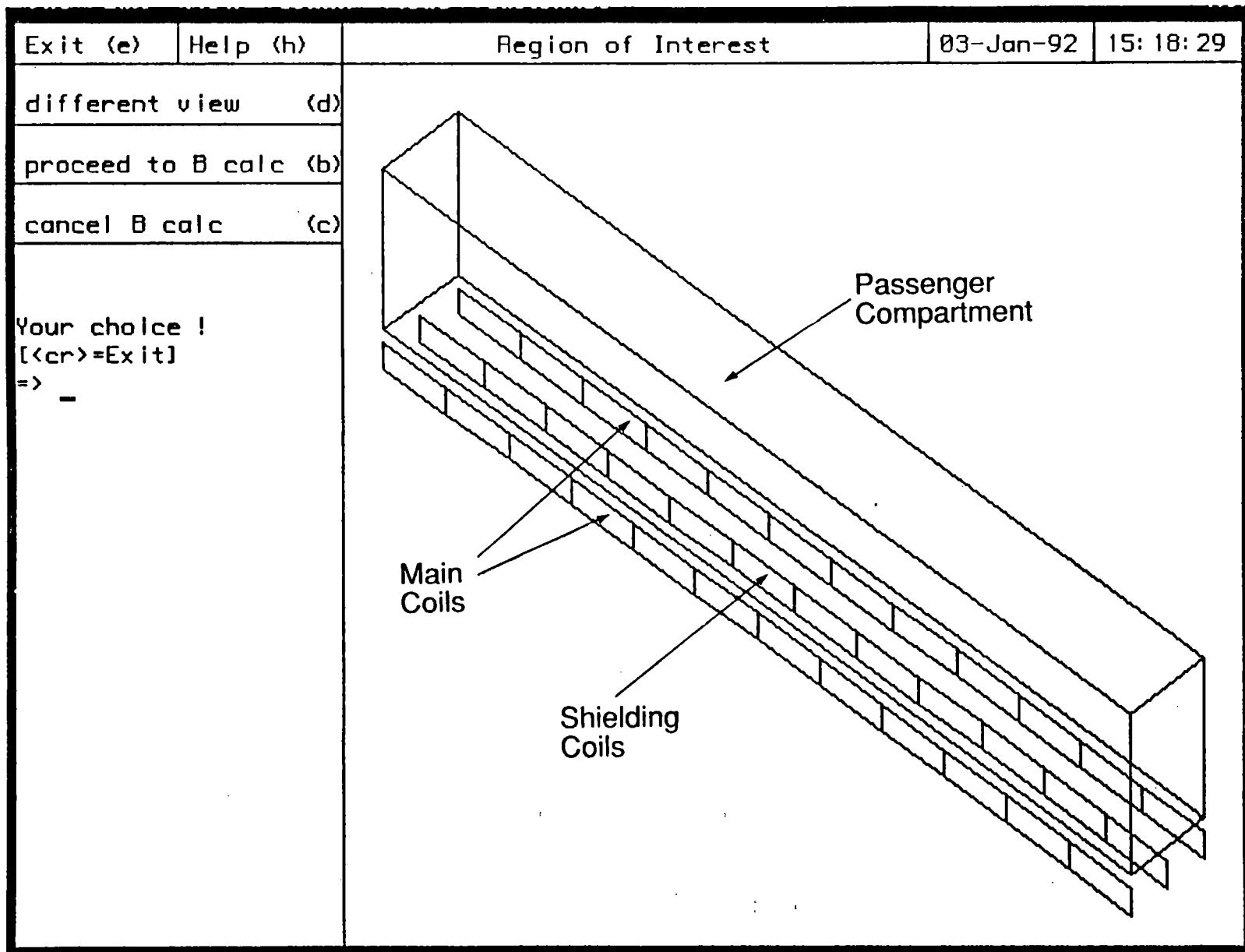
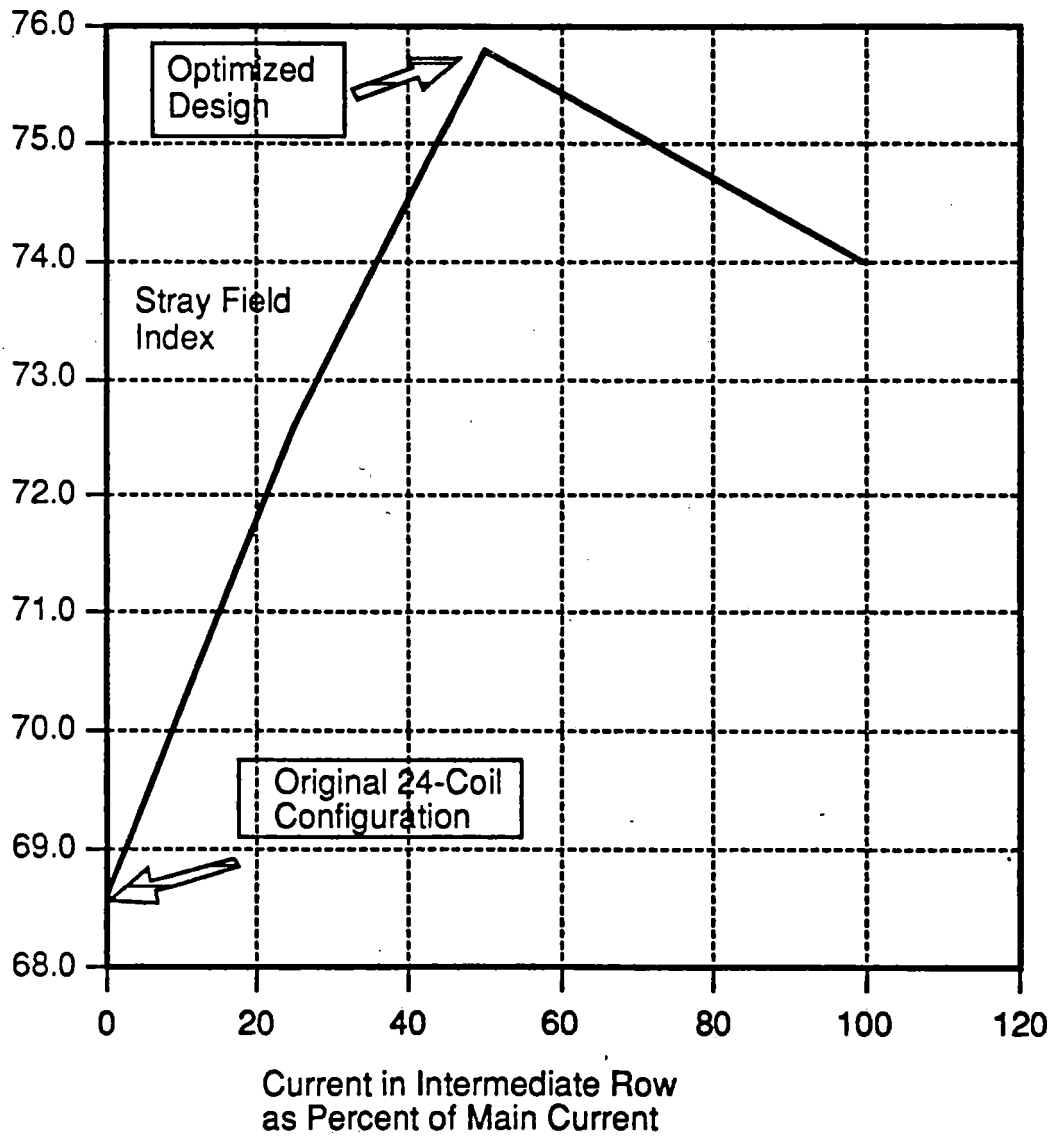


Figure 4.1.14. Shielding arrangement in which one row is added to the base 24-coil configuration.

Figure 4.1.15. Effect of Introducing One Intermediate Row of Shielding Coils.



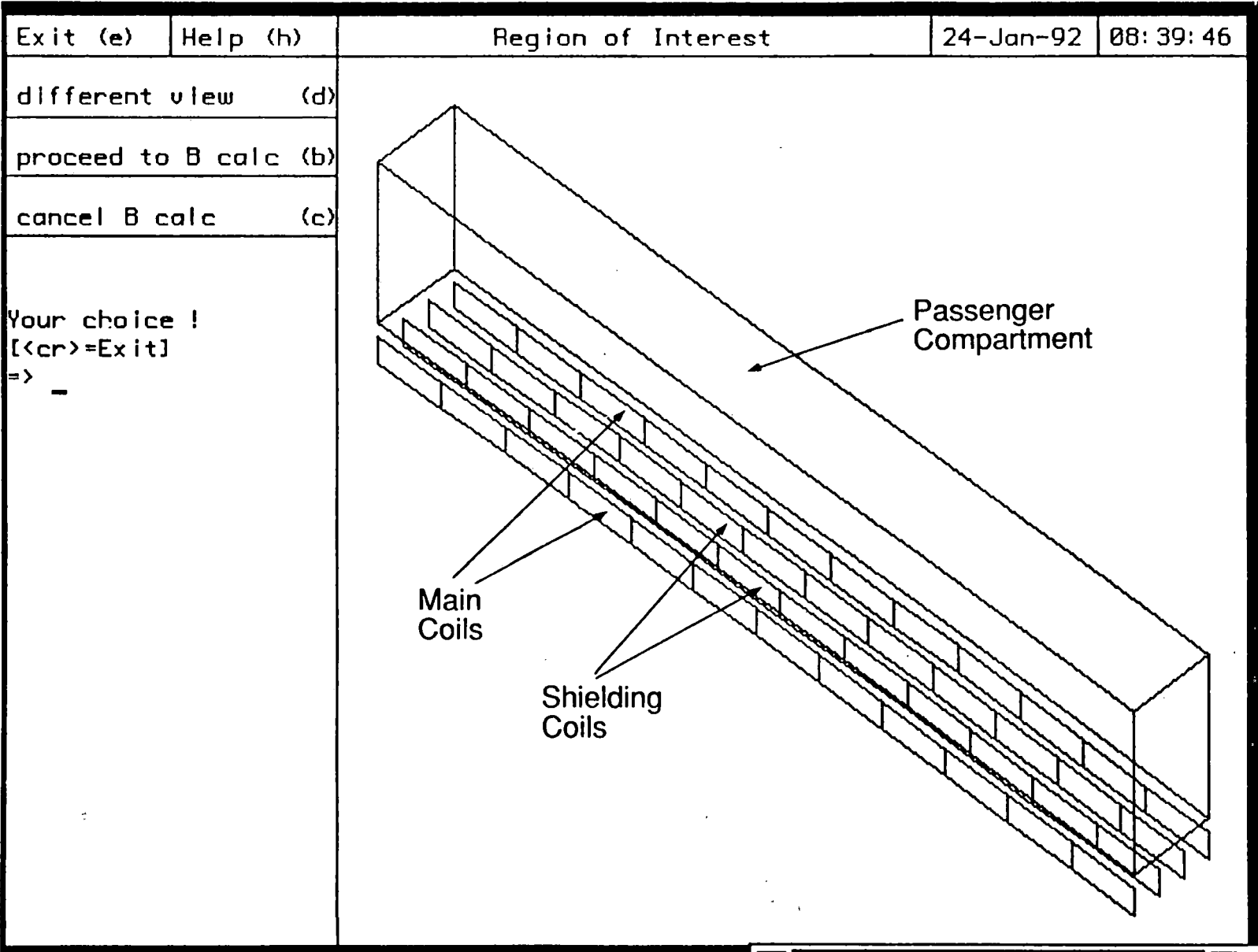
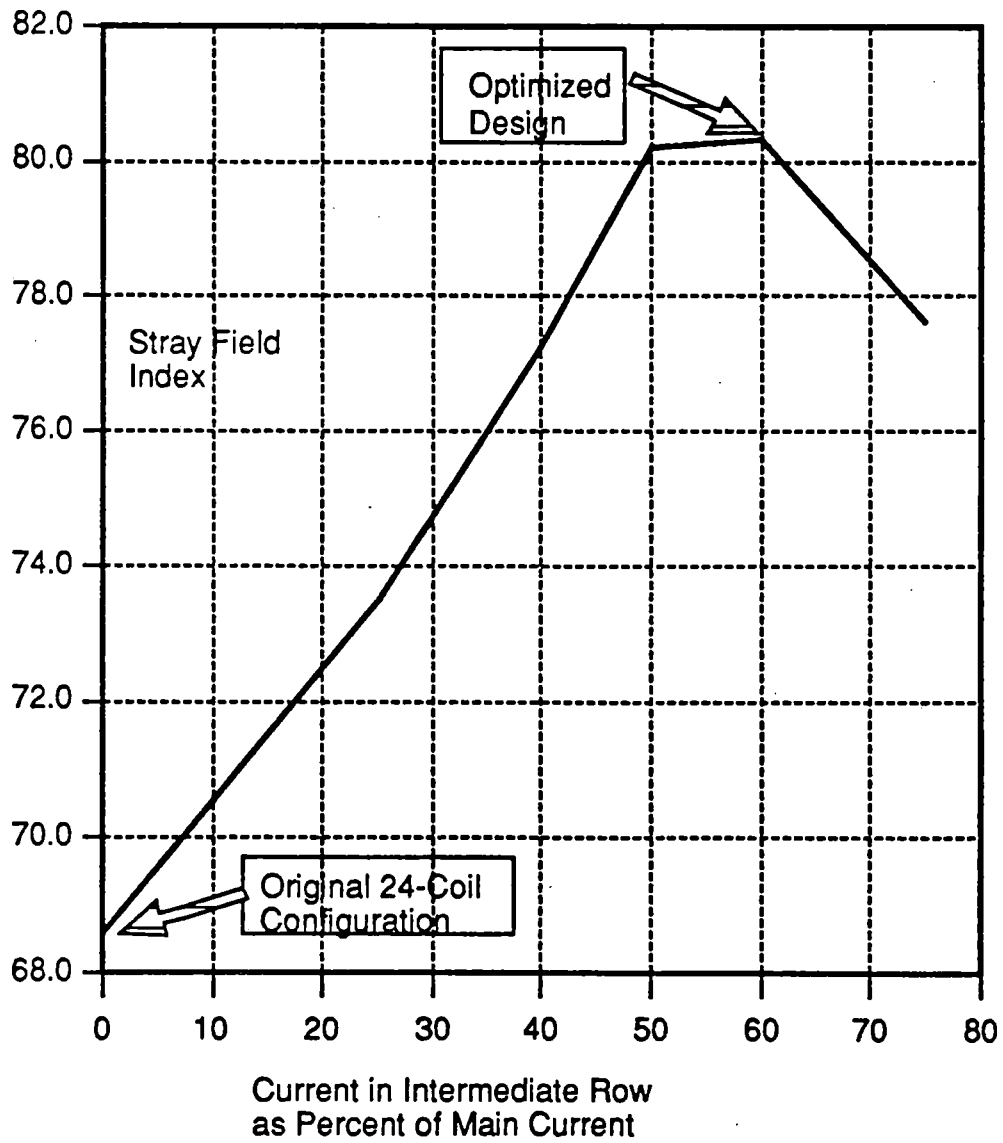


Figure 4.1.16. Shielding arrangement in which two rows are added to the base 24-coil configuration.

Figure 4.1.17. Effect of Introducing Two Intermediate Rows of Shielding Coils.



4.1.4 Conclusions

Reduction of the stray field in the passenger compartment has been investigated via two general design approaches. First, optimization of main coil location and orientation was found to influence the stray field index on the order of a few (up to five) percent. Second, the addition of shielding coils can be used to divert the flux lines from the passenger compartment. It was found that the 4-coil configuration is dominated by end-effects, and that shielding coils are more effective in the case of the 24-coil configuration. The shielding coils were arranged in the simplest configuration possible, viz., parallel to the main coils. More complex configurations, in which the coils are distributed in and around the passenger compartment, may prove more effective. However, it is our contention as a result of considerable work in this area that active shielding of this coil configuration would not be cost effective when compared to a combination of raising the vehicle further above the coils with passive shielding.

4.2 Passive Shielding

The addition of high permeability material, such as iron in the form of sheets, is effective in reducing the stray field at a cost of added system weight. The relationship between weight and maximum allowable stray field level is nonlinear, requiring considerable added material to achieve low field levels. The analysis presented in the previous sections on active shielding served also to point to the complexity of the flux lines surrounding the on-board superconducting coils. This information was used in scoping out a design path to arrive at passive shielding configurations using only iron sheets. It was decided that two approaches should be attempted in parallel; one was to concentrate on the passenger compartment only, so that iron sheets were placed immediately below the compartment and would wrap around the sides if necessary. The second approach was to attempt to influence the flux lines at the source, i.e. place iron structures in the immediate vicinity of the coils, without affecting the primary function of the coils; i.e., propulsion, levitation and stability. GE designs for passive shields, for Magnetic Resonance Imaging Superconducting magnets, have been built and successfully tested in the past. Experience gained in designing such shields was the basis for the choice of multiple-sheet approach since this allows the designer to vary the thickness of the iron to achieve the necessary degree of field reduction using the minimum amount of shielding material.

4.2.1 Stray Field Profile in the Absence of Shielding

The stray field profile was first determined by modeling two pairs of superconducting racetrack coils in the absence of any iron. Figures 4.2.1 and 4.2.2 illustrate the stray field profiles

generated by the racetrack coils which indicate that the 100 gauss line extends through the passenger compartment. Along the length of the vehicle, this region of high field extends about one meter past the ends of the racetrack coils. From these field profiles it was apparent that the superconducting coils needed to be shielded to reduce the stray field level immediately above the coils.

4.2.2 Analysis Codes

Two dimensional analysis

CAE2D is a GE proprietary software system providing engineers with a fully integrated, multi-disciplinary finite-element analysis capability. The CAE2D Computer Aided Engineering package was developed at the Engineering Systems Laboratory of GE Corporate Research and Development (GE-CRD) to solve common two-dimensional and axisymmetric problems in stress analysis, heat transfer, and electromagnetics. A graphical user interface system, geometric modeler, and totally automatic mesh generator are central to CAE2D and are common to all disciplines. In addition to pre- and post-processors, CAE2D provides finite-element analysis programs developed at CRD for all disciplines, as well as links to external analysis programs such as ANSYS.

Post-processing in electromagnetics allows the user to calculate fields, permeabilities, vector potentials, power loss, current densities, and magnetization. These values may be plotted along lines and arcs within the model, or they may be displayed as color iso-contours. Flux lines are available. Integrated values, such as energy, forces, and torque may be calculated.

Three dimensional analysis

H3D is a three-dimensional, nonlinear magnetostatic finite-element analysis package for modeling coil geometries in the presence of iron. It has the capability of modeling very large problems that contain up to 500,000 nodes. The coil source currents are modeled externally to the finite-element grid which allow any current path configuration to be generated without regards to the finite-element grid. This eliminates the complexity of building coils in the finite element mesh. H3D uses a hybrid finite element/harmonic solution method: The interior and exterior magnetic fields are represented as harmonic series; the field in the vicinity of iron is represented by finite elements. The results produced by H3D include the harmonic coefficients in the interior and exterior region and scalar potentials at the finite element nodal points. Appendix C is a technical paper describing the basis and capabilities of H3D.

To generate a 3-D model for H3D, a stand-alone 3-D grid generator is available that allows the user to build the 3-D model by interactively extruding a 2-D model in one dimension or importing the model from an external grid generator that produces an ANSYS PREP7 file. The post-processor allows the user to interactively specify lines, arcs, planes, and curved surfaces so that various magnetic values can be viewed on a computer workstation.

Computer Hardware Used in Passive Shielding Analyses

Two supercomputer systems were available and used in these analyses. The Convex C240 computer system is made up of four processors and 1 gigabyte of real memory. It is configured with 17.6 gigabytes of disk. The Convex C3220 computer system has 2 dedicated processors and is configured with 256 megabytes of real memory. It has 12 gigabytes disk capacity.

The two systems have a total of 22 Convex Integrated Disk Channel high-speed disks. Each system has a 9-track tape drive and an Ethernet tap connected via a VMEbus. The supercomputers are tightly coupled and are connected to maximize the data transmission bandwidth between them. User files systems cross-mounted between the two machines. This allows both computers to share system resources.

4.2.3 Shielding Examples

Approximately 20 three-dimensional shielding models were analyzed, with half placing the iron directly below or around the passenger car and the other half wrapping some or all of the iron around the superconducting coil cryostats. The finite element models were large, containing 85,000 to 160,000 nodes with 25,000 to 50,000 second order elements. Typical solution times were 40 or more hours of CPU on the Convex computer, with the typical turnaround time being about three days. The models were pre- and post-processed on DECstation 5000 workstations.

The dimensions of the models were 10 m in each of the three axis directions. The passenger car was assumed to have cross-sectional dimensions of 3 m by 3 m. Iron shielding plates extended 7 m along the length of the vehicle. Two pairs of racetrack coils were modeled. In all of these cases the assumption was that the bottom of the vehicle was only 0.25 m above the top of the racetrack coils. Figure 4.2.3 shows a typical finite element grid.

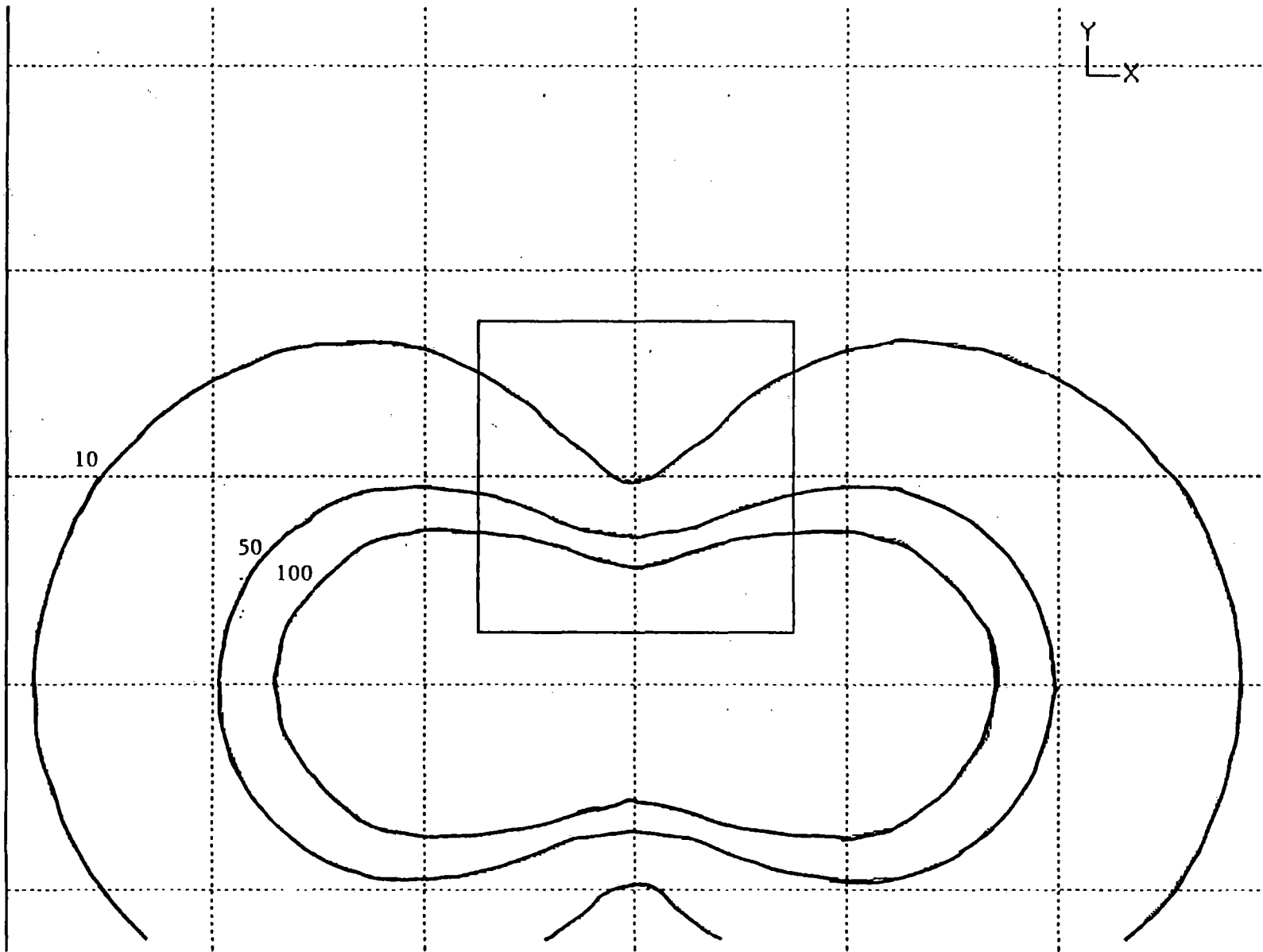


Figure 4.2.1. Train Car Without Shielding (cross-sectional view) Flux Density Iso-Contours in Gauss.

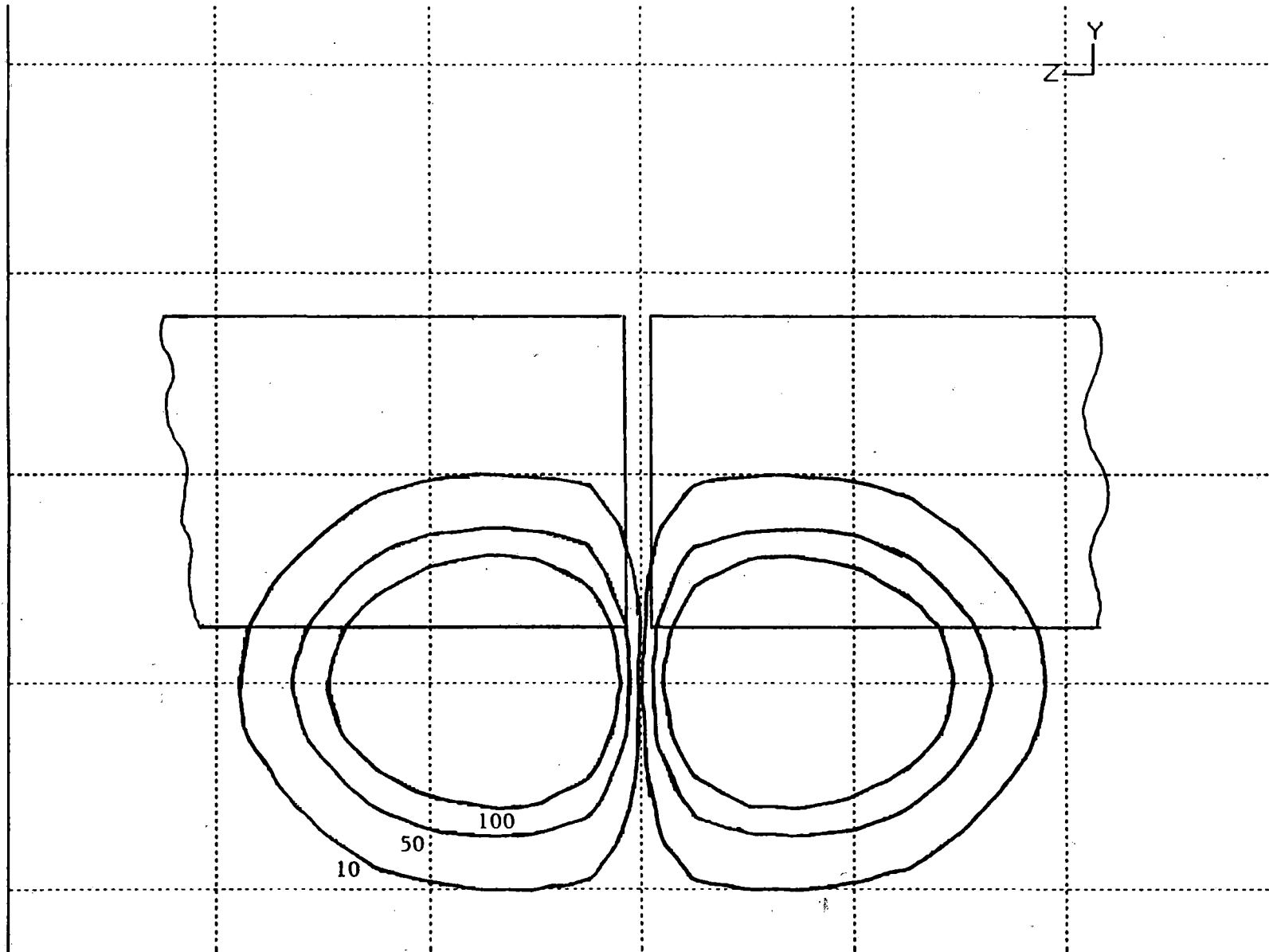


Figure 4.2.2. Train Car Without Shielding (side view) Flux Density Iso-Contours in Gauss.

134

Passenger compartment

Shield

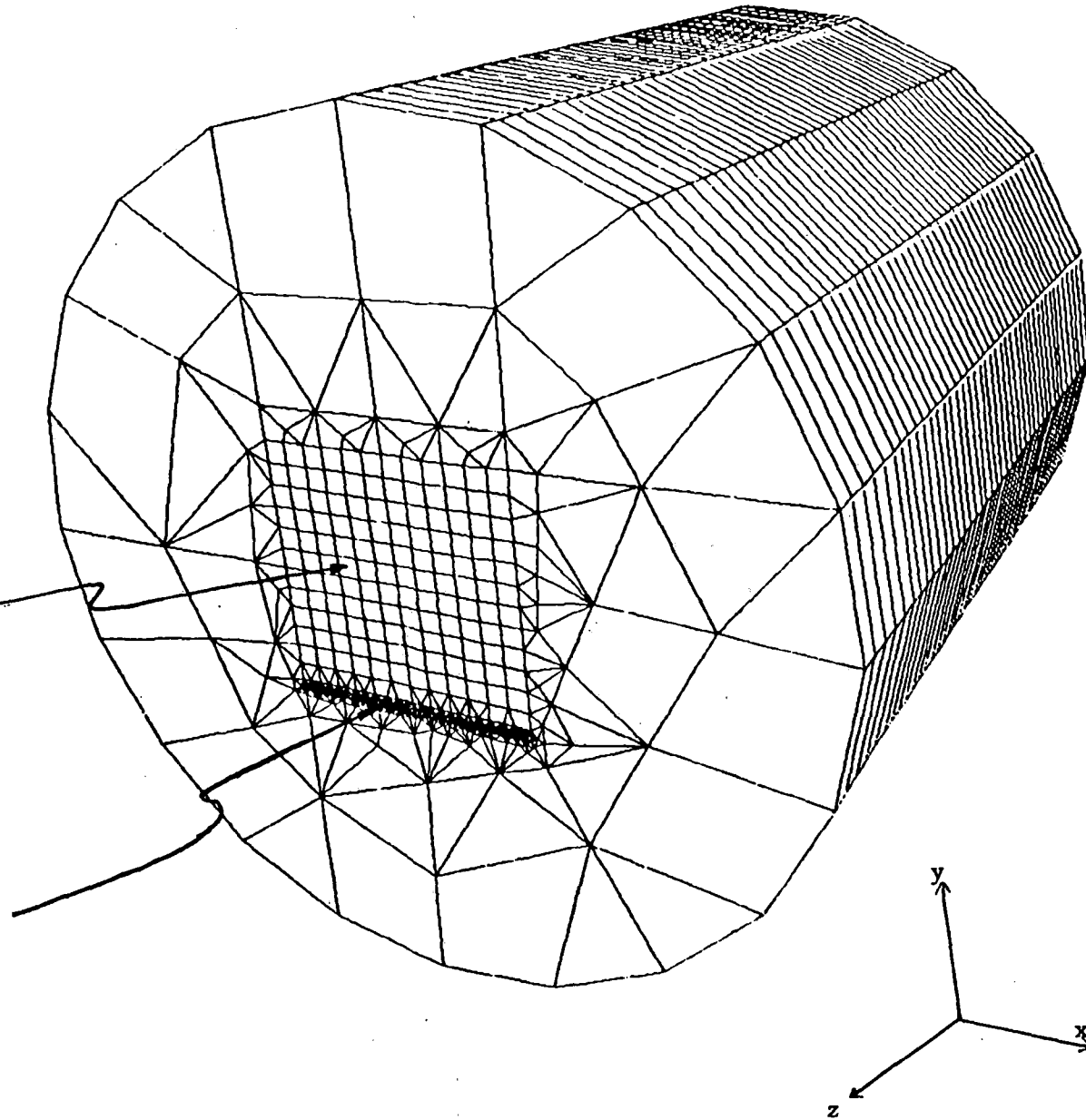


Figure 4.2.3. 3-D Finite Element Model.

Plate Shields on Train Car

The first approach was to place two thin (1 cm thick) plates, separated by a 5 cm space, directly below the bottom of the vehicle. Unfortunately, this proved ineffective in bringing the flux density level throughout the entire car down to an acceptable level. Figure 4.2.4 illustrates the effect of the shield.

Since the thin plates were not effective, a thicker (7 cm thick) plate was placed directly below the vehicle. Figure 4.2.5 illustrates clearly that the center of the car is at a reasonable level but the edges are not. This configuration allows the magnetic flux to "spill" around the edge of the shield and into the vehicle.

To address the problem of magnetic flux spilling around the shield, extensions of various lengths past the edge of the vehicle were tried in a series of models. Figure 4.2.6 shows a model, with a 1 m extension past each side, that is quite effective. The flux density level throughout the car is 50 gauss or less. Since a 1 m extension of the iron shield past the edge of the vehicle is not a very desirable solution, a model was made with the extensions "folded in" up the sides of the car. This geometry and this solution are illustrated in Figure 4.2.7. Again the flux density level is 50 gauss or less throughout the vehicle. The approximate weight of this model is 19100 kg per vehicle, which nearly doubles the vehicle weight.

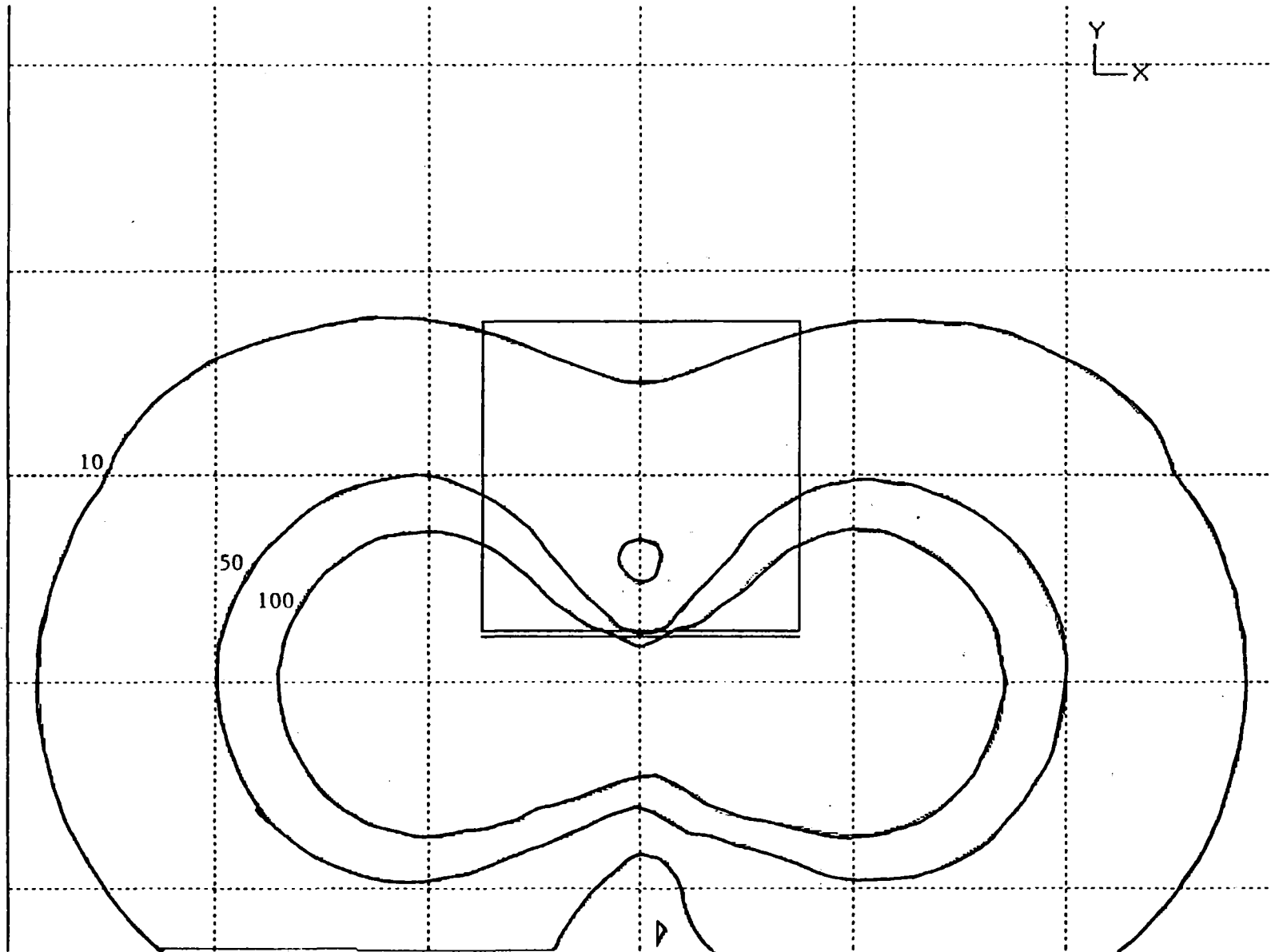


Figure 4.2.4. Two Thin (1 cm.) Plates Flux Density Iso-Contours in Gauss.

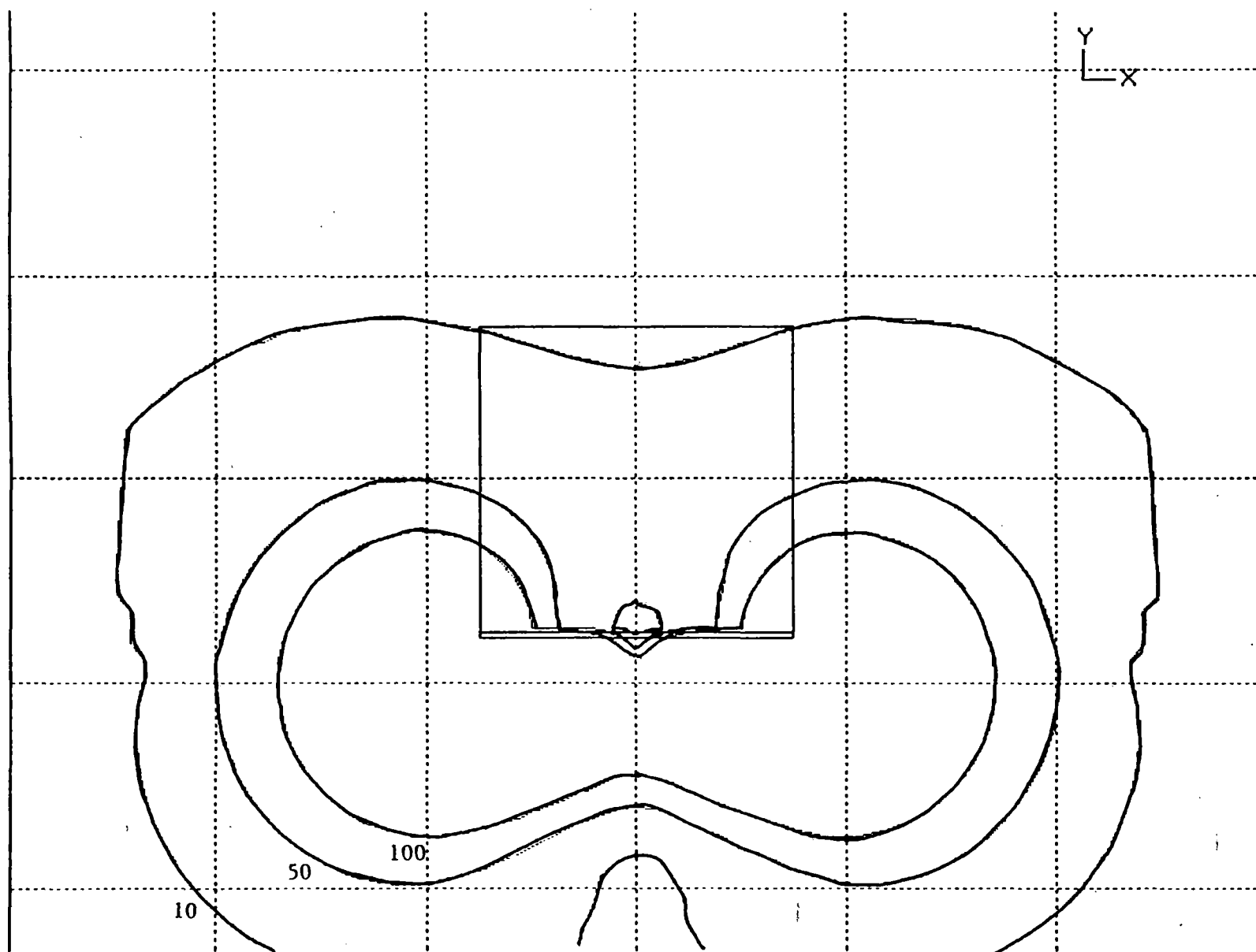


Figure 4.2.5. Thick (7 cm.) Plate Flux Density Iso-Contours in Gauss.

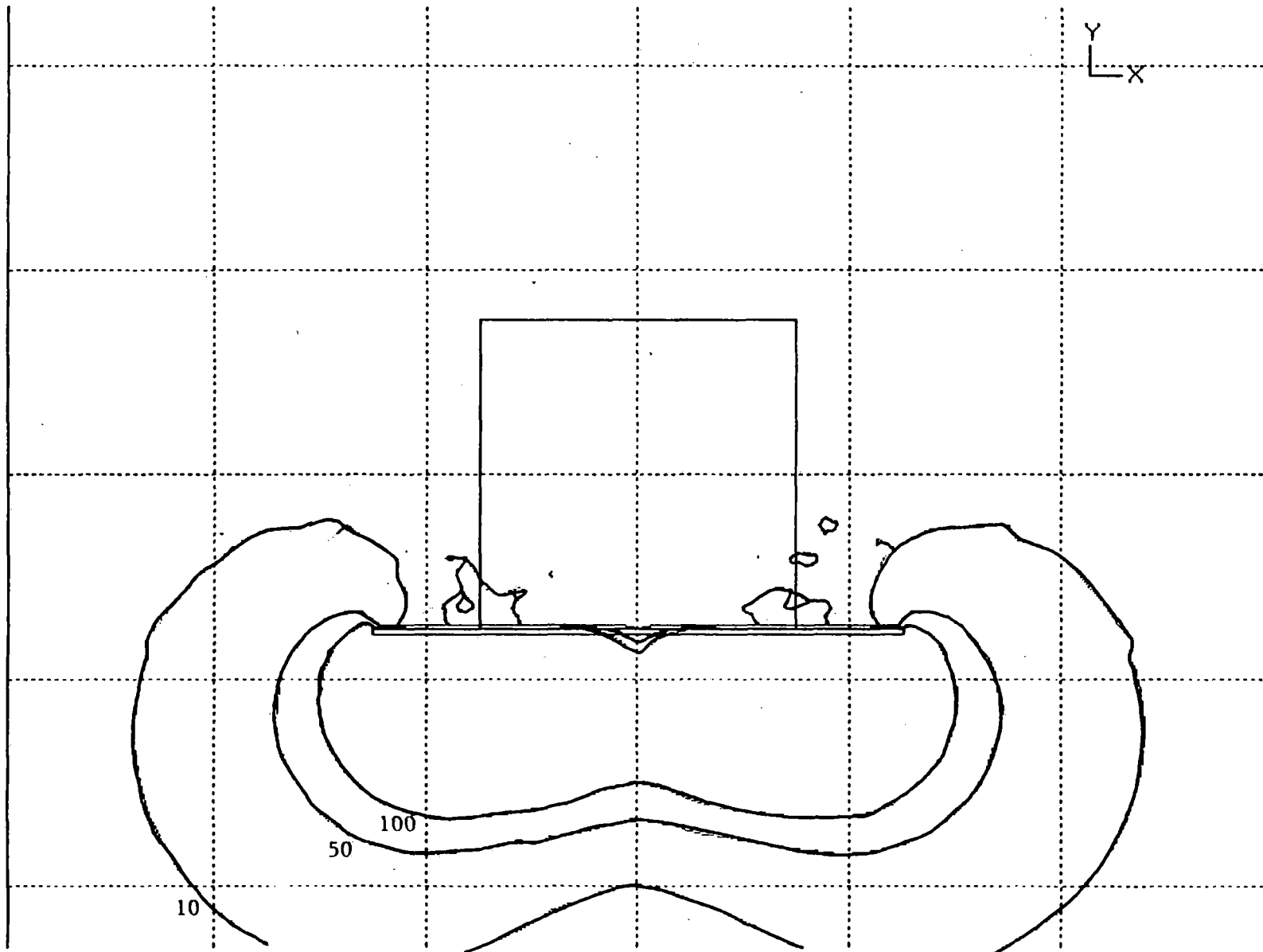


Figure 4.2.6. Thick (7 cm.) Plate With 1 Meter Extensions Flux Density Iso-Contours in Gauss.

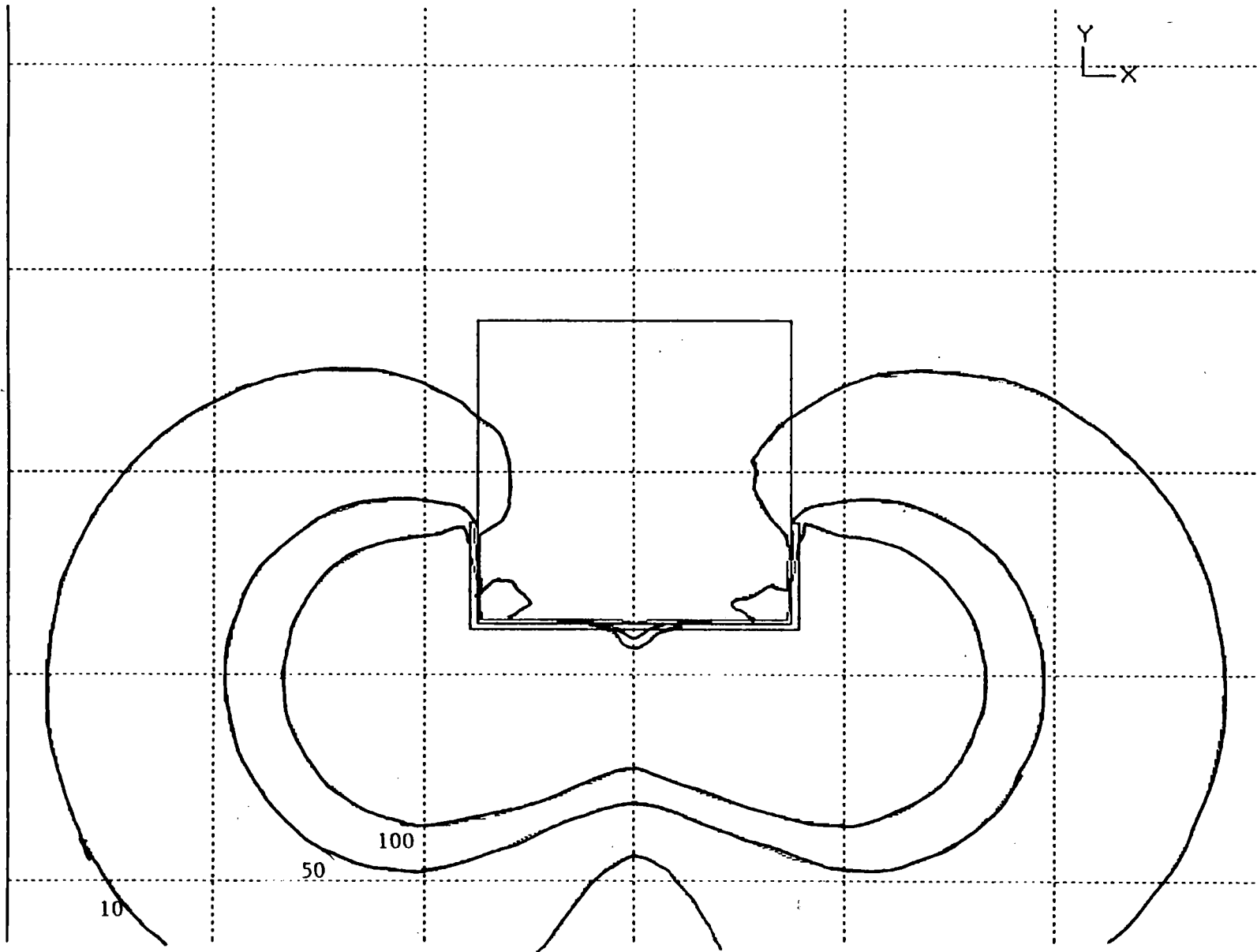


Figure 4.2.7. Thick (7 cm.) Plate With 1 Meter Side Shield Flux Density Iso-Contours in Gauss.

Channel-Shaped Shields around Coils

In a totally independent approach to shielding, a series of models were made in which the bulk of the iron material was applied to the outside of the cryostat vessel on three sides, forming a channel shape. This approach was chosen to determine if the desired flux density level in the vehicle could be achieved with less shield weight.

Initial models with relatively thin plates (2 cm thick) were totally ineffective. Models with 5 cm thick plates around the cryostats show that the plates do provide some reduction of the flux density in the vehicle, but not an appreciable amount. Figure 4.2.8 illustrates the geometry as well as the effect of the shield on the flux density in and around the vehicle, for a 5 cm thick channel shield with a 50 cm wide extension past the edge of the car. The iron shield is completely saturated near the coils. Since the iron is saturated, a thicker (7 cm thick) shield was modeled, resulting in an improvement as illustrated in Figure 4.2.9.

Because our previous experience in magnet shielding has convinced us that multiple iron shields separated by air gaps are more effective than single thick plates, a model was made with the 5 cm thick plates around the coil cryostats augmented with a 2 cm-thick plate under the vehicle. Figure 4.2.10 shows the geometry, along with a plot of flux density contours. For approximately the same weight as the 7 cm thick channel shield, this double shield is much more effective. The iron in the thin plate is saturated in a small area just above the coils, which is reflected in the fact that the bottom corners of the vehicle still contain flux densities greater than 100 gauss. In the next model an additional 2 cm-thick plate of width 30 cm was placed under the car edges to capture the magnetic flux escaping into the corners of the vehicle. This additional plate has the desired shielding effect, lowering the flux densities in the bottom corners of the car to the 50 gauss level, as illustrated in Figure 4.2.11. The approximate weight of this model is 15700 kg.

The channel-shaped iron shields around the coil cryostats do not adversely affect the field produced by the superconducting racetrack coils, which are required as part of the levitation, guidance, and propulsion systems. In fact, there is an enhancement of the field because of the close proximity of the iron. This field enhancement, of approximately 20%, allows a reduction of the superconducting coil current while meeting the design requirement. This allows a reduction of the stray field. The model of Figure 4.2.10 was solved with a 20% lower superconducting coil current. The field met the design requirements, and the high flux density in the bottom corners of vehicle was reduced to the 50 gauss level. This result is presented in Figure 4.2.12. The approximate weight of this shield is 15200 kg.

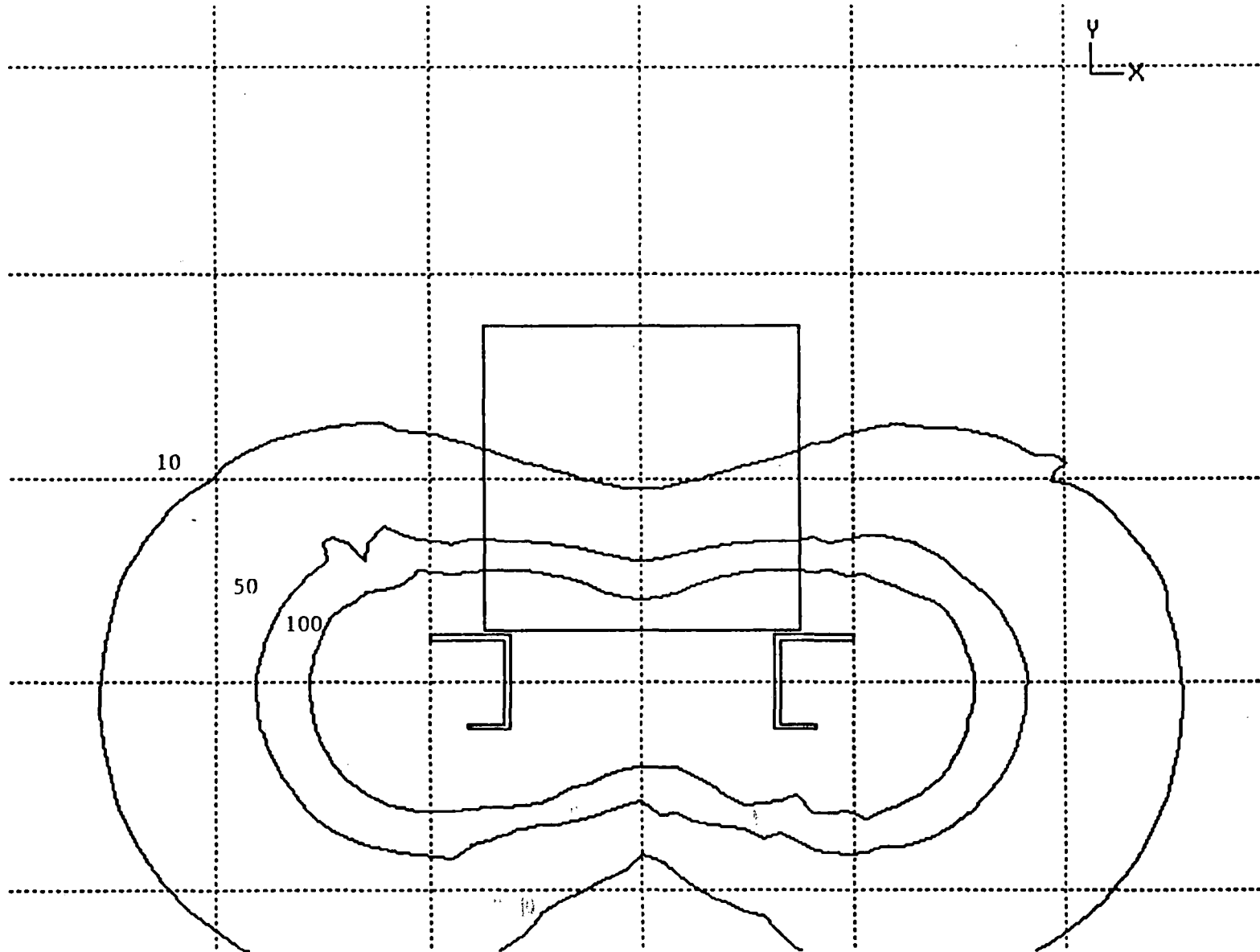


Figure 4.2.8. 5 cm. Channel With 50 cm. Extensions Flux Density Iso-Contours in Gauss.

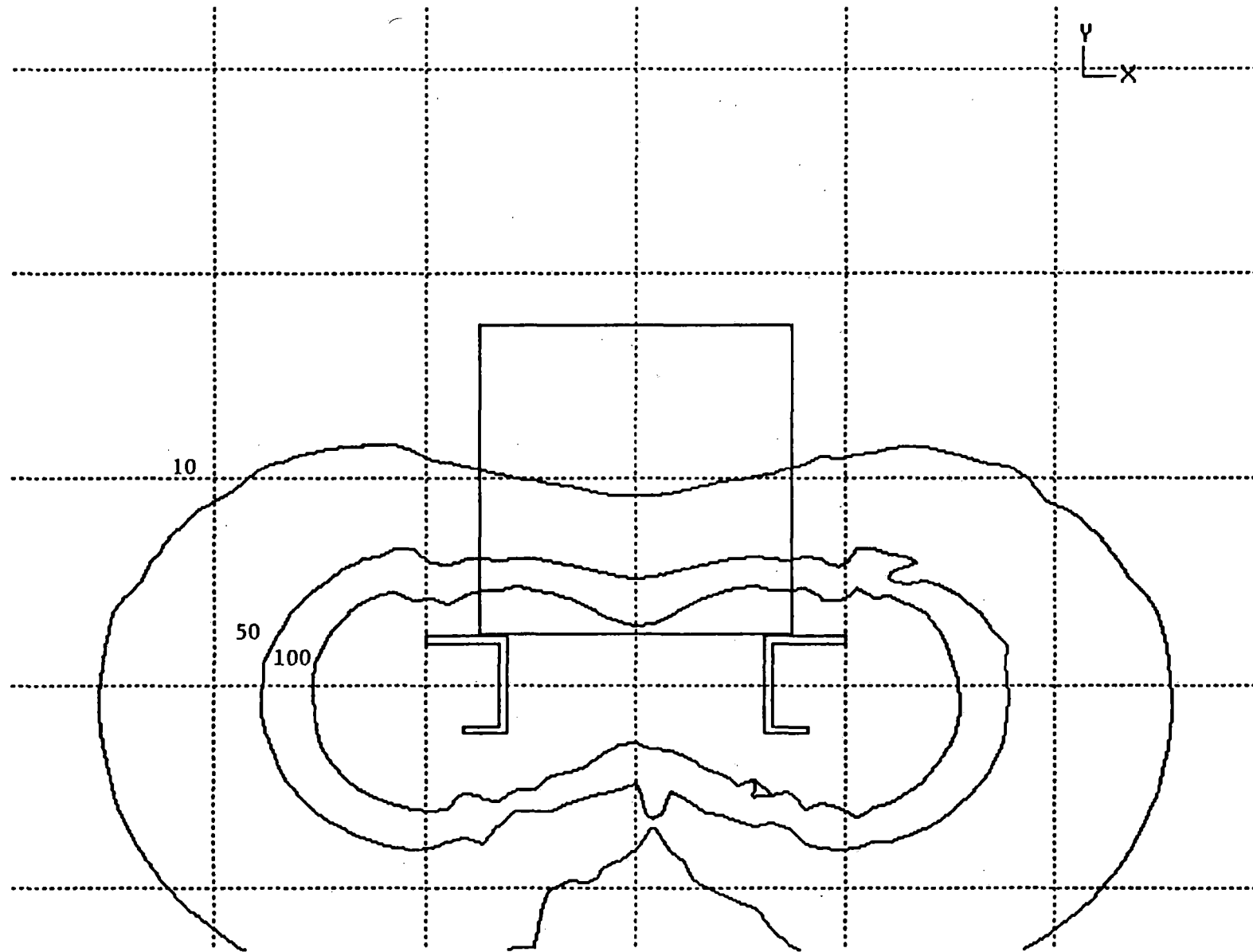


Figure 4.2.9. 7 cm. Channel With 50 cm. Extensions Flux Density Iso-Contours in Gauss.

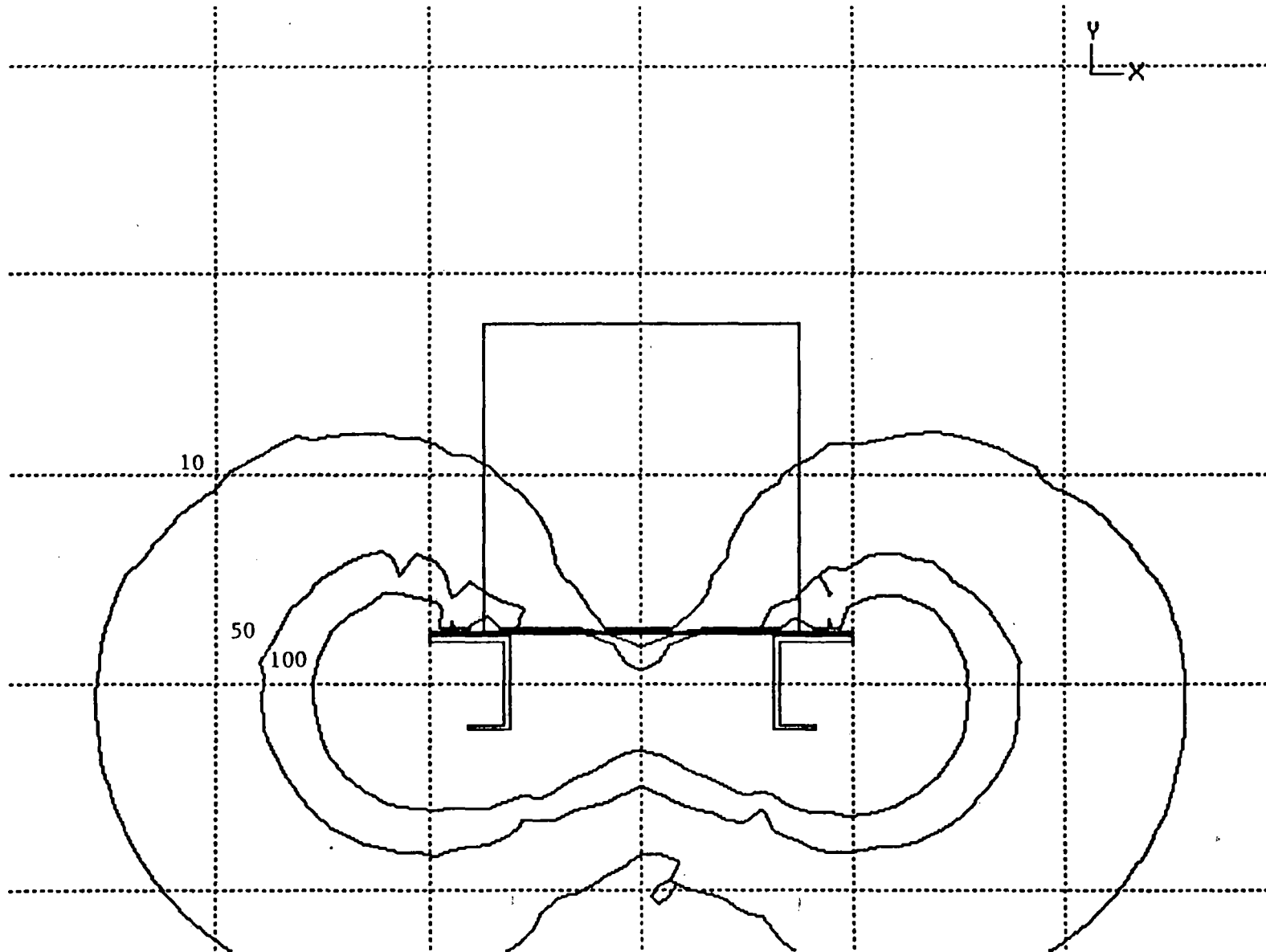


Figure 4.2.10. 5 cm. Channel + 2 cm. Plate With 50 cm. Extensions Flux Density Iso-Contours in Gauss.

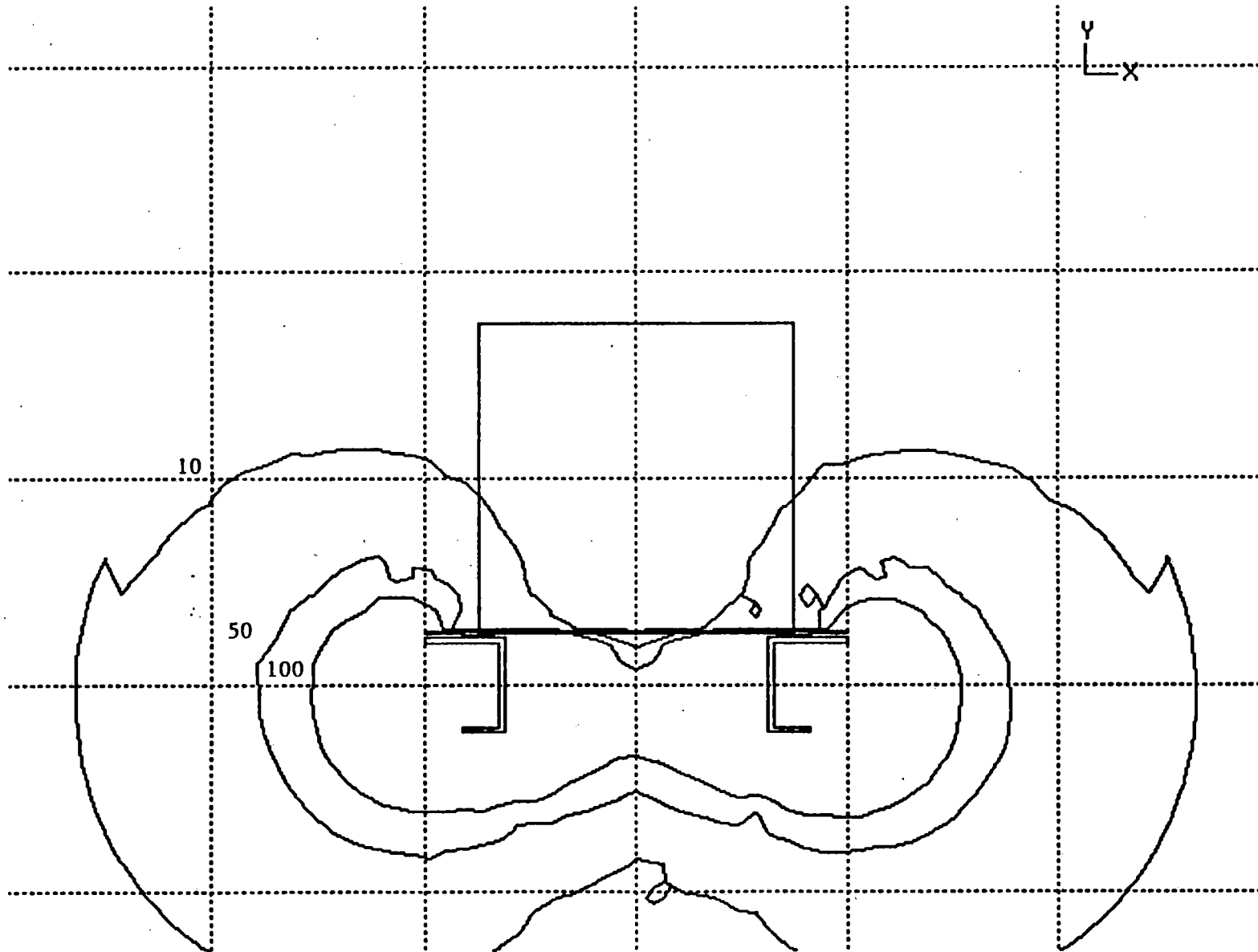


Figure 4.2.11. 5 cm. Channel + 2 cm. Plate With 50 cm. Extensions + Extra Corner Plate
Flux Density Iso-Contours in Gauss.

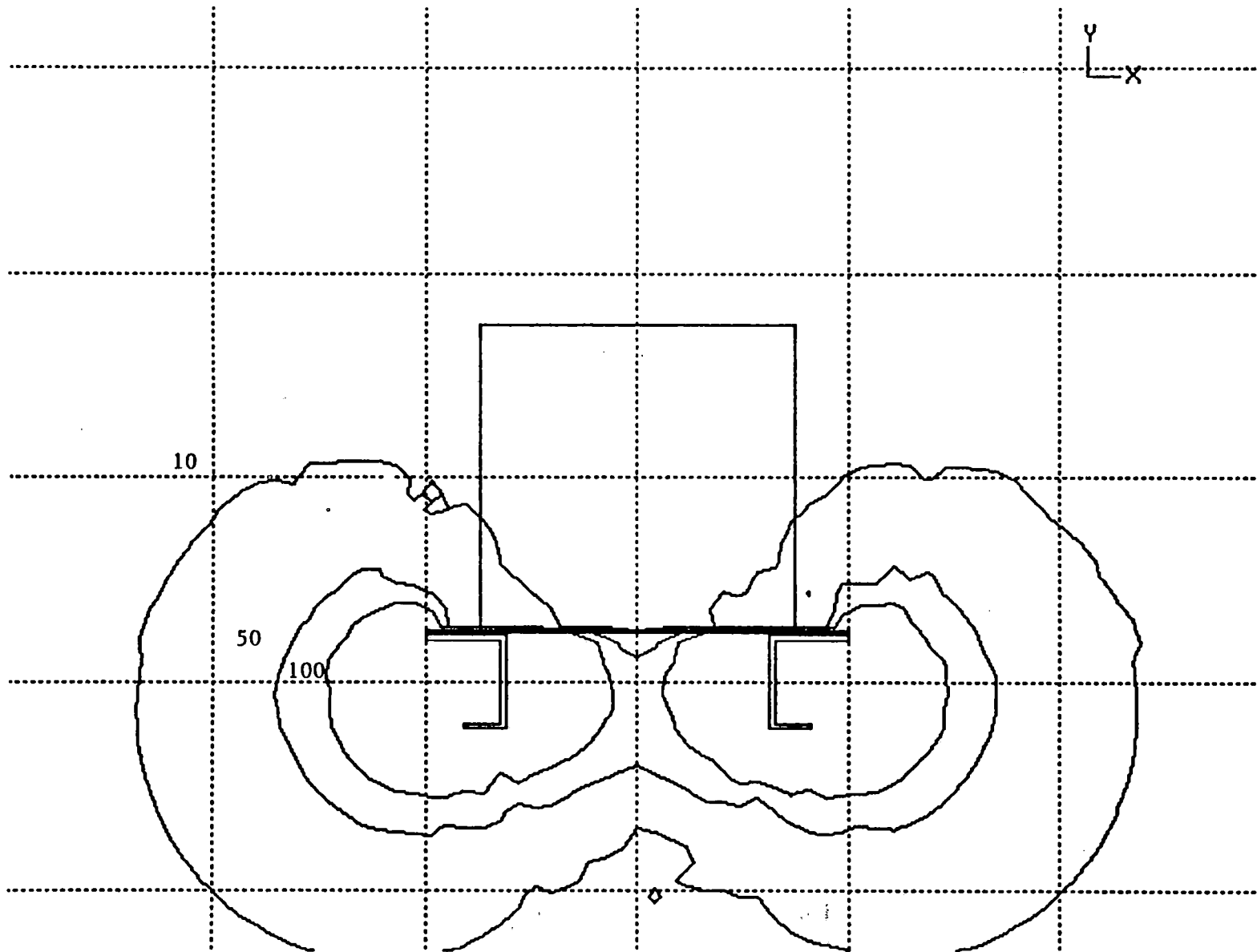


Figure 4.2.12. 5 cm. Channel + 2 cm. Plate With 50 cm. Extensions (Reduced Current 20%) Flux Density Iso-Contours in Gauss.

Repositioning the Vehicle

Another item of interest gleaned from these models is the variation in flux density level at different heights above the floor level, which reflects a reduction of flux density as one moves away from the coils. Figure 4.2.13 contains a plot of flux density level vs. distance above the floor of the car, through the region of highest flux density, for the unshielded vehicle. It can easily be seen that the flux density levels drop off quickly in the first half meter. Since the weight of iron needed to shield the vehicle is a critical issue, moving the vehicle higher is a reasonable approach.

To provide insight into the benefits of such a design modification without running interminable 3D analyses at 3 days apiece, it was decided to use two dimensional models to investigate shielding of the vehicle with the vehicle positioned at 0.75 meter above the top of the superconducting racetrack coils – a 0.5 m increase from the previous models. Some comparison models were made of models which had been solved with the three dimensional code. The field shapes in the cross-sectional plane compared quite well. In the unshielded model, at the vehicle floor the magnitude of the flux density was about 10% higher in the 2-D model as compared with 3-D. The flux density level also did not drop off as quickly in the 2-D model, e.g., at 1 meter above the floor, the flux density level was 90% higher in the 2-D model. Figure 4.2.14 shows the 2-D results of the unshielded model. In models which contained iron shielding, e.g., the model of Figure 4.2.10, the flux density level was approximately four times higher in the 2-D model as in the 3-D model. Figure 4.2.15 illustrates the 2-D results.

With these differences known, it was clear that our chosen two-dimensional model would give conservative results. In addition, it pointed out the gross errors which could be expected when using 2D models to model complex, fully 3D EM problems for maglev vehicle shielding. Various models were made of the raised vehicle. The channel shaped shields were not effective because most of the car requires only thin plates of steel.

A reasonably effective shield of plates on the bottom and sides of the vehicle was developed and is described here. The bottom of the car has plates of stepped thickness: 1 cm in the center, 3 cm at the edge. The vehicle sides also have stepped plates: 2 cm at the bottom, 0.25 cm near the top. A triangular wedge 2.5 cm on a side, placed at the intersection of the side and the bottom, provides additional iron material in the corner.

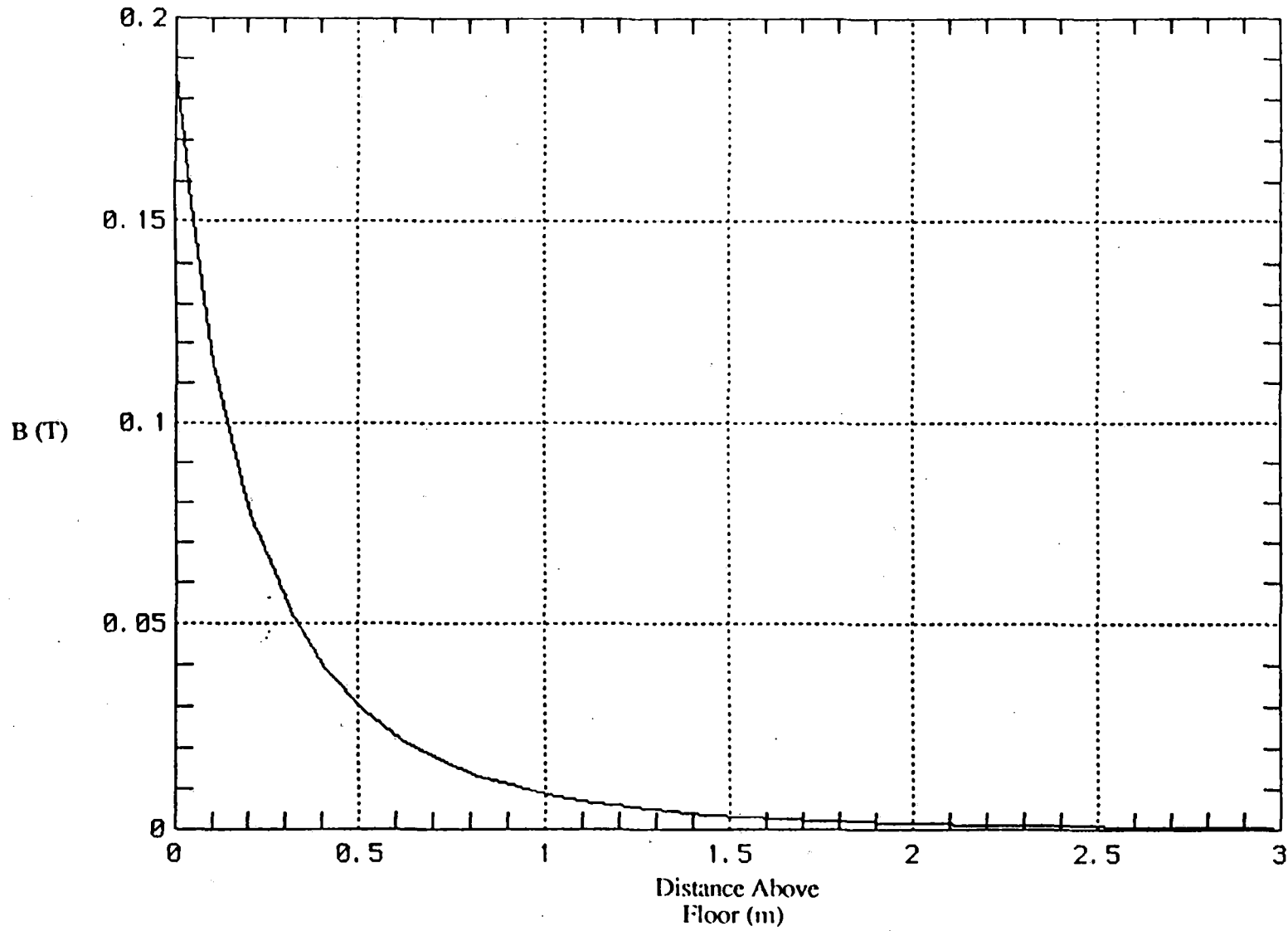


Figure 4.2.13. Flux density variation with vertical distance from coil set.

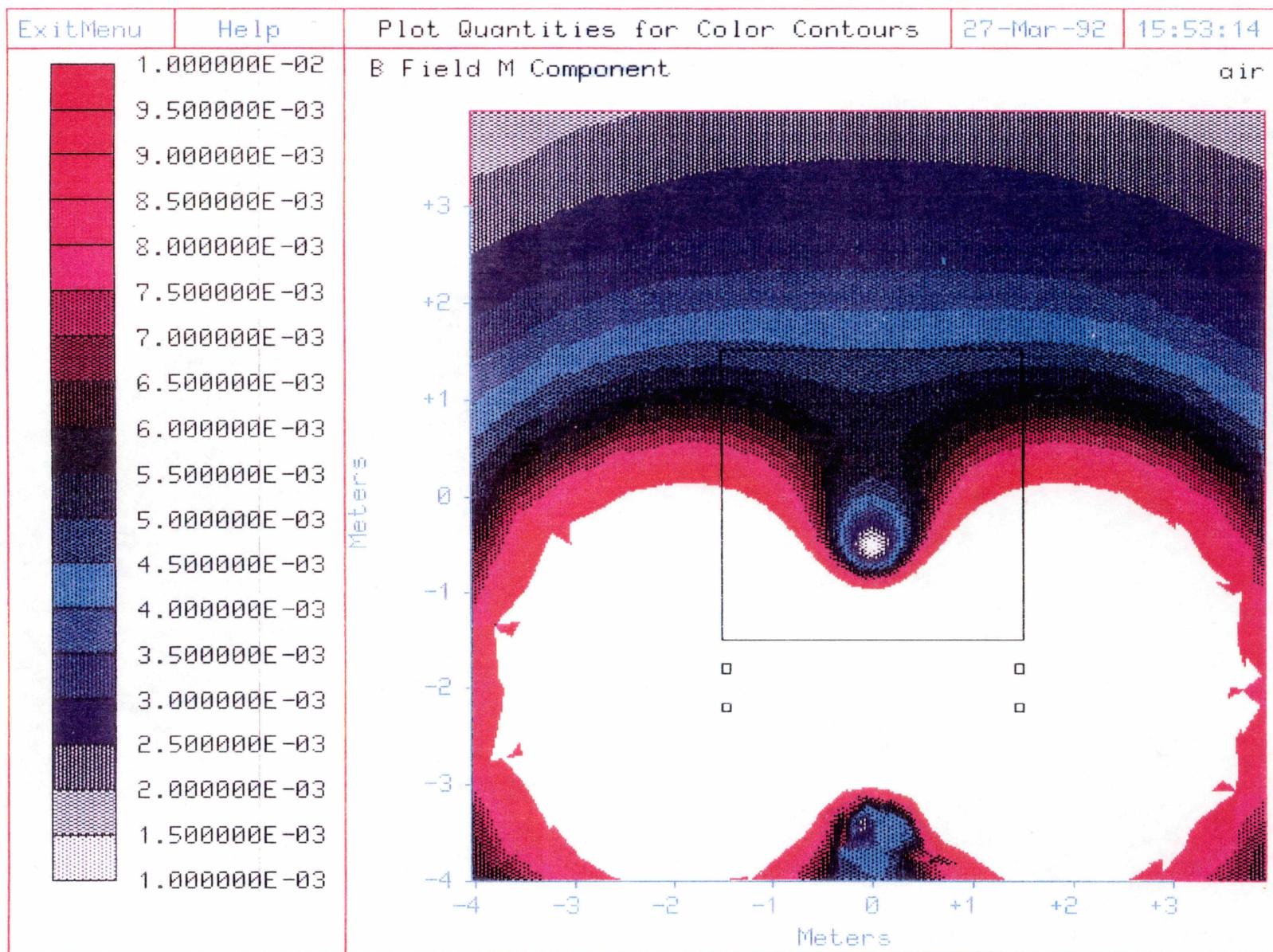


Figure 4.2.14. 2-D Model Without Shielding Flux Density Iso-Contours in Tesla.

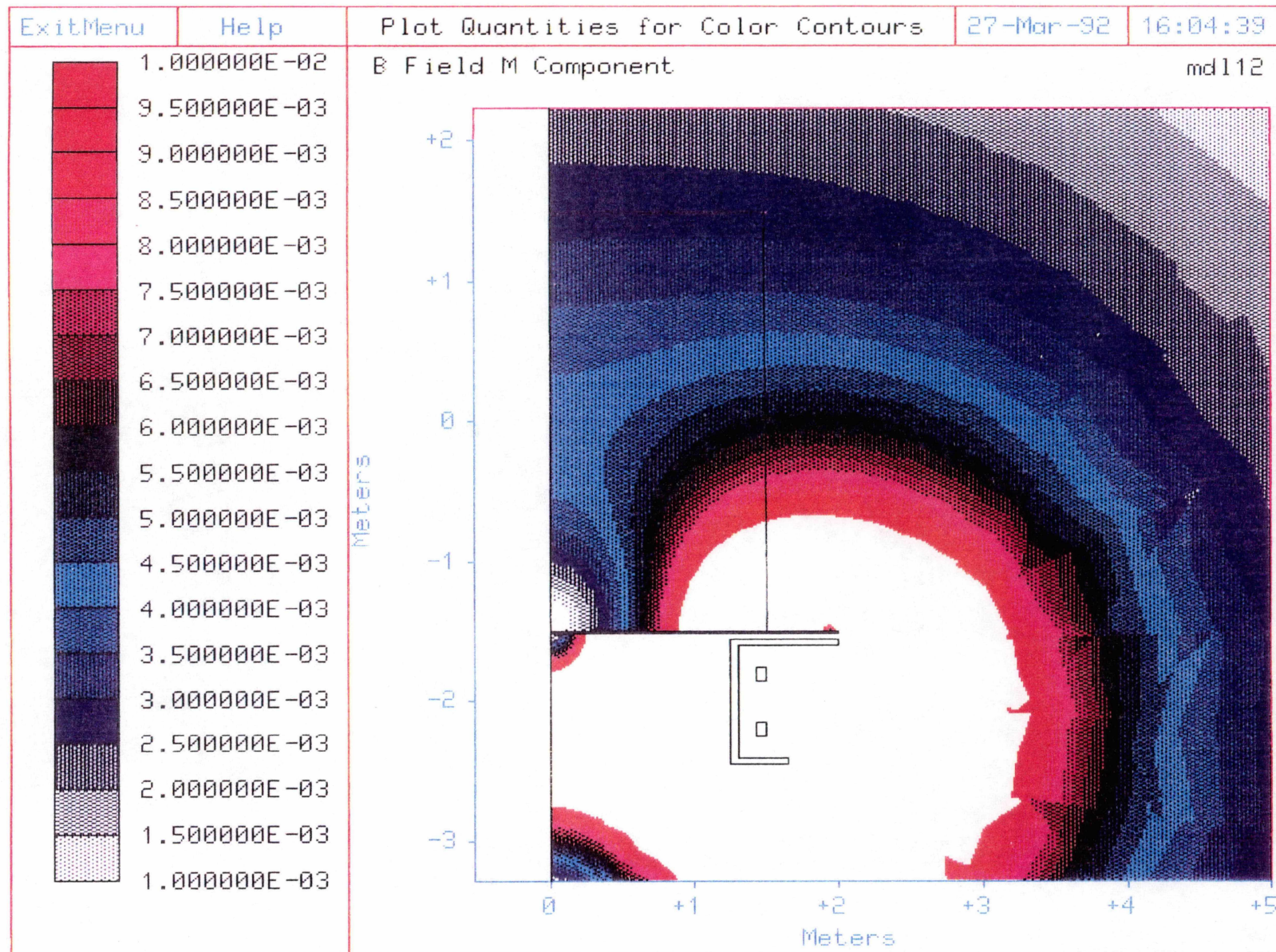


Figure 4.2.15. 2-D Half Model. Channel + Plate With Extensions Flux Density Iso-Contours in Tesla.

Figure 4.2.16 illustrates the results of a model with a side shield extending 1.5 m above the floor. Magnetic flux is seen to be "spilling" around the top of the shield and into the vehicle. In Figure 4.2.17 the side shield was extended another meter higher, to 2.5 m above the floor, correcting the problem. For this model, the flux density throughout the vehicle is below 35 gauss. The approximate weight of this model is a more reasonable, but still significant, 5600 kg. The two-dimensional model is very conservative and a three-dimensional model is required for comparison. It is obvious, though, that a significant weight advantage can be realized by moving the vehicle further above the coils. In addition, all the coil weights calculated for the models are conservative because a constant thickness was used for the length of 7 m. In reality, the thickness can be optimized in the third dimension.

4.3 Cost Estimate

The cost of passive shielding is not likely to be as much of an issue as its weight. In fact, even the excessively heavy 20000 kg shields would probably cost little more than \$50000 per vehicle. Active shielding, on the other hand, would increase the vehicle magnet cost by roughly 50 % if an additional row of coils were added, even if the number of ampere-turns in the shielding coils were somewhat less than that in the main coils. The cost of a magnet and cryostat is detailed in Section 5. As is noted in Section 5, the coil cost will not dominate the vehicle cost in any case. This is perhaps the most important conclusion of this study. Shielding issues will be dominated by the cost of the effects of the shielding choices, such as raising the vehicle and increasing frontal area and hence tractive power required, or by vehicle weight, rather than by cost.

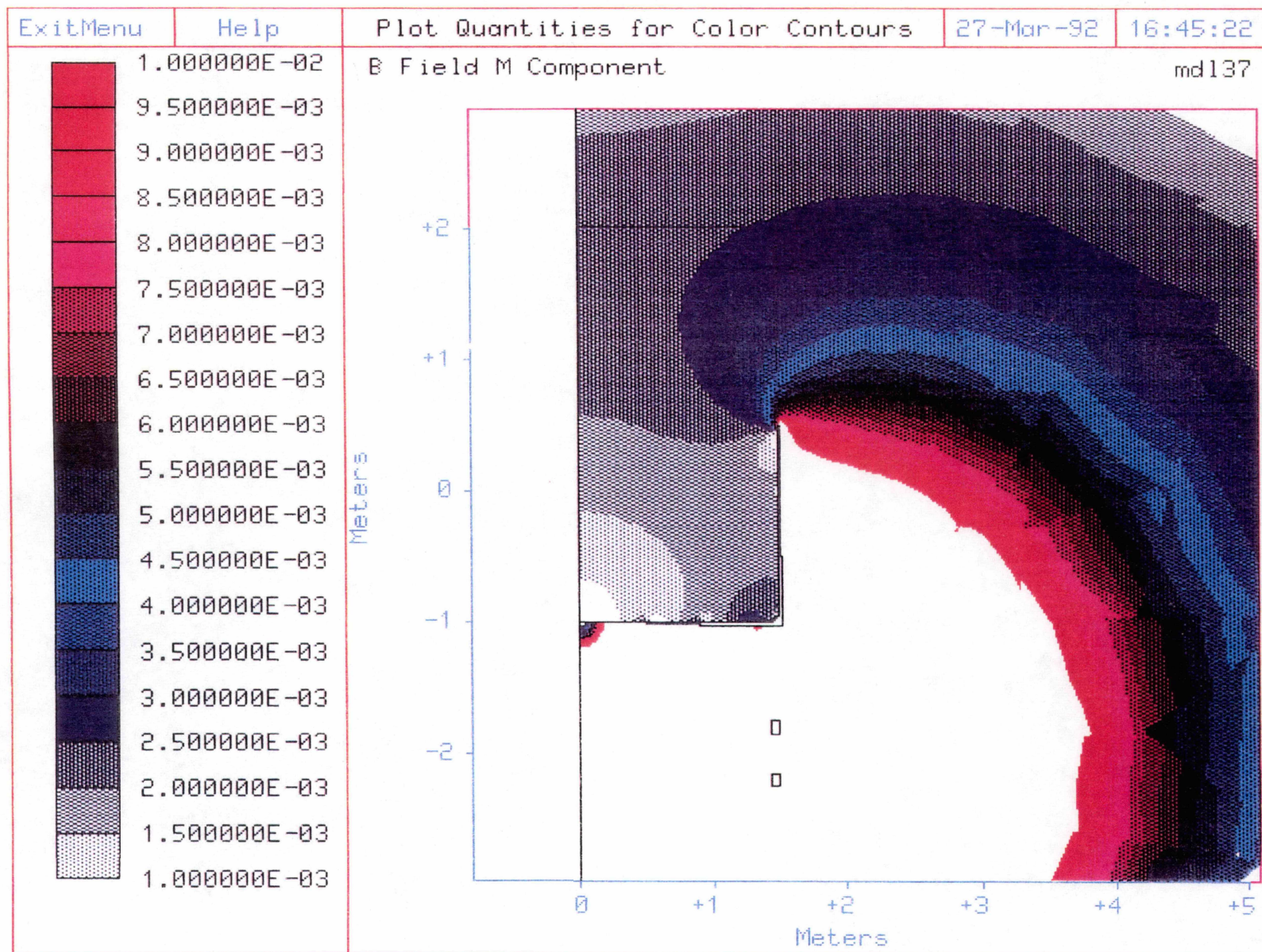


Figure 4.2.16. 2-D Half Model. Side Shield 1.5 m. High Flux Density Iso-Contours in Tesla.

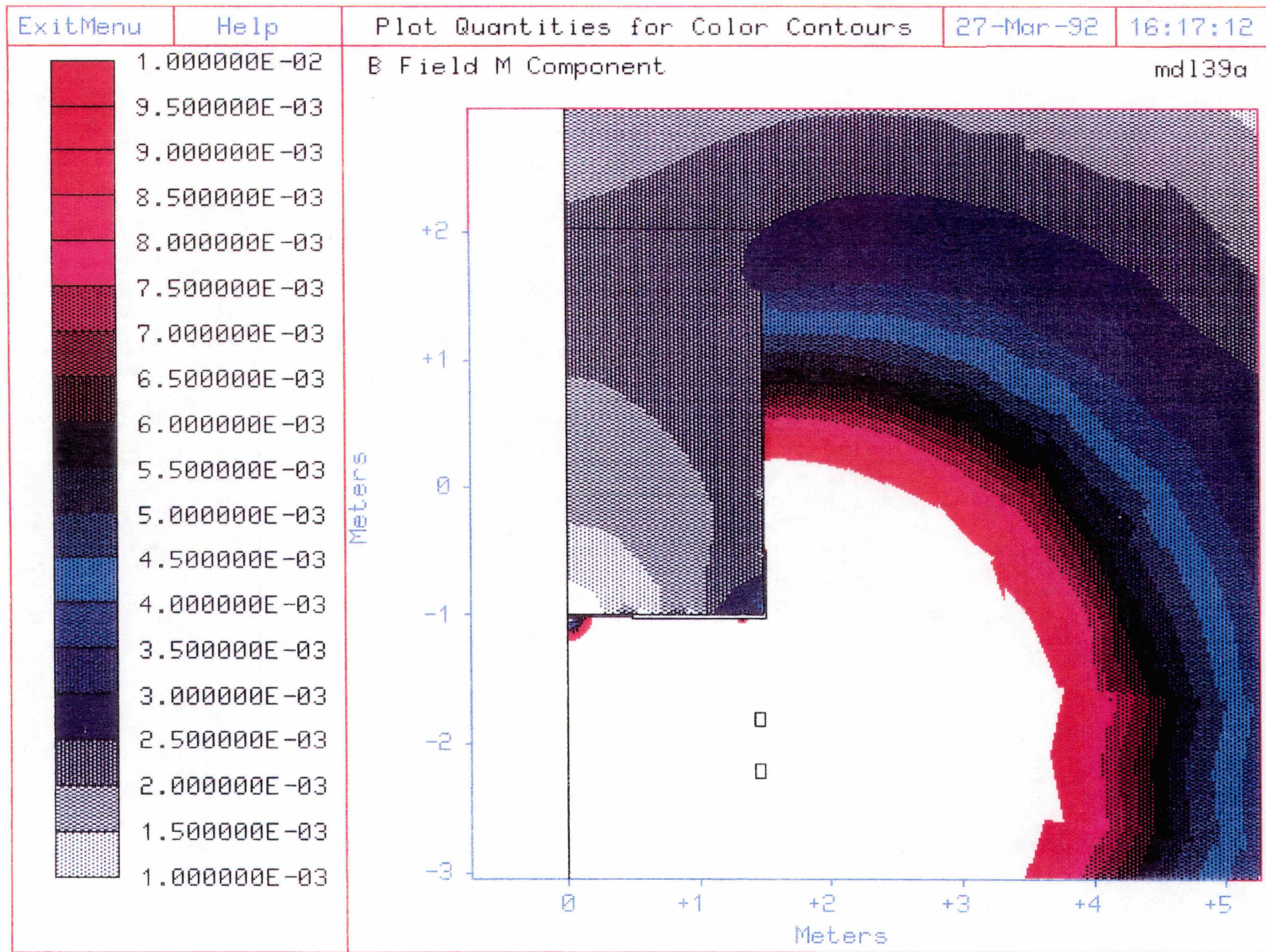


Figure 4.2.17. 2-D Half Model. Side Shield 2.5 m. High Flux Density Iso-Contours in Tesla.

SECTION 5: CRYOSTAT DESIGN

5.1 Structural Analysis

The structural analysis of the cryostat involves estimating the forces on the various cryostat members and the resulting stresses for the assumed design. The cryostat can be represented as a set of masses connected by support members. The individual deflections of the masses under the design loads must be evaluated to ensure that required clearances between members are maintained, and the deformations of the members caused by the location of the loads and reaction forces must be evaluated to ensure that the states of stress of the various members are within acceptable limits. The design involves the supports which will connect the coil and its support structure to the cryostat vacuum vessel. These supports must transmit the levitation, guidance and propulsion forces which act on the superconducting coil to the cryostat vacuum vessel, from where they are transmitted to the vehicle. In addition, there must be members which support the coil weight when the vehicle is resting on its auxiliary suspension at speeds below levitation speed.

For the purposes of this design, the forces that must be transmitted have been estimated from a cross section of the designs presented in the open literature. Specifically, the levitation force is taken to be 1.0 g, the guidance force 0.2 g, and the propulsion force 0.2 g. In all cases, a factor of safety is added to the support strengths to account for small variations of these forces from these values. The levitation (y-directed) force is based on simply maintaining the vehicle position, with the level of heave acceleration assumed to be small (≤ 0.05 g). The guidance (x-directed) and propulsion (z-directed) forces are based on the passenger comfort criterion, which most designs interpret as placing a limit at 0.2 g in either direction. The vehicle mass is taken to be 24000 kg, so a 1 g force corresponds to 235 kN. Therefore, the x, y, and z forces which the supports must transmit for an entire vehicle are 47, 235, and 47 kN, respectively. As for previous analysis, the coils are located, two to a magnet, in bogeys at the ends of each vehicle, with a magnet on either side of each bogey. Therefore, the forces from two magnets, or four coils, act on a typical mid-consist car. The forces which the coil supports must carry are therefore 12, 59, and 12 kN in the three coordinate directions.

The support design that has been developed consists of separate supports for each coil and avoids the difficulty of mechanically joining the coils and their support structures, which are each 2.5 m long, into a single stiff structure. These supports must not only carry the vehicle when levitation has been achieved, but they must carry the coil weight when the vehicle is riding on its auxiliary supports. We have chosen to transmit the vehicle levitation and propulsion forces using

one set of high strength members and to use a separate set of supports to carry the coil weight, which is small in comparison and in the opposite vertical direction. This approach allows the use of tension-only straps as these supports, which is advantageous from the design point of view when working with composites, as we will be. Another set of supports will transmit the guidance forces in the x direction. The physical positioning of the support members on the coil support structure is shown in Drawing A. Carbon fiber-reinforced composite straps are used for the y and z forces, while struts are used for the x forces. The former supports can carry only tension, and must be positioned accordingly, while the struts can carry both tension and compression.

These support members are added to the coil structural model, and we then superimpose the appropriate forces as body forces over the entire superconducting coil. While the forces are not actually distributed uniformly over the entire coil, the coil/support assembly is sufficiently stiff that this approximation is a good one. In actuality, the levitation and primary portion of the guidance forces act on the straight sides of the superconducting coil, while the drag forces act on the end turns. The loads on the straps and struts and the resulting deformations and deflections of important members of the cryostat and coil/support assembly will be computed using the 3-D structural finite element program ANSYS. The model for this problem comprises over 15000 nodes, runs for several hours on a Convex supercomputer and requires over 500 Mbytes of storage space for the stress solution alone.

A set of levitation supports, coil supports and guidance supports were designed to suspend the maglev magnet from the vacuum vessel. The levitation and the coil supports are chosen to be two tension-only Carbon-fiber reinforced epoxy strap members with a high pin diameter to thickness ratio for maximum strength. The guidance supports were specified to be tension-compression members of the same material. A 3D analysis was carried out when the train is completely levitated, and travels with maximum acceleration at a curve. The stresses in the support members and the coil and coil support structure were calculated and compared to the fatigue strength and the ultimate strength of the materials, respectively.

Special nomenclature for this section is described here: d_o represents the outer diameter of a tubular support member; d_p the pin diameter for a strap support pin; σ_b the breaking stress of a member; and σ_f the fatigue strength at 10^7 cycles.

5.1.1 Design of Suspension Members

Advanced composite structures are currently used as suspension members in numerous cryogenic systems [Morris 1982, 1989; Takeno 1985]. These lightweight members offer low

thermal conductivity, high strength and stiffness. A variety of fibers can be selected, like E-glass, S-glass, Kevlar, alumina, and carbon, depending on the required properties [Morris 1989]. In the application of a maglev train magnet, the material selection of the thermal isolator members is performed with the following objectives: (i) high fatigue strength (ii) high strength (iii) minimal heat leak. In this cryogen-free magnet system which is cooled by a two-stage cryocooler, the thermal conductivity of the thermal isolator members are examined in the following two ranges, that is 300-50 K, and 50-10K, which correspond to the first and second stage load, respectively. In the first temperature range E-glass and alumina are shown to have the lowest conductivity in reference [Takeno 1985]. In the second range carbon and alumina are shown to have the lowest conductivity in the same reference. If the only criterion was the low thermal conductivity, alumina fibers would clearly be the best choice. Examination of the fatigue strength of the fiber reinforced composites indicate that carbon composites are by far the strongest with a fatigue strength of 965 MN/m² at 10⁷ cycles [Morris 1989]. The corresponding fatigue strength of alumina and E-glass composites are shown to be 483 and 172 MN/m², respectively. Therefore, carbon-fiber reinforced epoxy structures are chosen for this system because of the superior fatigue strength of the material.

The design philosophy used to define the configuration of the thermal isolator members is to meet the fatigue and load requirements with a minimum cross-sectional area and maximum length within the cryostat dimensions. Typical shapes of these isolator members are tension-only straps, tension-compression tubes and struts and tension-compression-bending shells [Morris 1982]. Ultimate failure of tension-only strap members occurs at the straight leg-bend radius transition region by a combination of tension and bending. The strength of the strap is shown to be higher for high pin diameter to thickness ratio (d_p/t) [Morris 1989]. The typical fatigue strength to ultimate strength ratio for S-glass straps is shown to be about 0.25, at 10⁷ cycles [Morris 1982]. Ultimate failure of tension-compression struts occurs at the location of the lowest cross-sectional area by pure tension. Typically this failure mode occurs at much higher stress levels.

In this application of the maglev train magnet, three sets of thermal isolator suspension members were used. They consist of the levitation supports, the coil supports and the guidance supports presented in Table 5.1.1. The levitation supports are chosen to be two tension-only strap members. A high pin diameter to thickness ratio (d_p/t) of 14.23 is chosen for maximum strength. The width (w) of the levitation support straps was chosen to be smaller than the pin diameter of the strap (d_p) such that the straps can cross each other if they are rotated by 90 degrees. This allows the gap between successive coils to be as small as possible. For a complete vehicle levitation, the tensile stress on the straps is calculated to be 300 MN/m².

The guidance supports are chosen to be three tension-compression strut members. For a typical axial acceleration of ± 0.20 g, the stress is calculated to be ± 70.8 MN/m².

Member	d_p or d_o	w	t	A	L	σ_b σ_f
mm	mm	mm	mm ²	m	MN/m ²	MN/m ²
Levitation supports						
31.75	25.4	2.23	113.17	0.5	2350.0	587.5
Coil supports						
25.4	2.04	1.27	51.81	0.159	2555.3	638.8
Guidance supports						
12.70		1.5875	55.42	0.05	3503.0	965.3

Table 5.1.1. Dimensions and estimated properties of the suspension members

5.1.2 Analysis

A stress analysis was carried out on a full three-dimensional model of the magnet, which is shown in Figure 5.1.1. The model consisted of the superconducting coil, an aluminum collar, two side plates and a set of three suspension members. The dimensions of the support structure were determined in a previous chapter. It must be noted that, the straps are tension-only members assembled with no pretension. Therefore, in the case of compression they will become loose providing zero stiffness.

The first analysis dealt with the cooldown and electromagnetic forces caused by the coil itself. The second analysis included the cooldown, the electromagnetic forces caused by the coil itself, the levitation force of 1 g, the guidance force of 0.2 g and a propulsion force of 0.25 g. The levitation, guidance and propulsion forces are uniformly distributed on all the nodal points of the coil and superimposed on the electromagnetic forces caused by the coil itself. The stress analysis results are presented in graphical form in Figures 5.1.2 and 5.1.3, and tabular form in Tables 5.1.2 and 5.1.3.

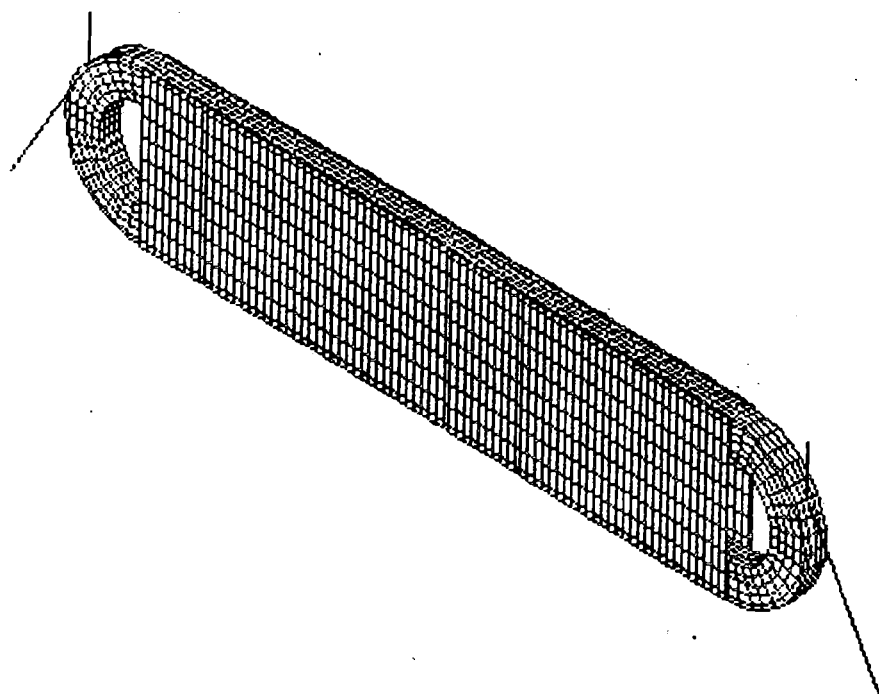


Figure 5.1.1. 3-D Finite element model of magnet assembly.

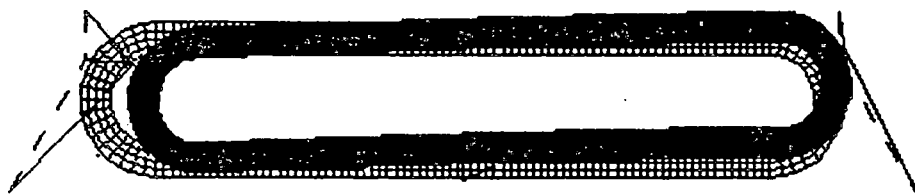


Figure 5.1.2. Displacement plot for case 2.

Case	a_x	a_y	a_z	Coil Composite			Aluminum			u_x	u_y	u_z
				Hoop Stress	Axial Stress	Radial Stress	Von Mises	Stress in MN/m ²	in mm			
1	0.0	0.0	0.0	-80.4 to 45.3	-0.72 to 21.3	-46.8 to 13.4	2.09 to 157.0	-4.08	-1.69	0.91		
2	0.25	1.0	0.2	-31.0 to 23.3	-0.45 to 20.3	-51.7 to 12.4	2.57 to 180.0	9.48	4.14	2.85		

Table 5.1.2. Stresses in the coil and aluminum of complete assembly

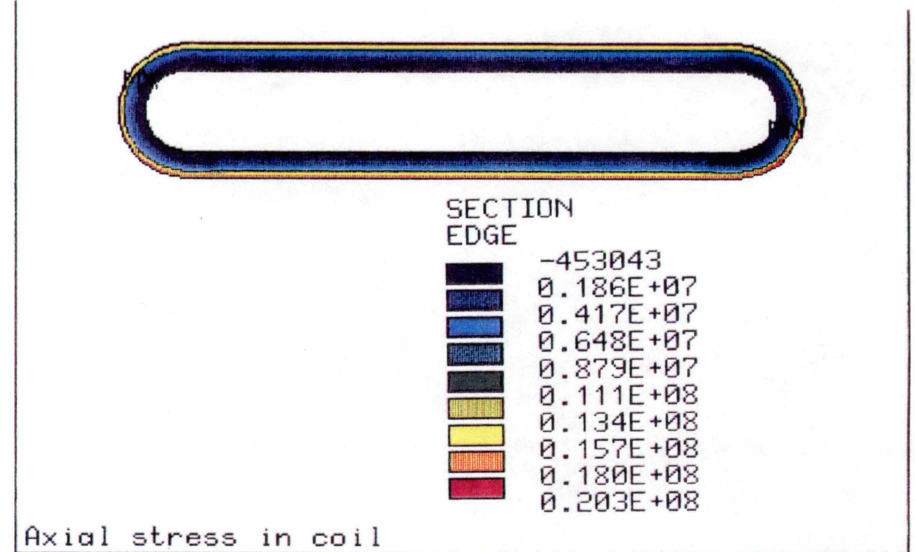
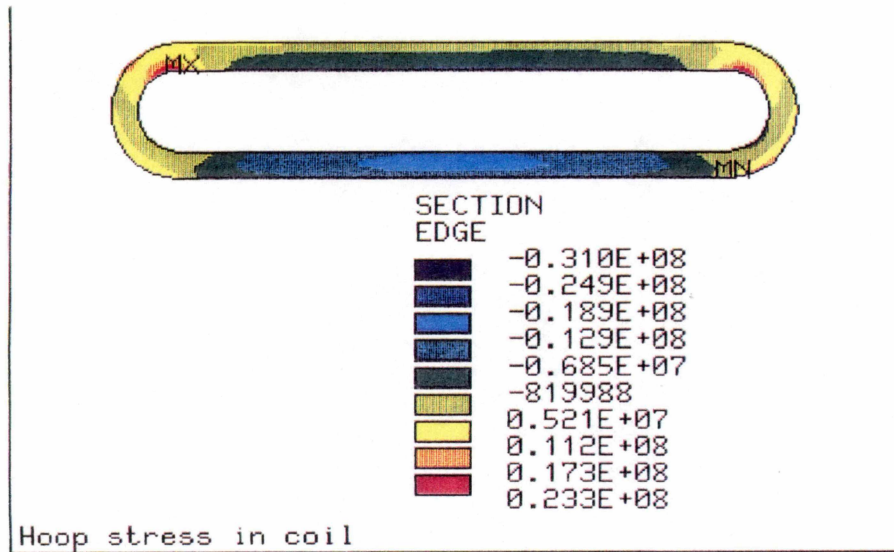
%	Member	Case 1	Case 2
	Stress in MN/m ²		
	Levitation supports		
1	209.6	306.88	
2	209.6	566.6	
	Coil supports		
1	396.5	0.00	
2	396.5	519.19	
	Guidance supports		
1	0.0	-259.7	
2	0.0	-259.7	
3	0.0	-259.7	

Table 5.1.3. Stresses in the suspension members

The two cases analyzed represent the extreme conditions under which the magnet operates. The first case represents the state at which the train is at a complete stop at the station, with the magnets energized. The second case represents the state at which the train is completely levitated, and travels with maximum acceleration at the worst turn.

The stresses in the levitation and coil supports, presented in Table 5.1.2, reach a maximum value of 566.6 and 519.19 MN/m², respectively, which is lower than the fatigue strength of the straps at 10⁷ cycles. In Case 2, the first coil support becomes loose since it cannot withstand any compression.

The maximum stress in the guidance support struts is shown to be ± 259.7 MN/m², depending on the sign of the guidance force. This yields a stress ratio of -1, for which in general, the fatigue strength is the lowest. Therefore, conservative fatigue criteria must be used.



160

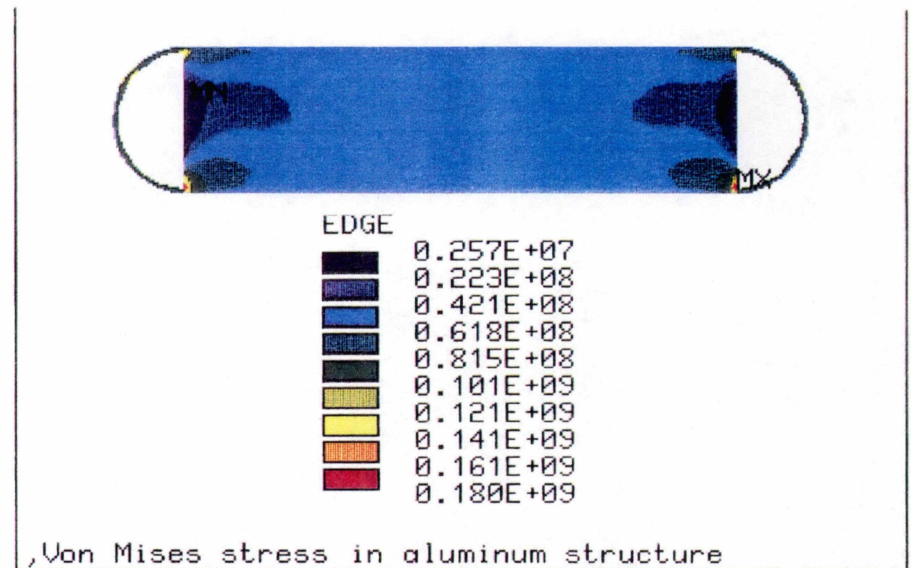
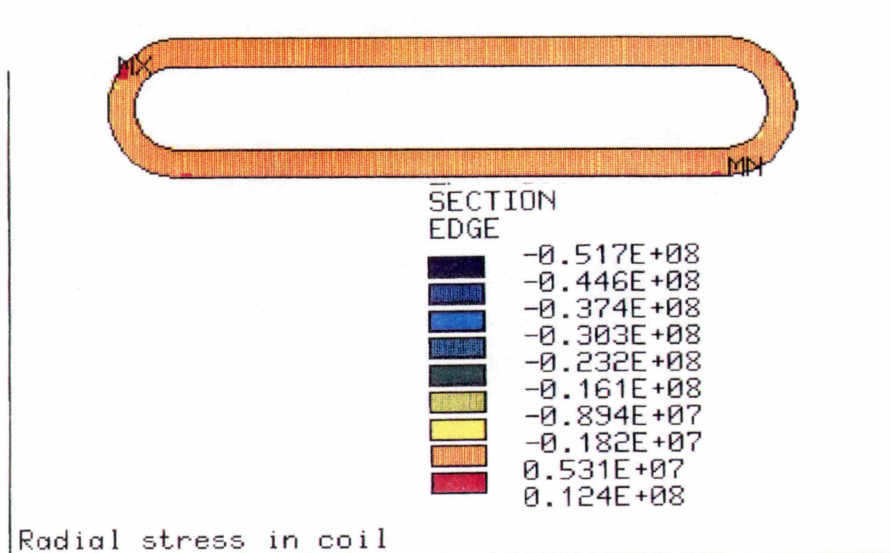


Figure 5.1.3(a-d). Hoop (a), Axial (b), Radial (c) coil stresses and von Mises (d) aluminum

The displacement plot presented in Figure 5.1.2 shows the deformation of the coil combined with the rigid body motion caused by the levitation, the guidance and the propulsion forces. The maximum and minimum stresses for both cases, are presented in Table 5.1.2. A close examination of the tabulated stresses indicated that they are below the strength of the associated material, which were tabulated in a previous chapter. The average stress distribution in the cross-section of the coil and aluminum support structure are presented in Figures 5.1.3. The radial stress is shown to be uniform, with an average value of 17.45 MN/m^2 . The hoop stress is shown to be maximum at the location where the curved section meets the straight section of coil. The axial stress in the coil is tensile throughout, with a maximum value of 20.3 MN/m^2 . The von Mises stress plot of the aluminum support structure clearly shows the stress concentration at the joint of the side plate to the collar. It has a maximum value of 180 MN/m^2 .

5.1.3 Conclusions

A set of levitation supports, coil supports and guidance supports were designed to suspend the maglev magnet from the vacuum vessel. The levitation and the coil supports are chosen to be two tension-only Carbon-fiber reinforced epoxy strap members with a high pin diameter to thickness ratio for maximum strength. The width of the levitation support straps was chosen to be smaller than the pin diameter of the strap such that the straps can cross each other if they are rotated by 90 degrees, allowing the gap between successive coils to be as small as possible. The guidance supports were specified to be tension-compression members of the same material. A 3D analysis was carried out when the train is completely levitated, and travels with maximum acceleration at a curve. The stresses in the support members and the coil and coil support structure were calculated.

Drawing A is an engineering layout showing all pertinent superconducting coil, coil support structure, and cryostat parts.

5.2 Thermal Analysis Including Refrigeration

The heat inputs to the cryogenic system are an important criterion in defining the design. Refrigeration requirements are based on these heat inputs, and these requirements in turn determine the types of cooling system the cryostat designer can possibly employ. Since our present study is predicated on the use of a two-stage Gifford-McMahon (GM) cryogenic refrigerator ("cryocooler"), the analysis presented here will proceed accordingly.

A two-stage GM cryocooler operates with helium gas as a working fluid, with the gas pressure and temperature following the Gifford-McMahon regenerative thermodynamic cycle [Gifford 1966]. The cryocooler consists of two mechanically separate parts – a compressor and a

cold head. The compressor, which may be of any workable design including rotary, reciprocating, scroll, or linear, brings helium gas at room temperature up to the desired high pressure, typically about 1.7 MPa. This high-pressure gas passes into the cold head through transfer lines, which can be long to allow mechanical separation of the two units, where it undergoes the rest of the cycle. This cycle includes a regenerative step where the gas exchanges heat with a high heat capacity material such as lead at low temperature. The low pressure gas then returns to the compressor through another line. The cold head provides two stations at which heat can be removed, referred to as the first and second stage stations because of the two-stage nature of the thermodynamic cycle. The second stage is the colder of the two, but significantly less heat can be removed there.

An important distinction of this cycle from that required for a helium reliquefier or recondenser is the absence of a Joule-Thompson (J-T) loop and valve. The J-T loop is an additional thermodynamic cycle required to cool the gas to below the GM cycle bottoming temperature of about 6 K. However, the small aperture size of the J-T valve typically leads to fouling with entrained oils that are typically used in compressor lubrication, which limits the mean time between failure (MTBF) of such a system to a few hundred hours. By contrast, the MTBF of a GM cryocooler is typically around 10,000 h. This important difference can lead to a dramatically improved system reliability and availability. In fact, the reliquefaction of helium has been evaluated for MRI systems by GE, and the difficulties with the required devices led us to eliminate plans for commercial introduction. By contrast, the GM cryocooler is widely used in the MRI industry as a shield cooler, which removes the conduction and radiation heat loads from the thermal radiation shields. While it would be desirable to improve the 10,000 h MTBF, and increases in cryocooler performance and reliability are being pursued, the GM cryocooler is clearly a commercially viable product. In addition to the issue of reliability, another difference between the G-M systems and reliquefiers is size and weight. While direct comparisons are necessarily difficult, and complicated by the different low temperatures provided by the cycles, a rough comparison was made by researchers at GE. The specific weight W_s and specific volume V_s , in kg/W and m^3/W , respectively, for G-M cryocoolers with a second stage cold temperature of 10 K and for Brayton cycle reliquefiers with a J-T loop and a 4 to 4.5 K low temperature can be given by the equations:

$$W_s (\text{G-M}) = 127Q^{-0.337}$$

$$W_s (\text{Brayton}) = 479Q^{-0.374}$$

$$V_s (\text{G-M}) = 0.23Q^{-0.431}$$

$$V_s (\text{Brayton}) = 1.05Q^{-0.325}$$

where Q is the cooling capacity at the low temperature. Solving these equations for a 2 W cooling capacity, which our magnet design calls for, we obtain weights of 100 and 370 kg and volumes of 0.17 and 0.84 m³ for the G-M and Brayton machines, respectively. Clearly the advantages of the G-M machine extend beyond reliability and include size and weight as well.

The performance of a GM cryocooler depends on the regenerator materials used and on the efficiency of the compressor, but systems are readily available which operate with an electrical power input of 5 kW and simultaneously provide 3 W of cooling at 9.5 K and 50 W at 42 K. The map relating the temperatures of the two stages to the heat inputs is referred to as a load map; Figure 5.2.1 presents a typical load map for a commercially available system. In this figure, the abscissa represents the first stage temperature and the ordinate the second stage temperature. Grid lines are drawn on the graph for various heat inputs to the first and second stages, with the intersections of the lines representing points at which the cryocooler performance was measured. The operating temperatures at intermediate points may be estimated from the load map.

The first step in the thermal design of a refrigerated magnet is to estimate the expected heat inputs to the cold mass and the thermal radiation shield. These heat loads determine the operating temperature of the cold head stations. The operating temperatures of the cold mass and thermal radiation shield will necessarily be somewhat higher than those of the cold head stations because of temperature differences across the thermal joints connecting the cold head to the cryostat components. This issue will be treated in more detail in a subsequent subsection describing the cryocooler interface, which connects the cold head to the cryostat. In addition, there will be temperature variation around the coil and shield because of the disparate locations of the point heat sink at the location of cold head attachment and the point heat inputs at the mechanical supports and distributed heat fluxes from radiation and residual gas conduction. The estimation of the first and second stage heat loads for our proposed cryostat design is presented here and will be followed by an estimate of the coil and thermal radiation shield operating temperatures. The heat loads on the radiation shield and cold mass are treated separately and are broken down by the mode of heat transfer.

3 WATT LEYBOLD CRYOCOOLER

(March 23, 1992)

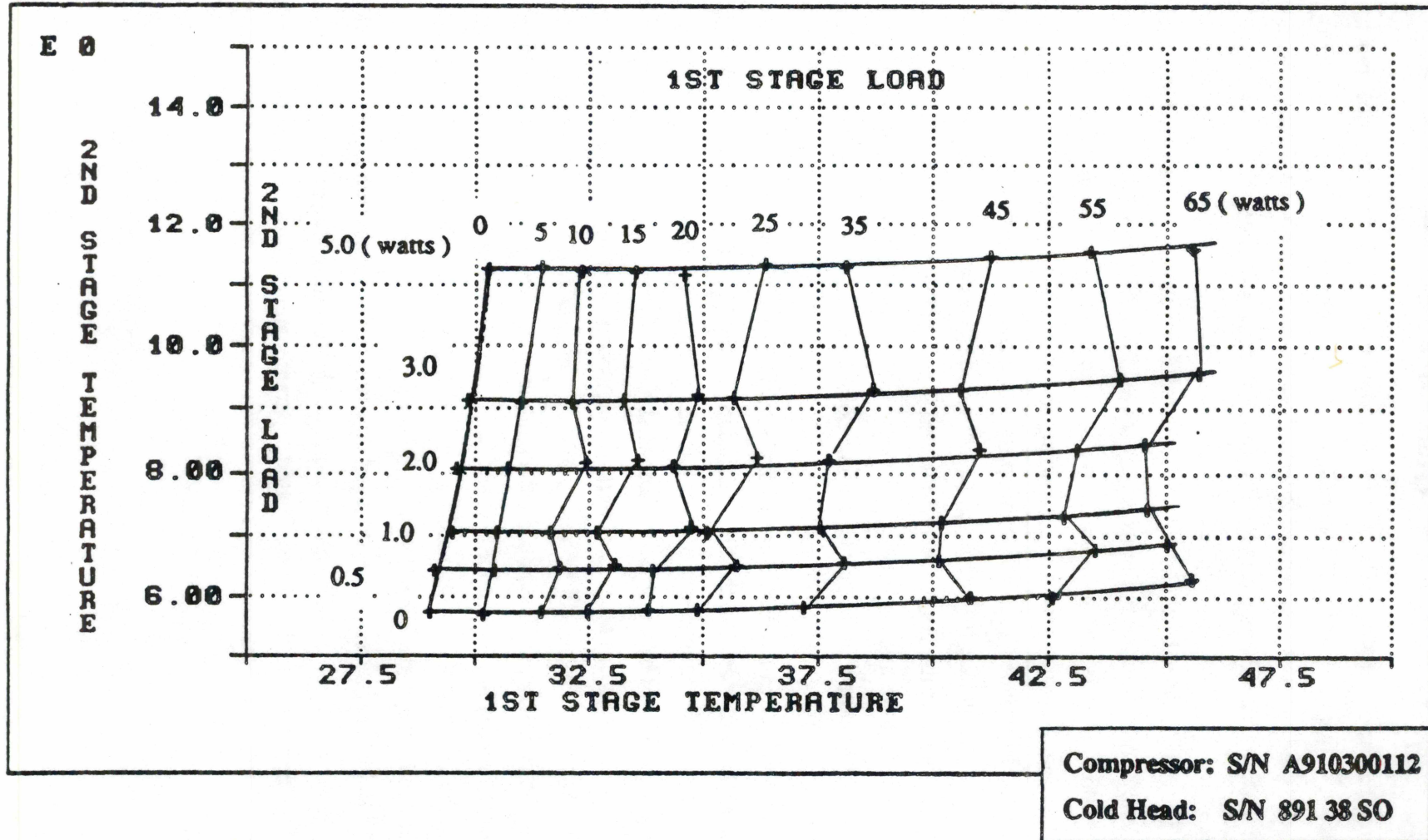


Figure 5.2.1. Load map for 5 kW G-M cryocooler.

We have assumed that a cryostat will enclose two coils regardless of the distribution of the coils along the vehicle. Since the proposed superconducting coil design is already very long, we feel that attempting to put more than two coils in a cryostat would be excessively problematic and costly – indeed, even the use of a single cryostat for two coils of such length leads to a cryostat length in excess of 5 m. The design of the cryostat is shown in Drawing A.

A major challenge in the implementation of a refrigerated magnet is the design of the cryocooler interface, which removes the heat from the cold mass and thermal shield. This interface has to perform several functions while being compact. First, since the cold head requires periodic maintenance (on the order of yearly), the interface should allow the cold head to be removed without breaking the cryostat vacuum. Indeed, the preferred design actually has openings allowing two cold heads to be connected to the thermal shield and cold mass simultaneously. Both may be used for the initial cooldown of the magnet, when the removal of large amounts of energy is required, and only one used for steady state operation. When the cold head in use must be removed for servicing, the other cold head may be engaged to cool the magnet. In this fashion, the system down time for cryocooler maintenance is eliminated. In addition to allowing this cold head removal, the interface must accommodate the current leads for the magnet. As will be shown in the following thermal design study, the bulk of the heat input to the cold mass and a significant amount of that to the thermal shield, come down these leads.

5.2.1 Thermal Radiation Shield

Radiation

Radiation heat transfer is the dominant mode in vacuum-jacketed cryostats. In order to minimize this heat transfer, a product referred to as superinsulation is commonly used. Superinsulation, also referred to as multilayer insulation or MLI, is a thin film, typically Mylar[®], which has a very thin layer (a few angstroms) of aluminum deposited on one or both sides. By wrapping a vessel in many layers of this material, the thermal radiation to the vessel is reduced greatly from that which would exist otherwise. It has been shown [Halaczek 1986] that the radiation through multilayer insulation from ambient temperature (nominally 300 K) to a shield operating at a temperature between 40 and 80 K can be represented by an equivalent conduction equation as

$$\dot{Q} = k_{\text{eff}} \frac{A}{t} DT \quad (5.2.1)$$

where \dot{Q} is the heat input in W, k_{eff} the effective thermal conductivity of the insulation in W/cm-K, A the vessel area in cm², t the thickness of the MLI layer in cm, and DT the temperature difference

between the ambient and cold vessels. For typical MLI applications in the temperature range of interest for this application, a conservative value of k_{eff} is 1.0 mW/cm-K [Halaczek 1986]. With a vessel area of approximately 10 m² and an MLI thickness of 1 cm, a thermal radiation shield operating at 40 K will receive 26 W of radiation from ambient.

Conduction

i) Down power leads

The conduction along the leads carrying the magnet current is often one of the dominant heat transfer modes to the magnet cold mass. For helium pool-cooled magnets, these leads can be cooled by counterflow of the boiloff helium vapor to minimize the heat input to the helium pool. For a refrigerated magnet, however, the absence of any boiloff vapor requires that these leads be heat-stationed at the first stage of the cryocooler in order to minimize their heat input to the cold mass. Since the leads cannot be electrically shorted to the cryostat, such heat stationing involves the implementation of a dielectric interface which is a good heat conductor in a vacuum. GE has developed such a technology by employing ceramics as the dielectrics and various materials to join the ceramics to the heat stations and the current leads. For the purposes of this analysis, we may simply assume that the conduction heat transfer along the current leads from ambient temperature to the cryocooler first stage temperature will be shunted through these interfaces so that the current leads can be divided into two sections - one carrying current between ambient temperature and about 40 K, and the other between about 40 K and the magnet operating temperature of about 10 K. The design of the two lead sections may then be performed to optimize each section for its temperature range. Since the latter temperature range is within that of ceramic superconductors, those materials represent the best choice for the cold lead section because there is no heat generation within the lead while carrying current. For the "warm" leads, most metals provide about the same heat input for a given current carrying capability because of the physical relationship between thermal and electrical conductivity (Wiedeman-Franz Law). Copper with a residual resistivity ratio (RRR – the ratio of ambient temperature resistivity to that at 10 K) of about 65 is the material of choice for our present generation of refrigerated magnets, and the analysis here will be based on RRR = 65 copper warm leads.

The length/area ratio of the warm lead is the critical parameter in determining its current-carrying capability. GE-CRD has developed optimization programs to design leads for any temperature range. The optimum copper lead design for carrying a current in the range 50 to 150 A from 300 K to a cold temperature of between 30 and 60 K has a heat input (from both heat conduction along and heat generation in the lead) to the cold end of 0.0435 I, where I is the

operating current in A. Therefore, for our operating current of 102 A, the total heat input (along two leads) to the first stage of the cryocooler is 8.9 W.

ii) Along support struts

The second major mode of conduction heat transfer is along the mechanical supports that maintain the coil position within the cryostat. As was discussed in the cold mass structural support discussion in Section 2, there will be three types of magnet supports, all made of graphite-epoxy composite with uniaxial graphite fibers in an epoxy matrix. The length and area of these supports were derived in Section 2 and are summarized in Table 5.2.1. These supports all connect the cold mass directly to the cryostat vacuum vessel at ambient temperature and are therefore thermally stationed along their length to the thermal shield so that the bulk of the heat transfer from ambient is shunted to the shield where the cryocooler has more capacity. The thermal shield is in turn supported from the cold mass with other supports; the heat input from the shield to the cold mass along these supports will be discussed in the next subsection. Note that the length in the table refers to that between ambient and the thermal station at which the support is heat sunk to the shield, not the total length of the support. The heat leak down each of these supports is given by

$$Q = \frac{A}{L} \int_{40}^{300} k dT \quad (5.2.2)$$

where Q is the heat leak in W, A , and L are the cross-sectional area and length to the thermal station in cm^2 and cm and k is the thermal conductivity in W/cm^2 . For this material, the integral of $k dT$ from 40 to 300 K is about 5 W/cm. The heat input represented by each set of supports is presented in Table 5.2.1, where n is the number of supports per magnet (two coils). The total conduction heat input along these supports to the thermal radiation shield is 2.34 W.

Support	L	A	n	Q
vehicle	30	1.13	4	0.75
coil	3	0.013	4	0.09
guidance	3	0.15	6	1.50
Total	-	-	-	2.34

Table 5.2.1. Heat inputs to the thermal shield along magnet mechanical supports

AC losses

As was previously shown in Section 3, the projected AC losses in the thermal shield after attenuation by the vacuum vessel and including a copper cladding on the vacuum vessel to optimize its skin depth are 6 W.

Other heat transfer modes exist, such as residual gas conduction through an imperfect vacuum and solid conduction down instrumentation leads, but these are negligible compared to those presented here. We therefore obtain a total first stage heat input of 43.2 W. A summary of the thermal shield heat inputs is presented in Table 5.2..2.

Mode	Source	Heat input (W)
radiation	vacuum vessel (via MLI)	26.0
solid conduction	vehicle and superconducting coil supports	2.3
solid conduction	current leads	8.9
ac losses	time varying fields	6.0

Table 5.2.2. Heat inputs to the thermal shield of the proposed magnet.

5.2.2 Magnet Cold Mass

Radiation

For vessels in the range from 50 K to 10 K, superinsulation is not used to limit radiation heat transfer, therefore, the radiation from the thermal shield to the cold mass is given by the radiation equation

$$\dot{Q} = \frac{\sigma A (T_w^4 - T_c^4)}{(1/\epsilon_w + 1/\epsilon_c - 1)} \quad (5.2.3)$$

where σ is the Stefan-Boltzmann constant ($5.67 \times 10^{-8} \text{ W/cm}^2/\text{K}^4$), A the cold vessel area in cm^2 , T_w and T_c the warm and cold vessel temperatures in K, and ϵ the emissivities of the respective vessels. For clean metal surfaces or a variety of possible coatings, the emissivities at these temperatures can be 0.05 or less; 0.05 is a conservative figure. Therefore, for a cold mass area of 10 m^2 and a thermal shield temperature of 40 K, the radiation heat transfer to the magnet cold mass is 37 mW. If the thermal shield temperature is 50 K, this figure rises to 90 mW.

Residual gas conduction

While residual gas conduction (the heat transfer via molecular motion of the gas in an imperfect vacuum) is negligible at the temperature of the thermal shield, it becomes significant for the cold mass. Heat transfer by this mode can be estimated from the equation derived by Knudsen [1986] for long coaxial cylinders as

$$\dot{Q} = \frac{A_1}{2} \left[\frac{\alpha_1 \alpha_2}{\left(\alpha_2 + \frac{r_1}{r_2} (1 - \alpha_2) \alpha_1 \right)} \right] \frac{\gamma + 1}{\gamma - 1} \sqrt{\frac{R}{2\pi}} \frac{p}{\sqrt{TM}} (T_2 - T_1) \quad (5.2.4)$$

where A_1 is the area of the cold cylinder, α_1 and α_2 the accommodation coefficients of the cold and warm surfaces, r_1 and r_2 the cold and warm cylinder radii, γ the specific heat ratio for the gas which transfers the heat, R the gas constant, T the temperature at the gauge measuring the pressure p , M the molecular weight of the residual gas, and T_1 and T_2 the temperatures of the cold and warm surfaces. Since all gases except helium will condense on the 10 K magnet cold mass, helium will be the residual gas of interest. Accommodation coefficients for helium at 10 and 50 K are approximately 0.7 and 0.52, respectively, M is 4, R is 8314 J/kgmol-K and γ is 1.67. Taking the radius ratio to be 1.0 for small clearance between the thermal shield and cold mass (each with an area of 10 m²), we may estimate the residual gas heat transfer as

$$\dot{Q} = 10/2 [0.425] * 4 * 36.38 * \frac{p}{34.64} * 40 = 357 p \quad (5.2.5)$$

where p is the pressure in Pa. Our experience shows that a pressure of about 1×10^{-6} torr, or 133×10^{-6} Pa, is readily achievable in a large cryostat. The resulting estimate of residual gas conduction heat transfer to the cold mass is 47 mW.

Conduction

i) Along cold mass support struts

Taking the same strut design used in the thermal shield analysis, and an integral kdT from 10 to 40 K of 0.03 W/cm, the heat input down 4 struts is 22 mW, as shown in Table 5.2.3.

Support	L	A	n	\dot{Q}
vehicle	20	1.13	4	0.007
coil	2	0.013	4	0.001
guidance	2	0.15	6	0.014
Total	-	-	-	0.022

Table 5.2.3. Heat inputs to the cold mass along magnet mechanical supports

i) Along thermal shield supports

The thermal shield supports can be small because they carry only the static and dynamic mass of the shield. Supports for this shield will be tubular graphite-epoxy composite struts with a wall thickness of 0.08 cm and a diameter of 2.5 cm for an area of 0.63 cm^2 , a length of 3 cm and an integral kdT from 10 to 40 K of 0.03 W/cm. Four struts will be used from each coil to the thermal shield, so the total heat input down the eight struts is 50 mW.

ii) Down power leads

For the cold section leads, we will base our design on the use of oxide superconductors of YBCO material. Other materials are available for such leads, including the bismuth and thallium compounds, but we have significant experimental experience with the YBCO material. For this material, there is no heat generation in the lead as there is with resistive leads. The heat transfer is by conduction only. The lead cross-sectional area should be chosen to provide a reasonable safety margin to the critical current density, and for these leads the length is unimportant. Typical parameters published recently for this material include an average thermal conductivity in the range from 10 to 50 K of 0.035 W/cm-K and a critical current density at 50 K in a 0.5 T field of 1000 A/cm^2 . We will be carrying 102 A per lead, so a lead cross-sectional area of 0.2 cm^2 will limit the current density to 510 A/cm^2 , or about half of the critical value at that field. For a lead length of 10 cm, the heat transfer down these leads is estimated to be 30 mW each, for a total heat input to the cryocooler second stage of 60 mW.

AC losses

As was previously shown in Section 3, the projected AC losses in the superconducting coil after attenuation by the vacuum vessel and thermal shield are 0.076 W.

A summary of the cold mass heat inputs is presented in Table 5.2.4. The total heat transfer to the cold mass is therefore between 0.3 and 0.35 W for a thermal shield temperature of between 40 and 50 K.

Mode	Source	Heat input (mW)
radiation	thermal shield	90
solid conduction	vehicle and superconducting coil supports	22
solid conduction	thermal shield supports	50
solid conduction	current leads	60
residual gas conduction	thermal shield	47
ac losses	time varying fields	76

Table 5.2.4. Heat inputs to the cold mass of the proposed magnet

5.2.3 Relation to Cryocooler Performance

We summarize the heat inputs to the magnet cold mass and thermal shield as (conservatively) 0.35 and 45 W, respectively. In order to determine the resulting coil and shield operating temperatures, we must first determine the operating temperature of the cryocooler cold head. Using the load map in Figure 5.2.1, for the operating point of our magnet, the first and second stage temperatures are about 6.5 and 38 K, respectively.

Two more points are important to this discussion. First, the temperatures reported above are those of the cryocooler cold head, not the cold mass and thermal shield. The cryocooler interface requires several thermal joints to facilitate assembly. Therefore, there will be some temperature rises across each of these joints, and they will serve to drive the operating temperatures of the coils and shield up slightly. Typical values for these temperature rises for a refrigerated MR magnet are 2.0 and 0.3 K for the first and second stages, respectively. Further, there will exist some temperature difference, around 0.5 K, around the coil and support structure because of the point heat inputs at the mechanical supports which are physically distant from the point heat sink at the cryocooler interface. A similar effect will be experienced for the radiation shield, creating a temperature difference from the hot spot to the interface of about 3 K. Therefore, the coils can be conservatively predicted to operate slightly below 7.5 K and the shield at around 43 K. Second, GE has developed designs in which the leads are demountable at both stages once the magnet is powered, which would reduce the first and second stage heat inputs by 25 and 30%, respectively, with a concomitant reduction in operating temperatures. Such demountable leads would require that the magnets operate in a persistent mode, GE's magnets are capable of doing with our superconducting joint technology. However, the potential advantages of leaving the leads

connected may outweigh this small temperature reduction, which is not really needed in the proposed design.

The most important of these points is that the coil operating temperature should be significantly below that which was assumed for the design of section 1. The actual peak coil temperature should be in the range of 7.5 K, compared to a 12 K critical temperature. This large margin will make the coil very stable in the face of small amounts of unexpected energy deposition.

5.3 Cryostat and Magnet Cost Estimate

The total cost of the vehicle magnet and cryostat is estimated here, assuming one bogey per vehicle. Each bogey contains two magnets, and each magnet two coils. The 170 kg of superconducting tape in each coil can be assumed to cost about \$50 per pound, for a cost of less than \$20,000 per coil, or \$80,000 per bogey. The bulk aluminum cryostat components and coil support structure represent a total weight of about 1600 kg. At \$11/kg for bulk aluminum, and adding 50% for fabrication costs, the total cost of these parts is estimated at \$30,000 per magnet, or \$60,000 per bogey. The two cryocoolers required for each magnet will cost about \$30,000, or \$60,000 per bogey. These three components therefore total about \$200,000 per bogey. Other parts, such as the graphite composite supports and miscellaneous hardware, will certainly bring the cost up to in the range of \$300,000 per bogey, or the same amount per vehicle (since each vehicle shares a two bogeys with its immediate neighbors). This amount could be compared to the estimated vehicle cost presented in the report of Grumman Corp. to NYSERDA (1991) of \$9 M as about 3% of the total vehicle cost. These costs are summarized in Table 5.3.1.

Component	Cost/magnet (k\$)	Cost/bogey (k\$)	Cost/vehicle (k\$)
superconductor	40	80	80
coil support structure and cryostat	30	60	60
cryocoolers (including compressors)	30	60	60
miscellaneous cryostat and external supports and contingency	50	100	100
Total	150	300	300

Table 5.3.1. Magnet and cryostat costs

SECTION 6: SUMMARY, CONCLUSIONS AND FUTURE RESEARCH RECOMMENDATIONS

6.1 Summary of Research Performed Under this Contract

This contract was to design a shielded superconducting magnet system for a prototype maglev vehicle. To ensure that the magnet design was consistent with operation of a passenger carrying maglev system, first order analyses of the motor and levitation systems were performed as well. This required a selection of the basic type of design, and since the purpose of this effort was not to determine the optimal maglev system design for a given application, the latest design proposed by the Japan Railways group was selected as a base case. This system consists of a linear synchronous motor with null-flux sidewall levitation coils; both the armature windings for the motor and the null-flux coils are located in the sidewalls of a U-shaped guideway. A nominal loaded vehicle weight of 24000 kg was chosen, and vehicle dimensions were taken to be 3 m by 3 m by 20-30 m.

The primary objective of the research was twofold: to determine whether a novel type of superconducting magnet was applicable to such a vehicle; and to determine what type of magnetic shielding would be required to limit the steady state magnetic field in the passenger compartment to a range of values significantly below that which would be attained without any shielding. This superconducting magnet uses cryogenic refrigerators to maintain it at the low temperature required for superconducting operation, and requires no liquid cryogenes. The elimination of these cryogenes, which have caused problems on past Japanese prototype systems, and the use of advanced, highly reliable cryorefrigerators for cooling were thought to represent significant advantages of this technology. The shielding approaches to be studied included active and passive shielding; the former meaning the use of other coils to limit the field away from the main vehicle coils and the latter meaning the use of ferromagnetic material in the vehicle structure to channel the magnetic flux to areas other than the passenger compartment.

Both of the primary objectives were met. A complete structural, thermal and electromagnetic design of the superconducting magnet and its cryostat was developed, and the refrigerated magnet technology was noted to represent a major advance over conventional helium pool cooled magnets for such a vehicle magnet. The cost of the magnet and cryostat were estimated based on experience in building similarly sized magnets for other applications. Several shielding approaches were investigated, and the advantages and disadvantages of each noted. The difficulty of reducing the

passenger compartment field to very low levels (below 20 gauss) became clear, and the weight and cost penalties associated with such reduction were estimated.

In addition to the primary objectives, the motor and levitation analyses were carried out in greater depth than originally anticipated. This was primarily a result of some very diligent efforts by some curious and capable investigators. As a result, some further conclusions and recommendations for future research were identified.

6.2 Conclusions of this Research Effort

This study has resulted in significant technical progress in the areas of superconducting coil design and electromagnetic shielding for maglev systems. While the research performed herein concentrated on the design of the superconducting coil and its cryostat and the shielding of the passenger compartment from its field, the ancillary efforts expended here can be used to develop a basic understanding the superconducting coil design requirements from a system level. The investigations into the motor design, power conditioning analysis for the motor, and null-flux coil interactions are felt by the authors to add significantly to the quality of the conclusions presented here. The conclusions of the study are listed in a short bullet form under the headings below, divided according to the four tasks of the research – superconducting magnet design, motor analysis, shielding, and cryostat design. These summary conclusions are also presented at the beginning of each section of the report.

Section 1: Superconducting magnet design

- Refrigerated superconducting magnets, wound with niobium tin superconductor and cooled by cryogenic refrigerators employing the Gifford-McMahon cycle, can be designed to meet the specifications required for the on-board vehicle magnets for a passenger-carrying maglev system using the superconducting coils as the excitation for a linear synchronous motor and a null-flux sidewall levitation system.

- The support of racetrack-shaped superconducting coils such as have been proposed for such maglev systems can be a difficult matter, and training of the coil – or even the inability to make design field – might be experienced if proper design and fabrication procedures are not followed.

- Using commercially available Gifford-McMahon cryocoolers for the magnet cooling, a temperature margin to quench of 4.5 K can be attained. With such a large margin, the coil would be expected to be very stable against quench.

- The size and weight of the refrigerated magnet will be less than those of a comparable pool cooled magnet, although the reductions would of course depend on the designs. The elimination

of one of the two thermal shields will reduce weight and volume, and the size and weight reductions in the refrigeration equipment will be significant.

- The refrigerated magnet concept is directly applicable to ceramic superconductors operating at higher temperatures, in the range of 20 K and above. The refrigeration power required would be reduced, or alternatively the heat leak to the magnet which can be removed would be increased with such a swap of conductor. Were technical materials which would operate at reasonable current density in the 40 K range available, the cryocooler could be replaced with a single stage machine and the thermal radiation shield eliminated, with commensurate reduction in cryostat size, weight and complexity.

Section 2: Levitation and motor interactions

- The linear synchronous motor design affects the overall cost and reliability of the maglev system greatly, and its optimization for a given system performance specification should be a high priority.

- The motor pole pitch can have a significant impact on the motor efficiency. The determination of an optimal pole pitch, which also affects the levitation of the vehicle, should be the first priority in motor design.

- The use of an advanced method of DC-AC inversion called Auxiliary Commutated Resonant Pole (ARCP), developed recently by GE, could be of significant benefit in reducing the cost and improving the reliability of the power conditioning circuitry for the linear synchronous motor.

- The null-flux levitation system exhibits a large lift to drag ratio, and is to be preferred over facing levitation systems. Heating of the null-flux coils by the transient currents which they carry as the vehicle passes them may be the limiting factor in their design, and may necessitate using multiple-turn coils at some cost penalty. This heating can be greater at low speeds, even before the vehicle is actually levitated, because of the longer time period over which the null-flux coils carry current. The null-flux coil pole pitch also can be optimized for a given superconducting coil length.

Section 3: Shielding

- The geometry proposed herein, with vertical plane superconducting coils along the sides of the vehicle, poses difficulties for active shielding. These difficulties are independent of whether the coils are concentrated in bogeys or distributed along the length of the vehicle, although the system with the coils in bogeys has a larger low-field region towards the center of the length of each vehicle. A small reduction in the passenger compartment field produced by the main coils was seen with the addition of active shielding coils along the centerline of the vehicle, although at increased cost and complexity.

- Passive shielding, using iron in the vehicle floor, side walls, and/or magnet cryostats, can significantly reduce the passenger compartment field from the case without shielding. Several designs were developed, and the optimal design uses iron in the cryostat vacuum vessel as well as the vehicle floor and side walls, with variable thickness for the three locations and along the vehicle length. The weight of the passive shielding required to reduce the field to values in the range of 20 gauss and below is prohibitive unless the vehicle is located a significant distance above the coils. A vertical separation of 1.5 m or higher may be required to maintain a field in the very low range of 5 gauss or below.

- While two dimensional analyses of the magnetic flux patterns can be useful to guide shielding designs, fully three dimensional analysis is a requirement to obtain results of useful accuracy on real geometries. Models required can be very complicated and take days of CPU time on a large supercomputer.

Section 4: Cryostat design

- A flat sided cryostat using stainless steel walls with a single aluminum thermal radiation shield will serve the purpose of maintaining two superconducting coils at the required temperatures while transmitting the vehicle levitation and propulsion forces exerted on the coils to the vehicle structure through carbon fiber reinforced composite straps and struts.

- The cryostat vacuum vessel should be clad with a layer of a high electrical conductivity material such as copper so that currents are set up in it to shield the superconducting coils within from the time varying magnetic fields which the motor and levitation operation entail. This shielding is necessary to reduce the AC losses in the coils to manageable levels. The heat generated in the cryostat will be carried away by convection at the speed at which the vehicle travels.

- A thermal interface connecting two cryocoolers to the thermal radiation shield and magnet support structure, and which will cool these members to their required temperatures, was designed. The interface employs high temperature superconductors for the leads which are heat stationed at the first and second stages of the cryocoolers to reduce the heat leak to the magnet structure. Dielectric interfaces with high thermal conductivity can be used to connect the leads to the thermal stations while carrying the magnet current. If the heat leak needs to be further reduced, a set of retractable leads can be designed. These would only be connected during the magnet powering.

6.3 Recommendations for Further and Related Research

Our recommendations for future research efforts are many and varied. The wide scope of these recommendations stems from the profession of the individuals who performed this research, as well as immature nature of the maglev technology, especially when experimental demonstrations are considered. The recommendations are presented here, in no particular order. Clearly individuals in different professions, or different beliefs about the role of maglev technology in the transportation infrastructure, would prioritize these proposals differently.

- The development of the superconducting coil presented herein is less than complete. Additional analytical and experimental effort aimed at understanding the level of AC losses, both hysteretic and from stabilizer eddy currents, is important to ensure that the operating temperature of the coils will be within the desired range. Accurately determining the level of field attenuation that the vacuum vessel (with and without cladding) and thermal shield would provide also requires further study. This study would involve the development and implementation of complex three dimensional models of the cryostat and magnet structures on a fine scale, and necessarily require much computer time and power for solution.

- The DC magnetic shielding analyses performed herein, while significant in scope and complexity, are by no means comprehensive. More effort should be expended to identify possible steel configurations which maximize the volume in the passenger compartment which lies below a given field level.

- The level to which the DC magnetic field in the passenger compartment must be reduced is a critical value in determining a viable design for the superconducting coils and shielding methods. This level must be specified by federal government agencies such as the EPA or FRA before an optimal maglev design involving electrodynamic levitation can be considered. Whatever research into the health effects of DC magnetic fields is required to settle this issue is a necessary precursor to the continued development of maglev systems for the United States. This leaves the issue of AC field levels untouched, and it must be addressed as well.

- While the motor and levitation analyses were not the primary focus of this study, the complete optimization of all coils involved in a maglev system of the basic geometry assumed here is not out of the question. Such an optimization would require inputs from the superconducting coil design, motor and levitation coil costs, shielding analysis, and power conditioning analyses. The probable outcome would be a minimized installed and life-cycle cost functional given a set of

initial assumptions. Comparison of an optimal design with similarly optimal designs using other modes of propulsion or levitation, including non-superconducting systems, could then be performed to better determine which system might be best for application in the U.S. This represents a significant piece of research, and one with a limited applicability because of the necessary restrictions on the geometry assumed, but it is a research effort which may be required if a design by consensus is to be sought.

- Several decisions which the Japanese researchers have made are of interest, and more direct interaction with them would clearly be fruitful if the political waters can be rendered sufficiently smooth. On a related note, the continuation of open dialogue between all participants in the federally funded U.S. efforts is a must.

- Improvements in technology which impact on a system such as maglev are always occurring. Research in this area must continue to keep abreast of future developments such as high-temperature superconductors. The refrigerated magnet technology presented herein can be easily extended to allow the application of coils wound with high-temperature superconductors once they become available in engineering quantities and consistent quality. The ACRP inverter technology presented here also represents a significant opportunity to develop a maglev system which is less expensive to build and maintain, while being more reliable than any system in the world today.

REFERENCES

1. ANSYS Engineering Analysis System Theoretical Manual, Swanson Analysis Systems, Inc., 1989.
2. Atherton, D.L., et al "Design, analysis and test results for a superconducting linear synchronous motor," Proc. IEE, Vol. 124, No. 4, April 1977.
3. Bechtel, "Design and Costs for a Generic 10-MW Utility Lead-Acid Battery Energy Storage Plant," Bechtel Group, San Francisco, CA, EPRI report AP-5845, Project 2123-6, June 1988.
4. Blanchard J. P., "Environmental Issues Associated with Superconducting Magnetic Energy Storage (SMES) Plants," Proc. Intersociety Energy Conversion Engineering Conf., IECEC-89, 1989.
5. DeDoncker R.W. and Lyons J.P., "The Auxiliary Resonant Commutated Pole Converter," Conference Record of 1990 IEEE Industrial Applications Society Annual Meeting, Seattle, WA, Oct. 7-12, 1990, pp. 1228-1235.
6. DeDoncker R.W. et al, "Characteristics of GTO's and High Voltage MCT's in High Power Soft-Switching Converters," Conference Record of 1991 IEEE IAS Annual Meeting, Sept 28-Oct 4, 1991. pp. 1539-1545.
7. GE Drive Systems, "GTO-IMD Induction Motor Drive," GE Drive Systems, Salem, Virginia, GEA-11280B.
8. Gifford, W.E., "The Gifford-McMahon Cycle," *Adv. in Cryogenic Engrg.* 11, 1966.
9. Grover, Inductance Calculations, Dover, 1946
10. Gyugi L. and Pelly B.R., "Static Power Frequency Changers," John Wiley, 1976.
11. Hayes W. F., "Magnetic Field Shielding for Electrodynamic Maglev Vehicles," International Conf. Maglev and Linear Drives, 1987, pp. 53-66.
12. Halaczek TL and Rafalowicz J, Heat transport in self-pumping multilayer insulation, *Cryogenics* 26, 1986, pp. 373-376.
13. Iwasa, Y. "Magnetic Shielding for Magnetically Levitated Vehicles," Pro. IEEE, vol. 61, No. 5, May 1973, pp. 598-603.
14. Kalafala A.K. - private communication
15. Key et al, "Power Conditioning Options for Central Station Rated Photovoltaic Power Plants," Conference Record of 1985 IEEE Photovoltaic Specialists Conference, October 21-25, 1985, pp. 1320-1325.

16. Knudsen M, *Ann. d. Physik* 31, 1910, p. 205; 32, 1910, p. 809; 33, 1910, p. 1435; 34, 1911, p. 592; and 6, 1930, p. 149.
17. Marconi Co., "Gate Turn-off Thyristor Data", Marconi Electronic Devices, Hauppauge, NY, Dec. 1987.
18. Mohan N. et al, "Power Electronics Converters, Applications and Design," John Wiley, 1989.
Morris, E.E., 1982, "Filament Wound Composite Thermal Isolator Structures for Cryogenic Dewars and Instruments", American Society for Testing and Materials, publication 768, pp.95-109.
19. Morris, V.L., 1989, "Advanced Composite Structures for Superconducting Super Collider," Supercollider 1, pp.525-535, Plenum Press.
20. Murphy J.M.D. and Turnbull F.G., "Power Electronic Control of AC Motors," Pergamon Press, 1988.
21. Okuma S., Sugiyama H., and Amemiya Y., "Magnetic Shielding for Magnetically Levitated Trains," *Electrical Engineering in Japan*, Vol. 100, No. 6, 1980, Translated from *Denki Gakkai Ronbunshi*, Vol. 100B, No. 12, December 1980, pp. 715-722.
22. Takeno, M. et al., 1985, "Thermal and Mechanical Properties of Advanced Composite Materials at Low Temperatures," ICMC, Boston, MA.
23. Tanaka, H., "JR Group Probes Maglev Frontiers," *Railway Gazette International*, July 1990.
24. Walker L.H. et al, "10MW GTO Converter for Battery Peaking Service," *Conference Record of 1988 IEEE/IAS Annual Meeting*, October 2-7, 1991, pp. 850-857.
25. Wilson, M.N., "Superconducting Magnets", Oxford University Press, New York, 1983.
26. Toshiba Corp. "Gate Turn-Off (GTO) Thyristor and Fast Recovery Diode (FRD) Data Book", Toshiba Corp., Japan, March 1991.
27. Ziogas P.D. et al, "A Computer-Aided Analysis and Design Approach for Static Voltage Source Inverters," *IEEE Transactions in Industry Applications*, Vol. IA-21, No. 5, Sept./Oct. 1985, pp.1234-1241.

APPENDIX A. APPROXIMATE DESIGN APPROACH FOR A SUPERCONDUCTING LINEAR SYNCHRONOUS MOTOR

The superconducting linear synchronous motor for high-speed, electrodynamically levitated ground transportation is very different from a conventional, iron-cored synchronous motor. Even so, the physical principles of both machines are very much the same and similar forms of approximate analysis, with suitable modifications, may be used to guide the sizing and initial optimization of these machines. This is also true of considerations related to the power electronics required to operate such machines. This brief report sets out a simplified analysis, suitable for manual calculations, that may be efficiently used for such initial design studies.

A.1 Geometrical Assumptions

The general arrangement of magnets on a vehicle is illustrated in Figure 3.1.1 [Tanaka 1990]. The vehicle magnets, corresponding to the rotor of a conventional synchronous machine, are superconducting coils (racetracks) supplying essentially constant magnetic fields. The track, corresponding to the stator of a conventional machine, is wound of normal conducting metals and insulated for relatively high voltages to handle the large power required (around 10 MVA). The track will also contain metal plates or coils to interact with the vehicle magnets for purposes of supplying the forces needed to levitate the vehicle. This is one of the major differences between the LSM and conventional machines. Others are, of course, the superconducting magnets producing the excitation field and the lack of iron anywhere in the magnetic circuit. In some systems, iron may be used for shielding of the passenger compartment, but this effect was not taken into account here for this first order analysis. The fluxes therefore spread all over space instead of being confined to particular paths. The production of force is different in each coil. Some coils will have only one side under a magnet part of the time and will also be subject to fringing fields at other times. These factors, plus others such as the lateral separation of the stator windings and interactions with the suspension system, make the precise analysis of a LSM very difficult indeed. Nonetheless it is possible to formulate an approximate analysis good for sizing and for understanding the tradeoffs involved.

The geometry for one phase of a typical LSM stator and one superconducting magnet is shown, in outline or filamentary form, in Figure 3.1.1. A typical cross section concept is shown in Figure 3.1.2 where a set of null flux suspension coils has been interposed (on the stator/track) between the vehicle magnets and the propulsion stator. The dimensions given are typical, taking into account the space needed for the conductors, cryostat, structures, and mechanical clearance. The flux density distribution for typical dimensions and excitation, because of the superconducting

magnets, as measured along the centerline of a stator coil is shown in Figure A.1 [Kalafala 1991]. The calculation is derived from an exact 3-D formulation whose sources are filamentary conductors. For the following analysis, the distribution was assumed to be uniform with a magnitude equal to that in the central region.

A.2 Basic Relations

If the vehicle magnets are always arranged in dipole pairs and the stator coils are one pole pitch long (1/2 wavelength), then voltage will be generated on only two coil ends at any time. Either both ends of one coil will be under the magnets, or one end each of two adjacent coils will be under the magnets. Since all the coils are assumed to be in series, the open circuit voltage per phase is given by

$$V_{oc \text{ rms}} = 2(N_m)(N_t)(B_{rms})(v)(h) \quad (\text{A.1})$$

where:

$V_{oc \text{ rms}}$ = rms voltage induced (volts rms)

N_m = number of magnet pairs on the vehicle

N_t = number of turns on a stator coil

B_{rms} = rms flux density over the stator coil area (T)

v = vehicle speed (m/s)

h = height of the coil (m).

The open circuit voltage may be taken in terms of the rms magnitudes of sinusoidal current and flux distributions, or it may be interpreted in terms of peak magnitudes (especially if the system is being operated in a "brushless DC" motor mode). The latter may be preferable if the effective fundamental power factor can be kept high enough and if the position of the vehicle relative to the track can be monitored well enough.

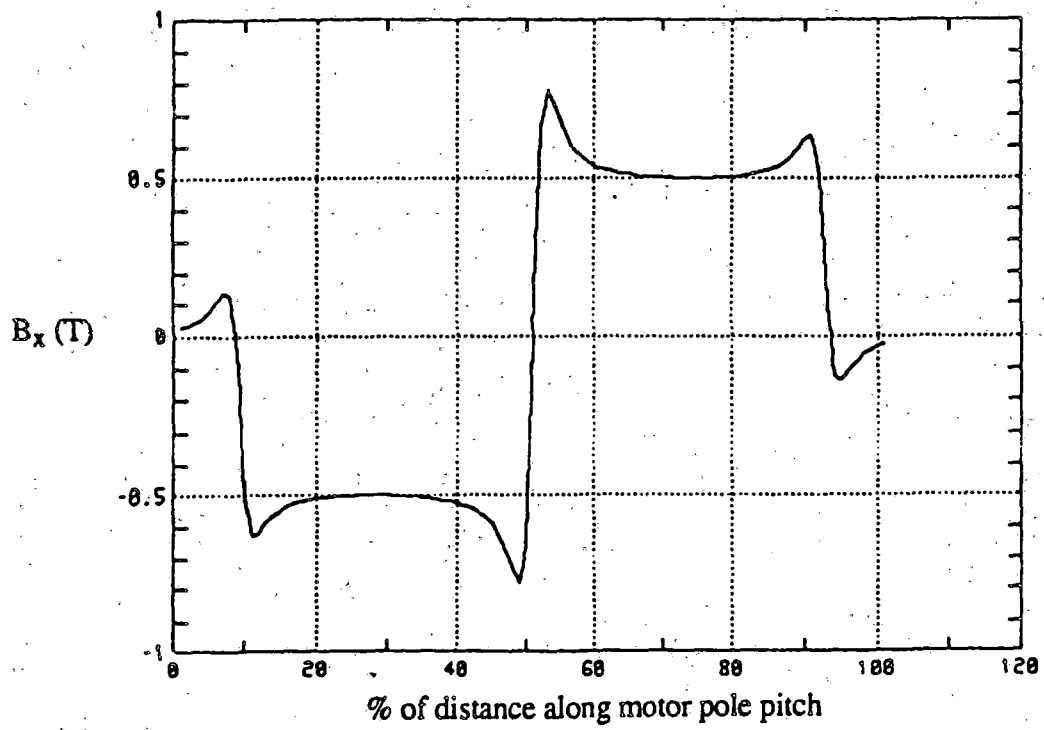


Figure A.1. Typical flux density distribution, in the plane of the stator, from the SC magnet.

The thrust developed by the stator has contributions from all three phases at any particular time. Since the stator coils will be spaced at 60 (electrical) degree intervals, there will always be a full stator coil under a magnet pair plus one end each of two adjacent coils in the other excited phases. The thrust per side, assuming that the vehicle position is known and that an "optimum" control strategy is implemented, is then given approximately by

$$T = (4)(Nt)(Nm)(I)(Brms)(h) \quad (A.2)$$

Where: I = phase current (amps rms).

A more detailed analysis (Atherton et al. 1977) will show the influence of track mutual inductance in raising the net effective inductance and the effects of control angle. For sinusoidal machines, optimum operation will be obtained when the current is not exactly in phase with the open circuit voltage. For "brushless DC" type of operation, best operation will be closer to the in-phase condition. What the best control strategy actually is will have to await consideration of the power converters and simulation of the total propulsion system. For the present purposes these considerations will be suppressed in favor of simplicity. Even though the results will vary approximately, they will show the trends and tradeoffs in order to guide the conceptual design.

Continuing with the assumption that the stator is a relatively conventional three-phase winding (at least in effect), there will be one full coil (Figure A.2a) for each wavelength of track (two pole pitches or one superconducting magnet set). The total length of wire l (m), including interconnections, in each wavelength is

$$l = (2)(Nt)(t+h)+t \quad (A.3)$$

Where: t = the pole pitch. (m)

If the winding is a meander (Figure A.2b) rather than a full coil then

$$l = (2)(Nt)(t+h) \quad (A.4)$$

The resistance per phase R (Ω) is then given by

$$R = (Np)(Nt)(r)(l)/(Ac) \quad (A.5)$$

where:

r = the resistivity of the stator conductor (ohm-m)

Ac = effective conductor cross section (m2)**

Np = total number of coils on the track = (Lb)/(2t)

Lb = length of a block (m)

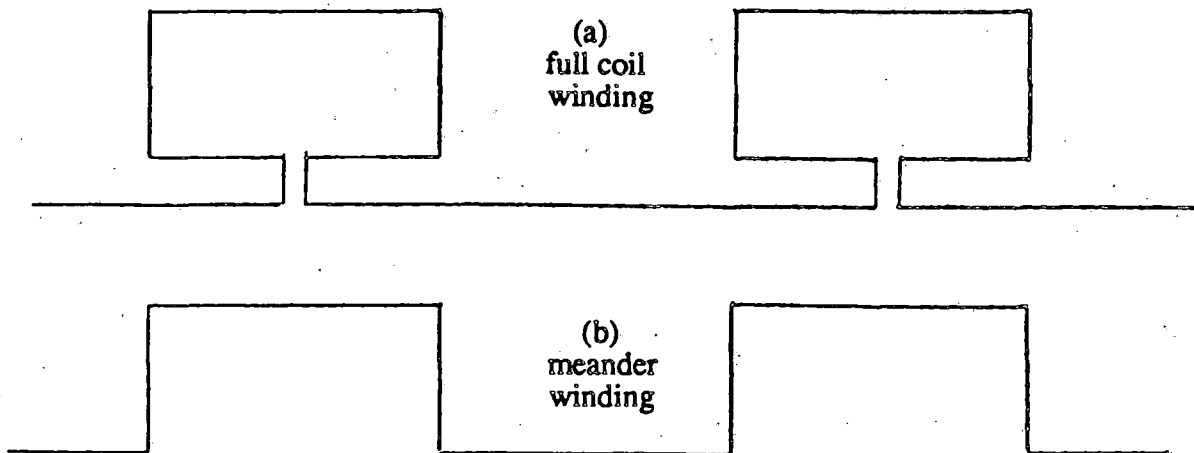


Figure A.2. Two winding concepts for the guideway.

The self inductance of the track requires complex calculations because of the 3-D nature of the fields and the mutual couplings with the other excited phases, the vehicle magnets, and the null flux coils. For the purposes of this approximate analysis, these effects will be neglected. The self-inductance of a planar rectangular coil may be calculated fairly precisely by means of a complex formula [Grover, 1946] but for our purposes an approximate expression is more useful and actually comes quite close in many cases. The self-inductance L (h) is given approximately by

$$L = (N_p)(\mu_0)(N_t^2)(h)(t)/[(K)(\sqrt{A})] \quad (\text{A.6})$$

and

$$K = [1+(0.9)(t+h)/(4)(\sqrt{A})] \quad (\text{A.7})$$

K is simply a reduction factor to correct the infinite solenoid inductance formula to an approximately correct value for the short coil actually used (with length \sqrt{A} , where A is the cross-sectional area of the stator coil in m^2).

The total voltage per phase V (rms volts) is then given by

$$V = (I)[R+V_{oc}+(j)(X_l)] \quad (\text{A.8})$$

where the line frequency

$$f = (v)/(2t) \text{ (Hz)} \quad (\text{A.9})$$

$$\text{and } X_l = (2)(\pi)(f)(L) \quad (\text{A.10})$$

A.3 Design Criterion

The principal factor limiting the practical length of a major section or block is the amount of reactive voltage. The reactive voltage increases with block length because the armature windings which are not interacting with the vehicle magnets must still be driven with alternating current. The resistance of a long length of coils which are producing no useful thrust also impacts track heating and motor efficiency but can be independently controlled, to some extent, by the appropriate choice of conductor cross section and material (track heating is usually not a problem because of the short times involved). System efficiency cannot be neglected in the final determination of system parameters, but the resistive voltage developed is a lesser factor since it is usually much smaller than the inductive voltage.

The inductance is, however, fixed by the other parameters of the system, i.e., coil turns (N_t). The length of a block is determined by how low a power factor can be tolerated in the drive system. The power factor directly impacts the size of the power converters and indirectly affects

the system efficiency. A poor power factor can have an even more severe effect on power converter sizing as a result of the nonsinusoidal waveform of the open circuit voltage. This point will be expanded upon later.

A measure of the power factor, which should be made as close as feasible to 1.0, is the ratio of open circuit voltage to reactive voltage which should be made larger. The objective here is to minimize the size of the power converters and the resistive losses.

$$V_{oc}/V_l = [(8)(\sqrt{A})(K)/(\pi)(U_o)][(N_m)/(N_p)] * [(B_{rms})/(N_t)(I)] \gg 1 \quad (A.11)$$

The number of coil turns (N_t) is, however, dictated by the required thrust, the attainable superconducting magnet flux density, the geometry, and the available line current. Hence

$$N_t = (T)/[(4)(N_m)(I)(B_{rms})(h)] \quad (A.12)$$

giving

$$V_{oc}/V_l = [(8)(\sqrt{A})(K)/(\pi)(U_o)][(h)(t)/(T)(N_p)] * [(B_{rms}^{**2})(N_m^{**2})] \gg 1 \quad (A.13)$$

Equation A.13 suggests that the vehicle magnets must have the highest possible flux density and that the number of magnet sets on the vehicle must be large. These quantities have a major effect by virtue of appearing squared.

Note that the vehicle length L_v (m) puts a limit on total magnet length in Equation A.13 so that the best that can be done is

$$(2)(N_m)(t) < \text{or} = L_v \quad (A.14)$$

This condition is realized when magnets are spread all along the length of the vehicle and several vehicles are connected as a consist if possible. If Equation A.14 holds, then

$$V_{oc}/X_l = [(8)(\sqrt{A})(K)/(\pi)(U_o)][(L_v)/(L_b)] * (h)(B_{rms}^{**2})[(N_m)/(T)] \gg 1 \quad (A.15)$$

The ratio expressed by Equation A.15 is then the best that can be achieved (within the limits of the approximation). Again, the total consist should be large but also the thrust per magnet set should be kept small. There should be a large number of voltage-producing elements with few turns so that the induced voltage is large but the inductance is low.

A further possible consideration is that if enough open circuit voltage could be realized, the power factor could actually be leading instead of lagging. In that case load-commutated inverters or

cycloconverters could be used to drive the stator. The simplification of the converters could then result in considerable cost savings.

A.4 Examples

A.4.1 Large Magnets on Bogeys

It is assumed that there are magnets and a track on each side of the vehicle and that there is a pair of magnet sets at the front and another at the back of the vehicle. This is the arrangement used when the magnets are mounted in bogeys. For this example take

thrust	$T = 50 \text{ Kn}$	flux density	$B_a = 0.6 \text{ T (rms)}$
coil height	$h = 0.5 \text{ m}$	magnet sets	$N_m = 2 \text{ (per side)}$
coil section	$A = 5 \text{ cm}^2$	vehicle length	$L_v = 30 \text{ m}$
pole pitch	$t = 2.5 \text{ m}$	speed	$v = 120 \text{ m/s}$

To achieve the required thrust of 25 Kn/side at an assumed 1000 A rms/side would, from Eq. A.2, require $Nt = 10.42$ turns. Assuming 10 turns at 1042 A, the open circuit voltage may be computed, from Eq. A.1, to be 1440 V rms.

The inductance, using Eq. A.6, is 204 μH /coil. Using the exact formula, from Grover (3), yields 419 μH . The discrepancy is due to the aspect ratio of the coil and will be much less with approximately square coils. The frequency, from Eq. A.8, is 24 Hz leading to a reactive voltage of 65.8 V/coil rms using 419 μH . The breakeven block length (for equal open circuit and reactive voltage) is then only 109.4 m - and then the power factor is only 0.707.

To estimate the efficiency of the propulsion electromagnetics, the losses are assumed to be due only to the resistance of the track. That is, losses associated with the rectification from the main power source and inversion to motor frequency are not included. For state of the art inverters and rectifiers, this is a reasonable assumption. The resistance per phase of the track is given by Eqs. A.3, A.4 and A.5 neglecting high-frequency effects. The conductor material is assumed to be 60% IACS aluminum at 20 °C, and the packing factor of the winding is assumed to be 70%. Since the coils call for multiple turns, it is assumed that winding is in the form of full coils so that Eq. A.3 applies for the length. The resistance/phase for this case is then 1.23 Ω giving an efficiency of 42.9 % and an adjusted power factor of 0.882. The power factor is higher as a result of the additional real power in track losses.

A.4.2 Magnets Along the Vehicle with Increased Flux Density

The assumptions of example No. 1 are used except that a slightly higher magnet flux density of 0.8 T rms is selected and the magnets occupy the entire length of the vehicle so $N_m = 6$. The value of 0.8 T for the magnet flux density is felt to be attainable with existing magnet technology, although at higher cost.

The number of turns and current required are now $N_t = 3$ and $I = 868$ amps rms. The open circuit voltage $V_{oc} = 1728$ V rms. The inductance/coil has dropped to $37.7 \mu\text{H}$, using Grover's formula [Atherton 1977] and the corresponding reactive voltage at 868 A rms and 24 Hz is 4.94 V/coil. The breakeven block length now becomes 1749 m, which is more respectable, but the power factor is still only 0.707.

For the efficiency calculation the same assumptions as for example No. 1 are used with revised parameters. The resistance per phase is 2.07Ω leading to an efficiency of 39.1 % with a power factor of 85.1 %.

A.4.3 Reduced Pole Pitch

This example is identical to No. 2 except that the pole pitch has been shortened to 0.5 m so that the vehicle magnets now have an approximately square cross section - $t = 0.5$ m and $N_m = 30$.

The approximate inductance formula (Eq. A.6) now yields $1.27 \mu\text{H}/\text{coil}$ for one turn. In comparison the exact formula gives an inductance/coil of $1.36 \mu\text{H}$.

The turns/coil and current/side are now $N_t = 1$ at 520 A rms, but the frequency has gone up to 120 Hz. The open circuit voltage $V_{oc} = 2880$ V rms and the inductive voltage is 0.533 V/coil (using $1.36 \mu\text{H}$) even at the higher frequency. The breakeven block length is 5,403 m, which is rather long. At about half that length (2 km) the reactive voltage is 1,440 V, yielding a power factor of 0.894.

Under the same assumptions as previously used, the resistance per phase is 0.514Ω for an efficiency of 87.8 % at a power factor of 0.954. However, since there is only one turn per coil required, a meander winding becomes quite practical so that Eq. A.4 now may be used for the length. The resistance/phase is then reduced to 0.343Ω yielding an efficiency of 91.5 %. The power factor probably does not change (and may increase) even though the real component of voltage has decreased since the meander winding will have a significantly lower inductance.

A.5 Effects of Peaked Open Circuit Voltage

The usual case in converter-powered drives is that the source is applying a modified square wave type voltage to a motor that has a rather low leakage inductance (~ 0.05 pu) and a sinusoidal or, at worst, trapezoidal back EMF or open circuit voltage waveform. The result is a distorted current waveform leading to harmonic heating and high peak currents. The high peak currents combined with voltage ringing and overshoot in the converter, especially under unusual or faulted conditions, determine the size of the semiconductors needed. The performance calculations presented here are based on approximately sinusoidal voltage and current or the fundamental components of the voltages and currents, which is acceptable for performance estimation but may be in serious error when attempting to size the power converters.

In the LSM application, the leakage inductance is quite high (0.32 pu) even in the best case (example No. 3). Hence, the harmonic content of the current will be severely limited, yielding an almost sinusoidal current waveform in many cases. Assuming a sinusoidal open circuit voltage, the voltage required at the power converter, to drive the LSM will be somewhat higher than the open circuit voltage because of the resistive and inductive components of the track impedance as shown in curve a. in Figure A.3. When the open circuit voltage is a peaked waveform, the voltage at the power converter becomes similar to Figure A.3 curve b. The peaks of the open circuit voltage combined with the large, phase-shifted component of voltage caused by the high leakage inductance result in peaks, at the end of the period as much as 40 % higher than for purely sinusoidal waveforms as illustrated in Figure A.3 curve c. Figure A.3 curve d shows the effect of clipping off the peaks of the open circuit voltage at the ends of the cycle by suitable shaping of the magnetic flux density distribution because of the superconducting magnets.

- The implications for total system cost are quite large - there may be a thousand power converters and only several hundred magnets. It appears that a more complex magnet design is warranted to minimize overall system cost. Such a design is illustrated in Figure A.4 (Kalafala 1991), where the total current has been redistributed to yield a better flux density distribution, hence open circuit voltage waveform. More detail on this technique is contained in a patent disclosure letter. An alternative approach may be to make the superconducting magnets circular while keeping the stator coils rectangular.

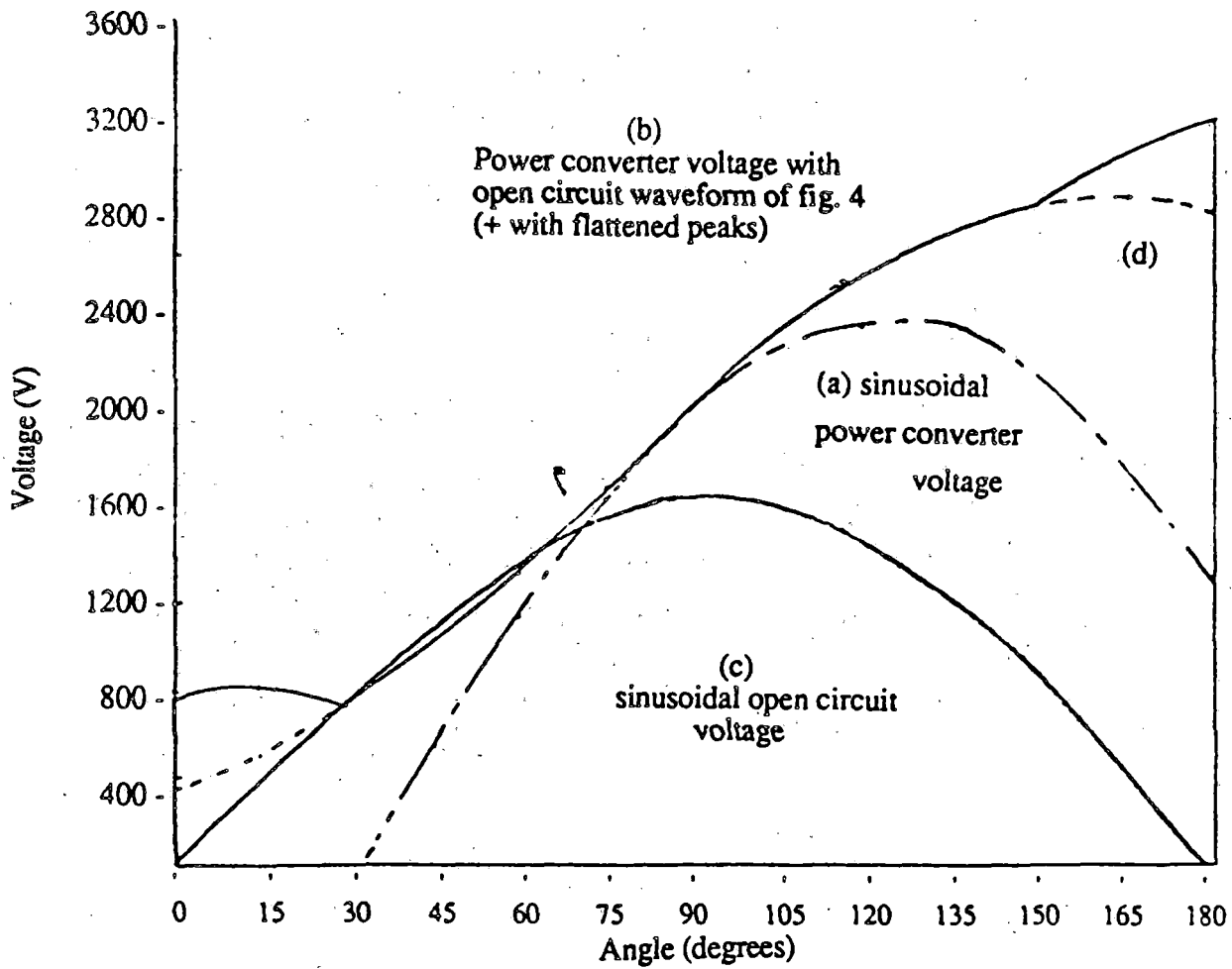


Figure A.3. Comparison of power converter terminal voltages for various flux density distributions.

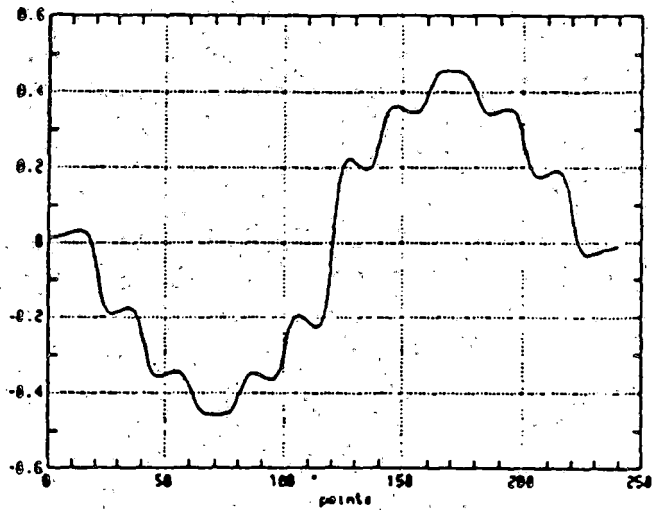
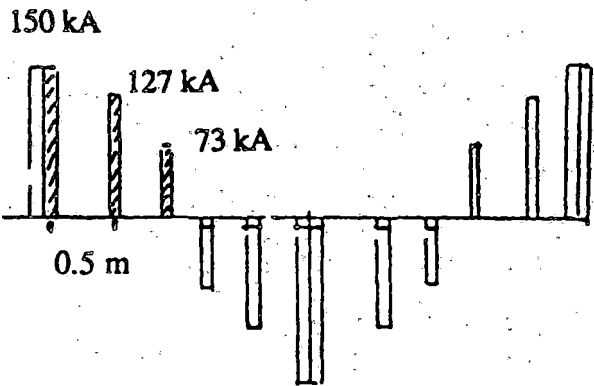


Figure A.4. Effect of redistributing the SC coil current.

If the effective leakage inductance is low enough, the effects will be less. How much effect the peaks at the ends of the half-cycle have on the power converter sizing will have to be evaluated. On the other hand, if the inductance is low, it should be possible to implement the "brushless DC" mode of operation. In that case, with 120° square waves of current, there will be no current at the ends of the half-cycle, and the effects of the peaking will be considerably reduced.

A.6 Conclusions

As has been shown previously, it appears that it is technically feasible to build a linear synchronous motor, long stator propulsion drive for magnetically levitated vehicles using superconducting magnets. If reasonable operating conditions for the motors can be achieved, the necessary power converters may be spaced at intervals of several kilometers. The cost penalty, to the system, in the size and number of converter stations required may then be minimized.

To achieve reasonable operating conditions, it is desirable to have as many voltage-producing elements as possible along a vehicle to maximize the utilization of attainable flux densities and to minimize the number of coil turns in the track. This translates into a tendency to short pole pitches and magnets distributed along the entire length of the vehicle. Of course, the desire to maintain the flux density in the passenger compartment at or below some level is at odds with the distribution of magnets along the vehicle, so factors other than purely motor performance will influence the choice of motor design for an actual system.

APPENDIX B. AC FIELDS FROM A 3-PHASE LINEAR WINDING

B.1 AC Fields from a 3-phase Linear Winding: Complex Exponential Formulation

The fields at any point are obtained from the time harmonic decomposition of the phase current waveform and the z-direction space harmonic decomposition of a single motor coil field. The observation point equation of motion couples these two series and gives the observed field.

The motor stator winding is considered to be a three phase winding with coil phases arranged abcabc... in the z-direction with wavelength λ . Let the phase-a current be expressed as a time-harmonic sum:

$$I(\omega t) = I(\theta) = A_0 + \sum_{n=1} (A_n \exp(jn\theta) + A_n^* \exp(-jn\theta)) \quad (\text{B.1})$$

where $\theta = \omega t$ is the electrical angle and A_n are the current harmonic coefficients. It should be noted that because the current waveform is purely real, the A_{+n} coefficients are complex conjugate pairs. Let the magnetic field due to one phase a coil be separated into time and space components:

$$B(x, y, z, t) = C(x, y, z)I \quad (\text{B.2})$$

(Here C has dimensions tesla/A, being the field due to unit current in the coil.) The field due to an infinite array of phase a coils laid out in the z-direction is:

$$B_a = I \sum_{k=-\text{inf}}^{+\text{inf}} C(x, y, z+k\lambda) \quad (\text{B.3})$$

which resolves into z-harmonics with fundamental period λ :

$$B_a = I(\theta) \left\{ D_0 + \sum_{l=1} (D_l(x, y) \exp(jl\alpha) + D_l^*(x, y) \exp(-jl\alpha)) \right\} \quad (\text{B.4})$$

where $\alpha = 2\pi z/\lambda$ is the spatial angle. The fields from the phase b and c windings can be determined similarly, accounting for the $\lambda/3$ displacement of those phase belts and $2\pi/3$ phase difference in θ :

$$\begin{aligned}
\mathbf{B}_{b,c} &= \mathbf{I}\left(\theta \pm \frac{2\pi}{3}\right) \sum_{k=-\text{inf}}^{+\text{inf}} \mathbf{C}\left(\mathbf{x}, \mathbf{y}, z \pm \frac{\lambda}{3} + k\lambda\right) \\
&= \mathbf{I}\left(\theta \pm \frac{2\pi}{3}\right) \left\{ D_0 + \sum_{l=1} \left(D_l(\mathbf{x}, \mathbf{y}) \exp\left(\pm j l \frac{2\pi}{3}\right) \exp(j l \alpha) + \right. \right. \\
&\quad \left. \left. D_l^*(\mathbf{x}, \mathbf{y}) \exp\left(\mp j l \frac{2\pi}{3}\right) \exp(-j l \alpha) \right) \right\} \tag{B.5}
\end{aligned}$$

where - applies to phase b and + to phase c. The total field then is obtained by summing all 3 phase contributions:

$$\begin{aligned}
\mathbf{B}_{\text{tot}} &= \left[A_0 + \sum_{n=1} \left(A_n \exp(j n \theta) + A_n^* \exp(-j n \theta) \right) \right] \times \\
&\quad \left[D_0 + \sum_{l=1} \left(D_l(\mathbf{x}, \mathbf{y}) \exp(j l \alpha) + D_l^*(\mathbf{x}, \mathbf{y}) \exp(-j l \alpha) \right) \right] \\
&+ \left[A_0 + \sum_{n=1} \left(A_n \exp\left(-j n \frac{2\pi}{3}\right) \exp(j n \theta) + A_n^* \left(j n \frac{2\pi}{3} \right) \exp(-j n \theta) \right) \right] \times \\
&\quad \left[D_0 + \sum_{l=1} \left(D_l(\mathbf{x}, \mathbf{y}) \exp\left(-j l \frac{2\pi}{3}\right) \exp(j l \alpha) + D_l^*(\mathbf{x}, \mathbf{y}) \exp\left(j l \frac{2\pi}{3} \right) \exp(-j l \alpha) \right) \right] \\
&+ \left[A_0 + \sum_{n=1} \left(A_n \exp\left(j n \frac{2\pi}{3} \right) \exp(j n \theta) + A_n^* \left(-j n \frac{2\pi}{3} \right) \exp(-j n \theta) \right) \right] \times \\
&\quad \left[D_0 + \sum_{l=1} \left(D_l(\mathbf{x}, \mathbf{y}) \exp\left(j l \frac{2\pi}{3} \right) \exp(j l \alpha) + D_l^*(\mathbf{x}, \mathbf{y}) \exp\left(-j l \frac{2\pi}{3}\right) \exp(-j l \alpha) \right) \right] \tag{B.6}
\end{aligned}$$

We recognize that

$$\exp\left(+j \frac{2\pi}{3}\right) = -\frac{1}{2} + \frac{j\sqrt{3}}{2} = \gamma \tag{B.7}$$

At this point it is useful to separate each of the sums into three parts premultiplied by γ , γ^2 or 1 and apply the relation

$$1 + \gamma + \gamma^2 = 0 \tag{B.8}$$

which permits cancellation of many of the terms in the expansion to give

$$\begin{aligned}
B_{\text{tot}} = & 3A_0D_0 + 3A_0 \sum_{m=1} (D_{3m} \exp(j3m\alpha) + D_{3m}^* \exp(-j3m\alpha)) \\
& + 3D_0 \sum_{q=1} (A_{3q} \exp(j3q\theta) + A_{3q}^* \exp(-j3q\theta)) \\
& + 3 \sum_{q=1} \sum_{m=1} \{ A_{3q} D_{3m}(x,y) \exp j(3q\theta+3m\alpha) + A_{3q}^* D_{3m}^*(x,y) \exp -j(3q\theta+3m\alpha) \} \\
& + 3 \sum_{q=1} \sum_{m=1} \{ A_{3q} D_{3m}^*(x,y) \exp j(3q\theta-3m\alpha) + A_{3q}^* D_{3m}(x,y) \exp -j(3q\theta-3m\alpha) \} \\
& + 3 \sum_{q=1} \sum_{m=1} \left\{ A_{3q-2} D_{3m-2}^*(x,y) \exp j((3q-2)\theta-(3m-2)\alpha) \right. \\
& \quad \left. + A_{3q-2}^* D_{3m-2}(x,y) \exp -j((3q-2)\theta-(3m-2)\alpha) \right\} \\
& + 3 \sum_{q=1} \sum_{m=1} \left\{ A_{3q-2} D_{3m-1}(x,y) \exp j((3q-2)\theta+(3m-1)\alpha) \right. \\
& \quad \left. + A_{3q-2}^* D_{3m-1}^*(x,y) \exp -j((3q-2)\theta+(3m-1)\alpha) \right\} \\
& + 3 \sum_{q=1} \sum_{m=1} \left\{ A_{3q-1} D_{3m-2}(x,y) \exp j((3q-1)\theta+(3m-2)\alpha) + \right. \\
& \quad \left. A_{3q-1}^* D_{3m-2}^*(x,y) \exp -j((3q-1)\theta+(3m-2)\alpha) \right\} \\
& + 3 \sum_{q=1} \sum_{m=1} \left\{ A_{3q-1} D_{3m-1}^*(x,y) \exp j((3q-1)\theta-(3m-1)\alpha) + \right. \\
& \quad \left. A_{3q-1}^* D_{3m-1}(x,y) \exp -j((3q-1)\theta-(3m-1)\alpha) \right\} \\
& \quad \quad \quad (B.9)
\end{aligned}$$

The constant terms and $n=3q$ "triplen" time harmonics and $l=3m$ space harmonics interact only with each other to give the stationary field components in the first three terms above, and pairs of forward and backward traveling waves at velocities $(n/l)v$, where v is the synchronous speed (4th and 5th terms above). All 4 combinations of $n=(3q-1, 3q-2)$ and $l=(3m-1, 3m-2)$ interact with each other giving forward traveling waves at velocities $(n/l)v$ for $n=3q-2$ combined with $l=3m-2$ (6th term) and $n=3q-1$ with $l=3m-1$ (9th term); backward traveling waves at velocities $-(n/l)v$ are obtained for $n=3q-2$ combined with $l=3m-1$ (7th term) and $n=3q-1$ with $l=3m-2$ (8th term).

With purely sinusoidal current and winding field waveforms, only the third double sum contributes to the total field, which is purely DC. This corresponds to ideal, harmonic-free motoring action.

When we consider the observation point moving at a z-velocity v :

$$\begin{aligned} z &= z_0 + vt \\ &= z_0 + \frac{p\theta}{2\pi} \end{aligned} \tag{B.10}$$

which can be rewritten in terms of α :

$$\alpha = \alpha_0 + \theta \tag{B.11}$$

the field at the moving observation point is:

$$\begin{aligned}
B_{m\theta v} = & 3A_0D_0 + 3A_0 \sum_{m=1} (D_{3m} \exp(j3m\alpha_0) \exp(j3m\theta) + D_{3m}^* \exp(-j3m\alpha_0) \exp(-j3m\theta)) \\
& + 3D_0 \sum_{q=1} (A_{3q} \exp(j3q\theta) + A_{3q}^* \exp(-j3q\theta)) \\
& + 3 \sum_{q=1} \sum_{m=1} \left\{ A_{3q-2} D_{3m-2}^*(x,y) \exp(-j(3m-2)\alpha_0) \exp(j(3q-3m)\theta) + \right. \\
& \quad \left. A_{3q-2}^* D_{3m-2}(x,y) \exp(j(3m-2)\alpha_0) \exp(-j(3q-3m)\theta) \right\} \\
& + 3 \sum_{q=1} \sum_{m=1} \left\{ A_{3q-2} D_{3m-1}(x,y) \exp(j(3m-1)\alpha_0) \exp(j(3q+3m-3)\theta) + \right. \\
& \quad \left. A_{3q-2}^* D_{3m-1}^*(x,y) \exp(-j(3m-1)\alpha_0) \exp(-j(3q+3m-3)\theta) \right\} \\
& + 3 \sum_{q=1} \sum_{m=1} \left\{ A_{3q-1} D_{3m-2}(x,y) \exp(j(3m-2)\alpha_0) \exp(j(3q+3m-3)\theta) + \right. \\
& \quad \left. A_{3q-1}^* D_{3m-2}^*(x,y) \exp(-j(3m-2)\alpha_0) \exp(-j(3q+3m-3)\theta) \right\} \\
& + 3 \sum_{q=1} \sum_{m=1} \left\{ A_{3q-1} D_{3m-1}(x,y) \exp(-j(3m-1)\alpha_0) \exp(j(3q-3m)\theta) + \right. \\
& \quad \left. A_{3q-1}^* D_{3m-1}(x,y) \exp(j(3m-1)\alpha_0) \exp(-j(3q-3m)\theta) \right\} \\
& + 3 \sum_{q=1} (A_{3q} \exp(j3q\theta) + A_{3q}^* \exp(-j3q\theta)) \\
& \times \sum_{m=1} (D_{3m} \exp(j3m\alpha_0) \exp(j3m\theta) + D_{3m}^* \exp(-j3m\alpha_0) \exp(-j3m\theta))
\end{aligned} \tag{B.12}$$

which corresponds to a translation of $-\omega$ in the frequency domain.

B.2 AC Fields from a 3-phase Linear Winding: Sine-Cosine Formulation

Here, the complex exponentials are replaced by the appropriate circular functions, which is more convenient for computation by eliminating complex domain calculations. The phase-a current is resolved to:

$$I(\theta) = E_0 + \sum_{n=1} E_n \cos n\theta + \sum_{n=1} F_n \sin n\theta \tag{B.13}$$

Here E and F are related to the complex A coefficients as

$$A_n = \frac{E_n}{2} - j \frac{F_n}{2} \quad (\text{B.14})$$

Similarly the \pm phase a coil field expressed as a complex exponential series in Eq. (3.3.4) may be written as

$$B_z = I(\theta) \left\{ G_0 + \sum_{l=1}^{\infty} (G_l(x,y) \cos(l\alpha) + H_l(x,y) \sin(l\alpha)) \right\} \quad (\text{B.15})$$

with G and H being related to D analogously to Eq.(B.4).

The total field then is

$$\begin{aligned}
\mathbf{B}_{\text{tot}} = & 3E_0G_0 + 3E_0 \sum_{m=1} (G_{3m} \cos(3m\alpha) + H_{3m} \sin(3m\alpha)) \\
& + 3G_0 \sum_{q=0} (E_{3q} \cos(3q\theta) + F_{3q} \sin(3q\theta)) \\
& + \frac{3}{2} \sum_{q=1} \sum_{m=1} \left\{ (E_{3q}G_{3m} - F_{3q}H_{3m}) \cos(3q\theta + 3m\alpha) + (E_{3q}H_{3m} + F_{3q}G_{3m}) \sin(3q\theta + 3m\alpha) \right\} \\
& + \frac{3}{2} \sum_{q=1} \sum_{m=1} \left\{ (E_{3q}G_{3m} + F_{3q}H_{3m}) \cos(3q\theta - 3m\alpha) - (E_{3q}H_{3m} - F_{3q}G_{3m}) \sin(3q\theta - 3m\alpha) \right\} \\
& + \frac{3}{2} \sum_{q=1} \sum_{m=1} \left\{ (E_{3q-2}G_{3m-2} + F_{3q-2}H_{3m-2}) \cos((3q-2)\theta - (3m-2)\alpha) \right. \\
& \quad \left. + (F_{3q-2}G_{3m-2} - E_{3q-2}H_{3m-2}) \sin((3q-2)\theta - (3m-2)\alpha) \right\} \\
& + \frac{3}{2} \sum_{q=1} \sum_{m=1} \left\{ (E_{3q-2}G_{3m-1} - F_{3q-2}H_{3m-1}) \cos((3q-2)\theta + (3m-1)\alpha) \right. \\
& \quad \left. + (E_{3q-2}H_{3m-1} + F_{3q-2}G_{3m-1}) \sin((3q-2)\theta + (3m-1)\alpha) \right\} \\
& + \frac{3}{2} \sum_{q=1} \sum_{m=1} \left\{ (E_{3q-1}G_{3m-2} - F_{3q-1}H_{3m-2}) \cos((3q-1)\theta + (3m-2)\alpha) \right. \\
& \quad \left. + (E_{3q-1}H_{3m-2} + F_{3q-1}G_{3m-2}) \sin((3q-1)\theta + (3m-2)\alpha) \right\} \\
& + \frac{3}{2} \sum_{q=1} \sum_{m=1} \left\{ (E_{3q-1}G_{3m-1} + F_{3q-1}H_{3m-1}) \cos((3q-1)\theta - (3m-1)\alpha) \right. \\
& \quad \left. + (F_{3q-1}G_{3m-1} - E_{3q-1}H_{3m-1}) \sin((3q-1)\theta - (3m-1)\alpha) \right\} \\
& \qquad \qquad \qquad \text{(B.16)}
\end{aligned}$$

Then the equation of motion (B.1) is substituted:

$$\begin{aligned}
B_{\text{mov}} = & 3E_0G_0 + 3E_0 \sum_{m=1} (G_{3m} \cos(3m\theta+3m\alpha_0) + H_{3m} \sin(3m\theta+3m\alpha_0)) \\
& + 3G_0 \sum_{q=0} (E_{3q} \cos(3q\theta) + F_{3q} \sin(3q\theta)) \\
& + \frac{3}{2} \sum_{q=1} \sum_{m=1} \left\{ (E_{3q}G_{3m} - F_{3q}H_{3m}) \cos((3q+3m)\theta+3m\alpha_0) \right. \\
& \quad \left. + (E_{3q}H_{3m} + F_{3q}G_{3m}) \sin((3q+3m)\theta+3m\alpha_0) \right\} \\
& + \frac{3}{2} \sum_{q=1} \sum_{m=1} \left\{ (E_{3q}G_{3m} + F_{3q}H_{3m}) \cos((3q-3m)\theta-3m\alpha_0) \right. \\
& \quad \left. - (E_{3q}H_{3m} - F_{3q}G_{3m}) \sin((3q-3m)\theta-3m\alpha_0) \right\} \\
& + \frac{3}{2} \sum_{q=1} \sum_{m=1} \left\{ (E_{3q-2}G_{3m-2} + F_{3q-2}H_{3m-2}) \cos((3q-3m)\theta - (3m-2)\alpha_0) \right. \\
& \quad \left. + (F_{3q-2}G_{3m-2} - E_{3q-2}H_{3m-2}) \sin((3q-3m)\theta - (3m-2)\alpha_0) \right\} \\
& + \frac{3}{2} \sum_{q=1} \sum_{m=1} \left\{ (E_{3q-2}G_{3m-1} - F_{3q-2}H_{3m-1}) \cos((3q+3m-3)\theta + (3m-1)\alpha_0) \right. \\
& \quad \left. + (E_{3q-2}H_{3m-1} + F_{3q-2}G_{3m-1}) \sin((3q+3m-3)\theta + (3m-1)\alpha_0) \right\} \\
& + \frac{3}{2} \sum_{q=1} \sum_{m=1} \left\{ (E_{3q-1}G_{3m-2} - F_{3q-1}H_{3m-2}) \cos((3q+3m-3)\theta + (3m-2)\alpha_0) \right. \\
& \quad \left. + (E_{3q-1}H_{3m-2} + F_{3q-1}G_{3m-2}) \sin((3q+3m-3)\theta + (3m-2)\alpha_0) \right\} \\
& + \frac{3}{2} \sum_{q=1} \sum_{m=1} \left\{ (E_{3q-1}G_{3m-1} + F_{3q-1}H_{3m-1}) \cos((3q-3m)\theta - (3m-1)\alpha_0) \right. \\
& \quad \left. + (F_{3q-1}G_{3m-1} - E_{3q-1}H_{3m-1}) \sin((3q-3m)\theta - (3m-1)\alpha_0) \right\} \\
& \quad \quad \quad (B.17)
\end{aligned}$$

B.3 AC Field Spectrum

The high symmetry of the rectangular three-phase winding coils with pole pitch exactly $1/2$ of the wavelength eliminates even harmonics from the spatial spectrum. In general, some even harmonic content may be expected. The 120 degree current waveform has no even or triplen harmonics by design, leaving 1,5,7,11,13... Therefore the AC field spectrum imposed on the field coil has only $6n$ harmonics. In the more general case with some even space and/or time harmonics, $6n-3$ harmonics will also be generated. Here this means that at cruising speed, a 72 Hz (3×24 Hz) component will also appear, which will be less effectively shielded than the 144 Hz component considered above. However, the even harmonic content could be expected to be relatively low, so that 144 Hz losses dominate the 72 Hz contribution.

APPENDIX C. 3D EM ANALYSIS PROGRAM H3D

The three dimensional electromagnetic analysis required for the shielding studies performed for this study was done using a GE-developed program called H3D. This appendix is a technical paper describing this computer program and its advantages and disadvantages relative to other programs available commercially.

MAGNETOSTATIC CANCELLATION ERROR REVISITED

Gary Bedrosian
GE Corporate Research & Development
Schenectady, New York 12301

Abstract – We examine the conditions under which finite element representations of magnetostatic fields using magnetic scalar potentials suffer from cancellation errors. We show that cancellation errors can arise from numerical roundoff at several points in the calculation, and that the magnetic field from a full scalar potential is not necessarily more accurate than the magnetic field from a reduced scalar potential. We also present a method for controlling cancellation error in the source term for reduced scalar potentials.

INTRODUCTION

The calculation of magnetostatic fields in three dimensions with a scalar potential has attracted the interest of researchers in the electromagnetic finite element community because of its inherent advantages over a vector potential: fewer unknowns per node and no gauge condition to satisfy. Seminal papers by Carpenter [1] and Zienkiewicz et al. [2] presented the basic formulation of a reduced magnetic scalar potential arising from the separation of the magnetic field, H , into the sum of two parts: H_s , the magnetic field produced by source currents in free space, and H_m , the magnetic field produced by magnetization of iron parts:

$$H = H_s + H_m \quad (1)$$

Since H_m is irrotational, it can be written as the negative gradient of a reduced scalar potential, Φ :

$$H_m = -\nabla \Phi \quad (2)$$

Simkin et al. pointed out in [3] that the reduced scalar potential formulation can lead to numerical errors in highly permeable materials because in those materials the two terms, H_s and H_m , are nearly equal in magnitude but opposite in direction; they went on to recommend splitting the problem region into a full scalar potential region (containing permeable materials) and a reduced scalar potential region (containing source currents). In the full (or total) scalar potential region, the total magnetic field is

$$H = -\nabla \Psi \quad (3)$$

The continuity of $n \times H$ at the interface between the two regions is strongly enforced by the integral

$$\Psi(p) = \Phi(p) - \int_{P_0}^p H_s \cdot dt \quad (4)$$

where dt is the path along (tangent to) the interface surface from an arbitrary point (p_0) where $\Psi = \Phi$ to the calculated point (p). Continuity of $n \cdot B$ is enforced in a weak sense by the imposition of a flux-type source term

$$n \cdot (\mu_0 \nabla \Phi - \mu_1 \nabla \Psi) = n \cdot \mu_0 H_s \quad (5)$$

Mayergoz et al. proposed reducing cancellation error by solving for the difference between the solution with the actual permeability and the solution with infinite permeability [4]. Since the magnetic field in iron for the infinite permeability case is exactly zero, the difference field is the same as the total field in iron. The difficulty with this method is finding an accurate numerical solution for infinite permeability. The authors suggest solving the infinite permeability problem approximately by assuming a large constant value for permeability. Unfortunately, this simple prescription creates another kind of error, since the magnetic field in the iron for finite permeability is not zero and so the difference field is not exactly equal to the total field. Also, the question of how high is high enough for the permeability will trouble the analyst.

Solving the infinite permeability case rigorously is tantamount to setting $\Psi = 0$ in (4) and (5) above. The necessary programming to do this amounts to the same basic capabilities for either the two-scalar approach or the infinite permeability approach. The first step is to identify one or more connected surfaces of permeable parts to calculate the integral in (4). Then one point is arbitrarily picked on each such bounding surface, and the integral in (4) is evaluated for all of the nodes on the surface(s). One must evaluate the integral accurately to maintain the path-independence of its value, which follows from

$$\oint_C H_s \cdot dt = 0 \quad (6)$$

where C is any closed contour on the surface between the regions.

It is certainly possible to write such a program, but is it necessary? Despite the possibility of cancellation error problems with the reduced scalar potential in highly permeable regions, McDaniel et al. reported acceptable numerical results [5]. Instead of writing a new program, they adapted a commercially available program for heat transfer by casting the electromagnetic equations into comparable thermal equations, with temperature taking the place of reduced scalar potential. We will see later that their representation of the source term as a surface integral because of their limited access to the volume shape functions was serendipitous. Unfortunately, their experience has had seemingly little impact on programs specifically written for electromagnetics.

We revisited the issue of cancellation error while writing a three-dimensional, nonlinear magnetostatic finite element analysis program. The original implementation used a two-scalar approach. However, we found it to be too cumbersome and prone to errors in matching solutions using (4) and (5). A detailed investigation of cancellation was in order. If we could use a reduced scalar potential everywhere without cancellation problems, the finite element program would be simplified for both the developers and the users. This paper describes the results of the investigation.

MATHEMATICAL FORMULATION

Maxwell's equations relevant to magnetostatic fields are

$$\nabla \times H = J_s \quad (7)$$

$$\nabla \cdot B = 0 \quad (8)$$

where B and H are connected by the usual relationship

$$B = \mu H \quad (9)$$

If H is split into $H_s + H_m$, then (7) is identically satisfied since

$$\nabla \times H = \nabla \times (H_s + H_m) = \nabla \times H_s - \nabla \times \nabla \Phi = J_s \quad (10)$$

Using (1), (2), and (9), Maxwell's divergence equation (8) becomes

$$\nabla \cdot (\mu \nabla \Phi) = \nabla \cdot (\mu H_s) \quad (11)$$

To convert (11) into a finite element matrix equation, let

$$\Phi = \sum_{j=1}^{\text{nodes}} \Phi_j N_j \quad (12)$$

where N_j are node-based shape functions and Φ_j are unknown coefficients. Using a Galerkin-type weighted residual method,

multiply (11) by one of the shape functions, N_i , and integrate over all volume

$$\sum_{j=1}^{\text{nodes}} \Phi_j \int_V N_i \nabla \cdot (\mu \nabla N_j) dV = \int_V N_i \nabla \cdot (\mu H_s) dV \quad (13)$$

The integral on the left-hand side of (13) is inconvenient as it stands because it involves a second derivative. It can be transformed to an integral involving only first derivatives with the divergence theorem

$$\int_V N_i \nabla \cdot (\mu \nabla N_j) dV = - \int_V \nabla N_i \cdot \mu \nabla N_j dV + \oint_S N_i \mu \nabla N_j \cdot dS \quad (14)$$

where S is the surface at the outer boundary of the problem. The right-hand side can be similarly transformed to obtain

$$\int_V N_i \nabla \cdot (\mu H_s) dV = - \int_V \nabla N_i \cdot \mu H_s dV + \oint_S N_i \mu H_s \cdot dS \quad (15)$$

Combining (14) and (15), the finite element equation is now

$$\sum_{j=1}^{\text{nodes}} \Phi_j \int_V \nabla N_i \cdot \mu \nabla N_j dV = \int_V \nabla N_i \cdot \mu H_s dV - \oint_S N_i \mu (H_s - \nabla \Phi) \cdot dS \quad (16)$$

This is the expression used in [3] for calculation of the reduced scalar potential solution.

One need not invoke the divergence theorem to evaluate the right-hand side integral in (13), since it involves only a first derivative. Because H_s satisfies both (7) and (8) in free space,

$$\nabla \cdot (\mu H_s) = (\nabla \mu) \cdot H_s + \mu \nabla \cdot H_s = (\nabla \mu) \cdot H_s \quad (17)$$

The $(\nabla \mu)$ in (17) can be written as the sum of two parts:

$$\nabla \mu = (\nabla \mu)^{\text{vol}} + (\Delta \mu) \delta(S) n \quad (18)$$

where $(\nabla \mu)^{\text{vol}}$ is the smooth change in μ due to nonlinearity within a material region and $(\Delta \mu) \delta(S) n$ is the abrupt change in μ at material interfaces. $\delta(S)$ is a delta function at the interface surface and n is the surface normal unit vector. The finite element equations can then be expressed as

$$\sum_{j=1}^{\text{nodes}} \Phi_j \int_V \nabla N_i \cdot \mu \nabla N_j dV = \oint_S N_i \mu \nabla \Phi \cdot dS - \int_V N_i (\nabla \mu)^{\text{vol}} \cdot H_s dV - \oint_S N_i (\Delta \mu) H_s \cdot dS \quad (19)$$

Note that S is the surface at the outer boundary of the problem, while S' includes all of the interfaces between regions with different permeabilities. Mathematically, (16) and (19) should lead to the same right-hand side of the finite element matrix equation. However, we will see in the next section that the right-hand side of (16) is prone to a type of cancellation error.

SOURCES OF CANCELLATION ERRORS

In this section, we will discuss sources of cancellation errors and present some numerical examples of each type. Cancellation errors in problems involving magnetostatic scalar potentials fall into three categories: (1) cancellation of H_s by H_m , (2) cancellation of source terms in volume integrals, and (3) numerical differentiation. Of the three types, only type 1 has received extensive discussion in the literature. We will show that types 2 and 3 actually dominate the overall error in the numerical solution.

Cancellation of H_s by H_m

Consider a sphere of radius a and permeability μ immersed in a uniform external field, H_s . In the interior of the sphere,

$$H_m = \left(\frac{\mu_0 - \mu}{\mu + 2\mu_0} \right) H_s \quad (20)$$

$$H = \left(\frac{3\mu_0}{\mu + 2\mu_0} \right) H_s \quad (21)$$

Since the field in the sphere is uniform, μ is constant whether the sphere is made of linear or nonlinear material. If the material is nonlinear, μ is a function of $|H|$. Assume for the moment that $\mu = 1000 \mu_0$ in (20) and (21). A 1% error in H_m would create a 334% error in H using (1) versus the exact value in (21). This would seem at first glance to be an irredeemable fault of the reduced scalar potential formulation in highly permeable regions.

The quantity of interest, however, is not H in the interior of the iron, where it is not directly observable, but the magnetization of the sphere, M , as seen from its effect on the field outside:

$$M = -H_m = \left(\frac{\mu - \mu_0}{\mu + 2\mu_0} \right) H_s \quad (22)$$

A 1% error in H_m creates a 1% error in M assuming linear μ . An error in the total magnetic field, H , only affects the error in M through the dependence of μ on $|H|$ in nonlinear materials:

$$\frac{\partial |M|}{\partial |H|} = \frac{\partial |M|}{\partial \mu} \frac{\partial \mu}{\partial |H|} = \frac{3\mu_0}{(\mu + 2\mu_0)^2} \frac{\partial \mu}{\partial |H|} |H_s| \quad (23)$$

An evaluation of (23) using material property curves for several types of steel found the maximum magnitude at roughly the same point: $|H_s| = 500,000$; $|H| = 100,000$; $|M| = 400,000$; $\mu = 13 \mu_0$. (Magnetic fields are in amperes/meter.) At that point, a 1% error in H_m would lead to a 4% error in H , which would in turn create only a 1% error in M due to an incorrect value for μ . At other values of saturation, the error in M due to nonlinear effects is less.

Qualitatively, there are three zones of saturation to consider. When the material is far below saturation, μ is large and cancellation errors in H are high, but M in (22) is insensitive to the resulting error because the leading factor is approximately 1 when μ is large. When the material is fully saturated, μ is small and cancellation errors in H are not overwhelming. The highest error occurs in a transition region, but even there the error is acceptable. Note again that H is not directly observable outside the sphere, only M . We conclude that the cancellation error in H in permeable materials is insufficient cause to abandon the reduced scalar potential.

Cancellation in Source Terms

We consider next the difference between (16) and (19) for calculation of the right-hand side of the finite element matrix equation. The surface integral over S in both (16) and (19) relates to the boundary condition at the boundary of the finite element region. In order to simplify the discussion, we will assume that the boundary has been handled by one of several methods beyond the scope of this paper. We are concerned here with the contrasting methods of calculating the right-hand side for nodes completely within the finite element grid. Consider the small two-dimensional example with first-order triangles shown in Figure 1.

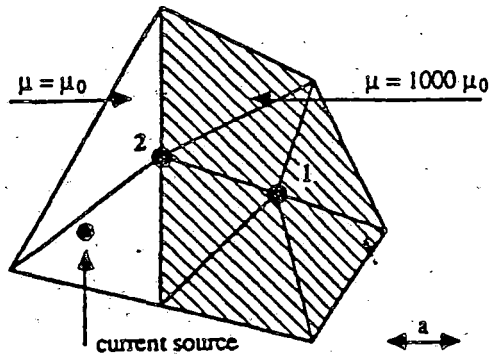


Figure 1. Finite Element Grid for Source Calculation

In Figure 1, the line source carries current I at a distance of a units from the interface between $\mu = \mu_0$ and $\mu = 1000 \mu_0 = \mu_1$. (All distances in Figure 1 are drawn to scale.) The right-hand sides (rhs) for nodes 1 and 2 were calculated using (16) and (19) respectively using progressively higher orders of Gaussian numerical integration. The integrations can also be performed analytically:

$$\text{rhs}(1) = \frac{I(\mu_1 - \mu_0)}{2\pi} [0.0] \tag{24}$$

$$\text{rhs}(2) = \frac{I(\mu_1 - \mu_0)}{2\pi} [0.653504076] \tag{25}$$

Tables 1 and 2 summarize the results [using the dimensionless quantities in brackets in (24) and (25) for comparison]:

rhs(1)	rhs(2)	order	points
-0.011698153	0.686137716	1	5
0.001918182	0.645299013	2	15
-0.000444303	0.654987040	3	30
-0.000098656	0.654349752	5	35
0.000026822	0.653314212	6	60

Table 1. Source Calculations Using Equation (16)

rhs(1)	rhs(2)	order	points
0.0	0.400000000	1	2
0.0	0.692307692	3	4
0.0	0.647549020	5	6
0.0	0.654596232	7	8
0.0	0.653316186	9	10

Table 2. Source Calculations Using Equation (19)

Note that the integration order column in the tables above is the order of polynomial that is integrated exactly with the respective Gaussian integration scheme, and the number of evaluation points counts all points in all elements (surface or volume).

We can draw three conclusions from a comparison of Tables 1 and 2 with (24) and (25). First, it is evident that (16) and (19) lead to identical matrix equations and right-hand sides, provided that the respective integrations are sufficiently accurate. Second, relatively high-order integration formulas are required for accurate calculations of the right-hand side using either (16) or (19). This is an interesting result because a first-order integration formula is exact

for the calculation of the stiffness matrix components on the left-hand sides of (16) or (19) for first-order triangular elements in two-dimensional and axisymmetric problems, or first-order tetrahedral elements in three-dimensional problems. Third, the surface integration in (19) removes the cancellation error from the calculation of the right-hand side for interior nodes (node 1 in Figure 1) and proves to be more efficient in terms of evaluation points for a given level of accuracy than the volume integration in (16).

These arguments are somewhat altered for nonlinear materials, but the essence remains. The volume term in (19) needs to be added to the integration if the variation of μ within the element is modeled. A good method is to calculate μ at each of the nodes of the element, and then calculate $\nabla \mu$ with the element shape functions. There will be discontinuous jumps in μ between elements within nonlinear materials as well as at surfaces between the materials and air. The author has found acceptable accuracy in three-dimensional problems with second-order elements by simply assuming constant μ in each element based on the value of $|H|$ at the respective centroids. For first-order elements, μ is constant within the element in any case.

Numerical Differentiation

Calculation of H_m from Φ in (2) or H from Ψ in (3) requires numerical differentiation using finite element shape functions. If $|H|$ is small, it does not automatically follow that Ψ is small, only that the difference between Ψ values at adjacent nodes is small. If the average value of Ψ is high and the elements are small, then significant cancellation errors (of a type) can occur when Ψ is numerically differentiated. To see how this can happen, consider the C-magnet model illustrated in Figure 2.

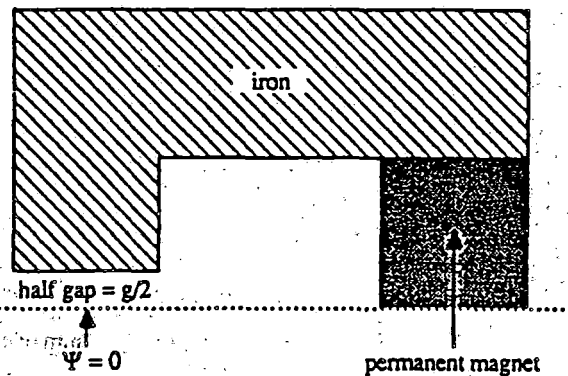


Figure 2. C-Magnet Model

Figure 2 shows the top half of the C-magnet above the symmetry plane. The C-magnet is driven by a permanent magnet source, and so the magnetic field in the entire region can be described by a total scalar potential, Ψ .

Figure 3 is an illustration of a first-order finite element grid at the center of the upper pole face. Node 2 is on the pole face and node 1 is one layer (thickness a) above node 2. If the z (vertical) magnetic field in the gap, H^{gap} , is approximately constant, then

$$\Psi_2 = - \int_0^{g/2} H^{gap} dz = - \frac{g H^{gap}}{2} \tag{26}$$

Matching $n \cdot B$ at the pole face, we have

$$H^{iron} = - \frac{\partial \Psi}{\partial z} = \frac{\Psi_2 - \Psi_1}{a} = \frac{\mu_0}{\mu_1} H^{gap} \tag{27}$$

where μ_1 is the permeability in the iron. The relative potential difference between nodes 1 and 2 is

$$\frac{\Psi_1 - \Psi_2}{\Psi_2} = \frac{2 \mu_0 a}{\mu_1 g} \tag{28}$$

which is a small number when $\mu_1 \gg \mu_0$ and $g \gg a$. Numerical differentiation in this region can result in significant error.

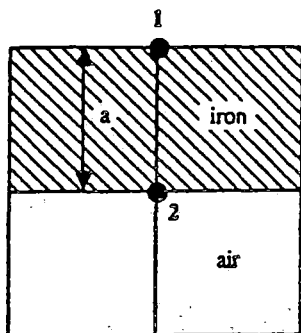


Figure 3. Detail of Finite Element Model at Pole Face

To test the effects of numerical differentiation error, we created three finite element models for a sphere with $\mu = 1000 \mu_0$ immersed in a constant external magnetic field, $|H_x| = \Psi/L$, where L was 10 times the radius of the sphere. In case 1, we used a total scalar potential with the center of the sphere at $\Psi = 0$. In case 2, we used a total scalar potential with the center of the sphere at $\Psi = \Psi_s$. In case 3, we used a reduced scalar potential with the center of the sphere at $\Phi = 0$ perforce. In all cases, we set an inhomogeneous Dirichlet boundary condition at the outer boundary of the grid by using the analytical solution. These models were solved with an in-house finite element program. Table 3 summarizes the results.

Case	Max. Rel. Error in $ H $
1. Total pot., cent. $\Psi = 0$	0.05%
2. Total pot., cent. $\Psi = \Psi_s$	3%
3. Reduced pot., cent. $\Phi = 0$	0.25%

Table 3. Comparison of Relative Errors in Total Magnetic Field

As case 2 clearly shows, using a total scalar potential does not guarantee a low error in the total magnetic field. The accuracy of case 3 might have been further improved if the software had been modified to use (19) to calculate the right-hand side rather than (16).

CONCLUSIONS

We have shown in this paper that cancellation errors in the finite element formulation of the magnetostatic field problem come from three sources: cancellation of the source field, H_s , with the reaction field, H_m ; cancellation in the integration of the right-hand side of the finite element matrix equation; and numerical differentiation. We have demonstrated that the first type of error is not as serious as previously supposed as long as one is interested in measurable fields outside iron parts. We have also shown that the total scalar potential formulation, contrary to previous reports, does not guarantee minimum cancellation error in iron. With these results, we can solve for a reduced scalar potential everywhere and maintain acceptable accuracy, simplifying both the analysis and the software.

ACKNOWLEDGEMENTS

The author appreciates having the opportunity to discuss this topic at length with M.V.K. Chari of the General Electric Company and I.D. Mayergoz of the University of Maryland.

REFERENCES

- [1] C.J. Carpenter, "Numerical Solution of Magnetic Fields in the Vicinity of Current-Carrying Conductors," *Proceedings of the IEE*, Vol. 114, No. 11, November 1967, pp. 1793-1800.
- [2] O.C. Zienkiewicz, J. Lyness, and D.R.J. Owen, "Three-Dimensional Magnetic Field Determination Using a Scalar Potential - A Finite Element Solution," *IEEE Transactions on Magnetics*, Vol. MAG-13, No. 5, September 1977, pp. 1649-1656.
- [3] J. Simkin and C.W. Trowbridge, "On the Use of the Total Scalar Potential in the Numerical Solution of Field Problems in Electromagnetics," *International Journal for Numerical Methods in Engineering*, Vol. 14, 1979, pp. 423-440.
- [4] I.D. Mayergoz, M.V.K. Chari, and J. D'Angelo, "A New Scalar Potential Formulation for Three-Dimensional Magnetostatic Problems," *IEEE Transactions on Magnetics*, Vol. MAG-23, No. 6, November 1987, pp. 3889-3894.
- [5] T.W. McDaniel, R.B. Fernandez, R.R. Root, and R.B. Anderson, "An Accurate Scalar Potential Finite Element Method for Linear, Two-Dimensional Magnetostatic Problems," *International Journal for Numerical Methods in Engineering*, Vol. 19, 1983, pp. 725-737.

APPENDIX D. COMPUTER PROGRAMS USED IN THIS STUDY

Numerous computer programs were employed in the performance of this research, most of which were developed at GE-CRD for this or other projects requiring similar analyses. Short descriptions of these programs, and their capabilities, are provided here.

ANSYS

This is a finite element analysis package available commercially, which performs stress and thermal analyses.

CAE2D

CAE2D is a general finite element analysis package containing many subprograms which perform analyses of structural, thermal, and electromagnetic problems. Its electromagnetic capabilities are limited to two dimensional and axisymmetric problems, but do include the modeling of time dependent problems involving eddy currents. Sophisticated graphical pre- and postprocessors are included in this package to aid in evaluation of results.

GE_MAGLEV

GE_MAGLEV was developed expressly for the purposes of this research. It models the field of a set of vehicle coils in space using the Biot-Savart law. It was linked with a three dimensional postprocessor to allow better evaluation of results.

H3D

Another GE-CRD developed program, H3D performs fully three dimensional steady state analysis of electromagnetic problems involving iron and conductors.

RACEFOR

RACEFOR computes the fields and forces inside and external to a racetrack shaped coil, including all effects. Elliptic integrals are used for the field formulation inside the coil, and integration of $J \times B$ to compute the forces.

SUITE-Q

This program performs quench analyses of superconducting coils, solving the coupled thermal and electrical circuit equations with the coils represented by several segments. All material properties are modeled properly at cryogenic temperatures, and the temperature variations are included. Material properties have been determined by experiment for all structural and technical materials which are used in the superconducting coil modules.

APPENDIX E. GLOSSARY

E.1 Nomenclature

The nomenclature and acronyms used in this report are presented here. The varied technical areas in which contributions were made, coupled with the varied contributors, complicates the nomenclature somewhat.

Physical dimensions:

- L coil length (of the straight sides for a racetrack)
- H coil height (overall)
- P_{nf} pitch of null-flux coils
- w coil width
- b coil build
- g transverse gap from superconducting coil to guideway
- δ vertical offset between superconducting coil and null-flux coil
- τ pole pitch of motor windings
- r, R position vectors

Electromagnetic parameters:

- J current density
- I current
- V voltage
- L inductance
- R resistance
- B magnetic flux density
- H magnetic field
- μ_0 free space permeability ($4\pi \times 10^{-7}$ T-m/A)
- Φ magnetic flux
- N turn count in a coil
- η efficiency
- pf power factor
- v frequency
- P power

Mechanical parameters:

- F force
- P pressure

σ stress

ϵ strain

T thrust

E.2 Acronyms and Technical Terms

The acronyms and uncommon technical terms used in this report are described here.

AC: alternating current (also used to denote a time varying magnetic field created by such currents)

CPU: time used by the central processing unit on a computer

DC: direct current (also used to denote a steady state magnetic field created by such currents)

EDS: electrodynamic suspension

EM: electromagnetic

G-M: Gifford McMahon thermodynamic cycle

GE: General Electric Co.

GTO: gate turn-off thyristor, an electronic device

J-T: Joule-Thompson thermodynamic cycle

JR: Japan Railways

MR: magnetic resonance

MRI: magnetic resonance imaging

PWM: pulse width modulation, a control logic for an inverter

RMS: root-mean squared

SCR: silicon controlled rectifier

quench: the transition from the superconducting to the normal resistive state in a superconductor

von Mises: a measure of the average stress state in a material

stray field index: a measure of the fraction of a passenger compartment which falls below a given magnetic field value

**PROPERTY OF FRA
RESEARCH & DEVELOPMENT
LIBRARY**

Novel Cryogen-Free Actively Shielded
Superconducting Magnets for MAGLEV Vehicles,
US DOT, FRA, NMI, ME Vermilyea, 1992 -11-
Advanced Systems